Dipl.-Ing. Thomas Haberkorn

Aircraft separation in uncontrolled airspace including human factors

DISSERTATION

zur Erlangung des akademischen Grades
Doktor der technischen Wissenschaften

eingereicht an der

Technischen Universität Graz

Betreuer
Ao.Univ.-Prof. Dipl.-Ing. Dr.techn. Reinhard Braunstingl

Institut für Mechanik

Graz, April 3, 2016

EIDESSTATTLICHE ERKLÄRUNG

AFFIDAVIT

Ich erkläre an Eides statt, dass ich die vorliegende Arbeit selbstständig verfasst, andere als die angegebenen Quellen/Hilfsmittel nicht benutzt, und die den benutzten Quellen wörtlich und inhaltlich entnommenen Stellen als solche kenntlich gemacht habe. Das in TUGRAZonline hochgeladene Textdokument ist mit der vorliegenden Dissertation identisch.

I declare that I have authored this thesis independently, that I have not used other than the declared sources/resources, and that I have explicitly indicated all material which has been quoted either literally or by content from the sources used. The text document uploaded to TUGRAZonline is identical to the present doctoral dissertation.

_____   _____

Datum / Date   Unterschrift / Signature

Preface

This thesis is submitted for the degree of Dr. techn. at the University of Graz, Austria. The research described herein was conducted under the supervision of Dr. Reinhard Braunstingl at the Institute of Mechanics, Faculty of Mechanical Engineering and Economic Sciences.

The present thesis is to the best of the knowledge of the author original, and has not been submitted at any other university. References and acknowledgments to other work are cited in the text and specified in the bibliography. The reports and results of the experiments contained in this work have been presented in the following publications:

T. Haberkorn, I. Koglbauer, R. Braunstingl, and B. Prehofer, "Requirements for Future Collision Avoidance Systems in Visual Flight: A Human-Centered Approach," *Human-Machine Systems, IEEE Transactions on*, vol. 43, no. 6, pp. 583-594, Nov 2013.

T. Haberkorn, I. Koglbauer, and R. Braunstingl, "Traffic displays for visual flight indicating track and priority cues," *Human-Machine Systems, IEEE Transactions on*, vol. 44, no. 6, pp. 755-766, Dec 2014.

The manuscript was created using LaTeX. The citation style *IEEEtran* was used, which is standard for IEEE Transactions journals and conferences.

Graz, April 3, 2016

Acknowledgments

The author gratefully acknowledges the pilots who participated in the experiments conducted for this thesis. The reviewers of the publications created for this thesis also contributed with valuable questions and remarks.

In this regard the author is indebted for the help received from of Dr. Ioana Koglbauer, who did suggest and supervise the design and statistical analysis of the experiments. Thanks also to the Institute of Mechanics, in particular Dr. Reinhard Braunstingl, for the provision of the flight simulator facilities and helpful remarks.

Everything should be made as simple as possible, but not simpler.

(Albert Einstein)

Abstract

Pilots who are flying in Visual Meteorological Conditions (VMC) have the ultimate responsibility of keeping proper separation from other aircraft. However, recent data provided by the UK Airprox Board shows that the numbers of close encounters are increasing, especially in situations of high traffic density and in uncontrolled airspace, where traffic information is not necessarily provided. In addition, a summary of past mid-air collisions reflect that most unintended air-proximity events happen due to poor execution of the see-and-avoid concept. This thesis addresses this problem by proposing and testing technological measures to support pilots in their decision-making process when flying in congested airspace. To reduce pilots' workload, various cockpit display variants utilizing predictive cues are designed and put to the test in experiments, yielding a feasible solution. Here, issues of human factors, such as physiological and psychological constraints are addressed. Apart from that, a simulator study investigated and reviewed pilots' reactions to imminent mid-air collisions in context with international regulation procedures. It was observed that about half of the avoidance maneuvers did not follow the right-of-way rules. In response to that, an algorithm for collision avoidance incorporating these rules is presented and applied to the dynamics of a small aeroplane. Such aircraft are used in the majority of flights involved in air proximity events. Optimal control methods are applied, yielding analytic results for the inertial acceleration during the avoidance maneuver.

Zusammenfassung

In letzter Instanz haben Piloten die Verantwortung, unter Sichtflugbedingen (VMC) ausreichend Distanz zu anderen in der Luft befindlichen Fluggeräten zu halten. Dennoch zeigen aktuelle Aufzeichnungen des UK Airprox Board, dass die Anzahl der nahen Vorbeiflüge insbesondere bei hoher Verkehrsdichte im unkontrollierten Luftraum ansteigt. In diesen Gebieten stehen nicht notwendigerweise Verkehrsinformationen zur Pilotenunterstützung zur Verfügung. Auch zeigt eine Übersicht über zurückliegende Zusammenstöße in der Luft, dass diese am häufigsten durch mangelhaftes Ausschauhalten verursacht wurden. Die vorliegende Arbeit nimmt dieses Problem als Anlass Maßnahmen zur Unterstützung von Piloten in Situationen mit hoher Verkehrsdichte vorzuschlagen und zu testen. Um die Arbeitsbelastung im Entscheidungsfindungsprozess zu verringern wurden zu diesem Zweck verschiedene vorausschauende Darstellungsvarianten für Cockpit-Displays entworfen und in Versuchsreihen gegenübergestellt. Hierbei wurden in erster Linie physiologische und psychologische Limitationen der menschlichen Wahrnehmung berücksichtigt. In einer weiteren Studie wurden Ausweichmanöver der Piloten in Kollisionsszenarien untersucht. Etwa die Hälfte dieser entsprach nicht den geltenden Luftverkehrsregeln. Dies als Anlass nehmend wurde ein Algorithmus zur Kollisionsvermeidung entworfen welcher auch die Ausweichregeln miteinbezieht. Die zugrunde gelegte Methode der optimalen Regelung liefert hierbei eine analytische Lösung für die inertialen Beschleunigungen während des Ausweichmanövers. Da die meisten nahen Vorbeiflüge zwischen Kleinflugzeugen stattfinden wurden Simulationsergebnisse für diese Flugzeugklasse berechnet und präsentiert.

Contents

List of Figures

List of Tables

1 Introduction

The main objectives addressed in this thesis are to suggest methods to avoid mid-air collisions and to reduce the workload of the pilot in visual flight. Flights operating in this regime are by regulations required to follow Visual Flight Rules (VFR) [1] [2]. Under VFR, the pilot is required to control the position and attitude of the aircraft visually, meaning with a clear view to outside references (like the horizon). This holds also with respect to maintaining separation to potentially hazardous objects like terrain, clouds or other aircraft.

For the latter, accident reports from the National Transportation Safety Board (NTSB) for the years 2010 to 2014 list 55 aircraft[1] involved in mid-air collisions [3]. These have to be seen as tip of the iceberg events, as they are the product of much more frequent *Airprox* events[2]. These are events reported to authorities when in the opinion of a pilot or an air traffic controller the distance between aircraft, speed and relative track have been such that the safety of the participants was compromised [4].
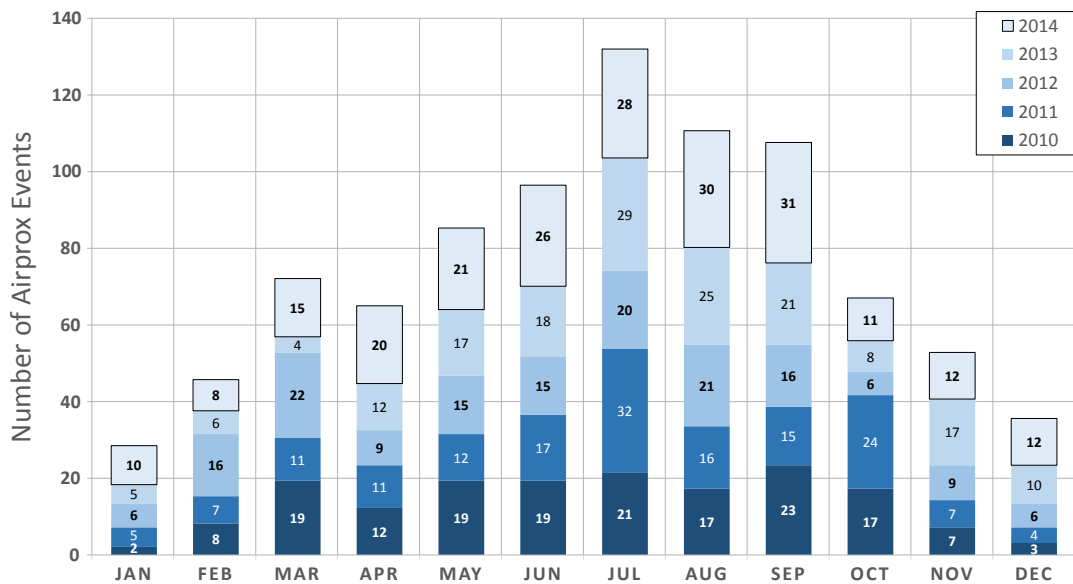
Figure 1.1: Number of Airprox events in the UK extracted from reports of the UK Airprox Board for the years 2010 to 2014. One airprox event refers to the encounter of two aircraft, as there was no encounter with three (or more) aircraft registered in this period.

---

[1]The number is odd because in one case an aircraft towing a glider was involved in a collision with another aircraft (NTSB Identification: CEN10FA115C).

[2]short for *Aircraft Proximity*.

The International Civil Aviation Organization (ICAO) requires national authorities to establish investigation and reporting procedures for these events. However, very few states freely make the findings of these events available to the public - e.g. Switzerland and the United Kingdom (UK). This thesis uses the particularly detailed data provided by the UK Airprox Board [5] to illustrate under which circumstances Airprox events occur. The objective is to recommend improvements to air traffic warning displays in the cockpit.

Fig. 1.1 shows the frequency of Airprox events in the UK from January 2010 to December 2014. In this period, 885 Airprox events were recorded. The bulk of incidents occur in the summer months, where daylight time is at its maximum. This suggests that a majority of incidents happened under VFR, where good visibility is mandatory (confirmed by [5]). The average number of Airprox events from 2010 to 2013 was 165 per year, which was surpassed in the year 2014 by 35%.

Facing this increase it is imperative that the conditions for Airprox events and midair collisions to occur have to be reviewed in this thesis. First, however, basic concepts of flight operation, notable midair collisions and mathematical tools to calculate evasion strategies are discussed in the following for proper introduction into the subject.

This thesis is structured as follows:

Section 1 addresses basic concepts needed to establish recommendations for on-board traffic display systems. This also includes a brief review of notable midair collisions. Furthermore, the human factors, which pose constraints on collision avoidance in visual flight, are introduced.

Section 2 presents an overview of the traffic information provided by commercial systems and other systems which are addressed by research.

Section 3 addresses the requirements for collision avoidance systems and the evading maneuvers pilots choose in a traffic conflict situation.

Section 4 identifies the potential for improvement of traffic displays for VFR. Furthermore, this section addresses VFR pilots' reaction and preferences to a traffic warning system during a simulated traffic conflict.

Section 5 describes a method for calculating the trajectory for evasion maneuvers of a small aeroplane and provides recommendations for its use.

1.1 Basic Concepts and Statistics

There are two sets of regulations determining how a flight can be operated: Instrument flight rules (IFR) and Visual flight rules (VFR). Flights under VFR depend solely on the visibility of outside features (e.g. the horizon, rivers, mountains, vegetation, other aircraft). Although aircraft operating under VFR are required to have a certain minimum of instruments (e.g. compass, altimeter, airspeed indicator) on-board[3] and in working condition, the view outside is the primary aid for navigation, orientation and separation

---

[3] for example in the United States: [6]

from still and moving obstacles. The minimum visibility conditions required for VFR flight are known as *visual meteorological conditions* (VMC) and are defined by national aviation authorities[4].

In contrast, the equipment and procedures required by IFR[5] allow a flight to be operated in instrument meteorological conditions (IMC), which are defined as less than the minimum visibility conditions specified for VMC. Most commercial airplanes are operated under IFR.

To separate flights, the whole navigable airspace is divided into three-dimensional regions[6], which have designations from A to G [8], in order of decreasing Air Traffic Control (ATC) regulation of flights. Airspace classes A to E are called *controlled airspace*, where ATC services are provided in accordance with the airspace classification.

Both class F and class G airspace are called *uncontrolled*, meaning that ATC services are not provided. Flights operating in these airspaces will typically be under VFR. However, traffic advisory for IFR flights in class F airspace regarding other IFR Traffic is provided *as far as practical* [8].

The main service provided by ATC is the separation of flights, which depends on the flight rules and the airspace classification (Table 1.1).

Class	Type of flight	Separation Provided
A	IFR only	All aircraft
B	IFR	All aircraft
	VFR	All aircraft
C	IFR	IFR from IFR
		IFR from VFR
	VFR	VFR from IFR
D	IFR	IFR from IFR
	VFR	Nil
E	IFR	IFR from IFR
	VFR	Nil
F	IFR	IFR from IFR as far as practical
	VFR	Nil
G	IFR	Nil
	VFR	Nil

Table 1.1: Overview of the separation provided for airspace classes and type of flight [8][a] (unless otherwise authorized).

[a]ICAO Annex 11: Air Traffic Services, Chapter 2, Appendix 4

In the UK, more than half of the total airspace is class G [9], which is reflected by the percentage of Airprox events in the UK (Fig. 1.2). Airprox events in controlled airspace

---

[4]for example in the United States: [7]

[5]See footnote 3.

[6]See airspaces in eastern Austria, for example, Fig. A.3.

comprise 39%, leaving the bulk in uncontrolled airspace in the UK.
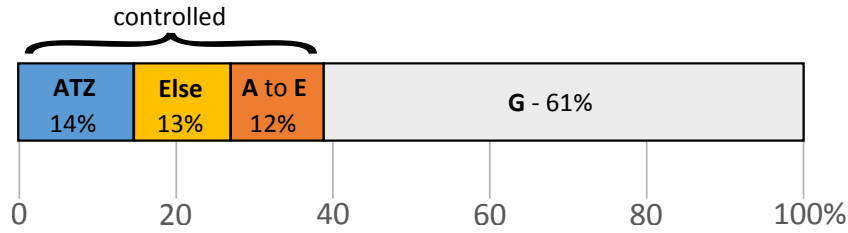
Figure 1.2: Airprox events in the UK in the years 2010 to 2014 [5]. ATZ refers to *Aerodrome Traffic Zones*, circular zones around an airport with a radius of 2 nautical miles (nm), extending from the surface to 2000 ft. All other airspaces (e.g. Military zones, Restricted areas, Offshore Safety Areas) are summarized in category *Else*. These airspaces are specific additions to ICAO airspaces [8] for the UK.

Fig. 1.3 illustrates the distribution of VFR/IFR for Airprox events. The left chart shows the percentage of aircraft involved in an Airprox regarding VFR or IFR and whether they are registered as a *small aeroplane*[7], as far as known.

Risk ratings[8] refer to the severity of the incidents, from E (false positive) to A (serious risk of collision).
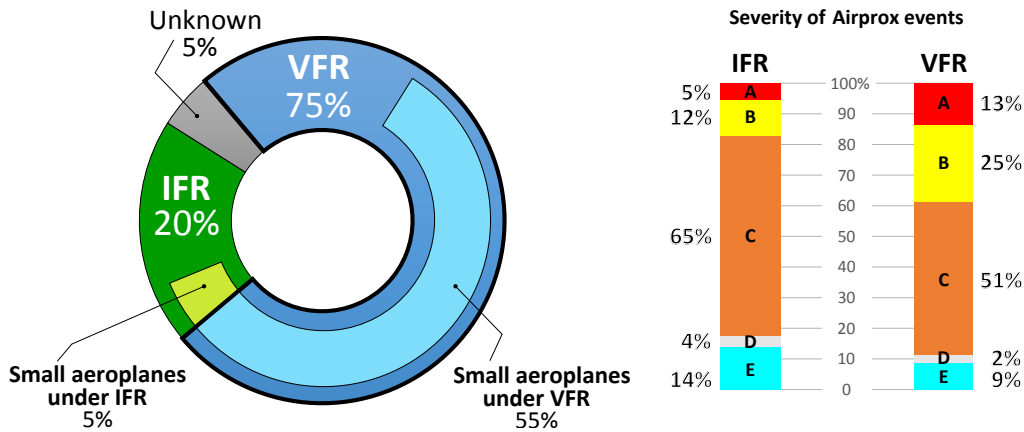
Figure 1.3: Distribution of the number of aircraft involved in Airprox events and their severity (risk ratings) regarding IFR and VFR operation in the UK from 2010 to 2014 [5]. The category **A** refers to high risk, **E** to a false positive.

Not only is the percentage of incidents for VFR flights almost four times the number for IFR, also the severity of incidents is rated to be higher. Further examination of the data provided by [5] shows that 89.8% of Airprox events happened with at least one VFR aircraft being involved and 60.1% of events had both aircraft under VFR. Furthermore, 50% of Airprox events happened between two small aeroplanes. This and the conjunction

---

[7]This category comprises aircraft with a maximum take-off mass of less than 5,700 kg (12,566 lb) [10]
[8]Table A.4 shows the full definition of the risk ratings.

of Figs. 1.2 and 1.3 point to small aeroplanes under VFR in uncontrolled airspace to be the area where measures for improvement should be applied to first. These should also concern *General Aviation* (GA)[9] type of aircraft, as a significant percentage of active GA aircraft in many countries are small aeroplanes[10].

An analysis of the altitude where Airprox events occur hints at a further area of improvement (Fig. 1.4).
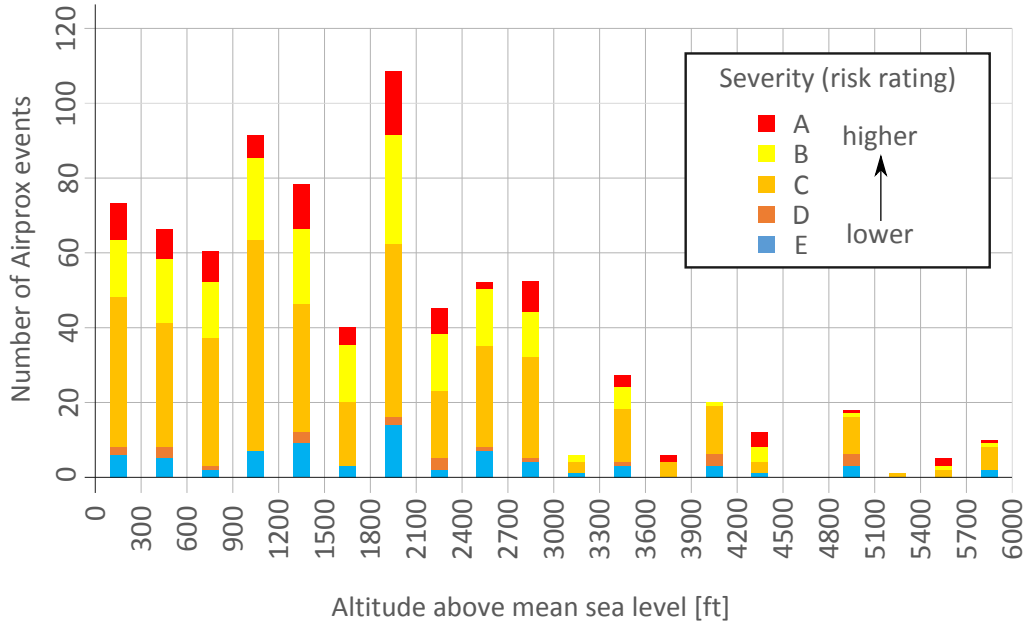
Figure 1.4: Altitude and severity of Airprox events in the UK from 2010 to 2014 [5]. The risk ratings refer to the severity of the incidents, from A (serious risk of collision) to E (false positive).

Although events where recorded up to an altitude of 36000 ft above mean sea level (MSL), only 10.4% occurred above 6000 ft. The rest shown by Fig.1.4 apparently also splits into below 3000 ft (77%) and from 3000 ft to 6000 ft (12%). This may be because of high traffic density at low altitude in the vicinity of aerodromes and airfields and G airspace (Fig. 1.2), which is located at low altitude.

The vertical separation in cruise flight is defined in the *Rules of the Air*[11] by ICAO. The vertical separation should follow the *semicircular rule* which determines the flight level[12]:

- if the magnetic track of the flight is between 0° and 179°, the tens-digit of the flight level should be odd (e.g. 010, 035, 150, 175)

---

[9]aircraft that are neither operated in commercial air transport operation nor in aerial work [10].

[10]for example in the United States: [11] [12].

[11]Appendix 3.1 in Annex 2 [1].

[12]The flight level is the pressure altitude in 100 ft units measured relative to 1013.25 hPa [13], e.g. flight level 110 refers to 11000 feet above mean sea level (which ICAO assigns to 1013.25 hPa atmospheric pressure [14]).

- if the magnetic track of the flight is between 180° and 359°, the tens-digit of the flight level should be even (e.g. 020, 045, 160, 185)

Furthermore, regardless of magnetic track, the ones-digit of the flight level for VFR should be a 5 (e.g. 065, 115) and for IFR a 0 (e.g. 070, 130).

The regulation of the avoidance of midair collisions further specifies the requirements for proper airmanship. In verbatim, ICAO defines these requirements as follows[13]:

> "It is important that vigilance for the purpose of detecting potential collisions be exercised on board an aircraft, regardless of the type of flight or the class of airspace in which the aircraft is operating."

and

> "An aircraft shall not be operated in such proximity to other aircraft as to create a collision hazard."

The exercise of these requirements in VMC (vigilance and avoidance) is generally known as the *see-and-avoid* principle. The pilot, regardless of flying in controlled or uncontrolled airspace, is obliged to continuously conduct a visual scan of the outside view in order to spot potential hazards. If such a hazard is detected, the pilot has to take evasive action to maintain separation.

When another aircraft is detected and in some way limits the own aircraft (ownship) in maintaining its heading and speed, ICAO further specifies which action ought to be taken. These are referred to as the Right-of-way rules [1], which assign priority to the encountering aircraft. The flight that has priority over another flight is allowed to maintain its heading and speed. It depends on the geometry of the encounter and the type of aircraft involved:

- Approaching head-on

  If a situation arises that two aircraft approach each other head-on and there is danger of collision, each shall alter their current trajectory to the right. In this case, neither aircraft has priority.
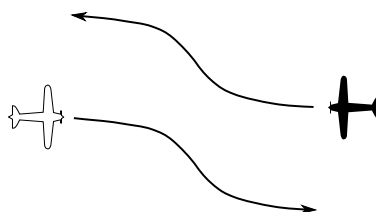
Figure 1.5: Evasion rule for head-on encounter geometry

- Landing

  An aircraft which is in flight shall give way to another aircraft landing or about to land. If two or more heavier-than-air aircraft are about to land on an aerodrome, the aircraft on a higher level shall give way to an aircraft which is at a lower level. However, power-driven heavier-than-air aircraft shall give way to gliders.

---

[13]chapter 3.2 in Annex 2 [1]

- Overtaking

An overtaking aircraft is an aircraft that
is not able to see the red or green nav-
igation light of another aircraft (left
and right sides, respectively), which is
the case when the overtaking aircraft
approaches from the *Aft sector* (Fig.
1.6). The aircraft which is being over-
taken has the priority and the other
one should alter its heading to the right
whether it is climbing, descending or in
horizontal flight.
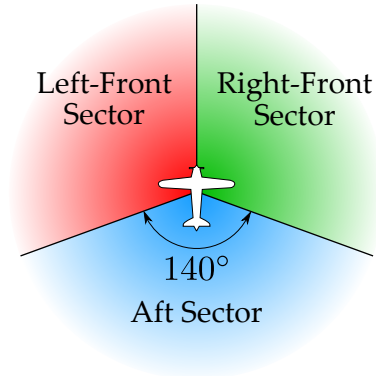
Figure 1.6: Sectors for the converging and overtaking rule [1].

- Converging

If an aircraft is approaching either from the Left-Front or Right-Front sector of Fig.
1.6, and there is danger of collision, the aircraft that has the other one on the right
side should give way, except in cases where different aircraft categories are involved. In
Fig. 1.7, the priority decreases from left to right: A balloon has priority over a glider,
power-driven heavier-than-air aircraft shall give way to airships, gliders and balloons. In
addition, power-driven heavier-than-air aircraft shall yield priority to towing aircraft.
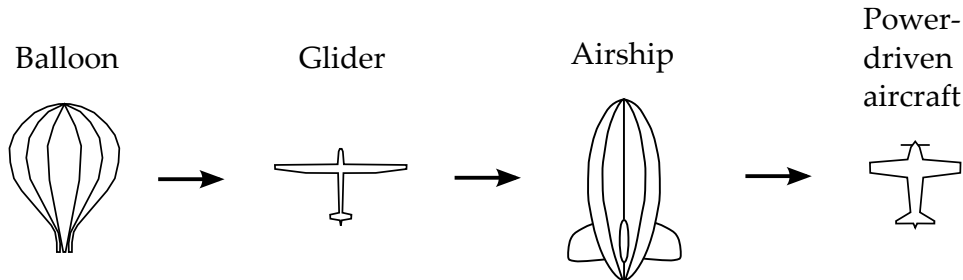
Figure 1.7: The Right-of-way rules in a converging encounter geometry follow a hierar-
chical structure depending on the category of aircraft involved [1]

Correct application of these rules depends on the vigilance of the pilots. Investigation
reports [3] show a breakdown of see-and-avoid to be the main contributing factor of past
midair collisions. Fig. 1.8 illustrates the probable causes of midair collisions during a
five year period, starting on January 1, 2010, as reported in the United States by the
NTSB.

All of the reports contain at least one reference to a breakdown of see-and-avoid or
inadequate visual lookout. Furthermore, 52% of midair collisions were solely attributed
to this cause. It is therefore useful to further illustrate human limitations affecting
the application of see-and-avoid and the circumstances under which they contribute to
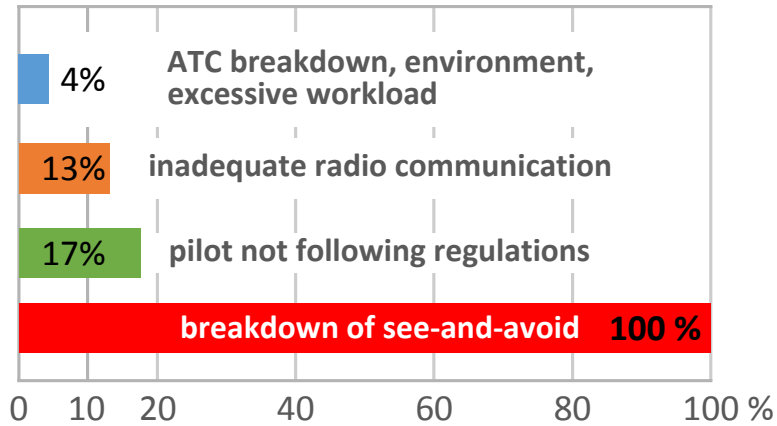
Figure 1.8: Contributing factors to midair collisions in NTSB reports, from January 1, 2010 to December 31, 2014 [3]. Each report may state multiple contributing factors. Environmental factors refer to sun glare, cloud cover and thermal updrafts.

midair collisions. This is done in the following section by examining notable midair collisions of the recent past.

1.2 Notable Midair Collisions

The Rules of the Air described in the previous section regulate the actions of pilots to avoid a midair collision. In order to successfully follow these rules, pilots have to apply the see-and-avoid principle by continuously scanning for other aircraft. The principle relies, however, primarily on human performance, which puts a limit to its effectiveness.

The previous Airprox statistics show that low flying small aeroplanes under VFR in uncontrolled airspace are more frequently affected by see-and-avoid problems than other flights. This section shows the problems associated with these conditions by the description of several mid-air collisions, which were extensively investigated and therefore provide a more detailed view on the human factors involved and of the dire consequences which ensue. Every mid-air collision is summarized by a short description followed by investigation findings about the contributing factors. The 3D-images illustrating the flight paths were created using a custom-written JAVA and NASA's WORLDWIND [15] library.

1.2.1 Mid-air Collision between Helicopter and Small Aeroplane

This accident occurred on August 8, 2009 at 11:53 Eastern Daylight Time (EDT) between a Piper PA-32R-300 airplane, and a Eurocopter AS350BA helicopter over the Hudson River near Hoboken, New Jersey at an altitude of 1,100 ft and a speed of about 93 knots (kts) for the Eurocopter and 150 kts for the Piper airplane [16]. The pilot and five passengers aboard of the helicopter and also the pilot and two passengers aboard the airplane were killed.
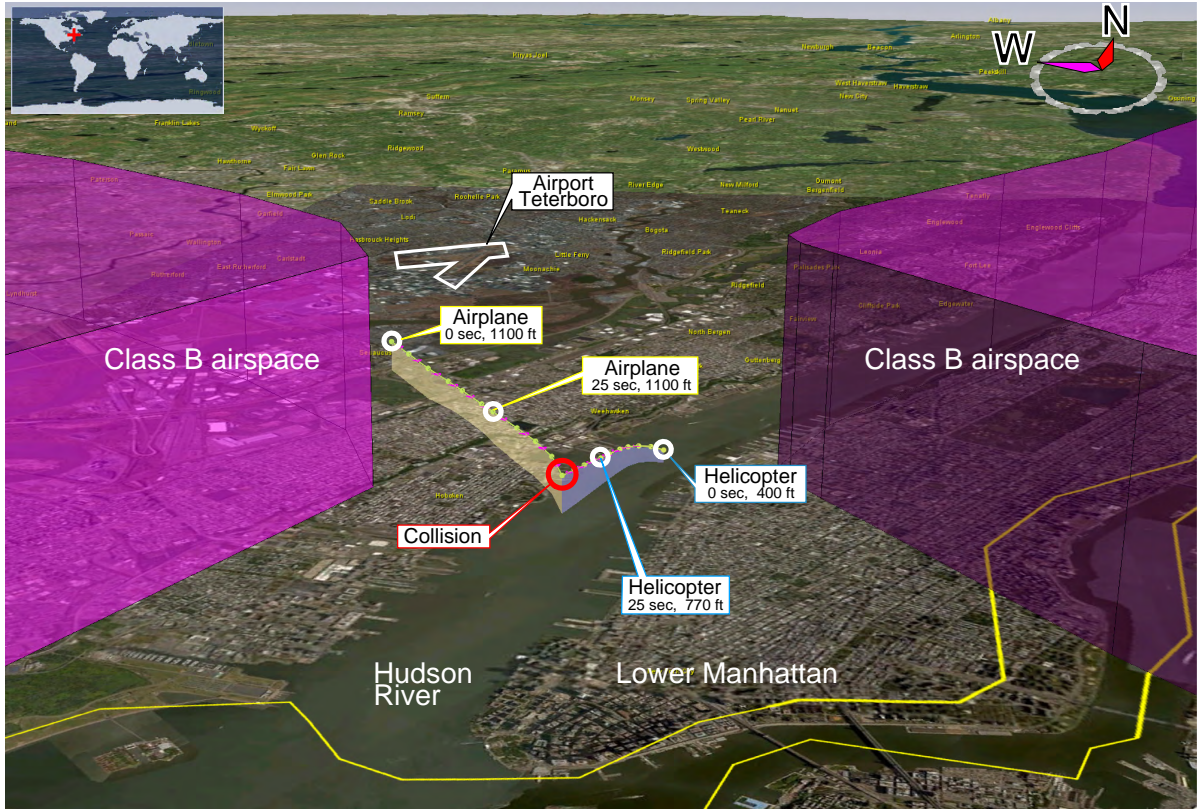
Figure 1.9: Mid-air collision over Hudson River.

The positions reconstructing the flight paths (Fig. 1.9) were gathered using radar and aircraft Mode C transponder data. The class B airspaces shown reach from 500 ft to 7000 ft for the left and from the surface to 7000 ft for the right class B airspace, respectively. This collision occurred in a corridor defined by these airspaces called the *Hudson River Class B exclusion area*, which was comprised of class G airspace (from the surface to 700 ft) and class E airspace (from 700 ft to 1100 ft). Both aircraft were operated under VFR. VMC conditions prevailed at the time and all around the accident location. The collision was witnessed by many people close to the Hudson River, including a ferry boat passenger who filmed the collision[14].

Contributing factors

The National Transportation Safety Board (NTSB) determined that one possible reason for the accident was a breakdown of the see-and-avoid concept. A cockpit visibility study (Fig. 1.10) revealed that the helicopter was from the viewpoint of the airplane below the horizon shortly before the collision. That in connection with high-rise buildings in

---

[14]Three frames of this film taken shortly before and after the collision are presented in Fig. A.12. The collision angle (the angle between the longitudinal axes of both aircraft at collision) determined from this footage was about 25°.

the background made it difficult for the pilot of the airplane to spot the helicopter in front of the low-contrast background.
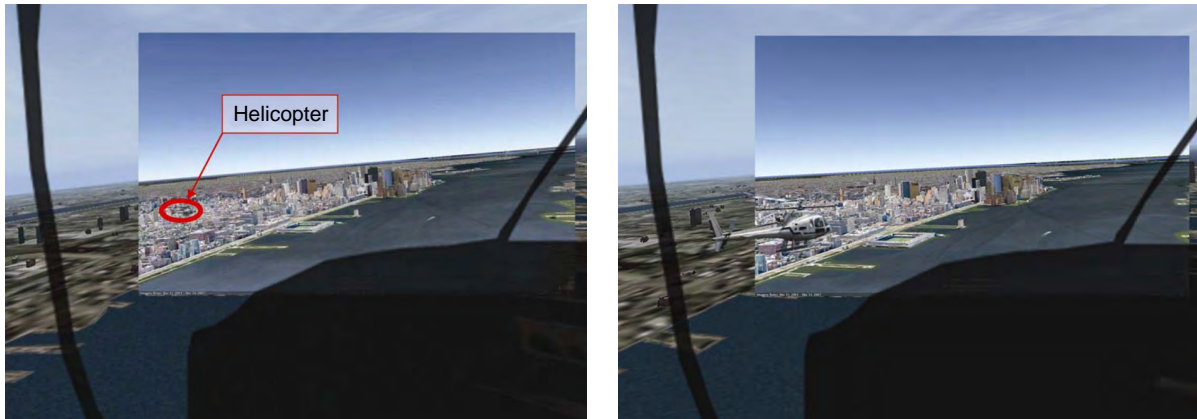
Figure 1.10: Simulation of the view outside the airplane's cockpit 5 seconds (left image) and 1 second (right image) before collision with the helicopter [16]

Another possible reason was a non-pertinent telephone conversation of the Teterboro Airport local controller, which distracted him from his ATC duties. There was also ineffective use of available electronic traffic information by ATC to maintain the awareness of nearby aircraft for both pilots. Radar data revealed that a conflict alert[15] was generated 11 times on the Teterboro and the Newark class B airspace controller's radar display. However, neither controller recalled hearing or seeing the alert. Furthermore, three other conflict alerts were generated during that time for the accident airplane and another aircraft, illustrating a high traffic density.

Also, inadequate communications among ATC facilities governing the Hudson River exclusion area and insufficient vertical separation regulation for aircraft operating in this airspace were identified as contributing factors.

1.2.2 Mid-air Collision of Electronic News Gathering Helicopters

On July 27, 2007 at 12:46 Mountain standard time (MST, UTC-7), two electronic news gathering helicopters from local television channels 3 and channel 15 collided over Phoenix, Arizona [17]. Each helicopter was of the type Eurocopter AS350B2 and operated under VFR. ATC was not required to provide separation to VFR traffic in the accident area and VMC conditions prevailed throughout the incident. An examination of the main rotor blades of the crashed helicopters revealed that they contacted each other about 2 feet from the end of each blade. The occupants on board both helicopters were killed.

The purpose of the flight of both helicopters was to cover a police pursuit in the streets below. Fig. 1.11 illustrates the accident sequence. The channel 3 helicopter was

---

[15]Automated aural and visual warnings to radar controllers of existing or pending conflicts among aircraft These alerts require immediate attention and action from the controller.
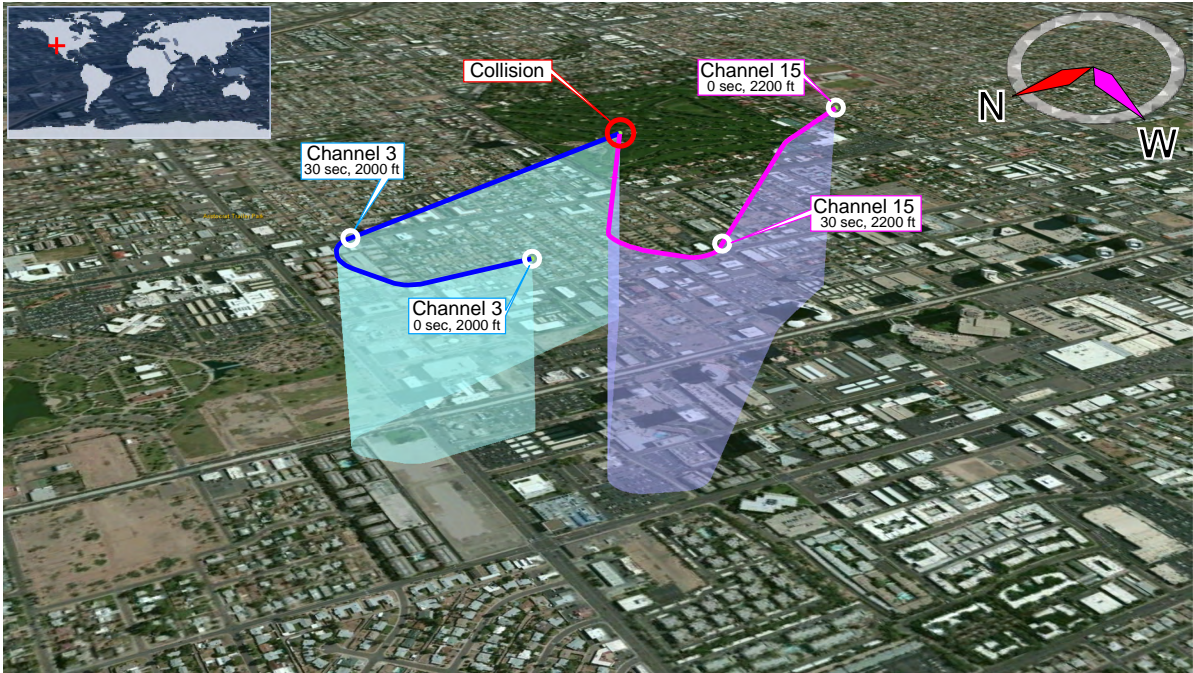
Figure 1.11: Position information of the channel 3 and the channel 15 helicopter [17]. The altitude of the collision was about 2000 ft.

equipped with an traffic advisory system (TAS) SkyWatch SKY497 from L-3 Communications, providing aural and visual warnings. This system would generate a warning when another aircraft would enter a virtual cylinder of 0.2 nm radius and ±600 ft centered on the channel 3 helicopter. However, together with the two helicopters involved in the accident, three additional news gathering helicopters and one from the police were operating in the vicinity. Due to the frequent alarms the system generated in this situation, the volume of the aural alert was turned down in order not to interfere radio communications and reporting.

Contributing factors

According to the NTSB, the probable cause of this accident was both pilots' failure to see and avoid the other helicopter [17]. Both of the pilots involved in the collision not only had to fly their aircraft but also had to report the situation unfolding below to their news broadcast station. Therefore, a contributing factor identified by the report was high workload of both pilots due to their additional role as reporters and because of multiple avoidance situations. The attention of the pilots was focused down towards the ground, which resulted in a breakdown of each pilot's awareness of the other helicopter. Also, existing collision avoidance equipment was not utilized as intended.

1.2.3 Mid-air Collision of Two Small Aeroplanes

This mid-air collision between a Cessna A150L, and a Piper PA28-140 occurred near Kinnelon, New Jersey (US) on August 7, 2004, at about 9:12 EDT [18]. The flights were personal flights conducted under VFR, with one pilot onboard each aircraft. VMC prevailed throughout the incident. After the collision, both aircraft hit the ground about 8 miles northwest of Essex County Airport (CDW), and 3 miles west-northwest of Lincoln Park Airport (N07). Both pilots were fatally injured.

Each aircraft was equipped with a GPS receiver, providing time, position and altitude data of the flights. Fig. 1.12 shows the flight paths reconstructed from the narrative of the accident report [18]. The Cessna departed at runway 09 from CDW at about 09:05:06, the Piper 3:44 minutes later at runway 19 from N07. The planes collided 7:14 minutes and 3:30 minutes into the flight of the Cessna and the Piper, respectively.
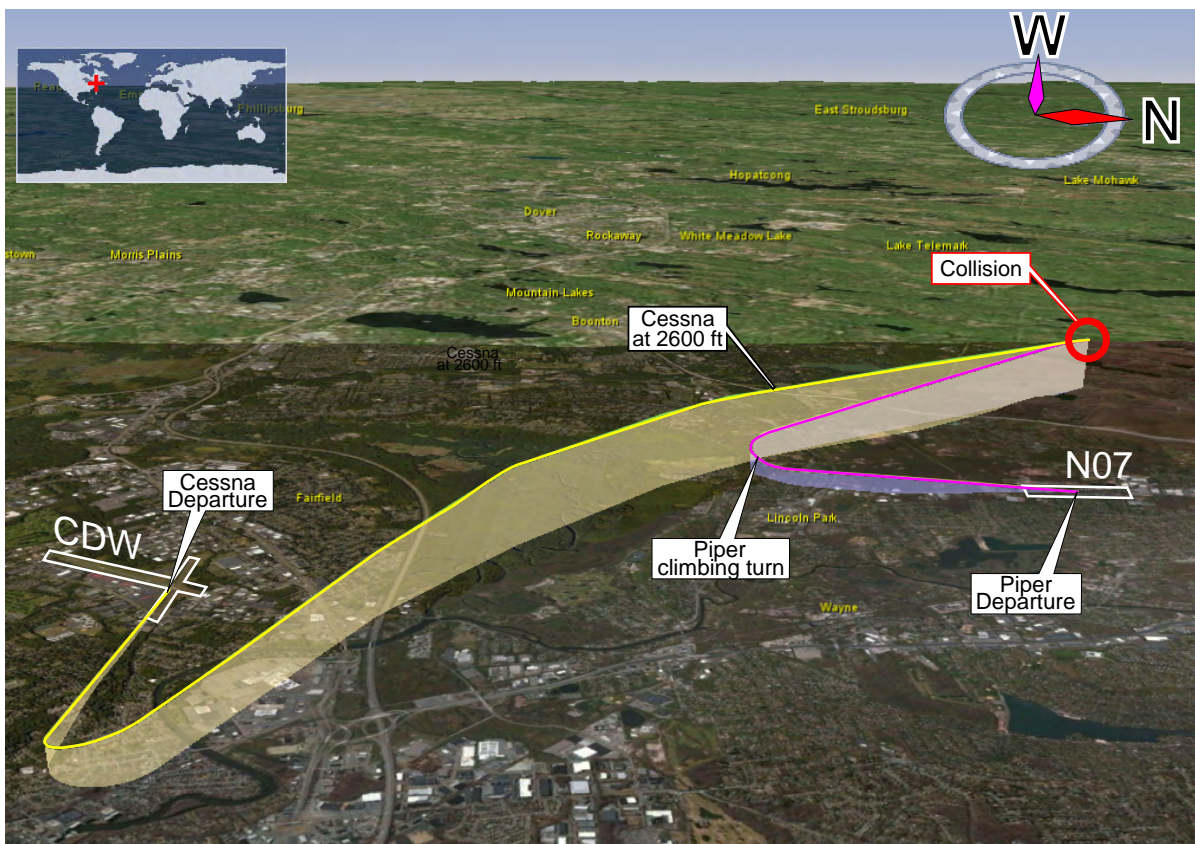
Figure 1.12: Reconstructed flight paths of the of the Cessna and the Piper [18].

Three minutes before the collision, the Cessna climbed to 2,500 ft, leveling at that altitude for one minute. Then the Cessna climbed to 2,600 ft approximately 2 minutes prior to the accident. The Piper, after departing to the south, entered a climbing right turn, to fly a track of 325°. The Piper was flying ahead and below the Cessna after its turn to the northwest. After completing the turn, the Piper continued to climb to an altitude of 2,680 feet, while being overtaken by the Cessna. Data from both GPS units

indicated that the two airplanes collided while in straight and level flight at 40° 57.948'
N 74° 21.678' W. The aircraft hit the ground about 8 miles northwest of CDW (Cessna
departure), and 3 miles west-northwest of N07 (Piper departure).

Contributing factors

To determine the visibility of each aircraft from the viewpoint of the pilot of the other
aircraft, ground track and ground speed from GPS and radar data was used to determine
the closure rate, relative azimuth and relative elevation. The accident occurred as a result
of inadequate visual lookout on the part of the pilots. Had he been scanning down and
to his right, the pilot of the Cessna had an approximately 21-second opportunity to
acquire the Piper during his level flight at 2,600 ft. Vice versa, the Piper pilot also had
a 21-second opportunity to acquire the Cessna, if he had been scanning forward and to
his left during his climbing turn. After that, the two airplanes continued to converge.
The calculations of the converging angle and a cockpit visibility study of both aircraft
revealed that at no time after 9:09:57, which was 2:23 minutes before the collision, could
the pilot of either airplane see the other.

   In accordance to the Rules of the Air [1] the Cessna had the right-of-way with respect
to the Piper.

1.2.4 Mid-air Collision of a Glider with a Tornado Military Jet

This accident between a Panavia MRCA Tornado military jet and the Glaser Dirks DG
100 glider occurred on June 23, 1998 at 14:37 CEST [19]. It took place in class E airspace
(Table 1.1) with both aircraft operating under VFR. The altitude at the moment of the
collision measured by the Tornado was 1,900 feet AGL. The airspeed at the moment
of collision was 57 kts for the glider[16] and 420 kts for the Tornado. Meteorological
conditions were sufficient for VFR flight at the time of the accident [19]. The sun was
62° above the horizon. The pilot of the glider was killed and the Tornado sustained heavy
damage. However, the operators of the Tornado (pilot and weapon system officer) were
not injured and able to land safely at Ramstein airbase.

   The Tornado approached the glider from the rear at an angle of 30°, which is equal
to the collision angle (Fig. 1.13), and at a left bank angle of 26°.

   The first impact was probably between the tip of the tank of the Tornado and a wheel
of the glider. This is deduced from the collision geometry and the fact that rubber from
a wheel of the glider was found on the tank of the military jet. The fuselage of the glider
was ripped at a length of 1.7 m by the empennage of the Tornado. Furthermore, the
left wing of the glider was separated.

Contributing factors

The accident report by the BFU [19] identified that the speed difference between the
two aircraft restricted the Tornado pilot's ability to avoid an imminent collision. It was

---

[16]estimated using aerodynamic characteristics of the glider [19].
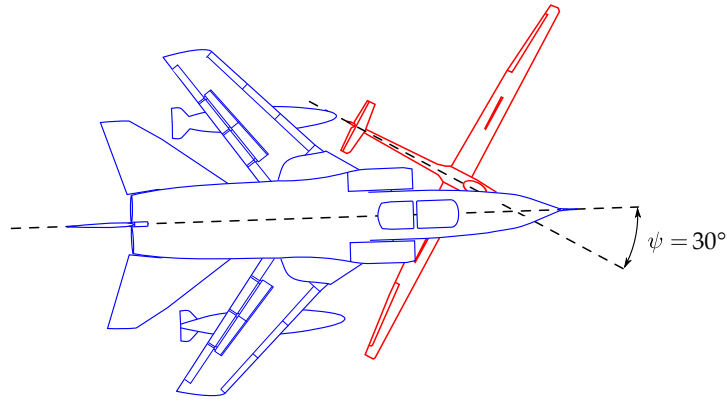
Figure 1.13: Illustration of the collision angle between the Tornado military jet and the Glaser glider [19]

determined that in order to see the gilder it had to be greater than 2 mrad, which is the angle of an 2 mm arc on a windscreen 1 m away from the eye of the pilot. Because the glider was approached from the rear at the same altitude, its visible cross-section area was mainly that of its fuselage at 0.81 m by 0.6 m, which is visible (asserting the 2 mrad-rule) from 400 m. This distance was covered by the Tornado in only 2 seconds, severely limiting the pilot's reaction. Also, additional glare from sun/cloud reflections could not be ruled out as contributing factors.

1.2.5 Summary

The mid-air collisions in this section illustrate that the see-and-avoid principle, while undoubtedly preventing many collisions, is subject to human limitations. Most prevalent were visual constraints in detecting the other aircraft in time, as VMC prevailed in each case presented. In the case of the collision over the Hudson river and between the Tornado and the glider, the eye's acuity threshold was likely to be the major contributing factor. Furthermore, because the human visual system is better at detecting moving objects than stationary ones [20], an aircraft on a collision course is particularly hard to detect [21]. This lowers the likelihood that such an aircraft can be detected.

Also, like in the collision over Kinnelon, visual obstructions like the own airframe further limit the ability to detect and react. High workload because of side tasks, especially in the case of the news helicopter collision, further lower pilots abilities to ensure proper separation.

1.3 Human Factors

The previous sections gave an introduction into air traffic regulations and discussed notable cases where limited capability to see and avoid conflicting traffic led to tragic consequences. The ability to take the appropriate action is constrained by human limitations surfacing both in mid-air collisions and Airprox events. In the following, these

constraints will be discussed in an effort to suggest methods for improvement.

Human and individual characteristics which influence behavior at work in a way which can affect health, performance and safety are generally referred by the term *Human Factors* (HF) [22]. Regarding technological processes, HF summarizes physiological and cognitive factors which collectively influence human-machine interaction. Despite technological measures to avoid hazards during aircraft operation, a pilot as a human is always the last and final level of authority to guarantee flight safety. Concerning midair collisions, it is therefore imperative to comprehend the factors under which a loss of separation might occur.

1.3.1 Visual Limitations

The see-and-avoid concept (section 1.1) requires pilots to continuously scan the environment outside the cockpit. In addition, on-board instruments have to be monitored, creating a transition in the scan between items in the cockpit and distant objects. It may require the human visual system several seconds [20] to refocus in order to provide a sharp image on the retina of the eye.

The Federal Aviation Administration (FAA) addresses the visual difficulties of traffic detection by providing improved scanning methods [20] [23]. The likelihood of spotting traffic is increased using a sequence of short, evenly-spaced eye movements that bring successive areas into the view. Each movement should not exceed 10° and allow the visual system at least 1 second to readjust. This procedure also helps to mitigate *Autokinesis*[17], which can lead pilots to falsely detect another aircraft in dark conditions and therefore can provoke an avoidance maneuver. However, albeit the overall usefulness of scanning procedure, the FAA also recognizes that its effectiveness is easily degraded by psychophysiological conditions such as preoccupation, fatigue, anxiety, illness or boredom [20].

Even with good meteorological conditions, a good medical status of the pilot and a proper scanning procedure in place, further issues have to be taken into consideration. One of which is the lack of optical contrast of other aircraft against a complex background, exemplarily illustrated in section 1.2.1 in the accident over the Hudson river. In such cases, the pilot's ability to visually detect and identify other aircraft is diminished by the interaction between the outline of an aircraft and the contours present in the background (Fig. 1.14a). This problem is more likely to appear when flying at lower altitudes in the vicinity of urban areas, where buildings, reflections, shadows and streets camouflage a potential collision threat [23]. In addition, even with favorable background, the contour quality of images projected onto the retina also decreases with distance (Fig. 1.14b).

Furthermore, visibility outside the cockpit is restricted by the fuselage and wings of the own aircraft. Fig. 1.15 shows the limitation of the field of view for a left-seated

---

[17]Autokinesis occurs when a stationary light is viewed against a dark background for about 6 to 12 seconds [24]. Here, the eye starts to move in a small but jerky way, which produces the illusion of movement of the light.

(a) with objects in the background (b) without objects in the background
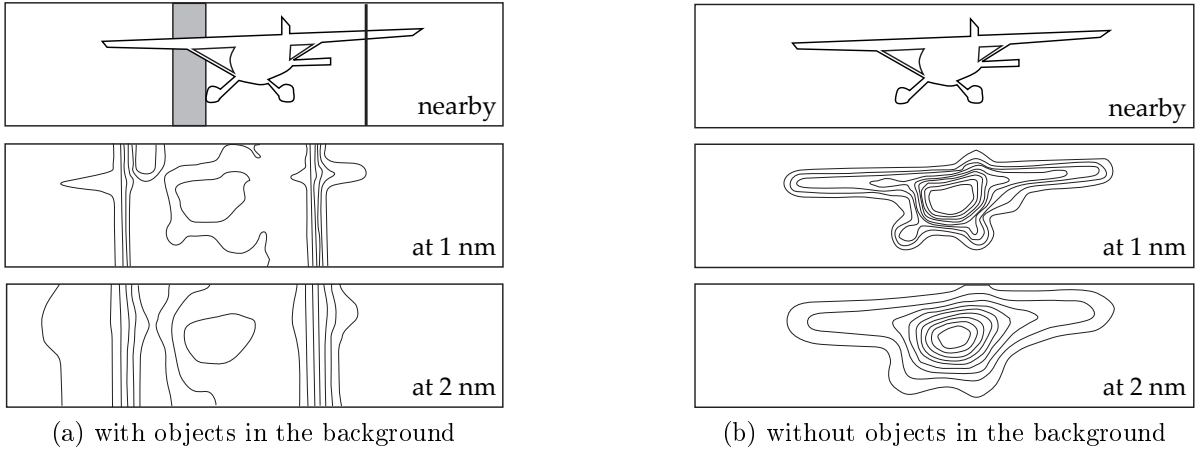
Figure 1.14: Visual quality of retinal images at different distances from the viewer [21]
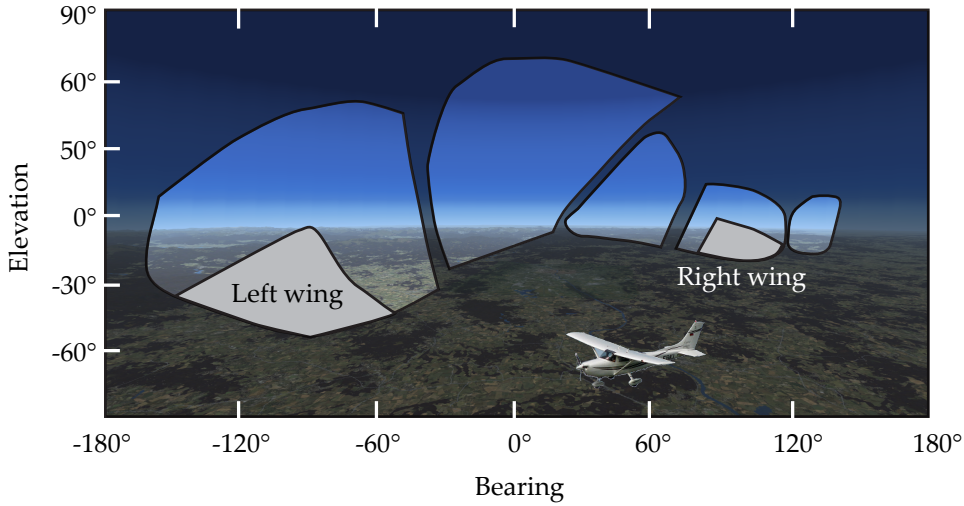
Figure 1.15: Restrictions to the visual field for a left-seated pilot of a low-wing aircraft

pilot of a low-wing GA-type aircraft [21]. This means that an unnoticed aircraft which is approaching from the right represents a particular danger to a pilot in the left seat. The issue of the wings blocking the line of sight is especially problematic if a low-wing aircraft converges a high-wing aircraft from above.

Another problem arises from the fact that an object on a collision course, aside from increasing in size in the outside view, appears to have no relative motion [20]. This makes it particularly hard to detect, because the human visual system is quicker in detecting moving objects than stationary ones.

16

1.3.2 Information Processing

The theory of information processing lies at the heart of human performance. Stimuli are seen as the first step in a multi-staged mechanism, which cause human actions (i.e. responses). Common models of information processing define these stages in terms of functions like sensing, thinking, and responding. The stages themselves consist of functions intended to describe behavior, memory and attention.

The model of information processing generally used in the aviation context by Wickens et al. (Fig. 1.16) covers four major activities in information processing: *Sensory Store*, *Perception*, *Decision-Response Selection*, and *Response Execution* [25].
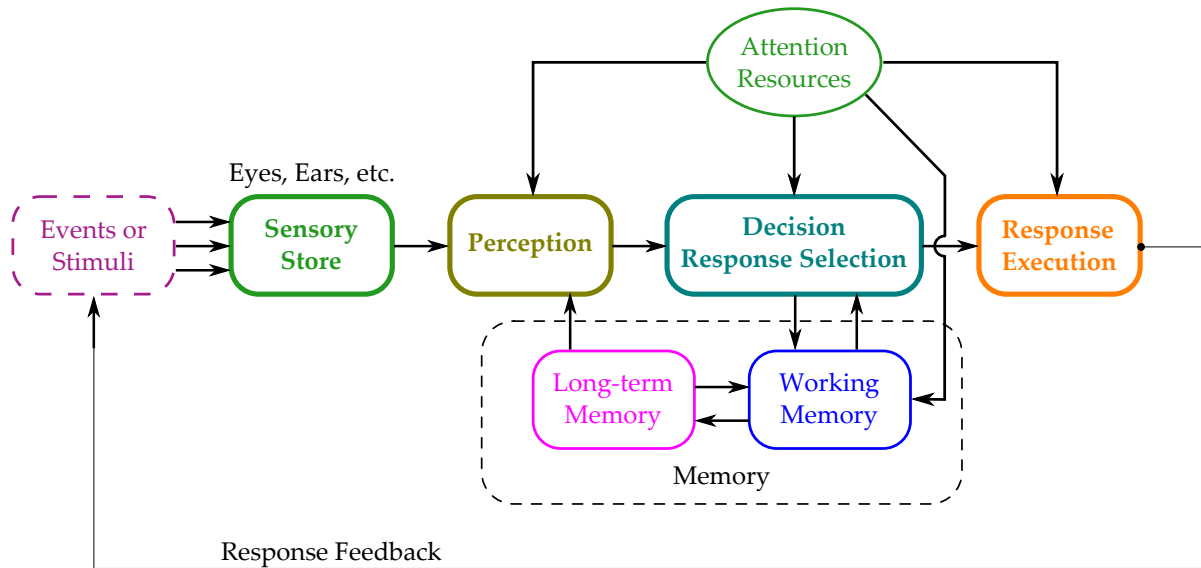
Figure 1.16: Model of human information processing [25]

The first stage, the *Sensory Store*, receives the external stimuli of the individual senses (e.g visual, aural). [26]. It is only able to retain information very briefly. After that it is overwritten with new input. The time until this happens is different across the senses: For example, visual stimuli are overwritten in is as little as 0.5 seconds, aural inputs in 3 seconds [27].

The ability of the next stage, *Perception*, is to detect, identify, and process physical stimuli. It is understood to be enabled through the use of *simulations* of the world [28] using memory [25]. Accordingly, literature [29], defines human memory as

> "A general ability, or faculty, that enables us to interpret the perceptual world to help organize responses to changes that take place in the world."

The cognitive simulation is continuously adapted, in order to be in accord with the cues received from the physical world. For a stimulus to be processed, it must first be detected. As the storage registers in the sensory store fill up with information, the individual has to prioritize what stimuli are going to be selected for interpretation. The *Attention Resources*, decide what tasks can be performed concurrently [25] and

furthermore influence the remaining stages until a response is executed. Prior knowledge and planning may advantageously influence the selection on which stimuli to prioritize [28]. Stress and preoccupation may diminish attention, focusing on stimuli that are of little relevance (a non-pertinent telephone call) while ignoring a major problem (aircraft on a collision course)[18].

A notable example of such a breakdown of situational awareness is the crash of Eastern Airlines 401 [30] where the aircraft slowly descended until ground impact. The flight crew failed to react to audible warnings of low altitude issued by the ground proximity warning system because they where preoccupied with fixing a burnt-out landing gear position indicator light. Potentially such an problem could also arise with on-board traffic warning systems, which aurally alarm the pilot of nearby aircraft [31].

Working Memory refers to a storage of a limited number of items (e.g. ideas, sounds, images) that we can manipulate and maintain at any point in time. It holds information for about 15–30 seconds and has a storage capacity of 7 ± 2 items [32]. Repetition of items increases the time this information stays accessible [25].

The *Long-term Memory* is able to store a large amount of information, whether it be perceptions, factual knowledge or memory of specific events. This information can be retrieved by short-term memory if necessary. Storing information long term is supported by encoding and rehearsal. Long-term memory is also apparently organized into two parts [32]: semantic memory and episodic memory. The first stores factual knowledge, such as learnt concepts of how things work and why. The latter refers to events, including people, places and other objects.

The next step is to form a decision and to select a response, based on the processed information accrued to this point. Multi-task performance regarding efficiency and error rate of the decision is dependent on the amount of involvement (called *workload*). High involvement with one task may lead an operator to disregard an other, more critical task [25]. For aviation, Parasuraman et al. [33] have shown that flying under high workload and with a reduced spare mental capacity could lead the pilots at some later point to a breakdown in performance. Under such circumstances, the capacity limitation in the short term memory is reached earlier and the likelihood for errors in a critical situation increases. Other factors diminishing performance are inadequate task planning, appearance of unexpected situations or access problems of a system (e.g. for a traffic alarm), time pressure, stress, communication barriers and poor knowledge of regulations.

The last stage of the model of information processing, *Response Execution*, refers to the processes after a decision has been made. Correct and timely response execution requires proper muscle coordination, which depends on the availability of attention resources (Fig. 1.16). When collision avoidance is concerned, inadequate allocation of attention, high workload or insufficient time to plan the avoidance maneuver may still result in inadequate execution.

However, research shows that performance is also decreased when the level of input or workload is very little [32] [34]. This is called the Yerkes-Dodson relation (Fig. 1.17), which states that human performance tends to be highest under moderate levels of

---

[18]See accident over the Hudson river, section 1.2.1.

workload. Automation in the cockpit therefore has to be carefully evaluated regarding human-machine interaction (HMI) to verify its usefulness.
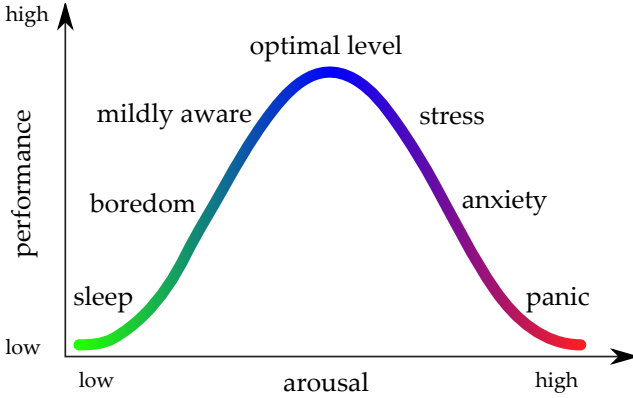
Figure 1.17: The empirical relationship between arousal and performance [32]

A useful practice to properly cope with high workload while flying (e.g. high-traffic situations) is training in a flight simulator. Practice in general stimulates *automaticity*[19], which enables automatic processing in a fast, parallel manner. Automaticity is achieved when performance is dependent on single-step, direct-access retrieval of solutions from memory [28]. It enables skilled-based behavior [25] and frees up attention resources for allocation to other matters such as perceiving additional stimuli [28].

After the response is selected and executed (e.g. muscle movement), changes manifest in the environment (feedback). The process is repeated using updated information and sensory stimuli.

1.3.3 Time to React
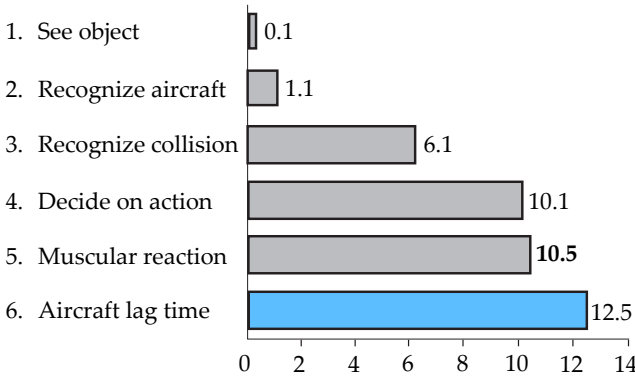
Figure 1.18: Time in seconds from the detection of an object to the implementation of an evasive maneuver [20] [36]

The time from the perception of a stimulus to a response execution depends on all the processes and factors described before. Regarding the avoidance of a mid-air collision, Appendix 1 of FAA advisory circular 90-48C [20] indicates the steps taken by the pilot in a military aviation setting (Fig. 1.18).

The model for information processing (Fig. 1.16) governs the steps 1 (see object) to 5 (muscular action), which consecutively take 10.5 seconds to complete.

---

[19]This refers to the process of practice an action so well that it does not require a conscious effort to carry it out [35].

Move back 7 meters from this illustration. From that distance, the second air-craft from below should mark the eye's acuity threshold.
At 400 knots closing speed, this airplane would cover the distance until impact in 12.5 seconds.
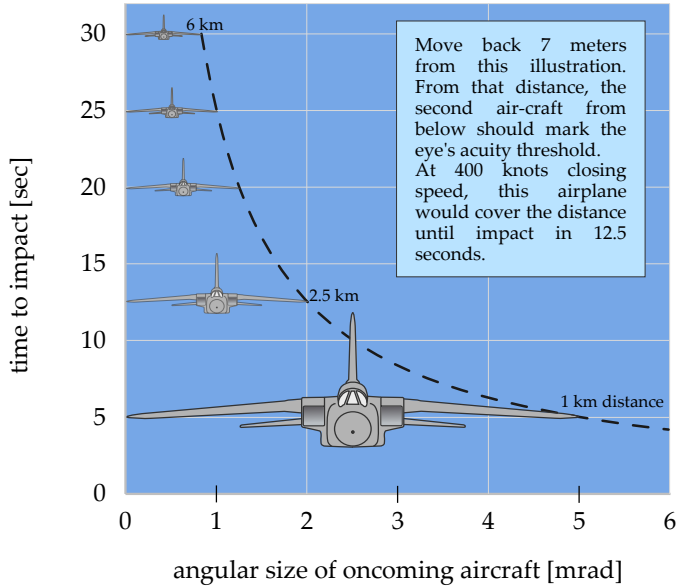
Figure 1.19: Time to impact vs. angular size of an oncoming aircraft including distance

The last step (aircraft response) is based on a responsive aircraft model, concluding the total time required from initial target acquisition to the completion of a successful avoidance maneuver to sum up to 12.5 seconds. However, the reaction time for lesser trained civil pilots is likely to be greater than that [21].

Additional factors diminishing performance are poor meteorological conditions, alcohol or other drugs and sleep deprivation[20] [23].

As far as approach geometry and speed are concerned, the most unfavorable odds occur when a very fast aircraft approaches head-on on a collision course. The small visual angle an aircraft presents shortly before collision may also make it impossible for a pilot to take evasive action in time (Fig. 1.19).

Furthermore, the approaching aircraft has to be even closer, before it presents a target of a detectable size, if only the fuselage contributes to the visual angle (like in the accident between the glider and the Tornado jet in section 1.2.4).

1.4 Implications for Traffic Displays

Because of safety measures and regulations, most tasks during flying follow a standard pattern and are therefore highly process driven. Examples are concurrent tasks such as flying the aircraft within its safety envelope, identifying and maintaining separation from air or ground hazards and performing navigation and communication. The pilots must filter relevant cues from the data stream generated by these tasks and gather useful information within and outside the cockpit to perform them. The responses are, as discussed, limited by human mental workload capacity and fallible human senses.

The see-and-avoid principle to avoid traffic therefore demands proper management of scanning time and mental resources. The scanning process could be supported by introducing a traffic display into the cockpit, enlarging the distance of detecting an aircraft above the visual range and enabling detection were visibility is obstructed. Thus, preparation time is increased before an encounter. Also, the time spent in steps 1 to 3 in Fig. 1.18 could be reduced, shortening the overall time to react. Especially the time for

---

[20]For instance, sleep deprivation of 16 hours corresponds approximately to a blood alcohol level of 0.5‰ [37] (Table A.3).

recognizing a collision (step 3), amounting for 48% of the 10.5 seconds needed to react, is amenable for reduction.

According to the FAA [38], the proportion of time allocated for scanning the cockpit instruments should be a maximum of 4 to 5 seconds for every 16 seconds of scanning outside (about 28% to 72%, respectively). When potential midair conflicts are detected, pilots should expect additional threats and continue to scan for other air vehicles that might also be in conflict [39]. This time constraint has to be kept in mind when designing a traffic display. On one hand, the decision on which action to take in traffic encounters has to be reduced. On the other hand, the additional time spent looking on a cockpit traffic display has to be small.

Research by Wickens et al. [40] provides preliminary insight into the influence of a traffic display on pilots' scanning behavior under VMC in traffic conflict and non-conflict trials. Two test conditions were investigated in a simulator. In the first one, the pilots were instructed by an air traffic controller (ATC) to fly avoidance maneuvers in a simulator without a traffic display.

Regarding the conflict trials in this experimental condition, pilots were scanning the cockpit instruments with a mean dwell time of 6.91 seconds, versus 2.7 seconds for the outside view (72% to 28%, respectively), Fig. 1.20.
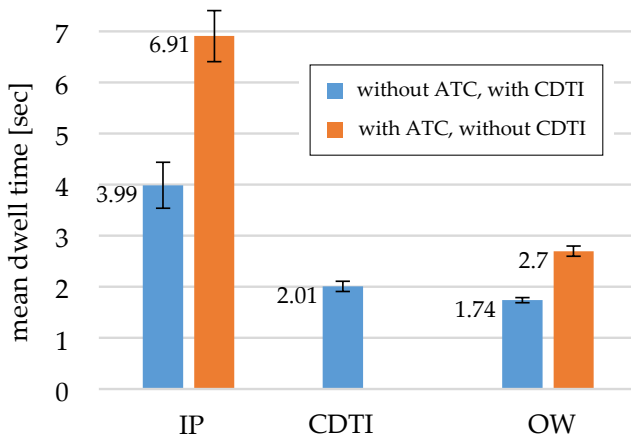
Figure 1.20: Mean dwell time during a traffic conflict for inside and outside cockpit features (IP: Instrument Panel, CDTI: Cockpit display of traffic information, OW: Outside World) [40].

In the second test condition, a traffic warning was issued by an on-board traffic display only. Here, pilots had to decide to perform an avoidance maneuver by themselves. The cockpit instruments had a mean dwell time of 6.91 seconds, versus only 2.7 seconds for the outside view (78% to 22%, respectively).

These findings show that pilots scanned the outside environment longer when they received traffic information and conflict resolution instructions from ATC compared to the situation when they relied upon a cockpit display for traffic information and self-selected avoidance maneuvers. Furthermore, none of the results comply with FAA scanning recommendations [20] [38]. The time needed for watching and understanding a display indication can thus be identified as a critical constraint for the design and evaluation of new traffic displays.

This thesis proposes several variants of traffic displays and rates them in this regard. The next chapter will review existing systems in order to create a baseline for development.

Also, step 4 in Fig. 1.18 (Decide on action), amounting for 4 seconds or 38% of the 10.5 seconds to react, provides an extra area for improvement. Not only the time spent

on deciding an action could be reduced, but also the errors in judgment. Regarding collision avoidance, research [41] shows problems in the application of the Rules of the Air [1]. Also, existing technology issuing avoidance maneuvers[21] does not address the Rules of the Air at all. There are no such systems to date which provide avoidance maneuvers for VFR operation.

Therefore, in addition to displaying traffic, a depiction of an avoidance route on a novel traffic display with the option of automatic maneuver execution could prove fruitful. Completing this chapter, the next section presents the basic principles of optimal control theory, which is used to calculate an avoidance route in chapter 5.

1.5 Basics of Optimal Control

According to the see-and-avoid principle, pilots are obliged to visually identify the traffic outside the cockpit and to avoid it when necessary using the proper right-of-way rules. Because of the limitations discussed in the previous sections, a technological solution indicating an avoidance route on a cockpit display could prove useful.

The following subsection introduces the concept of *penalty functions* as it is known in the field of control theory. This framework will be used in section 5 to calculate the avoidance maneuver the own aircraft should take in order to avoid a mid-air collision.

1.5.1 Penalty Functions

Central to control theory in general is the concept of a state, which is a set of m variables $\{x_1(t), x_2(t), \ldots, x_m(t)\}$ used to describe a dynamic system. In the following, these variables are represented by the components of the vector $\boldsymbol{x}(t)$, called the *state vector*. It holds the current values of the state variables of a system at time t. Analog to $\boldsymbol{x}(t)$, the input (or control) vector $\boldsymbol{u}(t)$ holds n input variables $\{u_1(t), u_2(t), \ldots, u_n(t)\}$, which influence the future values of the state variables. The relationship between the time derivative of the state $\dot{\boldsymbol{x}}(t)$, the current state $\boldsymbol{x}(t)$ and the control $\boldsymbol{u}(t)$ is called the *state equation*

$$\dot{\boldsymbol{x}}(t) = \boldsymbol{f}[\boldsymbol{x}(t), \boldsymbol{u}(t)] \tag{1.1}$$

with initial condition

$$\boldsymbol{x}(t_0) = \boldsymbol{x}_0 \tag{1.2}$$

This equation is used throughout the field of control theory. In general it represents a set of m coupled first-order ordinary differential equations which have to be integrated to acquire the state trajectory from initial time t_0 to final time t_f.

The task of optimal control is to find an optimal history of the control vector, $\boldsymbol{u}^*(t)$, which depending on the problem minimizes or maximizes a suitably designed scalar

---

[21]TCAS II traffic display, discussed in chapter 2.

penalty function P. Both minimum and maximum of P are characterized by the condition that the first-order effect of control variations is zero (stationarity condition). The sign of second-order effects further describe the nature of a stationary P. A positive sign refers to a minimum, a negative to a maximum of P at $\boldsymbol{u}^*(t)$, regarding a particular component $u_i(t) \in \boldsymbol{u}(t)$ (Fig. 1.21a).

The penalty function used in this thesis which both incorporates the final and transient effect of a control input is[22]

$$P = \Phi[\boldsymbol{x}(t_f)] + \int_{t_0}^{t_f} L[\boldsymbol{x}(t), \boldsymbol{u}(t)] \, \mathrm{d}t \tag{1.3}$$

Through integration of eqn. (1.1), $\boldsymbol{u}^*(t)$ forces the state from its initial value $\boldsymbol{x}_0$ on the so-called optimal state trajectory $\boldsymbol{x}^*(t)$ to $\boldsymbol{x}^*(t_f)$.

The first summand $\Phi[\boldsymbol{x}(t_f)]$ is the *final state penalty* (Fig. 1.21b), which is a scalar algebraic function of the final state $\boldsymbol{x}_f$. Its purpose is to provide a way for the final state to influence the optimal control $\boldsymbol{u}^*(t)$. The integral in the second summand is a function of the control at $t_0 \leq t \leq t_f$. In this thesis, this part is called *travel penalty*, the function L is called the *Lagrangian*. The functions Φ and L both have to be continuously differentiable.
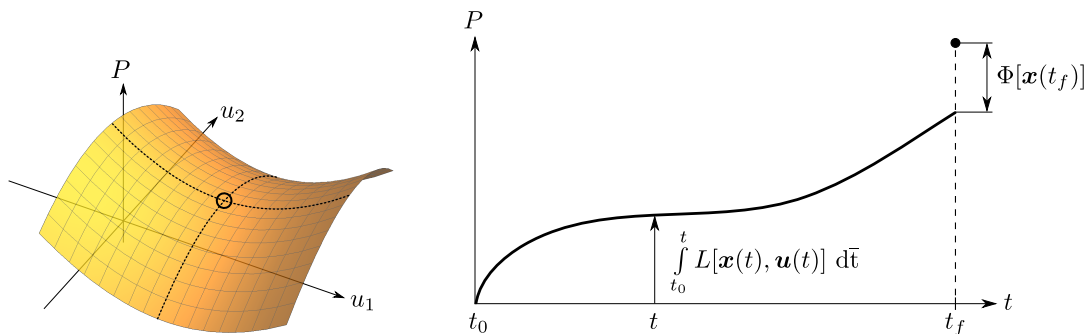
(a) Illustration of stationarity of P with respect to the control $\boldsymbol{u}$. At this point, the gradient $\partial P/\partial \boldsymbol{u}$ is $\boldsymbol{0}$. Here, the second derivative regarding u_1 is positive, indicating a minimum for this coordinate (vice versa regarding u_2).

(b) Components of the penalty function P. The slope of P in $t_0 \leq t \leq t_f$ (i.e. the integrand) is called the *Lagrangian*.

Figure 1.21: Stationarity and time dependence of penalty function P

To incorporate the state equations (eqn. (1.1)), an augmented penalty function is

---

[22]also called Bolza-type penalty function [42].

formulated using Lagrange's multiplicator method on the integrand of eqn. (1.3) [42]

$$J = \Phi[\boldsymbol{x}(t_f)] + \int_{t_0}^{t_f} \{L[\boldsymbol{x}, \boldsymbol{u}] + \boldsymbol{\lambda}^T(t)\, \boldsymbol{g}[\boldsymbol{x}, \boldsymbol{u}]\}\, \mathrm{d}t \qquad (1.4)$$

where $\boldsymbol{\lambda}(t)$ is called the adjoint vector and only depend on time. It is explicitly dependent on time. The function $\boldsymbol{g}$ contains the state (or dynamic constraint) eqns (1.1) in the following way:

$$\boldsymbol{g} = \boldsymbol{f}[\boldsymbol{x}, \boldsymbol{u}] - \dot{\boldsymbol{x}} = \boldsymbol{0} \qquad (1.5)$$

With $\boldsymbol{g}=\boldsymbol{0}$, the original penalty function P and J are numerically identical. The derivatives of J however, which will be utilized in acquiring stationarity, will now include the state equations.

Because the state equations and subsequently eqn. (1.5) have to be satisfied in the whole time interval $t_0 \leq t \leq t_f$, the adjoint expression appears in the integrand

$$J = \Phi[\boldsymbol{x}(t_f)] + \int_{t_0}^{t_f} \left\{ L[\boldsymbol{x}, \boldsymbol{u}] + \boldsymbol{\lambda}^T \left[\boldsymbol{f}[\boldsymbol{x}, \boldsymbol{u}] - \dot{\boldsymbol{x}} \right] \right\}\, \mathrm{d}t \qquad (1.6)$$

For convenience, a function called the Hamiltonian is introduced

$$H[\boldsymbol{x}, \boldsymbol{u}, \boldsymbol{\lambda}] := L[\boldsymbol{x}, \boldsymbol{u}] + \boldsymbol{\lambda}^T\, \boldsymbol{f}[\boldsymbol{x}, \boldsymbol{u}] \qquad (1.7)$$

which for the penalty function leads to

$$J = \Phi[\cdot] + \int_{t_0}^{t_f} H[\cdot]\, \mathrm{d}t - \int_{t_0}^{t_f} \boldsymbol{\lambda}^T\, \dot{\boldsymbol{x}}\, \mathrm{d}t \qquad (1.8)$$

The second integral, by product integration yields

$$\int_{t_0}^{t_f} \boldsymbol{\lambda}^T\, \dot{\boldsymbol{x}}\, \mathrm{d}t = \boldsymbol{\lambda}^T\, \boldsymbol{x} \Big|_{t_0}^{t_f} - \int_{t_0}^{t_f} \dot{\boldsymbol{\lambda}}^T\, \boldsymbol{x}\, \mathrm{d}t$$

and subsequently

$$J = \Phi[\boldsymbol{x}(t_f)] + \int_{t_0}^{t_f} \left(H[\cdot] + \dot{\boldsymbol{\lambda}}^T\, \boldsymbol{x} \right)\, \mathrm{d}t \; - \left(\boldsymbol{\lambda}^T(t_f)\, \boldsymbol{x}(t_f) - \boldsymbol{\lambda}^T(t_0)\, \boldsymbol{x}(t_0) \right) \qquad (1.9)$$

1.5.2 Calculus of Variations

The eqn. (1.1) describes how the control input $\boldsymbol{u}(t)$ determines the state trajectory $\boldsymbol{x}(t)$ from its initial value $\boldsymbol{x}_0$. At time $t = t_f$, the augmented penalty function given by eqn. (1.9) evaluates the effect of the control input, providing a way to rate different paths of $\boldsymbol{u}(t)$. The task is now to find a particular control input $\boldsymbol{u}^*(t)$, for which first-order effects of variations are zero. Every small excursion from $\boldsymbol{u}^*(t)$ will result in a less than optimal path.

It is important to note here that control variations also result in variation of the state [42], which influence the state trajectory at and beyond the time of application. Therefore, the idea to determine the stationary point is to vary $\boldsymbol{u}^*(t)$ and $\boldsymbol{x}^*(t)$ by a small amount and investigate the changes in J. Assuming a priori that $\boldsymbol{u}^*(t)$ and $\boldsymbol{x}^*(t)$ exist, the changes in J resulting from a nearby, non-optimal control $\boldsymbol{u}^* + \Delta\boldsymbol{u}$ and state $\boldsymbol{x}^* + \Delta\boldsymbol{x}$ are described by the Taylor expansion

$$J(\boldsymbol{u}^* + \Delta\boldsymbol{u}, \boldsymbol{x}^* + \Delta\boldsymbol{x}) = J(\boldsymbol{u}^*, \boldsymbol{x}^*) + \left[\frac{\partial J}{\partial \boldsymbol{u}}\Delta\boldsymbol{u} + \frac{\partial J}{\partial \boldsymbol{x}}\Delta\boldsymbol{x}\right] +$$
$$+ \left[\frac{1}{2}\Delta\boldsymbol{u}^T \frac{\partial^2 J}{\partial \boldsymbol{u}^2}\Delta\boldsymbol{u} + \Delta\boldsymbol{u}^T \frac{\partial^2 J}{\partial \boldsymbol{u}\,\partial\boldsymbol{x}}\Delta\boldsymbol{x} + \frac{1}{2}\Delta\boldsymbol{x}^T \frac{\partial^2 J}{\partial \boldsymbol{x}^2}\Delta\boldsymbol{x}\right]$$

for a continuously differentiable J and neglecting terms of higher order than 3. Every derivative has to be evaluated at $\boldsymbol{u}^*$ and $\boldsymbol{x}^*$. The first-order derivatives $\frac{\partial J}{\partial \boldsymbol{u}}$ and $\frac{\partial J}{\partial \boldsymbol{x}}$ are both row vectors

$$\frac{\partial J}{\partial \boldsymbol{u}} = \left[\begin{array}{cccc} \frac{\partial J}{\partial u_1} & \frac{\partial J}{\partial u_2} & \cdots & \frac{\partial J}{\partial u_n} \end{array}\right] \qquad \frac{\partial J}{\partial \boldsymbol{x}} = \left[\begin{array}{cccc} \frac{\partial J}{\partial x_1} & \frac{\partial J}{\partial x_2} & \cdots & \frac{\partial J}{\partial x_m} \end{array}\right]$$

with n elements for the control vector $\boldsymbol{u}$ and m elements for the state vector $\boldsymbol{x}$, respectively. The second-order derivatives are matrices: $\frac{\partial^2 J}{\partial \boldsymbol{u}\partial\boldsymbol{x}}$ is a rectangular matrix (n by m), the other two $\frac{\partial^2 J}{\partial \boldsymbol{u}^2}$ and $\frac{\partial^2 J}{\partial \boldsymbol{x}^2}$ are square matrices (n by n and m by m, respectively).

Switching to variation notation, indicating infinitesimal excursions from $\boldsymbol{u}^*$ and $\boldsymbol{x}^*$ leads to $\Delta(\cdot)$ becoming $\delta(\cdot)$, which together with $J(\boldsymbol{u}^* + \Delta\boldsymbol{u}, \boldsymbol{x}^* + \Delta\boldsymbol{x}) - J(\boldsymbol{u}^*, \boldsymbol{x}^*) =: \delta J$ yields

$$\delta J = \left[\frac{\partial J}{\partial \boldsymbol{u}}\delta\boldsymbol{u} + \frac{\partial J}{\partial \boldsymbol{x}}\delta\boldsymbol{x}\right] + \left[\frac{1}{2}\left(\begin{array}{cc}\delta\boldsymbol{u}^T & \delta\boldsymbol{x}^T\end{array}\right)\left(\begin{array}{cc}\frac{\partial^2 J}{\partial \boldsymbol{u}^2} & \frac{\partial^2 J}{\partial \boldsymbol{u}\partial\boldsymbol{x}} \\ \frac{\partial^2 J}{\partial \boldsymbol{u}\partial\boldsymbol{x}} & \frac{\partial^2 J}{\partial \boldsymbol{x}^2}\end{array}\right)\left(\begin{array}{c}\delta\boldsymbol{u} \\ \delta\boldsymbol{x}\end{array}\right)\right] \qquad (1.10)$$

The first bracket is called the *first variation* of J and is given the symbol $\delta_1 J$ for easier notation. For a stationary J, the partial derivatives $\frac{\partial J}{\partial \boldsymbol{u}}$ and $\frac{\partial J}{\partial \boldsymbol{x}}$ have to be both zero for arbitrary variations $\delta\boldsymbol{u}$ and $\delta\boldsymbol{x}$, resulting in $\delta_1 J = 0$. Calculating the partial derivatives

using eqn. (1.9) yields the vectors

$$\frac{\partial J}{\partial \boldsymbol{u}} = \frac{\partial}{\partial \boldsymbol{u}} \left(\int\limits_{t_0}^{t_f} H[\boldsymbol{x}, \boldsymbol{u}, \boldsymbol{\lambda}] \, \mathrm{d}t \right) = \int\limits_{t_0}^{t_f} \frac{\partial H}{\partial \boldsymbol{u}} \, \mathrm{d}t \qquad (1.11)$$

$$\frac{\partial J}{\partial \boldsymbol{x}} = \left. \frac{\partial \Phi}{\partial \boldsymbol{x}} \right|_{t_f} + \int\limits_{t_0}^{t_f} \left(\frac{\partial H}{\partial \boldsymbol{x}} + \dot{\boldsymbol{\lambda}}^T \right) \, \mathrm{d}t - \left(\left. \boldsymbol{\lambda}^T(t) \right|_{t_f} - \left. \boldsymbol{\lambda}^T(t) \right|_{t_0} \right) \qquad (1.12)$$

Inserting these expressions into the first variation and collecting the terms yields

$$\delta_1 J = \int\limits_{t_0}^{t_f} \left(\left[\frac{\partial H}{\partial \boldsymbol{u}} \right] \delta \boldsymbol{u} + \left[\frac{\partial H}{\partial \boldsymbol{x}} + \dot{\boldsymbol{\lambda}}^T \right] \delta \boldsymbol{x} \right) \, \mathrm{d}t + \left. \left(\left[\frac{\partial \Phi}{\partial \boldsymbol{x}} - \boldsymbol{\lambda}^T \right] \delta \boldsymbol{x} \right) \right|_{t_f} + \left. \left(\boldsymbol{\lambda}^T \delta \boldsymbol{x} \right) \right|_{t_0}$$
$$(1.13)$$

Because the state trajectory $\boldsymbol{x}(t)$ at t_0 is fixed at $\boldsymbol{x}_0$, the variation $\left. \delta \boldsymbol{x}(t) \right|_{t_0}$ is zero, nullifying also the last summand in eqn. (1.13). In order to attain $\delta_1 J = 0$, all three terms inside the square brackets have to be zero as well, to allow the variations $\delta \boldsymbol{x}$ and $\delta \boldsymbol{u}$ to have arbitrary values. This results in three conditions

$$\boldsymbol{0} = \frac{\partial H(\boldsymbol{x}, \boldsymbol{u}, \boldsymbol{\lambda})}{\partial \boldsymbol{u}} \qquad (1.14)$$

$$\dot{\boldsymbol{\lambda}}(t) = - \left(\frac{\partial H(\boldsymbol{x}, \boldsymbol{u}, \boldsymbol{\lambda})}{\partial \boldsymbol{x}} \right)^T \qquad (1.15)$$

$$\boldsymbol{\lambda}(t_f) = \left. \left(\frac{\partial \Phi(\boldsymbol{x})}{\partial \boldsymbol{x}} \right)^T \right|_{t_f} \qquad (1.16)$$

Whether these equations yield a solution $\boldsymbol{x}^*$ and $\boldsymbol{u}^*$ depends on the existence of $\delta \boldsymbol{u}$, which can be tested using a variational expression for eqn. (1.14)

$$\boldsymbol{0} = \frac{\partial^2 H}{\partial \boldsymbol{u} \, \partial \boldsymbol{x}} \, \delta \boldsymbol{x} + \frac{\partial^2 H}{\partial \boldsymbol{u}^2} \, \delta \boldsymbol{u} + \frac{\partial^2 H}{\partial \boldsymbol{u} \, \partial \boldsymbol{\lambda}} \, \delta \boldsymbol{\lambda}$$

The solution for $\delta \boldsymbol{u}$ of this equation and $\frac{\partial^2 H}{\partial \boldsymbol{u} \, \partial \boldsymbol{\lambda}} = \frac{\partial \boldsymbol{f}}{\partial \boldsymbol{u}}^T$ (derived from eqn. (1.7)) yields

$$\delta \boldsymbol{u} = \left(\frac{\partial^2 H}{\partial \boldsymbol{u}^2} \right)^{-1} \left(-\frac{\partial^2 H}{\partial \boldsymbol{u} \partial \boldsymbol{x}} \delta \boldsymbol{x} - \frac{\partial \boldsymbol{f}}{\partial \boldsymbol{u}}^T \delta \boldsymbol{\lambda} \right) \qquad (1.17)$$

Here, $\delta \boldsymbol{u}$ can only be obtained if the matrix $\frac{\partial^2 H}{\partial \boldsymbol{u}^2}$ is regular (i.e. invertible). This condition can be tested by examining the determinant of the matrix.

To summarize the differential equations that have to be solved to find a control input $\boldsymbol{u}^*(t)$, it is useful to further derive the definition of the Hamiltonian (eqn. (1.7)) with

respect to $\boldsymbol{\lambda}^T$

$$\dot{\boldsymbol{x}}(t) = \left(\frac{\partial H}{\partial \boldsymbol{\lambda}} \right)^T \tag{1.18}$$

and also to evaluate eqn. (1.15) with eqn. (1.7)

$$\dot{\boldsymbol{\lambda}}(t) = - \left(\frac{\partial L}{\partial \boldsymbol{x}} \right)^T - \frac{\partial \boldsymbol{f}^T}{\partial \boldsymbol{x}} \, \boldsymbol{\lambda} \tag{1.19}$$

Eqn.(1.14) provides $\boldsymbol{u}(t)$ for these differential equations in $\boldsymbol{x}$ and $\boldsymbol{\lambda}$. The boundary conditions are split: some are given are $t = t_0$ (by eqn. (1.2)) and some at $t = t_f$ (by eqn. (1.16)). Therefore, eqns. (1.18) and (1.19) describe a *two-point boundary value problem*.

Furthermore, the second bracket in eqn. (1.10) enables to qualify J at $\boldsymbol{u}^*$. It is named the second variation of J and is given the symbol $\delta_2 J$. The second partial derivatives using eqns.(1.11) and (1.12) yield the matrices

$$\frac{\partial^2 J}{\partial \boldsymbol{u}^2} = \int\limits_{t_0}^{t_f} \frac{\partial^2 H}{\partial \boldsymbol{u}^2} \, \mathrm{d}t \tag{1.20}$$

$$\frac{\partial^2 J}{\partial \boldsymbol{u} \partial \boldsymbol{x}} = \int\limits_{t_0}^{t_f} \frac{\partial^2 H}{\partial \boldsymbol{u} \partial \boldsymbol{x}} \, \mathrm{d}t \tag{1.21}$$

$$\frac{\partial^2 J}{\partial \boldsymbol{x}^2} = \left. \frac{\partial^2 \Phi}{\partial \boldsymbol{x}^2} \right|_{t_f} + \int\limits_{t_0}^{t_f} \frac{\partial^2 H}{\partial \boldsymbol{x}^2} \, \mathrm{d}t \tag{1.22}$$

Thus, $\delta_2 J$ is

$$\delta_2 J = \frac{1}{2} \left. \left(\delta \boldsymbol{x}^T \, \frac{\partial^2 \Phi}{\partial \boldsymbol{x}} \, \delta \boldsymbol{x} \right) \right|_{t_f} + \frac{1}{2} \int\limits_{t_0}^{t_f} \left[\left(\begin{array}{cc} \delta \boldsymbol{u}^T & \delta \boldsymbol{x}^T \end{array} \right) \left(\begin{array}{cc} \frac{\partial^2 H}{\partial \boldsymbol{u}^2} & \frac{\partial^2 H}{\partial \boldsymbol{u} \partial \boldsymbol{x}} \\ \frac{\partial^2 H}{\partial \boldsymbol{u} \partial \boldsymbol{x}} & \frac{\partial^2 H}{\partial \boldsymbol{x}^2} \end{array} \right) \left(\begin{array}{c} \delta \boldsymbol{u} \\ \delta \boldsymbol{x} \end{array} \right) \right] \, \mathrm{d}t$$

The matrix inside the integral called the Hessian matrix, which is symmetric because of the symmetry of second derivatives on the Hamiltonian. If the Hessian matrix is positive definite throughout the interval $t_0 \le t \le t_f$, then $\boldsymbol{u}^*$ and $\boldsymbol{x}^*$ constitute a local minimum of J. This case appears when the eigenvalues are all greater than zero. Conversely, if the Hessian matrix is negative definite, then $\boldsymbol{u}^*$ and $\boldsymbol{x}^*$ is a local maximum. Here, the eigenvalues are all less than zero. A saddle point of J, characterized by minima and maxima regarding different components of $\boldsymbol{u}$ and $\boldsymbol{x}$, is indicated by an indefinite Hessian matrix , where both negative and positive eigenvalues exist at $\boldsymbol{u}^*$ and $\boldsymbol{x}^*$.

Furthermore, if the final time t_f is not fixed but also can participate in minimizing/-

maximizing the penalty function J, variations due to different values of t_f have also to be considered. This is done by also taking the time derivative of J into account, which adds an extra variation to the right side of eqn. (1.13)

$$\delta_1 J(t_f) = \delta_1 J(t_f)\Big|_{\text{fixed}} + \frac{\mathrm{d}J(t)}{\mathrm{d}t}\Big|_{t_f} \delta t \tag{1.23}$$

Still, eqns. (1.14) to (1.16) have to be satisfied to zero out the first summand. The additional derivative with respect to time t, applying the chain rule for $\Phi[\cdot]$ and extracting the integrand from eqn. (1.8) yields

$$\frac{\mathrm{d}J(t)}{\mathrm{d}t}\Big|_{t_f} = \left(\frac{\partial \Phi}{\partial \boldsymbol{x}} \dot{\boldsymbol{x}}\right)\Big|_{t_f} + \left(\frac{\partial \Phi}{\partial t}\right)\Big|_{t_f} + \left(H - \boldsymbol{\lambda}^T \dot{\boldsymbol{x}}\right)\Big|_{t_f}$$

Because of eqn. (1.16), the term in the first parentheses is equal to $\boldsymbol{\lambda}^T \dot{\boldsymbol{x}}$. This cancels out with the right term in the third parentheses, resulting in

$$\frac{\mathrm{d}J}{\mathrm{d}t}\Big|_{t_f} = \left(\frac{\partial \Phi}{\partial t} + H\right)\Big|_{t_f} \tag{1.24}$$

This expression has to be zero for $\delta J_1(t_f) = 0$. If $\Phi[\cdot]$ does not explicitly contain the time t, the condition reduces to $H\big|_{t_f} = 0$, providing an extra condition for $\delta J_1(t_f) = 0$ to solve the two-point boundary problem for this special case. If additionally H is independent of time, it is zero throughout the interval $t_0 \leq t \leq t_f$.

1.6 Zero-Sum Differential Games

The worst possible example of a collision scenario between two aircraft is one in which the intruder follows the ownship. Whether this behavior is intentional or not plays no role for the evasive maneuver of the ownship. An evasion algorithm for the ownship using this worst case as a basis is the most cautious one regarding the movements of the intruder. These, however, can be modeled by limiting the degrees of freedom to also incorporate a straight[23] (or any other) course.

To model the nature of the unrestricted encounter, *zero-sum games* are one possibility, assigning the ownship the role of an evader and the intruder the role of a pursuer. For a zero-sum game, the sum of the payoff for each player is zero for every action. If the intruder increases its payoff by getting closer during an encounter, the evader will increase the distance, matching the gain in payoff.

Fig. 1.22a illustrates such a two-player game using discrete values in a so-called payoff matrix. In this example, if player E chooses action e_3 and player P chooses action p_2, then E gains 2 points and P loses 2 points.

---

[23]like the cases presented in section 1.2.

Player P

Actions ➜	p_1	p_2	p_3	p_4
e_1	35|-35	14|-14	8|-8	10|-10
e_2	20|-20	15|-15	12|-12	35|-35
e_3	40|-40	2|-2	10|-10	5|-5
e_4	-9|9	4|-4	11|-11	0|-0

Player E

(a) Gains and losses of each player

Player P
(minimizing)

Actions ➜	p_1	p_2	p_3	p_4
e_1	35	14	8	10
e_2	20	15	12	35
e_3	40	2	10	5
e_4	-9	4	11	0

Player E
(maximizing)
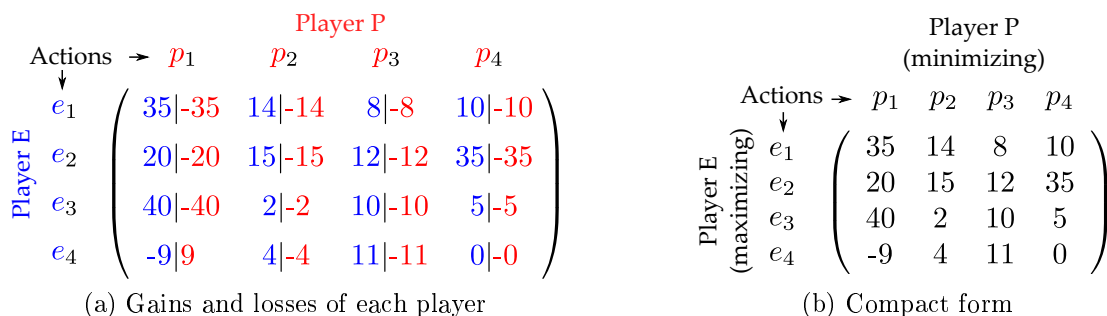
(b) Compact form

Figure 1.22: Examples of payoff matrices for a zero sum game

Each player's objective is to maximize its own payoff. Because it is a zero sum game, it is possible to write the payoff matrix in a compact form by discarding player P's payoff. The objectives of the players are now represented by player E trying to maximize the remaining payoff and player P trying to minimize it.

Each player has all the information about the payoff matrix and the opponent's strategy. If E (the maximizer) plays first, he should pick the row with the largest minimum, since he knows player P will subsequently pick the column with the minimum. Similarly, if P (the minimizer) plays first, he should pick the column with the smallest maximum, since he knows player E will subsequently pick the row with the maximum. These choices are called optimal, because they limit each player's losses. The optimal choices for the game in Fig. 1.22b are e_2 and p_3, regardless of who plays first, leading to a payoff of 12 points

$$\underbrace{\max_{e_j} \min_{p_i} J_{ji}}_{\text{(E plays first)}} = 12 = \underbrace{\min_{p_i} \max_{e_j} J_{ji}}_{\text{(P plays first)}} \tag{1.25}$$

with J_{ji} representing the values of the payoff matrix. Considering non-optimal choices leads to

$$J(e_j, p_3) \leq J(e_2, p_3) \leq J(e_2, p_i) \tag{1.26}$$

where (e_2, p_3) indicates a *game-theoretic saddle point*.

Considering the situation described at the beginning of this section between an pursuer and an evader, the payoff matrix J_{ji} is replaced by a continuous payoff function $J(\boldsymbol{u}_p, \boldsymbol{u}_e)$, where $\boldsymbol{u}_p$ and $\boldsymbol{u}_e$ represent control inputs[24] from Player P (pursuer) and Player E (evader). Here, the objective of the evader is to maximize the J and vice versa for the pursuer.

Similarly to eqn. (1.26), a saddle point is determined by

$$J(\boldsymbol{u}_e, \boldsymbol{u}_p^*) \leq J(\boldsymbol{u}_e^*, \boldsymbol{u}_p^*) \leq J(\boldsymbol{u}_e^*, \boldsymbol{u}_p) \tag{1.27}$$

---

[24]as discussed in section 1.5.1

where $\boldsymbol{u}_e^*, \boldsymbol{u}_p^*$ refer to a stationary function J. Therefore, the necessary conditions to acquire $\boldsymbol{u}_e^*, \boldsymbol{u}_p^*$ are those discussed in section 1.5.1. However, for that to work, the function J has to be designed in a way that the order of the maxi- and minimization has no effect [43] (like in eqn. (1.25))

$$\max_{\boldsymbol{u}_e} \min_{\boldsymbol{u}_p} J(\boldsymbol{u}_e, \boldsymbol{u}_p) = J(\boldsymbol{u}_e^*, \boldsymbol{u}_p^*) = \min_{\boldsymbol{u}_p} \max_{\boldsymbol{u}_e} J(\boldsymbol{u}_e, \boldsymbol{u}_p) \tag{1.28}$$

Because each player recognizes all of the other players options, the following actions will emerge:

1. given that the evader assumes that the pursuer will choose $\boldsymbol{u}_p$ to get the overall minimum of J, the pursuer try to will limit his losses. Therefore, he chooses a control which will provide the highest value of J possible in this situation.

2. given that the pursuer assumes that the evader will choose $\boldsymbol{u}_e$ to get the overall maximum of J, also the evader try to will limit his losses. Therefore, he chooses a control which will provide the lowest value of J possible in this situation.

Both players attempt to escape the saddle-point, denoted by $\boldsymbol{u}_p^*, \boldsymbol{u}_e^*$, but fail since each of them act on the prediction that the other player could punish an excursion by inflicting higher losses. These strategies resemble those described before in the discrete case. Since eqn. (1.28) applies all the methods for acquiring stationarity of J are valid (referring to $\delta_1 J(\boldsymbol{u}_e^*, \boldsymbol{u}_p^*) = 0$).

Analog to the augmented penalty function in section 1.5.1, the payoff function J chosen to describe the problem is

$$J = \Phi[\boldsymbol{\xi}(t_f)] + \int_{t_0}^{t_f} \boldsymbol{\lambda}^T(t) \, \boldsymbol{g}[\boldsymbol{\xi}, \boldsymbol{u}_e, \boldsymbol{u}_p] \, \mathrm{d}t \tag{1.29}$$

where $\boldsymbol{\xi}(t)$ is the state of the game (analog to eqn. (1.1)). The function $\Phi[\boldsymbol{\xi}(t_f)]$ describes the relative distance between the two players at time t_f. The integrand represents the dynamic constraints (movement abilities), given by the state equation

$$\dot{\boldsymbol{\xi}}(t) = \boldsymbol{f}[\boldsymbol{\xi}(t), \boldsymbol{u}_e(t), \boldsymbol{u}_p(t)] \tag{1.30}$$

with initial condition

$$\boldsymbol{\xi}(t_0) = \boldsymbol{\xi}_0$$

where $\boldsymbol{\xi}(t)$ describes the state trajectory, influenced by the control of the pursuer $\boldsymbol{u}_p(t)$ and of the evader $\boldsymbol{u}_e(t)$.

Analog to eqn. (1.8), J develops to

$$J = \Phi[\boldsymbol{\xi}(t_f)] + \int\limits_{t_0}^{t_f} \left(H[\boldsymbol{\xi}, \boldsymbol{u}_e, \boldsymbol{u}_p] - \boldsymbol{\lambda}^T \, \dot{\boldsymbol{\xi}} \right) \, \mathrm{d}t \tag{1.31}$$

Because the control terms in eqn. (1.31) only are influencing the Hamiltonian, the inequality (eqn. (1.27)) yields

$$\int\limits_{t_0}^{t_f} \left(H[\boldsymbol{\xi}, \boldsymbol{u}_e, \boldsymbol{u}_p^*, \boldsymbol{\lambda}] \right) \mathrm{d}t \leq \int\limits_{t_0}^{t_f} \left(H[\boldsymbol{\xi}^*, \boldsymbol{u}_e^*, \boldsymbol{u}_p^*, \boldsymbol{\lambda}^*] \right) \mathrm{d}t \leq \int\limits_{t_0}^{t_f} \left(H[\boldsymbol{\xi}, \boldsymbol{u}_e^*, \boldsymbol{u}_p, \boldsymbol{\lambda}] \right) \mathrm{d}t$$

Therefore, the value of integral in $t_0 \leq t \leq t_f$ will also have a saddle-point property, resulting in an optimal pair $\left\{ \boldsymbol{u}_e^*(t), \boldsymbol{u}_p^*(t) \right\}$. By induction, also the integrand (the Hamiltonian) at every instant of time has to have this property[25]:

$$H[\boldsymbol{\xi}, \boldsymbol{u}_e, \boldsymbol{u}_p^*, \boldsymbol{\lambda}] \leq H[\boldsymbol{\xi}^*, \boldsymbol{u}_e^*, \boldsymbol{u}_p^*, \boldsymbol{\lambda}^*] \leq H[\boldsymbol{\xi}, \boldsymbol{u}_e^*, \boldsymbol{u}_p, \boldsymbol{\lambda}] \tag{1.32}$$

and analog to eqn. (1.28)

$$\max_{\boldsymbol{u}_e} \min_{\boldsymbol{u}_p} H(\boldsymbol{\xi}, \boldsymbol{u}_e, \boldsymbol{u}_p, \boldsymbol{\lambda}) = H(\boldsymbol{\xi}^*, \boldsymbol{u}_e^*, \boldsymbol{u}_p^*, \boldsymbol{\lambda}^*) = \min_{\boldsymbol{u}_p} \max_{\boldsymbol{u}_e} H(\boldsymbol{\xi}, \boldsymbol{u}_p, \boldsymbol{u}_e, \boldsymbol{\lambda})$$

Finally, with the definition of the Hamiltonian (eqn. (1.7)), the stationary point yielding the optimal control $\boldsymbol{u}_p^*, \boldsymbol{u}_e^*$ can be calculated using eqns. (1.14), (1.18) and (1.19). Furthermore, the nature of the stationary point to match the objectives of the players has to be verified using the second-order conditions from section 1.5.2

$$\frac{\partial^2 H}{\partial \boldsymbol{u}_e^2} < \boldsymbol{0} \qquad\qquad \frac{\partial^2 H}{\partial \boldsymbol{u}_p^2} > \boldsymbol{0} \tag{1.33}$$
$$\text{(H is negative definite)} \qquad\qquad \text{(H is positive definite)}$$

---

[25] The condition that for an optimal path reaching from t_0 to t_f, every step taken also has to be optimal, is called Bellman's principle of optimality [42].

2 State of the Art Aircraft Separation Equipment

The previous sections introduced regulation and statistics in aircraft separation and the human factors which influence it. It has been shown that most Airprox events and midair collisions happen in uncontrolled airspace under VFR. One proposition of this thesis is to use traffic systems to minimize the time used for visually identifying traffic by aiding the pilot where to look outside the cockpit. In the following, a brief review of the systems currently in use is made to illustrate their benefits and deficiencies.

2.1 Traffic Displays in Production

In aviation, traffic avoidance system have a long history of development [44]. The first research on the concept was introduced in 1956 after two airliners collided over the Grand Canyon in Arizona. Decades later this lead to the development of the Traffic Alert and Collision Avoidance System (TCAS, Table 2.1), which is important to note because its symbology permeates also the systems for use under VFR. In its latest version (TCAS II Ver. 7.1), it provides aural and visual traffic and resolution advisories.

Table 2.1: TCAS family of traffic information systems

Traffic information conveyed to the pilot	Visualization example

TCAS I
The system provides symbolic depiction of moving traffic and its hazard level, compliant to FAA Technical Standard Order C147 [45]. Symbols are for non-threat traffic: ◇ in white or cyan, proximity intruder traffic: ◆ in white or cyan, potentially hazardous traffic: ● in yellow. These threat levels depend relative distance and on the time to the closest point of approach (section A.5.2). The ● symbol is associated with a Traffic Advisory (TA), which is accompanied by an audible alert. For all symbols, the relative altitude is provided numerically (e.g. +**04** for traffic 400 feet above).
Climb/descend movement is indicated by an up/down arrow next to the traffic symbol (no arrow if flying level). The system actively interrogates nearby Mode A, C and S transponders and is used in [46] [47], for example.
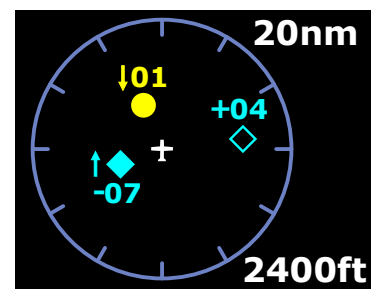
TCAS II

The system displays the traffic symbols in the same way as TCAS I, but for immediate collision threats additionally issues a Resolution Advisory (RA) [48]. Here, a square box in red indicates the threat's position. For RAs, a vertical avoidance maneuver for evasion is annunciated aurally by the system (e.g. *Climb*, *Descend*, *Maintain Vertical Speed*). In addition, a vertical speed indication is provided for the pilot, on which the desired and undesired vertical speed for evasion is indicated as a green and red band, respectively. Newer TCAS II display implementations include a pitch cue on the primary flight display,

which indicates the pitch angle (Fig. A.7) the pilot has to maintain to ensure separation. Furthermore, if the RA-triggering aircraft is also TCAS II-equipped, it will receive a reverse RA. The system actively interrogates nearby Mode A, C and S transponders and is used in [49] [50], for example.

Whereas in commercial aviation TCAS I and II represent the standard cockpit equipment for airborne collision avoidance, the introduction of a similar system for use in uncontrolled airspace and visual flight has only just begun. For use under VFR, current proprietary solutions acquire and display the position of other aircraft (Table 2.2). They also provide aural and visual traffic advisories in the form of alerts.

Table 2.2: Traffic information systems for VFR

Traffic information conveyed to the pilot	Visualization
TAS - Traffic Advisory System The symbolic depiction of moving traffic and its hazard level and proximity is based on TCAS I (no resolution advisories). Additional features vary among different manufacturers (e.g. audible advisories, moving map). The depicted representative solution also shows a travel direction attached to the traffic symbols. This type of display is used in [31] [51] [52] [53], for example.	
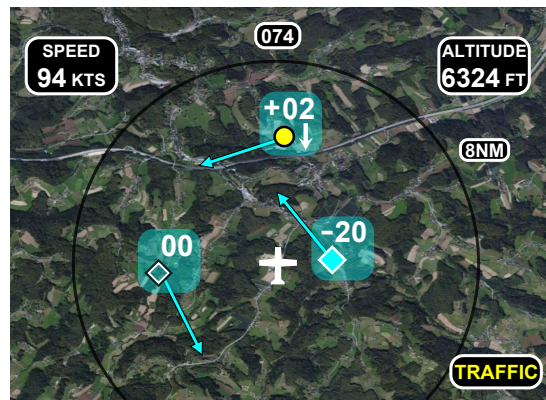
FLARM

This system is predominantly in use with gliders and helicopters. It Supports FLARM[1]-transponders and uses a proprietary threat calculation algorithm to determine air vehicle behavior. Audible advisory is also provided. To date, there are two display variants available [54] [55]:

a) LED-type: Circularly arranged bi-color light emitting diodes (LEDs) indicate the relative bearing of traffic, vertical LEDs its vertical offset. Green for proximity traffic, red for threat. Urgency is shown by flashing LEDs.

b) 'Radar'-like: Shows moving traffic around ownship, color and size of the arrow-symbol indicate the threat level and relative altitude. The latter is also indicated numerically together with a climb/descend indication in case of a threat.
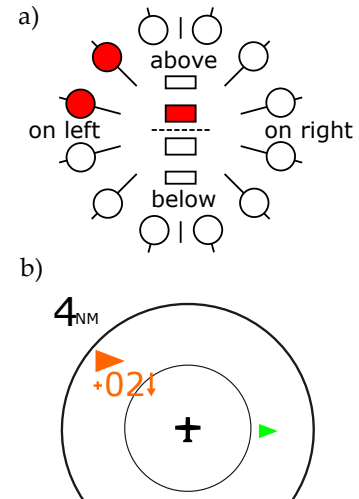
PTDD - Passive Traffic Detection Devices

This system detects transponder responses of other air vehicles triggered by active systems (like air traffic radar, TCAS). Numerical information is provided indicating relative altitude, climb/descend movement and relative bearing of the aircraft posing the highest threat. The system is able to depict a moving traffic indication for up to 3 traffic aircraft. Audible advisory and alert threat levels are also provided. This type of display is used in [56], for example.
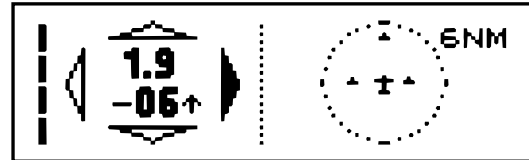
A comparison of Table 2.1 and 2.2 shows that the majority of currently used traffic warning systems for VFR flight use the same visualization standards as TCAS II [48], but without resolution advisories. However, TCAS II was not developed for the demands of VFR operations. TCAS II is a last-resort safety net, mandatory [57] for aircraft with a maximum take-off mass exceeding 5700 kg, or certified to carry more than 19 passengers. In the context of airline transportation and flight according to IFR, a number of studies have addressed the use of TCAS [58] [59]. However, these findings are not directly applicable to VFR flight where pilots bear the sole responsibility for separation according to the Rules of the Air [1]. So far, there is no consistent philosophy about the required criteria for triggering traffic alerts. The current VFR collision warning systems also do not provide RAs.

The rules of the air are specified for various conflict situations. For VFR pilots an additional challenge is to maintain adequate distance from terrain, clouds and other flying objects which are not necessarily equipped with transponders. However, the distribution

---

[1]name is derived from '**FL**ight al**ARM**'.

of position data among the aircraft is the key feature which the functionality of collision avoidance systems is built on. Some systems for VFR support data acquisition through the Automatic Dependent Surveillance-Broadcast (ADS-B, Table A.5), which provides more detailed and accurate information about the aircraft in the receiver's range than TCAS sensors (e.g. satellite-based position, speed and altitude data). Position reports are typically generated once per second.

Because ADS-B uses low-cost hardware compared to TCAS, it is expected to see widespread usage in the future. Furthermore, in the future the ability to sense traffic will be improved, since using ADS-B 'out' will be mandatory [60] with the FAA's implementation of the *Next-Gen* program [61]. Collision avoidance systems for VFR flight are therefore expected to become a viable product for major avionic producers, as well as cheaper through standardization.

2.2 Traffic Displays in Research

The current traffic warning systems for VFR flight show the relative positions of detectable air vehicles. Similar to TCAS, these systems determine the bearing and position of approaching aircraft and depict them according to their threat-potential. They use abstract icons which change their shape and colors depending on the urgency of the warning. Some systems depict the ownship as an aircraft symbol on top of a configurable moving map background. Except for passive traffic detection devices, all systems support ADS-B transmissions, which provide information including the air vehicle category, position, altitude and speed. Three systems additionally provide a predictive indication for the direction of travel ([31] [52] [53]). Therefore, all systems support the lower levels of situational awareness (i.e. detection of traffic) and furthermore provide visual and aural warnings.

However, conflict prediction can be supported better by using predictive display features [62] [63]. These provide automated support for the anticipation of potential midair conflicts. They enable faster understanding of a conflict scenario. Such features will be used in this thesis to design a traffic display suitable for the requirements of VFR flight.

It is important to note that the allocation of functions between human and automation needs to consider strengths and limitations of both humans and automation. A method for defining different types of automation which can support pilots in their 'see-and-avoid' functions is Parasuraman's (et al.) [64] framework of automation design. Such automation may include the acquisition and analysis of traffic information, the selection of decisions and maneuvers selection and the response selection. In addition, possible options with an even higher level of automation have also been described [64]. Such a system offers a range of decision and action alternatives, and narrows the selection or suggests only one alternative. The latter resembles the visualization of decision aids (e.g. RAs in TCAS II, Table 2.1), which were a noticeable improvement in terms of increasing the automation level of collision avoidance systems for airline pilots. Increasing the level of automation even further, the autopilot may execute an action with the approval of the pilot or alternatively allow the pilot a restricted length of time to veto the maneuver

before automatic execution. At even higher levels of automation the system only informs the pilot either after the autopilot has executed the maneuver or if it decides to do so. At the highest level of automation the system acts autonomously in disregard of the pilot, and decides everything on its own [64].

To investigate the effectiveness of different types of automation, Wickens et al. [65] compared a predictive track display with and without a 'threat vector' added to the predictive track of the own aircraft (top item in Table 2.3). The threat vector indicates the relative approach angle of another air vehicle and also the time until conflict, thus reducing the cognitive effort necessary to predict a conflict. Both indications were tested with flight instructors in single and multiple conflict scenarios in a flight simulator. The flight task involved the performance of avoidance maneuvers. The results showed that the time spent engaged in conflicts was significantly reduced by adding the threat vector to the predictive track in the display. The workload for pilots was not significantly reduced, however, possibly due to the added perceptual effort involved.

In another experiment design, Van Dam et al. proposed two variants named PASAS and XATP which display forbidden zones [66], the design of which is illustrated in the bottom item in Table 2.3.

PASAS shows heading and speed bands on the primary flight display (PFD) in orange depicting the heading and speed ranges to avoid in a traffic encounter. XATP depicts a wedge-shaped protected zone on the Navigation Display (ND) which the ownship's speed vector should avoid in a traffic conflict scenario. Both display modalities were evaluated with airline pilots in simulated multi-conflict scenarios [66]. The task was to maintain separation, but also to limit deviation from the original track and to re-capture the initial track after the avoidance maneuver. Five out of 7 pilots showed a preference for XATP compared to PASAS. XATP gave the pilots a better spatial and temporal mental picture of the situation, and resulted in better judgment of the intruder's relative velocity.

The use of XATP resulted in an improved conflict awareness as well as a better assessment of conflict geometry and urgency.

Similar approaches as the ones discussed above could be implemented in order to increase the automation level of collision warning and avoidance systems for VFR, which are the focus of this thesis. Cockpit automation generally enhances safety, and pilots' attitudes towards cockpit automation are positive. However, there are also concerns about the complexity of automation and necessary training. Also, automation may cause increased mental workload, diminished situational awareness and over-reliance [67] [68].

Display indications of the right-of-way have not yet been addressed by any system.

Table 2.3: Planar traffic displays in research

Name	Visualization example

Predictor-/Threat Vector Display

Aircraft icons indicate positions of ownship (in magenta) and intruders (in light gray) with paths projecting their predicted directions of travel. The lengths of the paths display the predicted aircraft positions 45 seconds into the future. In addition, a threat vector (TV) representing a separation closer than 1500 ft vertically or 3 mi laterally at the closest point of approach (CPA) defines a protected zone around the ownship. As a potential traffic conflict progresses, the predicted path of the intruder would move closer to the end of the TV as the predicted minimum separation decreases. Furthermore, the TV slides along the ownship's predictor line, moving closer to the ownship's aircraft symbol as the time to to CPA decreases. When the TV touches the predicted path of the intruder at CPA, separation is lost. Multiple intruders would produce multiple TVs.

Prohibited Heading/Speed Band and State Vector Envelope Display

These two display variants both are based on the calculation of the relative speed vector between the ownship and the intruder: $\vec{v}_{rel} = \vec{v}_{OS} - \vec{v}_I$ (Fig. (a) below). A loss of separation is defined as $\vec{v}_{rel}$ being inside the sector defined by the ownship position and the protected zone enveloping the intruder. Because the pilot of the ownship is only able to influence his aircraft's speed vector, it is desirable to shift said sector to the end of vector $\vec{v}_I$ (Fig. (b) below). This enables the visualization of a *forbidden zone* (FBZ), which the tip of the ownship's speed vector $\vec{v}_{OS}$ has to avoid in order to maintain separation.

Because the ownship's speed should remain within a safe interval ($v_l \leq |\vec{v}_{OS}| \leq v_u$), the FBZ is clipped by semi-annulus, defined by the ownship's minimum and maximum speeds.

The ownship symbol is displayed at the bottom of the screen pointing forward (heading up mode). Thus, flying a turn will rotate the FBZ and reducing/increasing the airspeed will shorten/lengthen the ownship's speed vector. FBZ can be displayed either split or with the FBZ displayed on the navigation display (PASAS in Fig. (c), and XATP in Fig. (d), respectively). Multiple intruders would produce multiple FBZ's/prohibited bands.

(c) Prohibited Heading/Speed Bands: PASAS
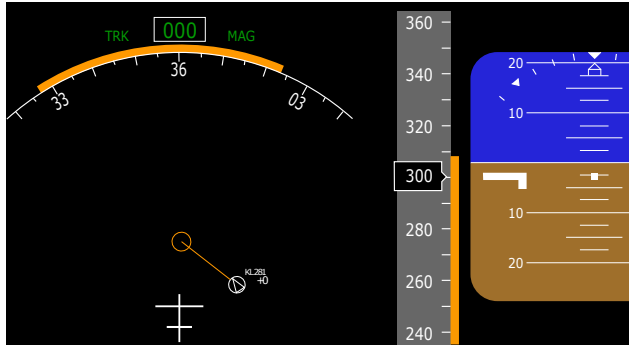
(d) State Vector Envelope Display: XATP
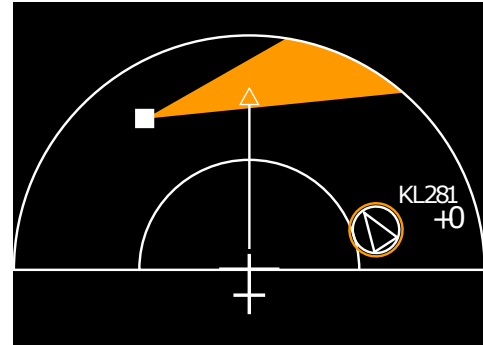
2.3 Pilot Responses to TCAS

Since most of the available studies refer to TCAS, there is little empirical evidence about pilots' use of collision warning systems in VFR flight so far. An interesting study based on real TCAS II events was conducted at Eurocontrol in 2010 [69] and provided insight into the current evasion maneuvers used in commercial airplane operation. The analysis of more than 1000 recorded Resolution Advisories (RAs) showed that 24% of them were handled imprecisely or incorrectly by the cockpit crews. In 10% of the cases the vertical speed during the maneuver was lower than instructed, and in 7% of the cases the vertical speed was higher than instructed. 7% of the analyzed RAs exhibited wrong maneuvers (e.g. a climb was conducted when a descent was instructed).

Research [41] [70] shows a similar picture. Here, the magnitude of pilots' collision avoidance reactions were evaluated in a fixed-base flight simulator with the intruding traffic shown on a 3-channel visual system, as well as on the primary flight display. Thirty two pilots participated in the study, and more than 80% of them were in possession of an Airline Transport Pilot License (ATPL). The pilots resolved the simulated traffic conflicts manually by following the TCAS II RA which instructed a vertical speed of +1500 ft/min (climb) [41]. The RA was shown on the primary flight display (PFD) as a pitch cue and vertical speed tape implementation [48]. The vertical speed was logged during the maneuver after 6 seconds and averaged over 10 seconds. The vertical speeds actually flown are shown in Fig. 2.1.

In the majority of the cases (72%) pilots overreacted and climbed too steeply, and 28% overshot the recommended climb at least 1000 ft/min. Two participants (6%) reacted so slowly to the RA that the instructed vertical speed had to be increased from +1500

to +2500 ft/min. Eighteen participants (56%) exceeded the instructed vertical speed by at least 500 ft/min, and one participant (3%) initially selected an incorrect maneuvering direction, but then immediately corrected the error.
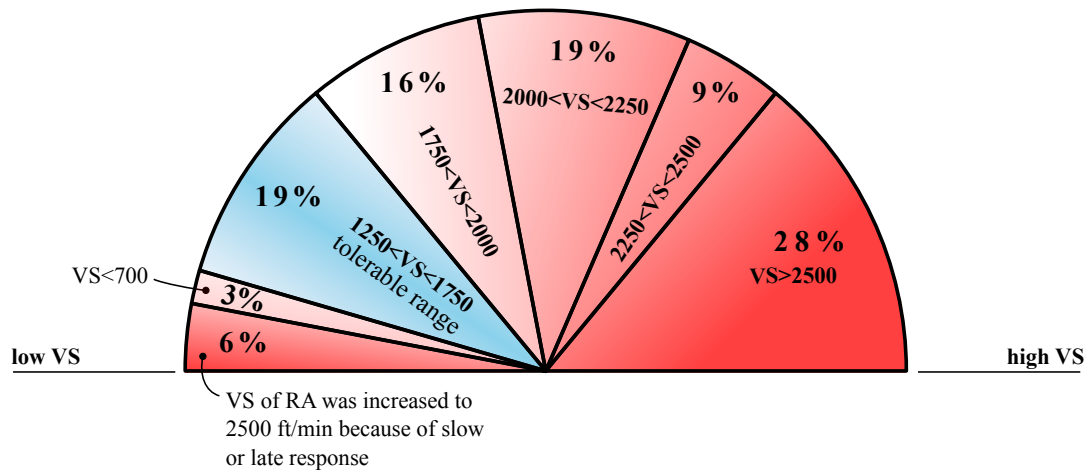
Figure 2.1: Distribution of aircraft responses for an instructed climb with a vertical speed (VS) of +1500 ft/min (basis: 32 participants) [41]. Deviations from the VS instructed by the RA were tolerated in the range of 1250 to 1750 ft/min. Maneuvers which were correct or within the range of tolerance are depicted by the blue sector in the pie chart.

Coso et al. [59] analyzed the pilots' reports about their responses to TCAS from the Aviation Safety Reporting System (ASRS) database [71]. From 248 cases, 77% complied with the RA and 8% reported non-compliance with the RA. The cases of non-compliance were either because the pilots preferred a maneuver which allowed them to keep the intruder aircraft in sight, or because a third aircraft was involved. In 15% of the cases the pilots believed that the RA would direct them into traffic, and therefore did not comply with it. In a few of the cases the pilots complied with the RA, but considered it appropriate to add a horizontal component to the avoidance maneuver. This study demonstrates that the availability of contextual information influences pilots' compliance with resolution advisories.

To summarize, these studies show that in many conflict situations pilots use other avoidance maneuvers, in terms of direction and maneuvering magnitude, than those instructed by TCAS. In some cases the pilots had difficulties in following the RAs precisely, in other cases they preferred to adopt a different avoidance maneuver.

2.4 Ways for Improvement

The main benefit of current VFR collision warning systems (Table 2.2) is the support they provide for identifying conflicting aircraft during flight. Although such systems are expected to reduce the number of midair collisions for small aeroplanes, their usability still needs to be evaluated.

Because of the visual scanning constraints posed by VFR which require that pilots primarily monitor the outside view, the time pilots spend watching the traffic display and deciding whether the detected aircraft is in conflict or not has to be reduced. This should be considered for the design and evaluation of future traffic displays for VFR.

VFR pilots in uncontrolled airspace have to visually identify traffic to apply *see-and-avoid*. As current technology does not provide sensor systems that guarantee detection of potential traffic conflicts, TASs (Fig. 2.2) are only considered as an additional safety tool for VFR flights, but not as the primary source of information. TCAS on the other hand is considered to even overrule ATC in case of conflicting advisories [72]. The view outside is not necessary to perform an avoidance maneuver. Thus, the design premises are different, influencing also the symbology used in the display. Therefore, an evaluation of the requirements for future collision avoidance systems in visual flight has to be done to identify design patterns for VFR traffic displays. The following section addresses this question by means of a flight simulator study.

Furthermore, the sensor technology of TCAS [48] is limited to providing for vertical RA's only. However, data acquisition using ADS-B [60] and Mode S [73] (Table A.5) provide rich information about the traffic in the vicinity. Methods to exploit that capability are also discussed in this thesis.

3 Evaluation of a TCAS-like Traffic Display for Visual Flight

The last chapter introduced traffic warning systems and displays both commercially available and in research. Recently introduced VFR traffic systems (TAS, Table 2.2) have adopted the same traffic symbology as TCAS, however, no studies have been conducted justifying their use in a visual flight environment. Furthermore, pilots' reaction to conflict situations using TCAS systems deviate from the instructed maneuvers (e.g. [59] [69], Fig. 2.1).

This suggests that a similar study should be conducted for TCAS-like systems for VFR, with the aim of identifying areas for further development[1].

3.1 Pilots' Decisions regarding Collision Avoidance

Regarding the introduction of TCAS-like systems for VFR, all the presented systems support pilots a great deal by sensing and displaying aircraft. Among these, conflicting aircraft are also highlighted, aiding in the maneuver-selecting process. However, pilots may still have difficulties in selecting and performing rule-based avoidance maneuvers, and thus a higher level of automation may be desirable.

When evaluating an avoidance maneuver in VFR flight, conformance to aviation regulations [1] represents the main criterion. However, practical experience and research [74] [75] show that pilots do not always conform to regulations when choosing their avoidance maneuver. The reason why pilots may decide to choose a specific avoidance maneuver deviating from the regulations is some greater expected value of the alternative maneuver. This maneuver is weighed against the perceived urgency, economic efficiency, complexity of the maneuver, anticipation of the effort required, and perceived safety [76]. Therefore, the selection of an avoidance maneuver among several alternatives may be influenced by aviation regulations, the goals of the pilot and maneuver 'stereotypes', instructions from air traffic control, or cockpit displays of traffic information.

Empirical evidence suggests that pilots' selection of an avoidance maneuver is based on decision heuristics rather than accurate decision making algorithms. Therefore pilots

---

[1]For reference: The procedure, methods and results of the following evaluation were published in

T. Haberkorn, I. Koglbauer, R. Braunstingl, and B. Prehofer, "Requirements for Future Collision Avoidance Systems in Visual Flight: A Human-Centered Approach," *Human-Machine Systems, IEEE Transactions on*, vol. 43, no. 6, pp. 583-594, Nov 2013.

were found to eliminate maneuvering alternatives with a highly anticipated cognitive effort necessary for carrying them out. An investigation of pilots' preferred avoidance maneuvers [74] found a bias for simple single-axis maneuvers (either vertical or horizontal) rather than more complex multiple-axis maneuvers. Furthermore, in the case of single-axis maneuvers pilots preferred vertical (85%) versus lateral maneuvers, which are considered to be more efficient as the pilots could maintain the heading of their initial route. The widely believed utility of single-axis maneuvers, especially of vertical ones is considered to lie in their lower complexity and control order [74].

Many previous studies show a significant preference on the part of pilots for vertical maneuvers rather than lateral maneuvers [62] [75–80].

A more surprising bias is pilots' preference for climbs rather than descents [74]. However, the right turn maneuvering tendency was reported rarely [75], despite the existence of aviation regulations which foresee such trajectory changes in the case of head-on conflicts.

Investigations of conflict avoidance maneuvers instructed by air traffic controllers demonstrate similar preferences [81] [82]. Research shows that air traffic controllers instructed vertical avoidance maneuvers more often than lateral avoidance maneuvers (68% versus 32%), with descents being instructed more often than climbs (18% versus 5%) [81].

Rantanen and Wickens [81] analyzed recordings of real-life collision avoidance instructions in order to validate a decision making model for air traffic controllers. The features of the model were designed in accordance with the expected utilities (e.g. expediency, traffic flow, visualization) for specific conflict geometries. The results confirmed the assumption that vertical maneuvers are preferred over lateral maneuvers. However, there was a preference for descents rather than climbs, because descents were considered to be more practical as they exploit gravity and lower the fuel consumption of the aircraft involved. Lateral turns were usually instructed at small or obtuse angles of convergence, instead of right angles.

In light of the reported decision making heuristics in order to select an avoidance maneuver [74], as well as the difficulties encountered by pilots using TCAS to perform within the tolerance margins of resolution advisories, an increase in the level of automation is considered to be a possible solution for aiding pilots in their collision avoidance performance.

3.2 Research Questions in Evasion Maneuvering

The following performance hypotheses were formulated according to previous research highlighted in the previous section:

1. Pilots perform more single-axis (either vertical or horizontal) than multiple-axis conflict avoidance maneuvers [74].

2. In the case of single-axis maneuvers, pilots perform vertical rather than lateral maneuvers [62] [74–80].

3. In the case of vertical maneuvers, pilots prefer climbs rather than descents [74].

4. In the case of lateral maneuvers, pilots exhibit a bias for right-turns [75].

In addition, the following hypotheses related to the traffic load condition are proposed:

5. It is expected that under the conditions of multiple conflicts the mental workload of analyzing the conflict, selecting and performing an avoidance maneuver and recapturing the initial track will be higher and the situational awareness of the pilots will be lower.

6. From the last point it is also expected that maneuver stereotypes will be more distinct under higher traffic load conditions.

To address these research questions, we conducted a study in a flight simulator equipped with a TCAS-like traffic display system. The pilots were able to experience simulated traffic conflicts, and could provide feedback regarding the most preferred types and levels of automation for a future collision avoidance system. Therefore, the type and level of system automation requested by the pilots could also be addressed.

3.3 Method

3.3.1 Participants

Eighteen pilots volunteered for the study (9 females and 9 males), aged 22 to 71 years (Mean = 42.27 years, SD = 13.34 years) with an average flight time of 652 hours. The information gathered in relation to total flight time and flight time with specific avionic equipment is provided in Table 3.1.

Flight time	N	%	Mean	SD	Median	Range
Total	18	100	652	192	318	35 to 3100
Traffic display	7	39	351	278	20	10 to 2000
Moving map/GPS	16	89	151	41	100	10 to 600
Glass cockpit	10	56	53	29	6	1 to 250
Autopilot	11	61	341	197	50	2 to 2000

Table 3.1: Flight experience of the participants. The first column shows the number of participants (N) and the second column shows the percentage (%) of participants who reported flight experience with different types of cockpit systems. Mean, standard deviation, median and range values refer to hours.

All of the participants were active pilots and were in possession of a license for piloting at least a single engine aircraft according to visual flight rules. Four pilots held additional licenses for instrument flight rules and commercial flight and two pilots had an Airline Transport Pilot License (ATPL). The female and male pilots were matched according to their total flight experience. Each pilot signed an informed consent form.

3.3.2 Equipment

For this study a fixed-base generic aircraft simulator at the Graz University of Technology [83] was used, which is equipped with a glass cockpit, genuine aircraft controls and two side-by-side seats. The 3-channel visual system uses a spherical screen with a radius of 3.5 m and a height of 3 m. Traffic was shown on the outside view of the flight simulator, as well as on a moving map[2] display. The display software was created using the JAVA programming language by the experimenters. The display hardware was provided by Becker Avionics, using a 6.5 inch screen with 640 x 480 VGA resolution and 16.2 million colors [84].

TCAS-like symbolism was used, resembling the implementation in TAS displays (Table 2.2). Traffic was therefore depicted as a cyan diamond symbol which changed to amber once a traffic alert was issued. A numeric indication of the relative altitude of conflicting aircraft was attached to each diamond symbol (Fig. 3.1). For all of the conflict scenarios

Figure 3.1: Example image of the moving map displayed in the cockpit. In accordance with TCAS-symbolism, the position of traffic on the map is indicated by a diamond and the relative altitude is shown as a 2-digit number [48].

in this experiment the relative altitude indication was 00, meaning that the conflicting aircraft were flying at the same altitude as the ownship. The ownship symbol was oriented forward and located a fixed position at the bottom of the display (heading up mode).

A traffic alert was either provided to the pilots when the oncoming aircraft was closer than 500 m, or when the time-to-collision was shorter than 24 seconds. In either case the

---

[2]The background map and traffic move, while the ownship maintains at a fixed location on the screen.

color of the oncoming traffic symbol changed from cyan to yellow and the word 'traffic' was repeated twice by a cockpit audio system.

The simulated oncoming traffic was displayed on the visual system of the simulator, either as a DeHavilland Beaver or a Grumman Goose aircraft.

The experimenter used a traffic generator to set the conflict scenarios which are described in the following section.

3.3.3 Flight Scenarios

Before a conflict scenario was arranged by the experimenter, the pilots were instructed to configure the aircraft for cruise and engage the autopilot. They were then flying level at a constant airspeed.

Regarding traffic load, both single and multiple conflict scenarios were defined. Therefore each traffic scenario consisted of one or two conflicting aircraft flying at the conflict angles illustrated in Figure 3.2. Single conflict scenarios either involved oncoming Aircraft Number 1 from 350° (called Scenario A), or Aircraft Number 2 from 10° (Scenario B). Multiple conflict scenarios simultaneously involved Aircraft Number 1 and 4 from 350° and 70° respectfully (Scenario C), or Aircraft Number 2 and 3 from 290° and 10° respectfully (Scenario D).

(a) Scenario A   (b) Scenario B   (c) Scenario C   (d) Scenario D
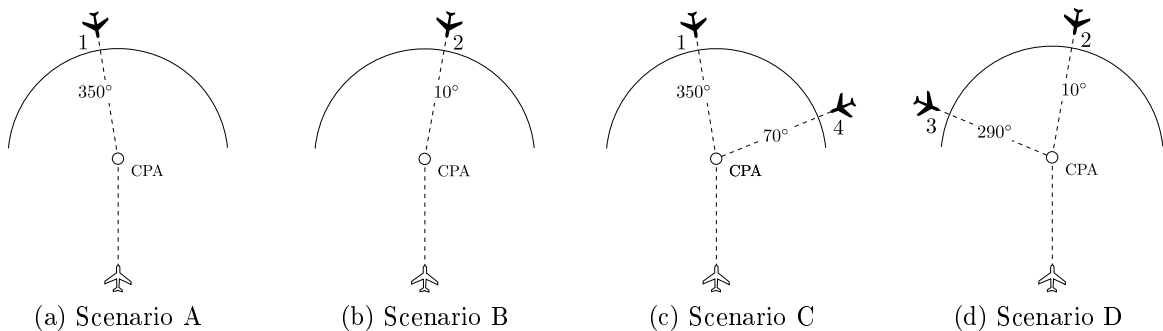
Figure 3.2: Relative bearings defined by a traffic generator used in the experiment. The ownship is the white aircraft at the bottom, and the black aircraft are conflicting. All of the involved aircraft are at the same altitude.

Aircraft number one was set 80 seconds and aircraft number two 85 seconds before the closest point of approach (CPA). Both of these conflicting aircraft were set at the same altitude as the ownship.

At this time the traffic was visible on the display, but was too far away to be visible on the visual system. The setup of the traffic display was identical for all of the maneuvers and pilots (e.g. arc range, heading up).

The traffic alert was generated 24 seconds before CPA. Up until this moment the pilots monitored traffic on the display and on the visual system of the simulator. At 24 seconds before CPA the traffic was easily recognizable. The pilots were instructed to disengage the autopilot and commence an avoidance maneuver immediately after the

traffic alert. Since the autopilot was engaged to fly at specific parameters, each conflict scenario had the same kinematic onset.

It should be noted that the conflicting aircraft were non-cooperative, meaning they did not perform any avoidance maneuvers. In reality this could happen if a pilot did not recognize a conflict, or if he/she made use of his/her right of way.

The pilots only received the traffic information which was visible on the traffic display and on the visual system of the simulator. They did not receive any information regarding the future behavior of the conflicting traffic.

3.4 Procedure

All of the pilots received a briefing regarding the functions and indications of the glass cockpit, autopilot and moving map which included the display of traffic information. In addition, the pilots also conducted a familiarization flight with the simulator and practiced traffic avoidance maneuvers. They were instructed to behave as if they were really flying, which meant that they should make use of both the visual scan from the cockpit and the indications of the traffic display for their collision avoidance maneuvers. It should be noted that regardless of the traffic displayed on the moving map, VFR rules state that pilots have to perform see-and-avoid tactics (section 1.1), which require that the traffic has to be detected outside [1]. Therefore the pilots only took evasive action after this condition had been met.

The traffic scenarios were embedded in a VFR flight from Bastia Airport (LFKB), along the east coast of the island of Corsica in the direction of Olbia Airport (LIEO), Sardinia. The pilots were instructed to fly at 6000 feet, with an indicated airspeed of 155 kts. For standardization purposes the pilots were instructed to engage the autopilot until a traffic alert had been generated. After the traffic alert was generated the pilots were instructed to disengage the autopilot and perform the conflict resolution maneuver manually. Once they were clear of any conflict the pilots had to return to their initial route and flight cruise configuration, as well as re-engage the autopilot.

The series of single conflict scenarios consisted of scenarios A and B repeated three times each, and the series of multiple scenarios consisted of three C and three D scenarios. Therefore each pilot encountered a total of twelve traffic conflicts.

The order of scenarios within each series was balanced using Latin squares in order to avoid sequence artifacts. The order of the series was counterbalanced throughout the experiment. The pilots were randomly assigned to each experimental order and yoked between genders.

Each of the twelve flight scenarios took about 5 minutes to complete. However, the entire experimental procedure including the briefing, familiarization flight and filling out the questionnaires lasted between 2 and 3 hours.

3.5 Dependent Measures

The flight performance measures were reaction time, magnitude and direction of the evasive maneuver after five seconds from starting the evasive maneuver. During the entire simulation the pilot's mechanical inputs on the control wheel and rudder, as well as the kinematic data were recorded for further analysis.

The range of each control input was defined from -1 to +1, marking the maximum possible deflection on either side of the elevator, aileron and rudder. The reaction time of the pilot was measured as the time between the traffic alert and the beginning of the avoidance maneuver. In order to distinguish the control actions which initiated the avoidance maneuver from the normal small control inputs during level flight, an action criterion a_C was defined as follows:

$$a_C = |\Delta\zeta| + |\Delta\eta| + |\Delta\xi|$$

$\Delta\zeta$ change of rudder control after traffic alert
$\Delta\eta$ change of elevator control after traffic alert
$\Delta\xi$ change of aileron control after traffic alert

Therefore, at maximum yoke and rudder deflection, a_C can theoretically reach a value of 3. A data logging program was used for post-processing. This data logger was started at the beginning of each scenario and worked with time steps of 0.1 seconds. The aircraft kinematic data and time of the traffic alert were recorded, as well as the values of the aileron, elevator and rudder control.

A trigger condition was defined in order to reliably and automatically determine the moment at which the pilots' evasive action began. A feasible condition for that was found to be $a_C > 0.09$, which was determined by adding 10% to the average noise level in a_C. In this way the reaction time was able to be defined as the time from the generation of the warning to the time of a_C exceeding 0.09. At this moment a deliberate evasion maneuver could be isolated from the random noise.

Furthermore, in order to evaluate the magnitude of the initial evasive maneuver only the values of the aircraft heading, pitch and vertical speed changes during the first 5 seconds after the start of the reaction were taken into consideration.

In addition, the pilots evaluated their mental workload and self-performance at the end of each series (single vs. multiple scenarios) using the mental demand and performance scales of the NASA Task Load Index [85]. The self-ratings ranged from -5 (very low) to +5 (very high). Similarly, situational awareness was subjectively evaluated by the pilots at the end of each series using the Situational Awareness Rating Technique (SART), as well as an adapted version of the SASHA_Q Questionnaire [86]. The ratings of the situational awareness items also ranged from -5 (either low, never or bad) to +5 (either high, always or good).

Finally, the pilots were questioned about their preferred types and levels of automation for a future collision avoidance system using yes/no answers and an space for open remarks and suggestions. The four-stage model of human-automation interaction proposed in [64] was very useful in terms of defining the types and levels of automation

required for the future designs of VFR collision avoidance systems.

3.6 Data Analysis

The pilots' responses were evaluated using the descriptive data analysis method. Also a χ^2-test was used in order to test hypotheses related to the pilots' preferred maneuvers. The effects of the traffic load on the pilots' reaction time, amplitude of heading, pitch and vertical speed changes, subjective workload and situational awareness were evaluated using univariate analyses of variance. The design of the evaluation process included three within-subjects factors: Traffic Load, Conflict Geometry and Trial (Table 3.2). In addition, gender was regarded as a between-subjects factor. The statistical significance level was set at $\alpha = 0.05$, and test results with $p \leq 0.05$ are presented. The results of the pilots' automation preferences for automation are presented descriptively.

Traffic Load	Single		Multiple	
Conflict Geometry	**Scenario A**	**Scenario B**	**Scenario C**	**Scenario D**
Trial	A1 A2 A3	B1 B2 B3	C1 C2 C3	D1 D2 D3

Table 3.2: Evaluation design

3.7 Results

3.7.1 Initial Aircraft Maneuvering

Two types of conflict geometries are addressed in this study: near head-on and crossing from either the left or the right. According to the regulations, both of the power-driven aircraft in a head-on conflict have to take evasive action by turning to the right [1]. Such a turn is registered as a positive change of heading. If two crossing aircraft are in conflict, the aircraft that has the other one to its left has right of way. Therefore the aircraft that has the other one to its right has to perform the avoidance maneuver. In this study the conflicting aircraft did not respect the priority rules and were non-cooperative, thus forcing the pilots to perform the necessary avoidance maneuvers even if they had the right of way.

The pilots' initial evasive actions for each traffic scenario are shown in Figs. 3.3a to 3.3d. These figures show the changes in heading and pitch 5 seconds after an evasive action was begun. The axes are oriented left-right for heading, and up-down for pitch. As Fig. 3.3a shows, the pilots' initial evasive response to the Aircraft 1 on a relative bearing of 350° was a left or right turn of up to 10°, or a change of pitch of up to 10° in a nose up or nose down attitude, or both.

In Scenario A and B (Figs. 3.3a and 3.3b, respectively) where oncoming Aircraft 2 came from a relative bearing of ±10°, the pilots' preference for left or right evasive

(a) Initial response during 3 trials of Scenario A (single conflict)

(b) Initial response during 3 trials of Scenario B (single conflict)

(c) Initial response during 3 trials of Scenario C (multiple conflict)

(d) Initial response during 3 trials of Scenario D (multiple conflict)
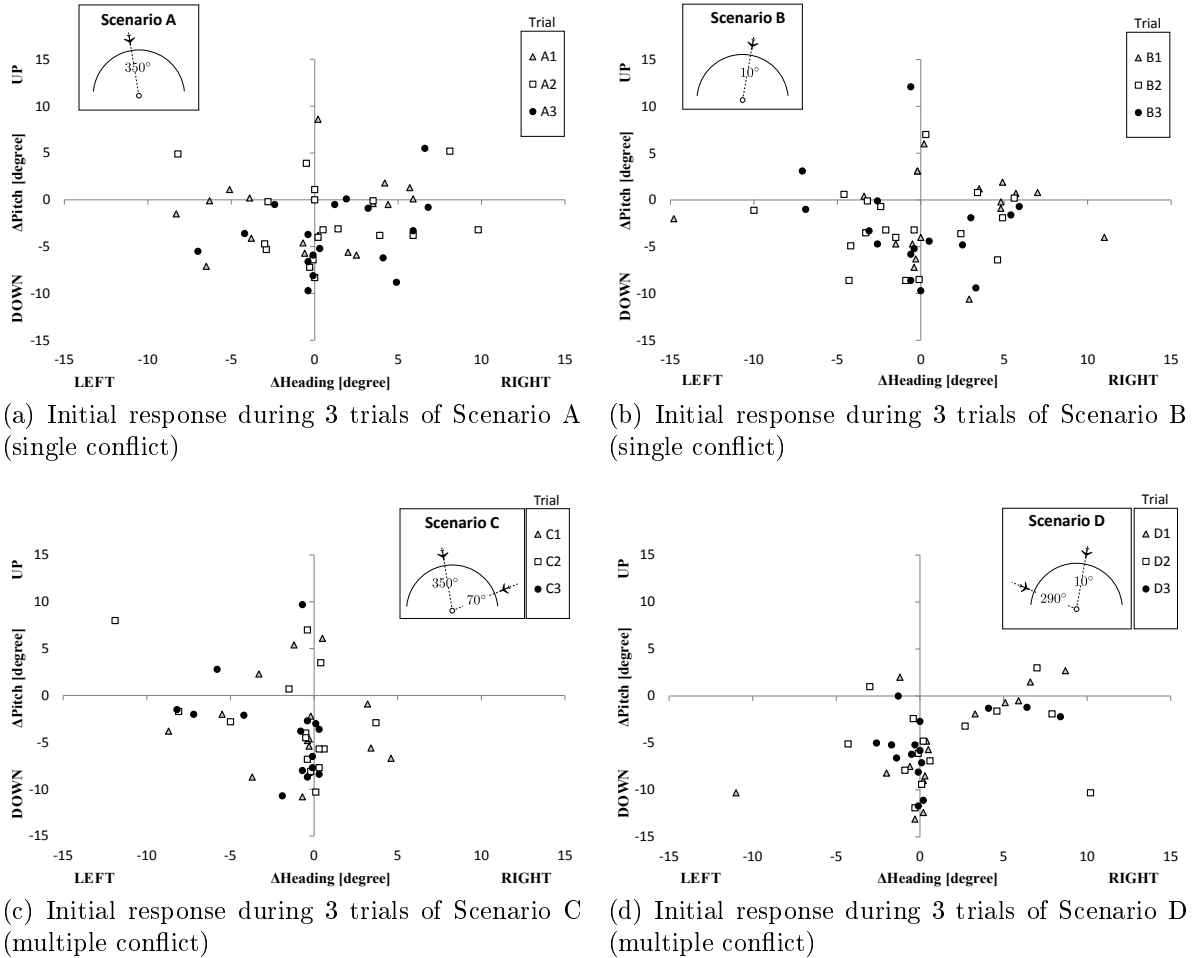
Figure 3.3: Initial change of pitch and heading performed by the pilots in response to the traffic warning during 3 trials of different conflict scenarios

turns as well as a predominant nose down attitude can be observed. The responses to the multiple traffic scenarios C and D (Figs. 3.3c and 3.3d, respectively) also exhibit a concentration of nose down evasions, but with a left turn tendency in Scenario C and a right turn tendency in Scenario D.

The distribution of the initial heading changes throughout all of the trials and scenarios (Fig. 3.4) do not consistently follow the right-of-way rules. It can be seen that heading changes to the left were more frequent than to the right. Therefore, the 4th hypothesis was not supported. Also, regardless of the direction, most of the heading changes remained below 5° at the beginning of the maneuver. Heading changes within this range accounted for 74% of the cases in Scenario A. Also, In 47% of the cases the pilots performed a left turn within 5°, and 11% of the pilots even exceeded a 5° heading change.

The other scenarios turned out to be even more left-leaning: the pilots confronted with Scenario B also responded with a left turn (50% responded with a turn of less
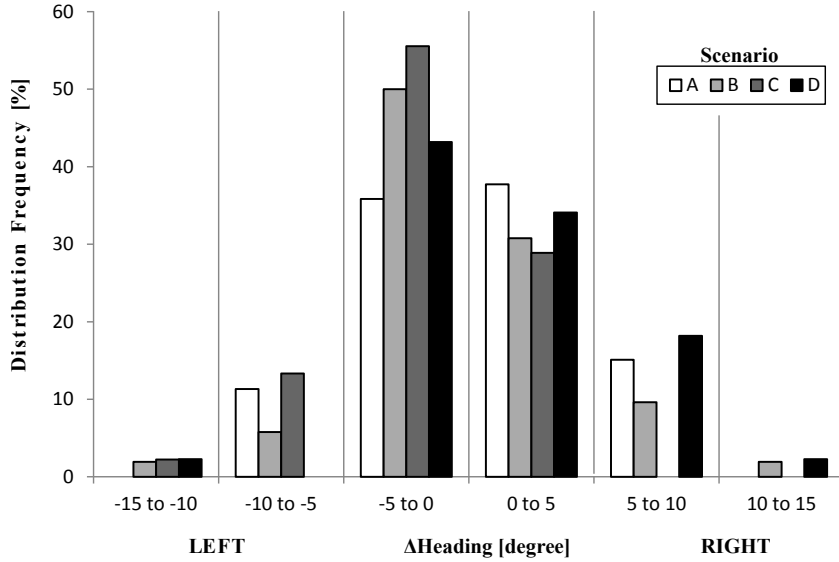
Figure 3.4: Distribution of initial heading changes performed by the pilots in response to the traffic warning throughout all of the trials for scenarios A, B, C and D

than 5°, compared to 31% to the right). No heading change was observed in 4% of the responses to Scenario B.

In Scenario C only 29% of the responses included an initial small right turn. Nevertheless, in most of the cases (56%) the pilots performed a small left turn. Finally, in Scenario D, 5% of the responses exhibited no heading change, while 34% of the responses involved a small right turn. 18% of these were a right turn of between 5° and 10°, and 2% were a right turn of between 10° and 15°. In this scenario the preference for a small left turn was observed in 43% of the cases.

A nose-down attitude - which also provides a better view of oncoming aircraft - was observed in most of the responses throughout all of the scenarios (Fig. 3.5).

Therefore, the 3rd hypothesis was not supported. Extreme pitch angles of between 10° and 15° up or down were only noticed in scenarios B, C and D. As illustrated in Fig. 3.6, after the first 5 seconds the most frequent vertical speeds were descending at a rate of up to 1000 ft/min, followed by a descent rate of between 1000 and 2000 ft/min, and finally climbing at a rate of up to 1000 ft/min. Less frequent but still important were excessive climbs and descents of more than 2000 ft/min, which challenged the safety envelope of the simulated aircraft.

3.7.2 Analysis of Preferred Maneuvers

The results of the χ^2-tests do not support the hypotheses 1 to 4. Although they failed to reach traditional levels of statistical significance, the results have practical importance. The descriptive results of the preferred maneuvers are listed in Table 3.3.

Single-axis maneuvers were chosen in 47% to 78% of the cases. Among the single-axis maneuvers there was a noticeable preference for vertical maneuvers, especially in cases
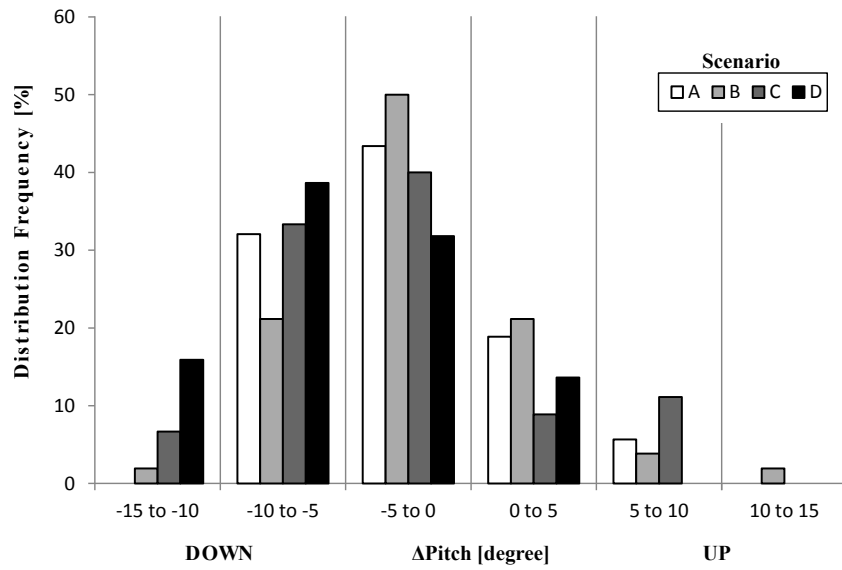
Figure 3.5: Distribution of initial pitch changes performed by the pilots in response to the traffic warning throughout all of the trials for scenarios A, B, C and D
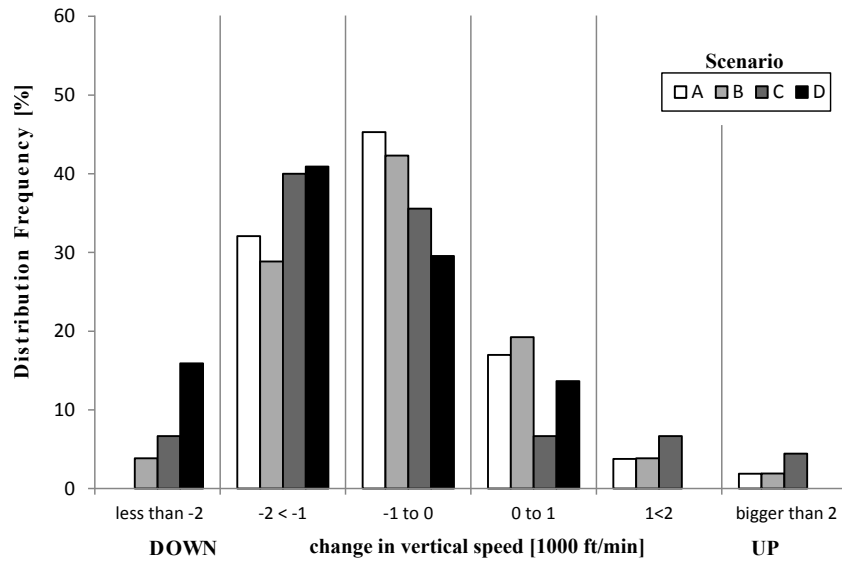
Figure 3.6: Distribution of initial vertical speed changes performed by the pilots in response to the traffic warning throughout all of the trials for scenarios A, B, C and D

Traffic load	Single conflict						Multiple conflict					
Geometry	A			B			C			D		
Trial	A1	A2	A3	B1	B2	B3	C1	C2	C3	D1	D2	D3
N	18	18	17	18	18	16	15	15	15	15	15	15
Maneuver complexity												
1 axis maneuver (%)	66.7	55.6	47.1	77.8	61.1	50	60	66.7	73.3	73.3	60	73.3
2 axis maneuver (%)	33.3	33.3	35.3	22.2	33.3	43.8	40	26.7	26.7	26.7	40	20
no axis tendency (%)	0	11.1	17.6	0	5.6	6.3	0	6.7	0	0	0	6.7
Type of axis preferred in case of single-axis maneuvers												
Vertical (%)	58.3	90	75	64.3	63.6	87.5	88.9	100	100	81.8	100	100
Lateral (%)	41.7	10	25	35.7	36.4	12.5	11.1	0	0	18.2	0	0
Direction of lateral maneuvers												
Left turn (%)	33.3	11.1	11.8	11.1	33.3	25	26.7	20	20	6.7	13.3	20
Right turn (%)	27.8	27.8	35.3	38.9	22.2	25	20	6.7	6.7	33.3	26.7	80
no heading change (%)	38.9	61.1	52.9	50	44.4	50	53	73.3	73.3	60	60	0
Direction of vertical maneuvers												
Pitch down (%)	50	61.1	64.7	44.4	66.7	75	73.3	73.3	86.7	66.7	80	93.3
Pitch up (%)	22.2	22.2	5.9	27.8	5.6	12.5	20	20	13.3	20	20	6.7
no pitch change (%)	27.8	16.7	29.4	27.8	27.8	12.5	6.7	6.7	0	13.3	0	0

Table 3.3: Analysis of preferred maneuvers

of multiple conflicts. When performing single-axis avoidance maneuvers, 76.5% of the pilots consistently opted for the same axis, either vertical (53%) or lateral (23.5%). Only 23.5% of the pilots alternated between vertical and lateral maneuvers during the trials.

During the evaluation of lateral preferences, the maneuvers which did not constitute a heading change of at least $\pm 3°$ were considered to be either unintended or pilot induced oscillations. Therefore these cases were classified as 'no heading changes'. Concerning only lateral maneuvers, the pilots exhibited a slight tendency to right-hand turns in order to avoid head-on conflicts in scenarios A and B. However, there were still a large number of left-hand turns and 'no heading changes' which did not conform to the regulations.

Furthermore, vertical maneuvers which did not constitute a pitch change of at least $\pm 1°$ were considered to be unintentional, and were classified as 'no pitch changes'. 44% to 93% of the maneuvers were classified as descents, compared to 5% to 28% of the maneuvers which were classified as climbs.

An additional analysis beyond the initial 5 seconds for head-on conflicts (Scenario A and B) shows that about 11% of the initially vertical maneuvers were complemented with a lateral component (3% right turns, 8% left turns).

3.7.3 Analysis of the Effects of Traffic Load on the Evasive Response of Pilots

The traffic load had a significant effect on the length of the pilots' reaction time to the traffic alert (Table 3.4). The reactions were significantly shorter during single conflict avoidance maneuvers (M = 3.23 s, SD = 0.80 s) compared to multiple conflict avoidance maneuvers (M = 4.03 s, SD = 0.98 s). The magnitudes of absolute heading changes,

Traffic load effects	F(1, 12)	p-value	η^2
Reaction time	7.87	0.01	0.39
Pitch change	6.46	0.026	0.35
Vertical speed change	4.41	0.058	0.27
Mental workload	6.40	0.02	0.31
Division of attention	6.16	0.02	0.30
Situation anticipation	5.62	0.03	0.28
Spare mental capacity	3.93	0.06	0.21

Table 3.4: Effects of traffic load

regardless of direction, were smaller during multiple conflicts than single conflicts, but the differences did not reach statistical significance. In addition, the traffic loads did have significant effects on the magnitudes of the initial absolute pitch changes. The amplitudes of the pitch changes were smaller during single conflicts (M = 4°, SD = 0.6°) than multiple conflicts (M = 5.2°, SD = 0.7°).

Regardless of the direction, the changes in vertical speed were greater during multiple conflicts (M = 1100 ft/min, SD = 157 ft/min) than single conflicts (M = 860 ft/min, SD = 144 ft/min). But this was a marginally significant effect.

With [$F_{2,24} = 3.51$, p = 0.04, $\eta^2 = 0.22$] the effect of the trial was significant throughout all of the scenarios, and points to a decrease in the magnitude of heading changes between the first (M = 3°, SD = 0.6°), second (M = 2.6°, SD = 0.6°) and third (M = 2.2°, SD = 0.5) trials. The effects of conflict geometry and gender were of no statistical significance.

These results partially confirm the 6th hypothesis, and demonstrate that an increase in traffic load resulted in a corresponding increase in magnitude of vertical maneuvering.

3.7.4 Effects of Traffic Load on the Subjective Responses of Pilots

The pilots' self-ratings of mental workload were significantly higher in regard to multiple conflict scenarios (Table 3.4) than single conflict scenarios (M = 0.79, SD = 0.75 and M = -0.96, SD = 0.95, respectively). The pilots' self-ratings of performance were lower

in multiple conflict scenarios than in single conflict scenarios, but the differences were of no statistical significance. In addition, the pilots' division of attention was higher in multiple conflict scenarios (M = 2.53, SD = 0.71) than in single conflict scenarios (M = 1.45, SD = 0.84). Not surprisingly, the pilots were able to anticipate the situation better in single conflict scenarios than in multiple conflict scenarios (M = 3.42, SD = 0.41 and M = 1.86, SD = 0.63, respectively), and had more spare mental capacity (M = 2.73, SD = 0.52 and M = 1.64, SD = 0.74, respectively). These results confirm the 5th hypothesis.

3.7.5 Requirements for the Automation of VFR Collision Avoidance Systems

Analysis of the pilots' requirements for future collision avoidance systems shows that 94.4% of the pilots demanded assistance in the form of a display indication of each aircraft within 5 nautical miles. About 61% of the pilots asked for an automatically generated avoidance route, while only 22.2% asked for several automatically generated avoidance routes.

44.4% of the pilots asked for an automatic selection of the avoidance route, as well as an automatic performance of the avoidance maneuver with the pilot's approval. However, a majority of the pilots (58.8%) would prefer a restricted amount of time in which they have the opportunity to veto before the avoidance maneuver is automatically executed. The option of only being informed after the automatic execution of the avoidance maneuver was rejected by 94.4% of the pilots.

72.2% of the pilots demanded an automatic return to the initial route subject to the pilot's approval following the performance of the avoidance maneuver. Fewer pilots (61.1%) demanded a restricted amount of time in which they could veto before the performance of the automatic return. The option of only being informed after the automatic performance of the return maneuver was rejected by 94.4% of the pilots.

Therefore, the optimum type of system automation was identified to include not only perception enhancing cues, but also decision making and response selection. The level of system automation required by pilots was situated at a medium level on the scale of Parasuraman et al. [64].

3.8 Discussion

The results point in general to areas of the collision warning systems for VFR which could be further improved. While the moving map with traffic alerts was useful for detecting conflicts, one of the main findings is that VFR pilots need more automation support in interpreting conflict situations and selecting and performing an avoidance maneuver.

In spite of the current aviation regulations, which demand right-turn maneuvers in a head-on conflict situation, it was found that pilots tend to choose both left- and right turn maneuvers. The results are similar to the findings of other researchers [75], who

found that only 55% of pilots avoid traffic by turning to the right. An explanation for this might be that the selection of a collision avoidance maneuver is not entirely the result of rule-based decision making, but rather the outcome of decision heuristics [74] [81]. This means that when choosing an avoidance maneuver pilots may intuitively weigh the urgency of conflict resolution, regulations, expediency, safety and other contextual characteristics. Research indicates that even if an avoidance route is commanded by the system, as TCAS II does, in many cases pilots do not follow the RAs precisely, or perform other maneuvers [59] [69] [70].

The preference for vertical maneuvers, and especially for descents could be explained by the lower complexity and control order of such maneuvers [74]. Interestingly, the descent stereotype may be found in pilots, air traffic controllers and also flying insects such as locusts, the latter definitely being well adapted to flight [87]. However, if collisions are less imminent, locusts will precede or accompany their descents with other steering maneuvers. The pilots in the study also received more benefits from descending maneuvers. They had a better forward view of the traffic situation, and they were able to maintain their initial flight route.

Another interesting result is the greater magnitude of pitch changes under conditions of multiple conflicts compared to conditions of single conflicts. An explanation for this might be that under conditions of multiple conflicts the pilot's heuristics manifest themselves more strongly, leading to the use of simple, low-order controls [74] with greater magnitude. The use of higher order controls requires more effort [74], and coping with multiple conflicts was indeed significantly more demanding for the pilots. Under conditions of multiple traffic it took them longer to initiate an avoidance maneuver, and they also reported a higher workload, as well as less spare mental capacity and anticipation. However, between the first and third trials there was a noticeable decrease in vertical speed changes throughout all of the maneuvers, which shows that the pilots learned to control their tendency to over-react.

Regarding the results of subjective ratings and aircraft maneuvering it is not surprising that pilots show a clear preference for more types and higher levels of automation in future VFR collision warning systems compared to current systems. The results fit within the framework for automation [64] showing that functions such as sensory processing, perception of traffic information, decision making and response selection should be automated. This shows us that the pilots found the selection and performance of those actions to be difficult. However, the level of automation required only reaches the medium scale described in [64]. The corresponding level of automation includes the automatic execution of the avoidance maneuver and return to the initial route with the pilot's approval. Although these results are useful for the specification of the type and level of system automation, future research is necessary to investigate if the system which will be developed according to pilots' requirements is optimal.

The procedure used in this study to simulate systems in an early stage of development and apply the framework for automation design [64] for identifying automation requirements can be applied beyond the aviation domain. This human-centered approach is safe, cost-effective and may positively influence the acceptance of new automated systems.

3.9 Limitations

During the experiment the pilots flew and interacted with the collision warning system. In addition, they were interviewed in regard to possible automated features which could optimize the system. The pilots were told that the study would not focus on their flying skills, but instead on their interaction with the collision warning system and possible ways to optimize the system. Therefore the pilots' maneuvering decisions were not questioned. No explicit feedback on the pilots' reasons for choosing a particular conflict resolution strategy was required.

The results regarding pilots' preferred maneuvers are limited in terms of their relevance to real flight for several reasons. First of all, only responses to head-on and crossing traffic which was flying at the same level were investigated. Furthermore, the non-cooperative nature of the conflicting aircraft may have influenced the selection of avoidance maneuvers. However, non-cooperative traffic might be encountered in real flight if a pilot fails to see and avoid another aircraft [88]. The VFR regulations concerning head-on collision avoidance clearly specify that each aircraft has to perform a right turn. Vertical avoidance maneuvers in VFR are not against the rules as long as they are associated with a right turn. Otherwise they need to be coordinated between the pilots in order to ensure separation. More research is therefore needed on pilot decision making and simulation networks which allow cooperation and communication between pilots.

Another limitation of this study is the lack of data on various fatigue aspects which may have influenced the reaction times and pilots' responses.

3.10 Future Developments

The automation of collision warning and avoidance systems for VFR will definitely be a topic of further research, although its practical implementation may still be far off in the future. Newly developed automated systems should be evaluated in terms of human performance consequences (e.g. mental workload, situational awareness, complacency and skill degradation), automation reliability, and the outcomes of decisions and actions, as well as their associated costs [64].

For the further development of a VFR collision warning system an enhanced traffic display is proposed which supports pilots both in anticipating the traffic situation and selecting an avoidance maneuver. The future development of collision warning systems for VFR should address pilots' limitations under conditions of multiple traffic. When alerting the pilot to one threat the system should not cause other pending conflicts to be invisible. The system should have a positive impact with the goal of reducing mental workload and enhancing situation awareness. A valuable aid under conditions of multiple traffic would therefore be the display of anticipatory cues in addition to traffic symbols. In addition, the indication of contextual information such as aircraft category, as well as VFR regulations regarding right of way should be considered.

The design of automation support for decision making could be based on a model

similar to the model of decision making proposed for the context of air traffic control [81]. This decision model calculates a 'utility score' of maneuver alternatives considering the expected utility of factors such as expediency and visibility of traffic to avoid. However, caution is necessary when the avoidance maneuvers are performed automatically. Future research with VFR pilots is necessary to determine the expected utility of control order and complexity when maneuvers are performed automatically.

Technical options for the selection of an avoidance maneuver might include an avoidance direction cue (e.g. to the right) if a collision is imminent, or an indication of predicted forbidden zones as proposed in [66]. Forbidden zones could apply the display principle of terrain caution and warning by using yellow and red areas. However, the markings will have to be kept simple and intuitive, even in the case of multiple conflicts. A particular aspect to be considered is the issue of contrasting human and automatic conflict resolutions [89] [90]. In this case adequate procedures for dealing with conflicting maneuvers proposed by humans and automation will be necessary. An example of this is the coordination procedure arranged between TCAS RA and Air Traffic Control [72] following the mid-air crash in Switzerland on July 1, 2002 [91].

Another aspect to be considered in future research is the timeline of traffic alerts. Unfortunately there is no accepted rule regarding the time and distance to the closest point of approach which trigger alerts in VFR. However, there are systems currently being used which generate an alert at a time closer to the predicted collision than the time used in this study. The question remains of whether an earlier warning would prevent the pilots from overreacting or provide an additional distraction.

Although there is already a large body of research on the sense-and-avoid concept for unmanned aerial vehicles (UAV), the findings of this study also provide a new perspective on the interaction between VFR aircraft and UAVs in civilian airspace. Grilley [92] states the rules unmanned aerial vehicles (UAV) are expected to follow resemble the priority rules applicable to VFR pilots [1]. Although there are already RA algorithms based on these rules [93], such a solution can be problematic if pilots of manned aircraft do not act according to the rules of the air, but instead rely on intuitive mechanisms and choose avoidance maneuvers which are inadequate or unexpected. On the other hand, if such an algorithm is installed in a UAV for the purpose of automatic collision avoidance maneuvers, pilots may find it comforting to know how the UAV will react during an encounter. This issue could be addressed in future research.

Nevertheless, caution is recommended for the implementation of automatic systems. Manned aircraft which do not transmit their position and category data pose an additional hazard. Non-responsive or non-cooperative traffic, as well as fallible traffic recognition capabilities [94] are a serious concern for aviation authorities in regard to the certification of UAVs. For the European Aviation Safety Agency the installation of appropriate anti-collision systems is a key issue in regard to the introduction of UAVs into non-segregated airspace [95] [96].

Although it is obvious that pilots require and demand improved system capabilities, there is one unresolved issue regarding collision avoidance training for VFR pilots. Future research should be dedicated to the development and evaluation of simulator training for VFR collision warning and avoidance systems. Airline pilots regularly attend simulator

training for TCAS, and VFR pilots might also profit from this type of simulator training. The training scenarios should include both single and multiple VFR conflict situations, as well as situations in which traffic is not sensed and signalized by a collision avoidance system. The latter situation is a limitation which will probably not be resolved in the near future. In addition, the training should be performed in networks of simulators in order to enable coordination between the pilots. Finally, pilots should be trained to only use collision warning and avoidance systems as an additional safety tool in order to avoid over-complacency.

4 Recommendations for Future Traffic Display Systems for Visual Flight

In the near future airspace capacity problems are expected to arise due to an increase in traffic. Under good visual meteorological conditions, Eurocontrol estimates that approximately 77000 small aeroplane flights flying a distance of about 10 million km take place in Europe every day [97][1]. Only 16% of these small aeroplanes were equipped with transponders, because in Europe transponders are not mandatory in every airspace class.

Despite the overall decline of accidents involving General Aviation aircraft, the numbers of near misses and midair collisions have not decreased in the past decades. As the AOPA reported in 2009 [98], this number has remained constant in contrast to other causes of accidents which have decreased over several decades. A major cause of midair collision accidents in VFR flight is the pilots' failure to 'see-and-avoid' each other (chapter 1). It is therefore necessary to develop a traffic display and collision avoidance system for VFR which is capable of showing conflicting traffic, issuing warnings and supporting pilots in their selection of appropriate collision avoidance maneuvers.

In an effort to reduce the number of midair conflicts and to improve flight safety, various manufacturers developed a number of Traffic Advisory Systems (TASs) for General Aviation (Table 2.2). The TASs use abstract traffic symbols which are similar to those used by the TCAS system (Table 2.1), which is used in commercial aviation. For flights under VFR in particular, high expectations have been placed on the new traffic visualization systems [99] to help pilots see-and-avoid[2] other air vehicles. Research shows, however, that pilots' interpretation of the TCAS-like traffic displays for VFR can be demanding both cognitively and in terms of time, and thus, it is prone to failure[3]. Furthermore, the pilots underestimate the time and distance to collision at the time when the warning is issued [100]. Thus, an earlier indication of conflict information should be considered.

The previous chapter evaluated a TCAS-like traffic warning display in a visual flight environment. These findings indicate that the investigated TAS does not optimally support higher level situational awareness of pilots during their avoidance maneuvers.

---

[1]In the cited report, the term *light aircraft* is used for aircraft with a maximum takeoff mass less than 5,700 kg, which are named *small aeroplanes* by ICAO [10]. In this thesis only ICAO definitions are used.

[2]See section 1.1 for reference.

[3]See section 3.8.

In conditions with multiple traffic the pilots reported higher mental demand and less spare mental capacity, they had problems in predicting the traffic situation and needed a longer time period to react to the traffic alert than compared to the single traffic condition. These issues should be addressed in the development of improved traffic displays because high workload reduces pilots' performance in other tasks and may lead to errors.

In the following, traffic displays using predictive features are discussed in order to address the issues stated above. Several display proposals are developed in this regard and evaluated[4] to identify viable solutions to increase pilots' traffic awareness.

4.1 Traffic Awareness and Predictive Traffic Displays

Traffic awareness goes beyond the perception of traffic. Applying the three levels of situational awareness that are introduced in [101], traffic awareness can be specified in terms of perception of the traffic flying in the vicinity (Level I), the understanding of its dynamics (Level II; e.g. relative altitude, relative speed, direction of motion), and the prediction of its future status (Level III; e.g. conflict/non-conflict, expected avoidance strategy). As soon as a conflict is imminent, the pilots must apply the rules-of-the-air for avoiding collisions.

According to VFR regulations [1], the proper avoidance maneuvers in flight require additional knowledge about the type of air vehicle encountered. For example, power-driven aircraft must give priority to gliders, airships or aerotowing aircraft. Currently, the aircraft category can be detected only when the pilots visually identify the intruding aircraft. There is no traffic advisory system that generates display information about the category of air vehicle and the applicable priority rules. Another issue highlighted by the study in chapter 3 is pilots' underestimation of the collision parameters (time and distance to the closest point of approach) when the traffic warning is issued [100]. In addition, pilots' response to the traffic warning is not always in compliance with the regulations (right-of-way rules [1]). Therefore, traffic displays for VFR should be improved to better support pilots' understanding and prediction of traffic situations and to reduce mental demand.

The findings in chapter 3 and [100] also indicate that the traffic warning itself does not provide sufficient support to VFR pilots in managing a conflict situation. It might be beneficial to provide better situational awareness support at a pre-warning stage, before a TCAS-like display would display a traffic advisory. The term 'conflict' is used to describe a traffic situation in which the air vehicles are so close that a collision risk exists and at least one pilot has to perform an avoidance maneuver. The information to understand and predict such a conflict includes the location of conflicting traffic relative to the own

---

[4]For reference: The procedure, methods and results of the following evaluation were published in

> T. Haberkorn, I. Koglbauer, and R. Braunstingl, "Traffic displays for visual flight indicating track and priority cues," *Human-Machine Systems, IEEE Transactions on*, vol. 44, no. 6, pp. 755-766, Dec 2014.

aircraft, its future flight direction and its threat potential. In addition, information about the category of the encountered air vehicles is necessary for determining the right-of-way in converging encounters, and could support the prediction of its relative movement.

Also, limitations of currently used displays have to be addressed. For example, a simulator study [102] evaluating the FLARM system[5] (Fig. 2.2), showed that although FLARM could support identifying other traffic, connecting the depicted traffic with the actual traffic outside the cockpit was biased for certain conflict geometries. This was evaluated by determining the angle between the pilots' perceived and the traffic's actual bearing. It is argued that for the FLARM system the error of displayed vs. actual traffic arises because the plane-of-reference of the display is parallel to the ground and not fixed to the own aircraft's body-fixed reference system. This makes it harder for pilots to locate oncoming traffic correctly while in a banked turn or climb/descend, because they are led to believe by the depiction on the display that it is fixed with respect to the own aircraft's reference system. A possible solution to counter this effect is to add a moving map to the display. In this way, it is clear to the pilots that they are watching a birds-eye view (parallel to the ground) of the situation.

Furthermore in cross-wind conditions, the direction of oncoming traffic will be off by the drift angle[6] relative to the symbol of the own aircraft on the display. Intuitively, this symbol should be aligned with the longitudinal axis of the own aircraft, but because of the sensor technology used it is actually aligned with the own aircraft's ground track. To avoid misconception by the pilot, this symbol should be aligned with the own aircraft's heading (*heading-up mode*).

Moreover, the experiment results in chapter 3 show that in multiple conflict conditions during VFR flight, traffic awareness and mental workload was a problem for pilots that occurred despite the use of a traffic display. Therefore, an evaluation experiment testing a new traffic display should feature a varying traffic load (single and multiple traffic).The findings also indicate that higher-level situational awareness in priority decisions should be enhanced. This can be done by depicting information such as the type of air vehicle encountered and the applicable priority rules which depend both on traffic geometry and the type of air vehicle. This information can be acquired from ADS-B transmissions [103]. However, a display concept is needed in order to provide this information to the pilots.

4.2 Proposed Traffic Visualization Concept

The last section and research[7] identified that predictive automation is worth pursuing in order to improve traffic displays. Furthermore, [62] and [65] show benefits of predictive automation in offloading the cognitive demand of the operators, who are enabled to perceive information which otherwise would have to be inferred.

---

[5]predominantly used in many European gliders
[6]difference between the aircraft heading and track
[7]See the traffic systems in research for reference (Fig. 2.3).

Coplanar depiction of traffic performs better than a 3D representation [104], because of the presence of ambiguity whenever a 3D volume of space is mapped to a 2D viewing surface. This leads to poorer judgment of relative and absolute distance as well as relative motion.

This section proposes a traffic display which integrates a moving map and three new display features which can enhance pilots' situational awareness in traffic conditions at a pre-warning stage: traffic is depicted as oriented air vehicle symbols, conflicts are depicted by a relative track cue, and the applicable priority rules are depicted by a priority line. The proposed cockpit display of traffic information should support pilots in their see-and-avoid task during visual flight.

These elements and a baseline variant which uses TCAS symbols are evaluated in an experiment with VFR pilots. The results of the experiment identify benefits and limitations of these display variants in terms of their effect on the rapidity and accuracy of conflict decisions, on the accuracy of priority decisions, on the mental demand, and on pilots' preferences.

4.2.1 Symbols of the Air Vehicle Category

An analysis of the data provided by the UK Airprox Board [5] shows that in 72% of incidents the aircraft involved were of different category (e.g. fixed wing aircraft vs. helicopter). Because of this mix, a graphical representation of the aircraft category is suggested for the proposed display system. In the following, the aircraft represented in the traffic display concept are part of the FAA's specification of *aircraft categories* [105].

The chart in Fig. 4.1 provides an overview of the aircraft categories involved in UK Airprox events in the period from 2010 to 2014. These form the basis for the selection of
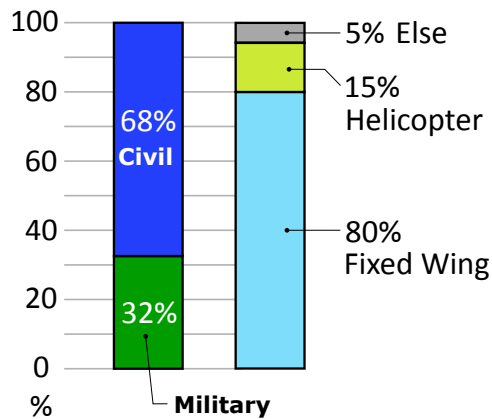
Figure 4.1: Percentage of Airprox events from 2010 to 2014 across various types of aircraft [5]. An entry in a specific class means out of the two aircraft involved at least one was of said category. Notable sub-groups of the class *Fixed Wing* are commercially operated aircraft (21%) and gliders (6%). The class *Else* is comprised of parachutists, balloons and unidentified aircraft.

aircraft categories to depict in the display concept. The symbols designed to represent the aircraft categories in the proposed display system are illustrated in Fig. 4.2.

Furthermore, unlike the TCAS symbols, the air vehicle symbols are oriented (with the exception of the balloon shape). Thus they can indicate directional information of the traffic. Before an air vehicle becomes visually detectable, the pilots can glance at the display what type of air vehicle they are encountering and infer which priority rule
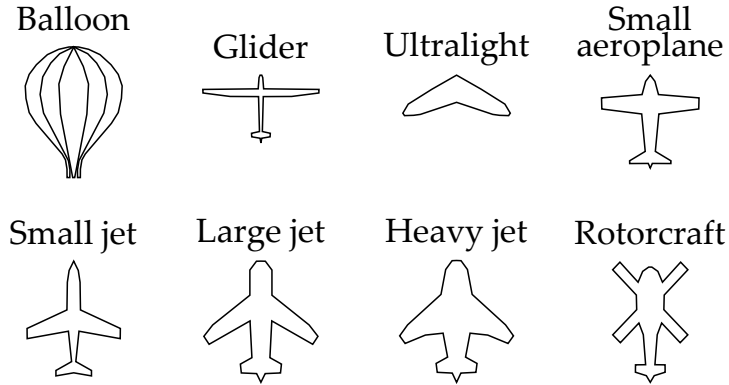
Figure 4.2: Air vehicle category symbols for civil aircraft. Military aircraft would use the same symbols but with a dark gray fill color.

would apply in case of conflict. The priority in case of conflict can be inferred as a function of the collision geometry and the type of air vehicle encountered. Furthermore, pilots' mental picture of the other aircraft and its approaching speed can be inferred at a pre-warning stage.

The information needed to enable the depiction of the category is provided by ADS-B transmissions [103]. If the category is unknown (non ADS-B traffic), TCAS symbols are used.

4.2.2 Relative Trackline

The indication of the relative track vector is introduced in order to reduce the cognitive effort needed for the prediction of a conflict or non-conflict situation. This cue represents a trackline depicting the predicted linear path of the encountered aircraft *relative* to the ownship. This 'relative trackline' is attached to the intruding air vehicle. Its direction is identical to that of the relative velocity vector between the threat aircraft and the ownship. It intersects the ownship in the event of a predicted collision, and it passes outside of the ownship when there is no potential conflict predicted. The reasoning behind this method is shown by geometrical analysis of the approach (Fig. 4.3).

The geometry and velocities are given by the vector equation that would result in the two air vehicles meeting at the same location at the same time $t = t^* > 0$:

$$\boldsymbol{r_{21}} + \boldsymbol{v_1} \cdot t^* = \boldsymbol{v_2} \cdot t^* \tag{4.1}$$

$$\text{with } \Delta\boldsymbol{v} = \boldsymbol{v_2} - \boldsymbol{v_1} \quad \rightarrow \quad \boldsymbol{r_{21}} = \Delta\boldsymbol{v} \cdot t^* \tag{4.2}$$

This means that if the relative speed vector $\Delta\boldsymbol{v}$ drawn from the other aircraft points at the ownship, a collision will happen if neither aircraft changes speed or flight direction. If $\Delta\boldsymbol{v}$ does not point at the ownship ($\varphi \neq \psi$), the perpendicular distance between $\Delta\boldsymbol{v}$ and the ownship shows the separation at the closest point of approach. In order to
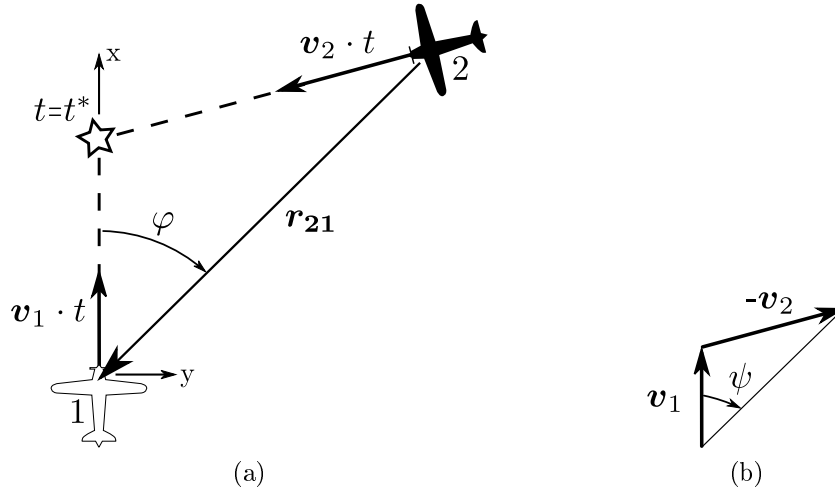
Figure 4.3: (a) Top view of a collision scenario. The angle φ denotes the relative bearing angle. The vector $\boldsymbol{r_{21}}$ describes the position of the ownship relative to the intruder. The xy-plane is parallel to the earth's surface. The time of the collision is marked with $t=t^*$, assigning the depicted traffic situation to $t=0$. (b) The angle of relative track ψ. A collision occurs for $\varphi = \psi$. The vectors $\boldsymbol{v_1}$ and $\boldsymbol{v_2}$ refer to the velocity of the ownship and the intruder, respectively.

display this 'passing distance' on the display, $\Delta\boldsymbol{v}$ is scaled by assigning the length of the vector $\boldsymbol{r_{21}}$ to it, yielding the 'relative trackline'.

If either the ownship or the approaching aircraft is maneuvering or changing speed there are two possible outcomes: the relative trackline veers towards the ownship symbol (minimum passing separation is decreased) or it veers away (separation is increased). The display of the relative trackline allows the pilots to see at a glance which aircraft poses an imminent threat and which does not. Therefore, pilots using this display no longer need to infer and predict.

4.2.3 Priority Cue

To further reduce pilots' mental demand in traffic situations a dedicated priority cue is depicted as a line parallel to the relative track vector, which indicates that the conflicting air vehicle has the right-of-way. It is depicted only in case of conflict and only when the conflicting air vehicle has the right-of-way.

The method for determining the priority line is based on the Rules of the Air [1] and takes into consideration both the conflict geometry and the category of air vehicles involved.

Regarding geometry, the proposed system evaluates the angle of relative track ψ (Fig. 4.3) with respect to the sectors shown in Fig. 4.4.

1. The Center Sector: If two aircraft are approaching approximately head-on as in the center sector depicted in Fig. 4.4, each air vehicle must alter its course to the

right. Therefore, no vehicle has exclusive priority. In this case, no priority line is shown.

2. Left and Right-Front Sector: If two power-driven aircraft are converging, the one which has the other aircraft on its right hand side must give way. Thus, it has to give priority and allow the other aircraft to proceed on its course and speed. In addition, if one air vehicle is power-driven and the other one is not (e.g. gliders), the power-driven one must give way and yield priority (Fig. 4.5b). For the same conflict geometry illustrated in Fig. 4.5a and Fig. 4.5b, the priority rule is different because the air vehicles encountered are of different categories. In Fig. 4.5a the ownship has the right-of-way and in Fig. 4.5b the glider has the right-of-way.

3. Aft Sector: If one aircraft overtakes the other, the overtaken aircraft has priority. The overtaking aircraft shall keep out of the way of the other aircraft by altering its heading to the right.
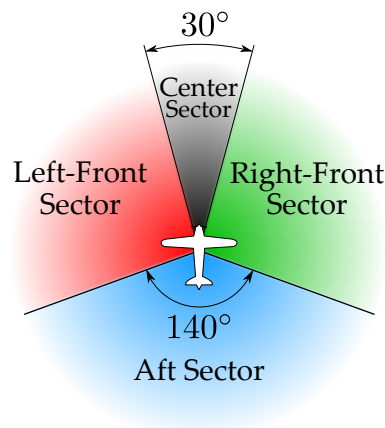
Figure 4.4: Sectors around the ownship used to determine the priority rules. All sectors refer to the relative track between the ownship and the intruder.

The only sector angle specified by regulations [1] is the one of the aft sector. The angle of the center sector is not defined there and for this display concept chosen to be 30°. This also defines the angular extent of the remaining left and right sectors.

Both priority and predictive cues are displayed if the time until minimal separation is less than 45 seconds, or the approaching air vehicle is within 1.5 nautical miles (nm) in horizontal and ±200 feet in vertical distance. These values are derived from thresholds for traffic advisory of current systems (section 2.1) and using expert advice for meaningful thresholds in VFR operations.
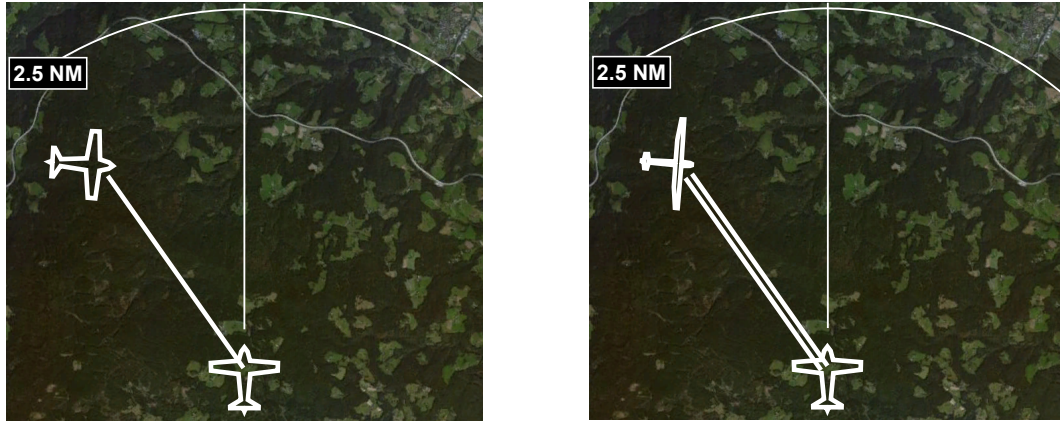
(a) A conflict with a power-driven aircraft of category 'Light'. Ownship has the right-of-way.

(b) Conflict with a 'Glider'. Glider has the right-of-way.

Figure 4.5: The new conflict visualization concept. In this example the ownship is a power-driven aircraft depicted at the bottom of the display. (a) and (b) show a conflicting air vehicle at a pre-warning stage. The relative track vector is the line connecting the conflicting intruder with the ownship. In (b), the priority trackline is depicted parallel to the relative trackline showing that the conflicting air vehicle has priority.

The proposed integration of a moving map is combined with a range arc. The visualization represents a physical map and uses satellite imagery from [15].

The data necessary for the prediction and priority features can be made available by ADS-B messages, which have a broadcast rate of around 1/sec [103]. For this study, continuous movement of the traffic on the traffic display is assumed. For a real-world implementation, this can be achieved by using state estimation algorithms (e.g. a Kalman filter) that are state of the art in navigation and control of air vehicles.

4.3 Method

The appropriateness of the proposed traffic display variants to solve the operational problems identified in sections 3.8 and 4.1 has to be determined. Supporting evidence (e.g. indicators and metrics of traffic awareness, mental demand, decision time and pilots' preferences) is gathered to test whether the display solutions are suitable to match operational demands. The new display concept will be considered acceptable if it proves to be superior to other displays in at least one criterion, and if it is not significantly poorer in any other criteria.

4.3.1 Display Variants

The experiment is designed to evaluate the features of the proposed display concept by comparing different display variants (Fig. 4.6).
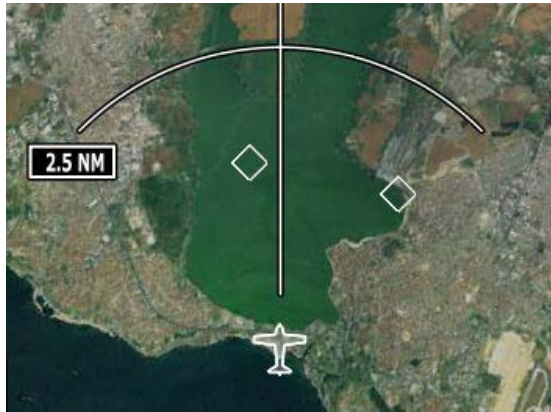
(a) Display variant A: The baseline display. Diamond shapes denote positions of intruding air vehicles. The ownship is depicted by a small aeroplane symbol.
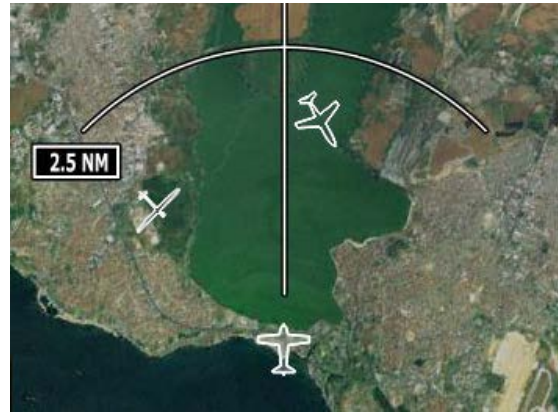
(b) Display variant B: Oriented air vehicle symbols denote positions and direction of intruding air vehicles (here: glider from left, small jet ahead).
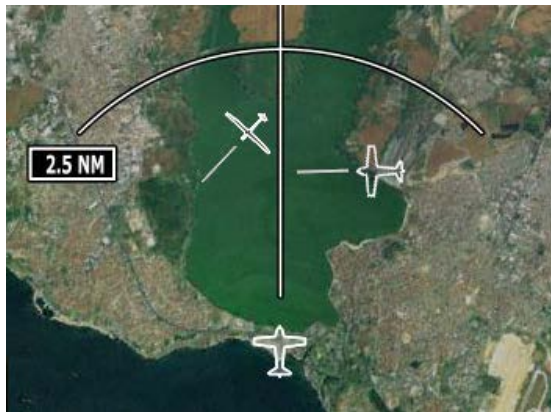
(c) Display variant C: Oriented aircraft symbols with 'absolute' trackline denote positions and directions of intruding air vehicles (here: glider ahead, small aeroplane from right).

(d) Display variant D: Oriented aircraft symbols with relative trackline (here: glider from left on a predicted collision course with the ownship, small aeroplane ahead). The relative line shows if traffic is on collision course or not.

(e) Display variant E. The full implementation of the proposed display concept in section 4.2: Oriented aircraft symbols with relative track & priority line (here: glider from left has priority, small aeroplane ahead).

Figure 4.6: Display variants in the experiment

By using the display variants B, C, D and E, the display concept itself is varied in order to evaluate the effectiveness of different types and levels of predictive cues. These variants are compared to a baseline (variant A), which uses TCAS-like diamond symbols (Fig. 4.6a).

The display variant B, Fig. 4.6b, shows only the oriented air vehicle symbols, without other predictive cues. The display variant C (Fig. 4.6c) displays the direction of travel in the form of an 'absolute track' which is a line of fixed length in the direction in which the intruder is moving. It allows pilots to see the direction of the velocity vector of the threat aircraft.

The display variant D (Fig. 4.6d) draws a 'relative trackline' as a predictive cue. Lastly, display variant E (Fig. 4.6e) combines all components of the proposed display variants (relative & priority trackline). This display variant has the highest level of predictive automation but also the most clutter.

An overview of the predictive cues of all display variants is given in Table. 4.1.

Display variant	traffic position	vehicle type	absolute track	relative track	priority cue
A	✓	-	-	-	-
B	✓	✓	-	-	-
C	✓	✓	✓	-	-
D	✓	✓	-	✓	-
E	✓	✓	-	✓	✓

Table 4.1: Predictive cues visualized on the display variants

4.3.2 Hypotheses

The display of predictive cues is expected to enhance high-level situational awareness and to reduce mental demand, as in [65]. When the pilots see the relative trackline (variants D and E), they rely on a lower level of cognitive activity (e.g. perception) and do not have to remember and infer in order to understand and predict the situation. Thus, according to results in [62] [106], working with the display variants D and E is expected to be easier, faster and to meet better pilots' preferences than the variants A, B, and C. However, if the addition of cues is redundant and overloading, the relative track and the priority cue (variants D and E) will increase display clutter [107]. In this case it will degrade situational awareness, and increase time consumption and mental demand of the pilots compared to the variants A, B and C.

The following hypotheses were formulated accordingly:

1. The display variant significantly influences the decision time. The decision time will be shorter using the displays of the relative and priority track (variants D and E) compared to the display of the absolute track (variant C), the display of the directional aircraft symbol (variant B), and the baseline variant A.

2. The display variant significantly influences the accuracy of conflict decisions. The accuracy will be better using the displays of the relative and priority track (variants D and E) compared to the display of the absolute track (variant C), the display of the directional aircraft symbol (variant B), and the baseline variant A.

3. The display variant significantly influences the accuracy of priority decisions. The accuracy will be better using the display of the priority cue (variant E) compared to the displays which lack this feature (variants A, B, C and D).

4. The display variant significantly influences the mental demand. The mental demand will be lower using the displays of the relative and priority track (variants D and E) than with the display of the absolute track (variant C), the display of the directional aircraft symbol (variant B), and the baseline variant A.

5. The display variant significantly influences pilots' preferences. The pilots will prefer the displays of the relative and priority track (variants D and E) to the display of the absolute track (variant C), the display of the directional aircraft symbol (variant B), and the baseline variant A.

4.3.3 Participants

Twenty-one pilots volunteered to participate in the study (4 females and 17 males), aged from 21 to 76 years (Mean M=40.7 years, standard deviation SD=3.5 years), with an average total flight time of 2677.8 (SD=1152.9) flight hours and a median of 600 flight hours. Fifteen pilots reported having experience with traffic warning systems, mostly TCAS, with an average experience of M=1854.2 (SD=811.7) flight hours with a median of 300 flight hours. All the participants gave their informed consent.

4.3.4 Apparatus

A dedicated JAVA program for both trajectory generation and the test environment was created for the experiment (Figs. A.1, A.2 and A.4, respectively). Using this programs, a moving map was displayed on a flat 14 inch monitor for the experiment with a scale[8] of 0.6 nm per cm. The ownship position was depicted by a symbol resembling a small aeroplane located at the bottom of the display and the map had a track-up orientation. The update interval of the display was 100 ms. The experimenter used an instructor station installed on a PC for selecting the traffic scenarios on the moving map and for data acquisition. The participant and the experimenter, as well as their desktops were partly separated by an opaque wall.

4.3.5 Procedure

The task of the participants was to watch different traffic scenarios and to press a key if they detected that a collision with the ownship was imminent. When the participants

---

[8]display dimension is illustrated by Fig. 4.7

reported a conflict they were asked to decide which air vehicle had the right-of-way. The participants were informed that the decision time and accuracy were the focus of the experiment.

Every traffic scenario involved the ownship and two other air vehicles flying in the vicinity at the same altitude and with constant heading. As the ownship symbol was fixed on the display, the map background and the traffic moved relative to it. At the beginning of each trial the participants watched a 6 cm by 6 cm cross shown at the center of the display (Fig. 4.7). The cross was removed after 3 seconds of fixation, therefore marking the starting time of the trial. This procedure was adopted from Spapé et al. [108].

Six trials were conducted for each display variant (A to E):

1. Two familiarization trials were conducted to demonstrate the display variant, one with and one without a conflict. The experimenter could address any interpretation mistakes in the training trials. This happened once. When the participants confirmed that they understood the display variant and that no additional training was needed, the tests began. No participant required additional training.

2. Four test trials with two collision and two non-collision scenarios (Fig. 4.8) were conducted.

Order effects were counterbalanced using a Latin square scheme. Each aircraft trajectory was defined to cover 40 seconds of flight. The experiment lasted about one hour. According to the methodology proposed by [108] there was a equal number of collision and non-collision geometries (Fig. 4.8). The conflict geometry 2 represents a crossing conflict with the glider on the left side which is mirrored by the conflict between the two small aeroplanes represented in geometry 3. The type of conflicting air vehicles was varied between the geometries 2 and 3 (unpowered glider versus powered small aeroplane) which resulted in different priority rules. These conflict geometries were relevant for the evaluation of variant E. In order to calculate the time to CPA, the method shown in section A.5.1 was used.
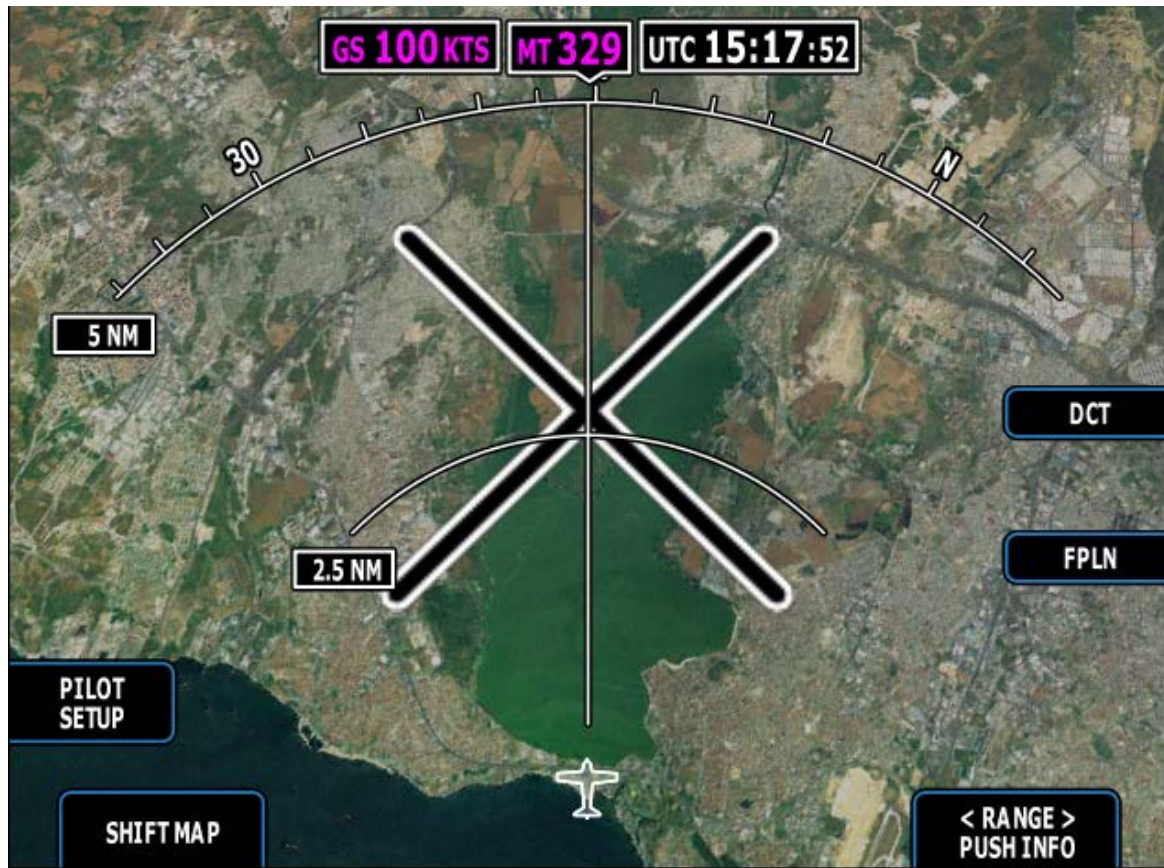
Figure 4.7: Fixation cross to center the participants' gaze on the center of the screen. This picture has the same width and height as the depiction used in the experiment.

| Geometry 1 (G1) | Geometry 2 (G2) | Geometry 3 (G3) | Geometry 4 (G4) |
| No Collision | Collision | Collision | No Collision |
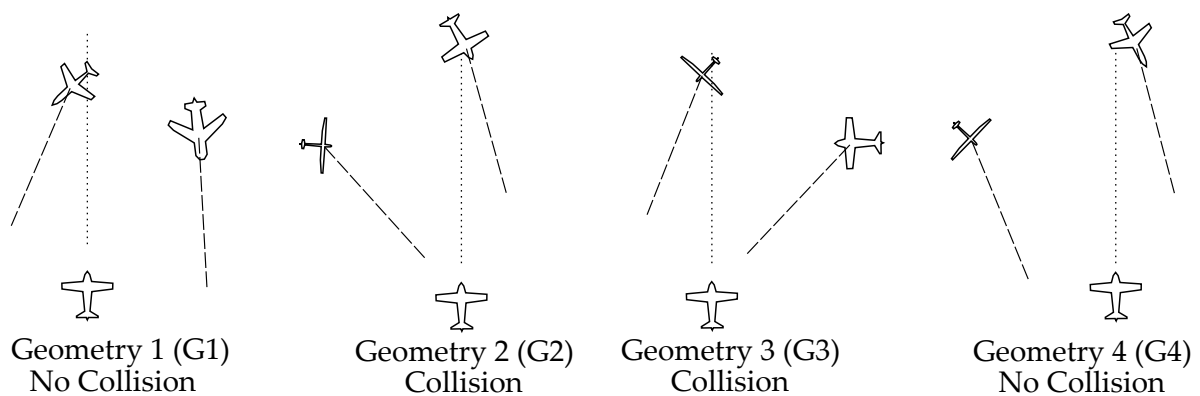
Figure 4.8: Conflict geometries used for analysis, including the path of relative motion for the intruders (not to scale). The initial aircraft positions were set in a way that the condition to display predictive and priority cues were met (CPA less than 45 seconds away, see section 4.2.3). Similar to TCAS traffic advisories, this triggered display variants C, D and E to display their predictive cues (absolute or relative trackline).

71

4.3.6 Dependent Measures

The decision time, the accuracy of conflict and priority decisions, the mental demand, and the preference ratings are the dependent variables of this study. The decision time was measured from the beginning of each flight scenario until the participant decided if the traffic was in conflict and pressed the response key. If the participant decided that there was a conflict, the experimenter asked which air vehicles were in conflict and which rules of the air [1] would apply, and recorded the answers. These data were further processed to determine the accuracy of the decision conflict/non-conflict and of the priority or right-of-way decisions. After each trial, the participants rated the mental demand associated with the decision using an electronic subscale of The NASA Task Load Index [85] with a range from very low (0) to very high (20). Furthermore, at the end of the experiment the participants rated their preference for all display variants on a scale from 1 (very good) to 5 (very bad)[9].

4.3.7 Independent Factors

The display variant was an independent within-subjects factor with five levels (variants A, B, C, D and E). Four geometries were used for each display variant. The combination of independent factors and dependent measures is presented in Table 4.2.

Display	for all variants, A to E			
Geometry	G1	**G2**	**G3**	G4
Decision time	t	t	t	t
Accuracy of collision decisions	c	c	c	c
Accuracy of priority decisions	—	a	a	—
Mental demand	d	d	d	d
Pilots' preferences	p			

Table 4.2: Experiment Design. The symbols in the fields represent the data analyzed in the experiment: t-decision time in seconds, c - accuracy of collision decisions, a - accuracy of priority decisions, d - ratings of mental demand and p - preference scores. G1 and G4: non-conflict geometries, **G2** and **G3**: conflict geometries.

4.3.8 Data Analysis

For testing hypotheses 1, 4 and 5, the data were analyzed using repeated measures analysis of variance (ANOVA) with the display variant (5 levels) as within-subjects factor (Table 4.2). Results were considered at α of 0.05.

Due to the violation of the sphericity assumption, the Greenhouse-Geisser adjustment was applied [109]. For the analysis of variance the conflict geometry was treated as an independent within-subjects factor (4 levels). However, the effects of conflict geometry

---

[9]This corresponds to the grading scheme used in Austrian schools.

are not reported. The conflict geometry was varied in order to test the displays in conflict and non-conflict situations and to create a sufficient number of conflict and priority cases.

For significant ANOVA tests, Tukey's Honestly Significant Difference (HSD) post-hoc tests were used for pairwise comparisons between display variants. Here, six post-hoc tests were performed: between variant D and each of the variants A, B, C; between variant E and each of the variants A, B, C. Due to the multiple statistical tests used to verify these hypotheses, an alpha correction was performed using the classical Bonferroni procedure described in [110]. This lead to the verification of the hypotheses related to post-hoc tests with a corrected alpha of $\alpha^* = \alpha/6 = 0.008$.

The second and third hypotheses were tested using a χ^2-test in order to analyze differences in decision accuracy between display variants. Results were considered at α of 0.05. For the second hypothesis six additional χ^2-tests were calculated: between variant D and each of the variants A, B, C; between variant E and each of the variants A, B, C. The corrected alpha was $\alpha^* = \alpha/6 = 0.008$. For the third hypothesis four additional χ^2-tests between the variant E and each of the variants A, B, C and D were calculated using a corrected alpha $\alpha^\dagger = \alpha/4 = 0.013$.

4.4 Results

4.4.1 Decision time

The effect of the display variant on the decision time was significant [$F_{2.08,41.59} = 28.77$, $p < 0.0001$, $\eta^2 = 0.59$]. The display variant accounted for 59% of the variance. The results of Tukey's HSD tests (Fig. 4.9) show that each display of the relative track (variants D and E) resulted in significantly shorter decision times than the variants A ($p < 0.0001$), B ($p < 0.0001$) and C ($p < 0.0001$). Thus, the first hypothesis was confirmed.
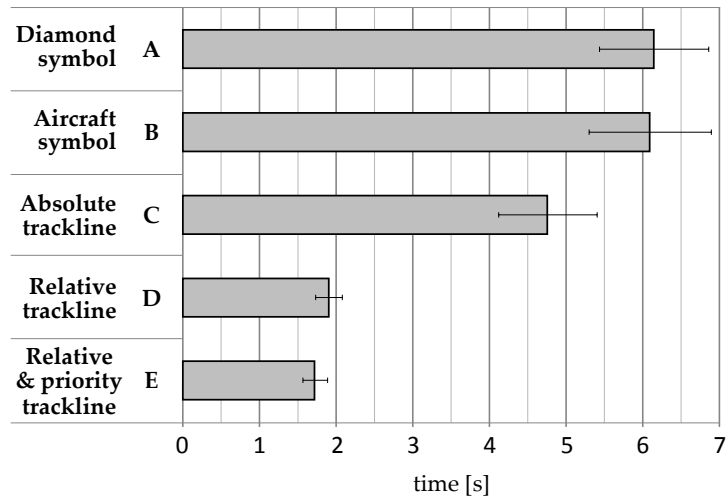
Figure 4.9: Means and standard deviations of decision time by display variant

4.4.2 Accuracy of Conflict Decisions

The results of the χ^2-tests indicated no significant differences in accuracy of conflict decisions among the display variants. The second hypothesis was not confirmed. The error data are presented in Table 4.3.

Display		Errors	Number of valid trials	Percentage
Diamond symbol	A	8	83	9.64
Aircraft symbol	B	8	84	9.52
Absolute trackline	C	6	84	7.14
Relative trackline	D	0	84	0.00
Relative & priority trackline	E	0	84	0.00

Table 4.3: Erroneous conflict decisions

4.4.3 Accuracy of Priority Decisions

Differences in the accuracy of right-of-way decisions between display variants did not reach statistical significance. The third hypothesis was not confirmed. The priority decisions were investigated only for the geometries 2 and 3 which involved conflicts. The descriptive results of the error analysis are presented in Table 4.4.

Display		Errors	Number of valid trials	Percentage
Diamond symbol	A	3	41	7.32
Aircraft symbol	B	3	42	7.14
Absolute trackline	C	2	42	4.76
Relative trackline	D	2	42	4.76
Relative & priority trackline	E	1	42	2.38

Table 4.4: Erroneous priority decisions

4.4.4 Mental Demand

The type of display significantly influenced mental demand $F_{2.11,42.30} = 15.13$, p<0.0001, $\eta^2 = 0.43$]. The results of Tukey's HSD (Fig. 4.10) show that mental demand for the display variant E was significantly lower than for the variants A (p<0.0001), B (p<0.001) and C (p<0.003). The mental demand for the display variant D was significantly lower than for the variant A (p<0.0001), B (p<0.001) and C (p<0.002). Thus, the fourth hypothesis was confirmed.
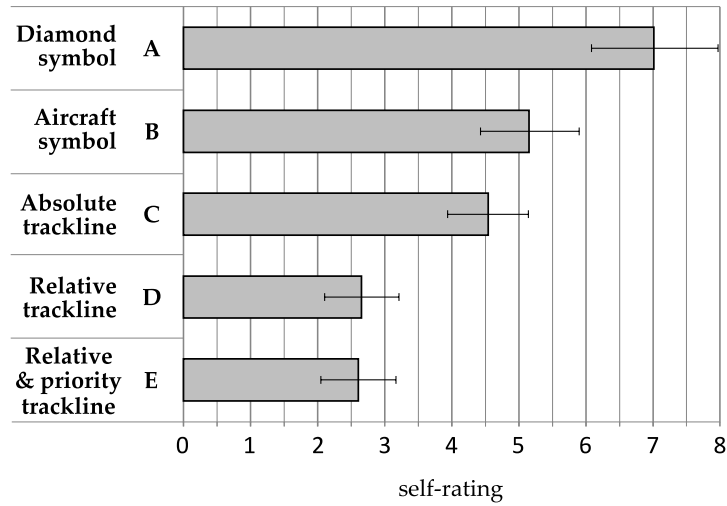
Figure 4.10: Means and standard deviations of mental demand ratings for each display variant. The rating scale ranged from 0 (very low) to 20 (very high).

4.4.5 Pilots' Preferences

Pilots' preferences for the display variants were significantly different [$F_{2.13,42.64} = 46.03$, p<0.0001, $\eta^2 = 0.69$]. The Tukey's HSD tests (Fig. 4.11) show that the display variant D scored significantly higher than the variants A (p<0.0001), B (p<0.0001) and C (p<0.0001). The display variant E scored significantly higher than the variants A (p<0.0001), B (p<0.0001) and C (p<0.003). The fifth hypothesis was confirmed.
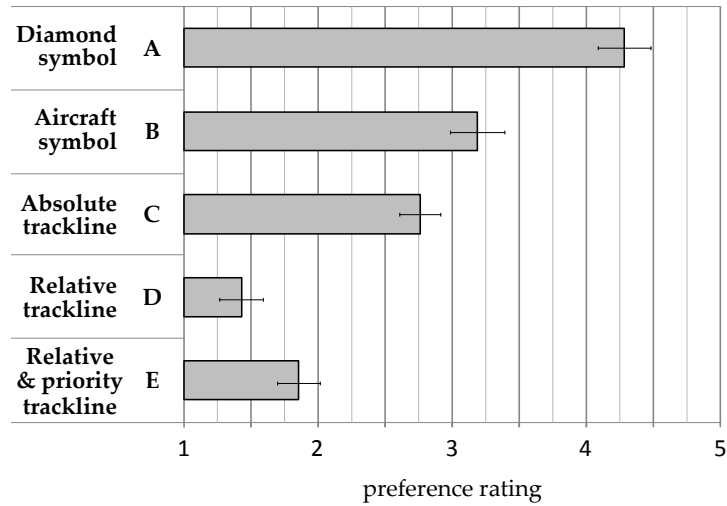
Figure 4.11: Means and standard deviations of pilots' preference ratings for each display variant. The scale ranged from 1 (very good) to 5 (very bad).

4.5 Discussion

This chapter proposed and evaluated new traffic display variants to enhance pilots' understanding and prediction of traffic situations and to reduce the mental demand posed by this task. The investigated traffic displays are intended to support pilots in their see-and-avoid task in visual flight at a pre-warning stage. The objective is to reduce the scanning time of the traffic display, which could potentially allow VFR pilots to spend more time on scanning the outside view. The experiment evaluated if the displays of the relative and priority track can improve pilots' conflict and priority decisions, reduce the decision time and mental demand posed by the task and meet pilots' preferences. This study was motivated by previous findings which addressed problems encountered by VFR pilots in managing multiple traffic situations [100].

The proposed display variants for visual flight present critical traffic information (e.g. type of air vehicle) which is available from emerging technologies such as ADS-B and Mode-S 'Extended Squitter' transponder. New traffic indications showing the type and orientation of the air vehicles encountered as well as the relative track and priority cues were developed to support pilots in their decisions. However, possible limitations of the proposed display concept caused by increased display clutter have been expected, as well as in [107].

4.5.1 Decision Time

The results show that the type of display significantly influences the rapidity of conflict decisions. Thus, the first hypothesis was confirmed. The main finding is that pilots needed significantly shorter time to decide whether the displayed air vehicle was in conflict with both the relative (variant D) and the relative and priority trackline (variant E) as opposed to the absolute trackline (variant C), the oriented air vehicle symbol (variant B) and to the currently used TCAS-like symbols (variant A).

On average, the pilots watched the display variant E for about 1.7 seconds and the variant D for 1.9 seconds to make a conflict decision. For the same task they needed an average of 6.1 seconds with the TCAS-like symbolic (variant A), 6.1 seconds with the oriented air vehicle symbols (variant B) and 4.7 seconds with the absolute trackline (variant C). These results show that the use of a traffic display could distract VFR pilots from their main task of monitoring the view outside the cockpit.

However, the total decision time obtained in the experiment is not directly comparable with the average dwell time reported in [40] because of the different methods used. In the present study, the pilots watched a display only once until they decided whether there was a conflict or not. In [40] the traffic display was watched several times and an average dwell time was reported. Notwithstanding these methodological differences, previous research is noteworthy for emphasizing the importance of measuring and reducing the time pilots spend on scanning a cockpit display of traffic information.

4.5.2 Accuracy of Conflict and Priority Decisions

The display variant did not significantly influence the accuracy of conflict and priority decisions. Therefore, the second and the third hypotheses were rejected.

An explanation for the lack of significant differences in the accuracy of priority decisions between the variant E (showing the 'priority trackline') and the variants B, C and D is that pilots inferred the priority rule from the information provided by the type of air vehicle and the conflict geometry (Fig. 4.8, geometry 2 and 4, unpowered glider versus powered small aeroplane). Therefore, they obtained comparable levels of accuracy for their priority decisions. The comparable performance obtained with variant A which does not show the type of air vehicle but abstract TCAS-symbols may be explained: when the variant A was tested pilots were told that the air vehicles in conflict had the same category.

Surprisingly, there was one pilot who made an erroneous priority decision despite the visualization of the priority cue in the variant E. Analysis of his data showed that his most preferred variants were D and E. However, this pilot proposed a dimming of the map background to make the traffic indication more salient. These changes should be considered for the future development of the display concept.

4.5.3 Mental Demand

The mental demand related to the conflict decision task was significantly influenced by the display variant. The pilots reported significantly lower mental demand when using the relative and priority trackline (variant E) as compared to the oriented air vehicle symbols (variant B), to the baseline (variant A) and to the absolute trackline (variant C). Mental demand ratings were significantly lower for variant D than compared to variant A, B and C. Thus, the fourth hypothesis was confirmed. The results indicate that the lower amount of predictive information being conveyed in the variants A, B and C makes them more demanding.

4.5.4 Pilots' Preferences

The display variant significantly influenced pilots' preferences. The analysis of pilots' ratings shows that both the relative (variant D) and the relative and priority trackline (variant E) scored significantly better than the oriented air vehicle symbol (variant B), the baseline variant A and the absolute trackline (variant C). Thus, the fifth hypothesis was confirmed.

In summary, the display of the relative and priority trackline (variant E) was superior to the variants C, B and A with respect to decision time, mental demand and pilots' preferences. The relative track (variant D) allows shorter decision time, lower mental demand and received significantly better preference ratings than the variants A, B and C.

An explanation for the lack of significant differences in the accuracy of conflict and priority decisions among the display variants might be that for pilots the conflict decision task was essential when using each display variant. However, more time was spent when using the variants A and B and C, as compared to variants D and E. The results show that VFR pilots prefer the display variants D and E which posed lower mental demand and allowed for shorter decision times than the variants A, B and C.

The evaluation strategy was to consider a new display acceptable if it proves to be superior to other displays in at least one criterion and if it is not significantly poorer in any criteria (decision time, accuracy of conflict and priority decisions, mental demand and pilots' preference). The variants D and E were superior to the variants A, B and C in three criteria (decision time, mental demand and pilots' preferences) and were not significantly poorer in any criteria.

The use of predictive automation displaying the relative and priority trackline significantly reduced decision time, mental demand and was preferred by the pilots. These findings confirm previous research on predictive automation [62] [65] [106].

The results of the experiment show that currently used TASs could be optimized with the implementation of predictive cues such as the relative & priority trackline. However, before an implementation of the new displays for real VFR operations can be recommended more research is needed in order to validate these results.

4.5.5 Limitations

Although the experiment shows clear benefits in displaying the type of air vehicle and the relative and priority trackline, some limitations should be pointed out. The study evaluated only the symbology for glider, small aeroplane and small and large jets (Fig. 4.8). Future tests should consider all the proposed symbols (Fig. 4.2). Furthermore, the laboratory experiment was necessary to determine reliable decision times, but did not provide a realistic flight environment.

Another limitation is that only horizontal conflict geometries were applied in the experiment. Horizontal as well as vertical conflict geometries should be applied as described in [80]. Future research should also include vertical traffic geometries and the indications of relative altitude and position of traffic which are currently used in TCAS-like displays [53].

Furthermore, there are limitations of the proposed display design. A display concept for highlighting the tracklines, the air vehicle symbols and the dimming of the moving map (e.g. traffic and terrain layers) should be evaluated in the future. The map background is a common feature of currently used TASs (Fig. 2.2) which integrate traffic and navigation information. However, the impact of display clutter caused by the integration of traffic and map display has to be considered in future experiments. A map-free version of the traffic display as well as an integrated version of the map and traffic display should be evaluated.

Furthermore, only the visual modality of the traffic display was evaluated. Future research should also investigate multimodalities (i.e. additional visual and aural information).

4.6 Conclusion of this Chapter

The previous study shows that the currently used traffic displays for visual flight could be further improved to support pilots in the prediction of traffic situations and to reduce mental demand and display scanning time. Although further evaluation experiments during simulated and real flight are necessary, the results show that the indication of the relative & priority trackline is a promising engineering solution to the problems encountered by VFR pilots in multiple traffic situations (e.g. prediction, mental demand). An essential aspect is the time spent watching a display until the pilot decides whether the indicated traffic is a conflict or not. The VFR pilots should not be distracted by any display from their primary task to monitor the environment outside the cockpit.

5 Evasion Trajectories

The methods shown for calculating the predicted path of the intruder in the previous chapters were based on the assumption of constant speed and heading of both participants of the traffic situation (section 4.2.2). The underpinning premise was to inform the pilot visually about the encounter speed and direction without causing excessive workload. After observing the display, the pilot of the ownship is obliged to visually identify the traffic outside of the cockpit and to avoid it when necessary using the proper right-of-way rules.

While this procedure is deemed best practice by regulation, one might go a step further and ask whether displaying an avoidance route and/or automatic execution of such could prove useful. Also, 60% of pilots in the study of section 3 recommended such an option.

In the following, a theoretical framework for the calculation of such evasion trajectories will be laid out.

5.1 Evading Moving Obstacles

This section deals with the calculation of predicted movements for an intruder and the evasion response of the ownship governed by a zero-sum game as described in section 1.6).

The aim is to calculate an avoidance route in a collision scenario as a measure of last resort. This route can be used as a basis for a traffic display and also enable synthesized aural commandos aiding the pilot in his response selection (section 1.3.2). Furthermore, the method of calculating the evasion maneuvers should not be limited only to one direction (as in TCAS), but also be able to produce multidimensional trajectories. This may also open an opportunity to use the avoidance route as a basis to determine control inputs for an autopilot algorithm.

For this line of reasoning it is assumed that the approaching aircraft does not follow the Rules of the Air. However, these may be implemented at a later stage to allow for a broader field of operation.

Based on the methods described by section 1.5, it is first necessary to define a state equation and a payoff function for the game (eqn. (1.31)). The overall state of the game $\boldsymbol{\xi}$ is composed of both the states of the pursuer $\boldsymbol{\xi}_p$ and the evader $\boldsymbol{\xi}_e$ as

$$\boldsymbol{\xi}(t) := \boldsymbol{\xi}_p(t) - \boldsymbol{\xi}_e(t) \tag{5.1}$$

with

$$
\boldsymbol{\xi}_p = \begin{pmatrix} x_p \\ y_p \\ z_p \\ \dot{x}_p \\ \dot{y}_p \\ \dot{z}_p \end{pmatrix} \qquad\qquad \boldsymbol{\xi}_e = \begin{pmatrix} x_e \\ y_e \\ z_e \\ \dot{x}_e \\ \dot{y}_e \\ \dot{z}_e \end{pmatrix} \tag{5.2}
$$

in the time interval $t_0 \leq t \leq t_f$. Here, the upper three elements represent the the predicted coordinates of the pursuer and the evader in an inertial frame, respectively. Thus, $\boldsymbol{\xi}(t)$ holds the relative distance and velocity of the traffic participants. The initial condition of the game $\boldsymbol{\xi}(t_0) = \boldsymbol{\xi}_0$ defines these quantities at the onset of an encounter.

The state equation (eqn. (1.1)) for the linear and time-invariant pursuer and evader yields

$$
\dot{\boldsymbol{\xi}}_p = \boldsymbol{P}\,\boldsymbol{\xi}_p + \boldsymbol{Q}\,\boldsymbol{u}_p
$$
$$
\dot{\boldsymbol{\xi}}_e = \boldsymbol{P}\,\boldsymbol{\xi}_e + \boldsymbol{Q}\,\boldsymbol{u}_e
$$

with $\boldsymbol{u}_p = (\ddot{x}_p \ \ddot{y}_p \ \ddot{z}_p)^T$ and $\boldsymbol{u}_e = (\ddot{x}_e \ \ddot{y}_e \ \ddot{z}_e)^T$ defining the control inputs of the pursuer and evader, respectively. A simple multiplication shows that the constant system and input matrices $\boldsymbol{P}$ and $\boldsymbol{Q}$ for this linear, time-invariant system turn out to be

$$
\boldsymbol{P} = \left(\begin{array}{ccc|ccc} 0 & 0 & 0 & 1 & 0 & 0 \\ 0 & 0 & 0 & 0 & 1 & 0 \\ 0 & 0 & 0 & 0 & 0 & 1 \\ \hline 0 & 0 & 0 & 0 & 0 & 0 \\ 0 & 0 & 0 & 0 & 0 & 0 \\ 0 & 0 & 0 & 0 & 0 & 0 \end{array} \right) \qquad \boldsymbol{Q} = \begin{pmatrix} 0 & 0 & 0 \\ 0 & 0 & 0 \\ 0 & 0 & 0 \\ 1 & 0 & 0 \\ 0 & 1 & 0 \\ 0 & 0 & 1 \end{pmatrix}
$$

This leads to

$$
\dot{\boldsymbol{\xi}} = \boldsymbol{P}\,\boldsymbol{\xi} + \boldsymbol{Q}\,\boldsymbol{u} \tag{5.3}
$$

with $\boldsymbol{\xi} = \boldsymbol{\xi}_p - \boldsymbol{\xi}_e$ and $\boldsymbol{u} = \boldsymbol{u}_p - \boldsymbol{u}_e$.

To include a measure of relative distance and also the controls of the evader and the pursuer aircraft, the payoff function (eqn. (1.3)), which is minimized by the pursuer and maximized by the evader (eqn. (1.27)) is modeled as

$$
J(\boldsymbol{u}_p, \boldsymbol{u}_e) = \frac{1}{2}\,\boldsymbol{\xi}^T(t_f)\,\boldsymbol{S}\,\boldsymbol{\xi}(t_f) + \frac{1}{2} \int\limits_{t_0}^{t_f} \boldsymbol{u}_p^T\,\boldsymbol{W}_p\,\boldsymbol{u}_p \ \mathrm{d}t - \frac{1}{2} \int\limits_{t_0}^{t_f} \boldsymbol{u}_e^T\,\boldsymbol{W}_e\,\boldsymbol{u}_e \ \mathrm{d}t \tag{5.4}
$$

The eqns. (5.3) and (5.4) formally describe a linear system with quadratic quality

criteria [43] [111]. The first summand reflects the distance of the two aircraft at time t_f and represents the final payoff function Φ. The second and third summand represent the accumulated control effort in the interval $t_0 \leq t \leq t_f$ of the pursuer and the evader, respectively.

The objective of the pursuer is to use its controls $\boldsymbol{u}_p$ to minimize J, meaning to lower the final passing distance at $t = t_f$ while simultaneously limit the control effort used, because only finite energy sources can be tapped while maneuvering. The control terms also enable to include dynamic equations containing the aerodynamic capabilities of the aircraft.

The evader's objective is obviously to maximize the final passing distance while also minimizing its control effort. These at first glance conflicting optimizations on the evader are resolved into two minimizations by using a negative sign[1] on the control effort of the evader in eqn. (5.4).

This way, optimal control problem can be written in a concise way

$$J(\boldsymbol{u}_p^*, \boldsymbol{u}_e^*) = \min_{\boldsymbol{u}_p} \max_{\boldsymbol{u}_e} J(\boldsymbol{u}_p, \boldsymbol{u}_e)$$

The matrices $\boldsymbol{S}$, $\boldsymbol{W}_p$ and $\boldsymbol{W}_e$ are diagonal positive definite weighing matrices

$$\boldsymbol{S} = \left(\begin{array}{ccc|ccc} \frac{1}{s_{xy}^2} & 0 & 0 & 0 & 0 & 0 \\ 0 & \frac{1}{s_{xy}^2} & 0 & 0 & 0 & 0 \\ 0 & 0 & \frac{1}{s_z^2} & 0 & 0 & 0 \\ \hline 0 & 0 & 0 & 0 & 0 & 0 \\ 0 & 0 & 0 & 0 & 0 & 0 \\ 0 & 0 & 0 & 0 & 0 & 0 \end{array} \right) \tag{5.5}$$

$$\boldsymbol{W}_e = \left(\begin{array}{ccc} \frac{1}{a_{e,xy}^2} & 0 & 0 \\ 0 & \frac{1}{a_{e,xy}^2} & 0 \\ 0 & 0 & \frac{1}{a_{e,z}^2} \end{array} \right) \qquad \boldsymbol{W}_p = \left(\begin{array}{ccc} \frac{1}{a_{p,xy}^2} & 0 & 0 \\ 0 & \frac{1}{a_{p,xy}^2} & 0 \\ 0 & 0 & \frac{1}{a_{p,z}^2} \end{array} \right) \tag{5.6}$$

which define a prolate or oblate spheroid in an inertial frame, depending on the choice of the lower right element in these matrices (x and y axes are parallel to the horizon).

The matrices $\boldsymbol{W}_p$ and $\boldsymbol{W}_e$ define the relative weights of the control effort along horizontal and vertical axes for the pursuer and the evader, respectively. Because $\boldsymbol{u}_p$ and $\boldsymbol{u}_e$ are measured in an inertial frame, the upper left and the center element of the matrices $\boldsymbol{W}_p$ and $\boldsymbol{W}_e$ have to be equal in order for the control effort to be invariant when turning in the horizontal plane. If additionally the lower right element is equal to the other two, also the control effort of climbs and descends is independent of aircraft attitude.

However, in the following, the opportunity to set the lower right element at a different value will still be kept open by using a unique symbol, because bank and pitch angles

---

[1]See comment in section 1.5.1.

are expected to be limited for the intended application[2] and therefore also the impact on the control effort. The upside to this is to be able to weigh vertical vs. horizontal maneuvers.

The matrix $\boldsymbol{S}$ weighs the final cost term to the control cost terms and also the influence of the horizontal vs. the vertical distance between the two air vehicles. If $s_{x,y} = s_z$, the final cost is determined by a spherical protection envelope around the evader.

The Hamiltonian (eqn. (1.7)) of this system described by eqn. (5.3) and (5.4) yields

$$H = \frac{1}{2} \left(\boldsymbol{u}_p^T \ \boldsymbol{W}_p \ \boldsymbol{u}_p - \boldsymbol{u}_e^T \ \boldsymbol{W}_e \ \boldsymbol{u}_e \right) + \boldsymbol{\lambda}^T \left(\boldsymbol{P} \ \boldsymbol{\xi} + \boldsymbol{Q} \ \boldsymbol{u} \right)$$

The adjoint vector $\boldsymbol{\lambda}$ is only a function of time (section 1.5) and contains 6 elements, defined by the number of rows in the matrices $\boldsymbol{P}$ and $\boldsymbol{Q}$. A multiplication using eqns. (5.2) and the above definitions for the matrices and control terms yields

$$H = \frac{1}{2} \left(\frac{\ddot{x}_p^2}{a_{p,xy}^2} + \frac{\ddot{y}_p^2}{a_{p,xy}^2} + \frac{\ddot{z}_p^2}{a_{p,z}^2} - \frac{\ddot{x}_e^2}{a_{e,xy}^2} - \frac{\ddot{y}_e^2}{a_{e,xy}^2} - \frac{\ddot{z}_e^2}{a_{e,z}^2} \right) +$$

$$+\lambda_1 \left(\dot{x}_p - \dot{x}_e \right) + \lambda_2 \left(\dot{y}_p - \dot{y}_e \right) + \lambda_3 \left(\dot{z}_p - \dot{z}_e \right) + \lambda_4 \left(\ddot{x}_p - \ddot{x}_e \right) + \lambda_5 \left(\ddot{y}_p - \ddot{y}_e \right) + \lambda_6 \left(\ddot{z}_p - \ddot{z}_e \right)$$

Applying the calculus of variations, first H has to be derived with respect to the controls $\boldsymbol{u}_p$ and $\boldsymbol{u}_e$ (eqn. (1.14)). This yields

$$\frac{\partial H}{\partial \boldsymbol{u}_p} = \boldsymbol{0}$$

$$\begin{pmatrix} \frac{\ddot{x}_p}{a_{p,xy}^2} + \lambda_4 \\ \frac{\ddot{y}_p}{a_{p,xy}^2} + \lambda_5 \\ \frac{\ddot{z}_p}{a_{p,z}^2} + \lambda_6 \end{pmatrix} = \begin{pmatrix} 0 \\ 0 \\ 0 \end{pmatrix}$$

$$\frac{\partial H}{\partial \boldsymbol{u}_e} = \boldsymbol{0}$$

$$\begin{pmatrix} -\frac{\ddot{x}_e}{a_{e,xy}^2} - \lambda_4 \\ -\frac{\ddot{y}_e}{a_{e,xy}^2} - \lambda_5 \\ -\frac{\ddot{z}_e}{a_{e,z}^2} - \lambda_6 \end{pmatrix} = \begin{pmatrix} 0 \\ 0 \\ 0 \end{pmatrix}$$

These equation vectors can be written in a concise way:

$$\boldsymbol{W}_p \ \boldsymbol{u}_p + \boldsymbol{Q}^T \ \boldsymbol{\lambda} = \boldsymbol{0} \qquad \text{for the pursuer terms}$$

$$\boldsymbol{W}_e \ \boldsymbol{u}_e + \boldsymbol{Q}^T \ \boldsymbol{\lambda} = \boldsymbol{0} \qquad \text{for the evader terms}$$

The controls therefore read

$$\boldsymbol{u}_p = -\boldsymbol{W}_p^{-1} \ \boldsymbol{Q}^T \ \boldsymbol{\lambda} \tag{5.7}$$

$$\boldsymbol{u}_e = -\boldsymbol{W}_e^{-1} \ \boldsymbol{Q}^T \ \boldsymbol{\lambda} \tag{5.8}$$

---

[2]roll angle $\approx \pm 20°$, pitch angle $\approx \pm 10°$

A solution for $\boldsymbol{u}_p$ and $\boldsymbol{u}_e$ exists when term in the first parentheses of eqn. (1.17) for both controls is invertible. After calculation using the above vector equations, these matrices turn out to be

$$\frac{\partial^2 H}{\partial \boldsymbol{u}_p^2} = \boldsymbol{W}_p \qquad \frac{\partial^2 H}{\partial \boldsymbol{u}_e^2} = \boldsymbol{W}_e$$

Therefore, the matrices $\boldsymbol{W}_p$ and $\boldsymbol{W}_e$ have to be regular for the solution to exist. This is the case for non-zero elements on the main diagonal (eqn. (5.6)).

Next, eqn. (1.18) and (1.19) are applied to determine the state-adjoint system

$$\dot{\boldsymbol{\xi}} = \left(\frac{\partial H}{\partial \boldsymbol{\lambda}}\right)^T = \boldsymbol{P}\,\boldsymbol{\xi} + \boldsymbol{Q}\,(\boldsymbol{u}_p - \boldsymbol{u}_e)$$
$$\Rightarrow \dot{\boldsymbol{\xi}} = \boldsymbol{P}\,\boldsymbol{\xi} - \boldsymbol{Q}\,(\boldsymbol{W}_p^{-1} - \boldsymbol{W}_e^{-1})\,\boldsymbol{Q}^T\,\boldsymbol{\lambda} \tag{5.9}$$

$$\dot{\boldsymbol{\lambda}} = -\left(\frac{\partial H}{\partial \boldsymbol{\xi}}\right)^T = -\begin{pmatrix} 0 & 0 & 0 & \lambda_1 & \lambda_2 & \lambda_3 \end{pmatrix}^T$$
$$\Rightarrow \dot{\boldsymbol{\lambda}} = -\boldsymbol{P}^T\,\boldsymbol{\lambda} \tag{5.10}$$

which is in matrix form

$$\begin{pmatrix} \dot{\boldsymbol{\xi}} \\ \dot{\boldsymbol{\lambda}} \end{pmatrix} = \begin{pmatrix} \boldsymbol{P} & -\boldsymbol{Q}\,(\boldsymbol{W}_p^{-1} - \boldsymbol{W}_e^{-1})\,\boldsymbol{Q}^T \\ \boldsymbol{0} & -\boldsymbol{P}^T \end{pmatrix} \begin{pmatrix} \boldsymbol{\xi} \\ \boldsymbol{\lambda} \end{pmatrix} \tag{5.11}$$

The boundary condition (eqn. (1.16)) with the final payoff function $\Phi = \frac{1}{2}\,\boldsymbol{\xi}^T(t_f)\,\boldsymbol{S}\,\boldsymbol{\xi}(t_f)$ using eqn. (A.1) yields

$$\boldsymbol{\lambda}(t_f) = \left(\frac{\partial \Phi}{\partial \boldsymbol{\xi}}\right)^T\bigg|_{t_f} = \boldsymbol{S}\,\boldsymbol{\xi}(t_f) \tag{5.12}$$

There are two ways to calculate the adjoint vector $\boldsymbol{\lambda}$ to obtain the controls described by eqn. (5.7) and (5.8). The first one uses a separation approach [111]

$$\boldsymbol{\lambda}(t) := \boldsymbol{K}(t)\,\boldsymbol{\xi}(t) \tag{5.13}$$

which for the controls (eqn. (5.7) and (5.8)) yields

$$\boldsymbol{u}_p = -\boldsymbol{W}_p^{-1}\,\boldsymbol{Q}^T\,\boldsymbol{K}(t)\,\boldsymbol{\xi}(t) \tag{5.14}$$

$$\boldsymbol{u}_e = -\boldsymbol{W}_e^{-1}\,\boldsymbol{Q}^T\,\boldsymbol{K}(t)\,\boldsymbol{\xi}(t) \tag{5.15}$$

Combining eqns. (5.9) and (5.10) and the time derivative $\dot{\boldsymbol{\lambda}} = \dot{\boldsymbol{K}}\,\boldsymbol{\xi} + \boldsymbol{K}\,\dot{\boldsymbol{\xi}}$ yields

$$\dot{\boldsymbol{K}}\,\boldsymbol{\xi} + \boldsymbol{K}\,\left(\boldsymbol{P}\,\boldsymbol{\xi} - \boldsymbol{Q}\,(\boldsymbol{W}_p^{-1} - \boldsymbol{W}_e^{-1})\,\boldsymbol{Q}^T\,\boldsymbol{\lambda}\right) = -\boldsymbol{P}^T\,\boldsymbol{K}\,\boldsymbol{\xi}$$

With $\boldsymbol{R}^{-1} := \boldsymbol{W}_p^{-1} - \boldsymbol{W}_e^{-1}$ this simplifies to

$$\left(\dot{\boldsymbol{K}} + \boldsymbol{K}\,\left(\boldsymbol{P} - \boldsymbol{Q}\,\boldsymbol{R}^{-1}\,\boldsymbol{Q}^T\,\boldsymbol{K}\right)\right)\,\boldsymbol{\xi} = -\boldsymbol{P}^T\,\boldsymbol{K}\,\boldsymbol{\xi}$$

The state $\boldsymbol{\xi}$ cancels on both sides, creating an opportunity to calculate the matrix $\boldsymbol{K}$ using the *Matrix-Riccati* equation

$$\dot{\boldsymbol{K}} = \boldsymbol{K}\,\boldsymbol{Q}\,\boldsymbol{R}^{-1}\,\boldsymbol{Q}^T\,\boldsymbol{K} - \boldsymbol{P}^T\,\boldsymbol{K} - \boldsymbol{K}\,\boldsymbol{P} \tag{5.16}$$

This matrix differential equation can be solved using numerical methods. The integration has to be done backwards in time from t_f to t_0, because of the boundary condition, which is obtained from eqns. (5.12) and (5.13):

$$\begin{aligned}\boldsymbol{\lambda}(t_f) &= \boldsymbol{S}\,\boldsymbol{\xi}(t_f) = \boldsymbol{K}(t_f)\,\boldsymbol{\xi}(t_f) \\ &\Rightarrow \boldsymbol{K}(t_f) = \boldsymbol{S}\end{aligned} \tag{5.17}$$

A graphical representation of the numerical results for $\boldsymbol{K}(t)$ (*Separation-Riccati* approach, eqn. (5.16)) is presented in Fig. A.13. Using the solution $\boldsymbol{K}(t)$ from eqn. (5.13) (which is a 6x6 matrix), the state $\boldsymbol{\xi}(t)$ can now be obtained with eqns. (5.9) and (5.13)

$$\begin{aligned}\dot{\boldsymbol{\xi}}(t) &= \boldsymbol{P}\,\boldsymbol{\xi}(t) - \boldsymbol{Q}\,(\boldsymbol{W}_p^{-1} - \boldsymbol{W}_e^{-1})\,\boldsymbol{Q}^T\,\boldsymbol{K}(t)\,\boldsymbol{\xi}(t) \\ &\Rightarrow \dot{\boldsymbol{\xi}}(t) = \left[\boldsymbol{P} - \boldsymbol{Q}\,(\boldsymbol{W}_p^{-1} - \boldsymbol{W}_e^{-1})\,\boldsymbol{Q}^T\,\boldsymbol{K}(t)\right]\,\boldsymbol{\xi}(t)\end{aligned} \tag{5.18}$$

The numerical integration of this equation with the boundary condition $\boldsymbol{\xi}(t_0) = \boldsymbol{\xi}_0$ leads to the state trajectories $\dot{\boldsymbol{\xi}}(t)$.

This method is, while feasible, not the only way to calculate the controls $\boldsymbol{u}_p$ and $\boldsymbol{u}_e$. because of the numerical integration needed to obtain $\boldsymbol{K}(t)$. Furthermore, if the final time t_f is not fixed, the Riccati-Separation method (eqns. (5.13) and (5.16)) requires an integration step each time t_f changes. Limited hardware capability onboard an aircraft may therefore restrict the applicability for this method.

In the following, a second method of obtaining $\boldsymbol{\lambda}(t)$ is presented, which allows to calculate the elements of $\boldsymbol{K}(t)$ and subsequently $\boldsymbol{u}_p$ and $\boldsymbol{u}_e$ algebraically.

When looking at eqn. (5.11) from a control-systems point of view [43] [111], an approach using *transition matrices* comes to mind. These describe the evolution of the state from t_0 to $t \in [t_0, t_f]$. Given the state at a reference time, the state at any other time is given by the mapping

$$\begin{aligned}\boldsymbol{\xi}(t) &= \boldsymbol{T}_\xi(t, t_0)\,\boldsymbol{\xi}(t_0) \\ \boldsymbol{\lambda}(t) &= \boldsymbol{T}_\lambda(t, t_0)\,\boldsymbol{\lambda}(t_0)\end{aligned}$$
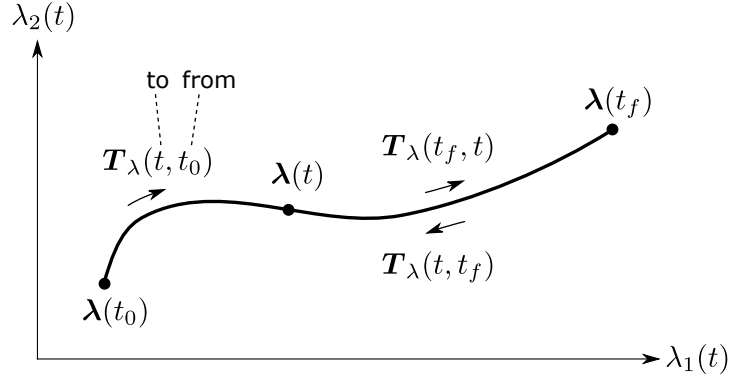
Figure 5.1: Illustration of the evolution of a state (in this case, $\boldsymbol{\lambda}(t)$) described by a transition matrix. The axes of this chart, λ_1 and λ_2, are examples for two components of $\boldsymbol{\lambda}$. The time t is defined in the interval $t_0 \leq t \leq t_f$

The transition matrix (for example, $\boldsymbol{T}_\lambda$) takes two parameters (Fig. 5.1), defining the time span with respect to reference time. From this, it follows that for $\boldsymbol{\lambda}(t_0) = \boldsymbol{T}_\lambda(t_0, t_0)\,\boldsymbol{\lambda}(t_0)$ the transition matrix $\boldsymbol{T}_\lambda(t_0, t_0)$ has to be the identity matrix. Per definition, it is also possible to link transition matrices

$$\boldsymbol{\lambda}(t_f) = \underbrace{\boldsymbol{T}_\lambda(t_f, t) \cdot \boldsymbol{T}_\lambda(t, t_0)}_{\boldsymbol{T}_\lambda(t_f, t_0)}\,\boldsymbol{\lambda}(t_0)$$

and to go backwards in time

$$\boldsymbol{\lambda}(t) = \boldsymbol{T}_\lambda(t, t_f)\,\boldsymbol{\lambda}(t_f) \tag{5.19}$$

It is derived using the Laplace transform (section A.5.3) of the equation for $\boldsymbol{\lambda}$ (eqn. (5.10))

$$s\,\bar{\boldsymbol{\lambda}}(s) - \boldsymbol{\lambda}(0) = -\boldsymbol{P}^T\,\bar{\boldsymbol{\lambda}}(s)$$
$$\bar{\boldsymbol{\lambda}}(s) = \left[\left(s\boldsymbol{I} + \boldsymbol{P}^T\right)^{-1}\right]\,\boldsymbol{\lambda}(0)$$

Here, $\boldsymbol{I}$ denotes the identity matrix, in this case of dimension 6x6. The inverse Laplace transform yields

$$\boldsymbol{\lambda}(t) = \mathscr{L}^{-1}\left\{\left(s\,\boldsymbol{I} + \boldsymbol{P}^T\right)^{-1}\right\}\Bigg|_0^t \boldsymbol{\lambda}(0) = \mathscr{L}^{-1}\left\{\left(s\,\boldsymbol{I} + \boldsymbol{P}^T\right)^{-1}\right\}\Bigg|_{t_f}^t \boldsymbol{\lambda}(t_f) \tag{5.20}$$

A comparison with eqn. (5.19) yields the desired transition matrix

$$\boldsymbol{T}_\lambda(t, t_f) = \mathscr{L}^{-1}\left\{\left(s\,\boldsymbol{I} + \boldsymbol{P}^T\right)^{-1}\right\}\Bigg|_{t_f}^t$$

A note on calculating this matrix should be made here. As of today, the inverse Laplace transform function in symbolic math software like MATLAB or Wolfram Mathematica does not support the time for the lower boundary to be other than zero. Therefore, to calculate $\boldsymbol{T}_\lambda(t, t_f)$, a transformation from the interval $[t_f, t]$ to $[0, t_f - t]$ has to be made. For example in Wolfram Mathematica, this reads

T$_\lambda$=InverseLaplaceTransform[Inverse[s*IdentityMatrix[6] + Transpose[P]], s, t - tf]

which yields

$$
\boldsymbol{T}_\lambda(t, t_f) = \begin{pmatrix}
1 & 0 & 0 & 0 & 0 & 0 \\
0 & 1 & 0 & 0 & 0 & 0 \\
0 & 0 & 1 & 0 & 0 & 0 \\
t_f - t & 0 & 0 & 1 & 0 & 0 \\
0 & t_f - t & 0 & 0 & 1 & 0 \\
0 & 0 & t_f - t & 0 & 0 & 1
\end{pmatrix}
\tag{5.21}
$$

Inserting $\boldsymbol{\lambda}(t) = \boldsymbol{T}_\lambda(t, t_f)\, \boldsymbol{\lambda}(t_f)$ into the control equations (eqns. (5.7) and (5.8)) and using eqn. (5.12) for $\boldsymbol{\lambda}(t_f)$ yields

$$
\boldsymbol{u}_p = -\boldsymbol{W}_p^{-1}\, \boldsymbol{Q}^T\, \boldsymbol{T}_\lambda(t, t_f)\, \boldsymbol{S}\, \boldsymbol{\xi}(t_f)
\tag{5.22}
$$

$$
\boldsymbol{u}_e = -\boldsymbol{W}_e^{-1}\, \boldsymbol{Q}^T\, \boldsymbol{T}_\lambda(t, t_f)\, \boldsymbol{S}\, \boldsymbol{\xi}(t_f)
\tag{5.23}
$$

To eliminate $\boldsymbol{\xi}(t_f)$, the state $\boldsymbol{\xi}$ from eqn. (5.3) has to be also expressed using the transition matrix approach. This can be achieved like before by applying the Laplace transform[3], using the state at time t as the lower boundary

$$
s\, \bar{\boldsymbol{\xi}}(s) - \boldsymbol{\xi}(0) = \boldsymbol{P}\, \bar{\boldsymbol{\xi}}(s) + \boldsymbol{Q}\, \left(\bar{\boldsymbol{u}}_p(s) - \bar{\boldsymbol{u}}_e(s) \right)
$$

$$
\bar{\boldsymbol{\xi}}(s) = (s\boldsymbol{I} - \boldsymbol{P})^{-1}\, \boldsymbol{\xi}(0) + (s\boldsymbol{I} - \boldsymbol{P})^{-1}\, \boldsymbol{Q}\, \left(\bar{\boldsymbol{u}}_p(s) - \bar{\boldsymbol{u}}_e(s) \right)
$$

Applying the inverse Laplace transform, this time involving the convolution theorem, yields the state at time t_f

$$
\boldsymbol{\xi}(t) = \boldsymbol{T}_\xi(t, 0)\, \boldsymbol{\xi}(0)\ +\ \int_0^t \boldsymbol{T}_\xi(\tau, 0)\, \boldsymbol{Q}\, \boldsymbol{u}_p(\tau)\, \mathrm{d}\tau - \int_0^t \boldsymbol{T}_\xi(\tau, 0)\, \boldsymbol{Q}\, \boldsymbol{u}_e(\tau)\, \mathrm{d}\tau
\tag{5.24}
$$

with $\boldsymbol{T}_\xi(t, 0) = \mathscr{L}^{-1}\left\{ (s\, \boldsymbol{I} - \boldsymbol{P})^{-1} \right\}\Big|_0^t$ and $\boldsymbol{T}_\xi(\tau, 0) = \mathscr{L}^{-1}\left\{ (s\, \boldsymbol{I} - \boldsymbol{P})^{-1} \right\}\Big|_0^\tau$.

Like in eqn. (5.20), eqn. (5.24) can be reformulated to include $\boldsymbol{\xi}(t_f)$:

---

[3]See also eqn. (A.20) for reference.

$$\boldsymbol{\xi}(t_f) = \boldsymbol{T}_\xi(t_f,t)\,\boldsymbol{\xi}(t) + \int\limits_t^{t_f} \boldsymbol{T}_\xi(t_f,\tau)\,\boldsymbol{Q}\,\boldsymbol{u}_p(\tau)\,\mathrm{d}\tau - \int\limits_t^{t_f} \boldsymbol{T}_\xi(t_f,\tau)\,\boldsymbol{Q}\,\boldsymbol{u}_e(\tau)\,\mathrm{d}\tau \qquad (5.25)$$

where $\boldsymbol{T}_\xi(t_f,t) = \mathscr{L}^{-1}\left\{(s\,\boldsymbol{I} - \boldsymbol{P})^{-1}\right\}\Big|_t^{t_f}$ and $\boldsymbol{T}_\xi(t_f,\tau) = \mathscr{L}^{-1}\left\{(s\,\boldsymbol{I} - \boldsymbol{P})^{-1}\right\}\Big|_\tau^{t_f}$.

Analog to the calculation of $\boldsymbol{T}_\lambda(t,t_f)$ before, the input for $\boldsymbol{T}_\xi(t_f,t)$ using Wolfram Mathematica reads

$\boldsymbol{\mathrm{T}}_\xi$=InverseLaplaceTransform[Inverse[s*IdentityMatrix[6] - P], s, tf - t]

which yields

$$\boldsymbol{T}_\xi(t_f,t) = \begin{pmatrix} 1 & 0 & 0 & t_f - t & 0 & 0 \\ 0 & 1 & 0 & 0 & t_f - t & 0 \\ 0 & 0 & 1 & 0 & 0 & t_f - t \\ 0 & 0 & 0 & 1 & 0 & 0 \\ 0 & 0 & 0 & 0 & 1 & 0 \\ 0 & 0 & 0 & 0 & 0 & 1 \end{pmatrix} \qquad (5.26)$$

With the control eqns. (5.22) and (5.23), eqn. (5.25) reduces to

$$\boldsymbol{\xi}(t_f) = \boldsymbol{T}_\xi(t_f,t)\,\boldsymbol{\xi}(t) + (\boldsymbol{B}_e - \boldsymbol{B}_p)\,\boldsymbol{S}\,\boldsymbol{\xi}(t_f) \qquad (5.27)$$

using this terms as a shorthand:

$$\boldsymbol{B}_e = \int\limits_t^{t_f} \boldsymbol{T}_\xi(t_f,\tau)\,\boldsymbol{Q}\,\boldsymbol{W}_e^{-1}\,\boldsymbol{Q}^T\,\boldsymbol{T}_\lambda(\tau,t_f)\,\mathrm{d}\tau$$

$$\boldsymbol{B}_p = \int\limits_t^{t_f} \boldsymbol{T}_\xi(t_f,\tau)\,\boldsymbol{Q}\,\boldsymbol{W}_p^{-1}\,\boldsymbol{Q}^T\,\boldsymbol{T}_\lambda(\tau,t_f)\,\mathrm{d}\tau$$

Collecting $\boldsymbol{\xi}(t_f)$ on the left side of eqn. (5.27) yields

$$\boldsymbol{\xi}(t_f) = \left((\boldsymbol{I} + \boldsymbol{B}_p - \boldsymbol{B}_e)\,\boldsymbol{S}\right)^{-1} \boldsymbol{T}_\xi(t_f,t)\,\boldsymbol{\xi}(t)$$

which is finally inserted into eqns. (5.22) and (5.23) to yield the controls

$$\boldsymbol{u}_p = -\boldsymbol{W}_p^{-1}\,\boldsymbol{Q}^T\,\boldsymbol{T}_\lambda(t,t_f)\,\boldsymbol{S}\left((\boldsymbol{I} + \boldsymbol{B}_p - \boldsymbol{B}_e)\,\boldsymbol{S}\right)^{-1} \boldsymbol{T}_\xi(t_f,t)\,\boldsymbol{\xi}(t)$$

$$\boldsymbol{u}_e = -\boldsymbol{W}_e^{-1}\,\boldsymbol{Q}^T\,\boldsymbol{T}_\lambda(t,t_f)\,\boldsymbol{S}\left((\boldsymbol{I} + \boldsymbol{B}_p - \boldsymbol{B}_e)\,\boldsymbol{S}\right)^{-1} \boldsymbol{T}_\xi(t_f,t)\,\boldsymbol{\xi}(t)$$

Inserting transition matrices (eqns. (5.21) and (5.26)) into the controls (which represent the accelerations of the aircraft) and multiplying all the matrices leads to the useful algebraic solution

for the pursuer: (5.28)

$$\ddot{x}_p = \frac{3\ a_{p,xy}^2\ (t-t_f)[x_p - x_e + (t-t_f)(\dot{x}_e - \dot{x}_p)]}{(a_{e,xy}^2 - a_{p,xy}^2)(t-t_f)^3 + 3\ s_{xy}^2}$$

$$\ddot{y}_p = \frac{3\ a_{p,xy}^2\ (t-t_f)[y_p - y_e + (t-t_f)(\dot{y}_e - \dot{y}_p)]}{(a_{e,xy}^2 - a_{p,xy}^2)(t-t_f)^3 + 3\ s_{xy}^2}$$

$$\ddot{z}_p = \frac{3\ a_{p,z}^2\ (t-t_f)[z_p - z_e + (t-t_f)(\dot{z}_e - \dot{z}_p)]}{(a_{e,z}^2 - a_{p,z}^2)(t-t_f)^3 + 3\ s_z^2}$$

for the evader: (5.29)

$$\ddot{x}_e = \frac{3\ a_{e,xy}^2\ (t-t_f)[x_p - x_e + (t-t_f)(\dot{x}_e - \dot{x}_p)]}{(a_{e,xy}^2 - a_{p,xy}^2)(t-t_f)^3 + 3\ s_{xy}^2}$$

$$\ddot{y}_e = \frac{3\ a_{e,xy}^2\ (t-t_f)[y_p - y_e + (t-t_f)(\dot{y}_e - \dot{y}_p)]}{(a_{e,xy}^2 - a_{p,xy}^2)(t-t_f)^3 + 3\ s_{xy}^2}$$

$$\ddot{z}_e = \frac{3\ a_{e,z}^2\ (t-t_f)[z_p - z_e + (t-t_f)(\dot{z}_e - \dot{z}_p)]}{(a_{e,z}^2 - a_{p,z}^2)(t-t_f)^3 + 3\ s_z^2}$$

This can be written more succinctly:

$$\boldsymbol{u}_i = 3\ (t-t_f)\begin{pmatrix} \frac{a_{i,xy}^2}{N_{xy}} & 0 & 0 & \frac{a_{i,xy}^2(t-t_f)}{N_{xy}} & 0 & 0 \\ 0 & \frac{a_{i,xy}^2}{N_{xy}} & 0 & 0 & \frac{a_{i,xy}^2(t-t_f)}{N_{xy}} & 0 \\ 0 & 0 & \frac{a_{i,z}^2}{N_z} & 0 & 0 & \frac{a_{i,z}^2(t-t_f)}{N_z} \end{pmatrix}\boldsymbol{\xi}(t) =: \boldsymbol{H}_i(t)\ \boldsymbol{\xi}(t)$$

where $i = \{p, e\}$, $N_{xy} = (a_{e,xy}^2 - a_{p,xy}^2)(t-t_f)^3 + 3\ s_{xy}^2$, $N_z = (a_{e,z}^2 - a_{p,z}^2)(t-t_f)^3 + 3\ s_z^2$.

This expression is linked to the elements of matrix $\boldsymbol{K}$ in eqn. (5.13) through eqns. (5.14) and (5.15):

$$\boldsymbol{u}_i = -\boldsymbol{W}_i^{-1}\ \boldsymbol{Q}^T\ \boldsymbol{K}(t)\ \boldsymbol{\xi}(t) = \boldsymbol{H}_i(t)\ \boldsymbol{\xi}(t)$$

$$\Rightarrow\ \boldsymbol{K}(t) = -\left(\boldsymbol{Q}^T\right)^{-1}\ \boldsymbol{W}_i\ \boldsymbol{H}_i(t)$$

The eqns. (5.28) to (5.29) provide the accelerations for the pursuer and the evader. Assuming constant mass, Newton's second law provides the corresponding forces. The next section will review the physical constraint of these forces and how they affect the controls.

5.2 Equations of Motion

The differential game method for pursuit-evasion discussed in the previous section is built only on the kinematic quantities of the system. As there are no restrictions on the movement of the two players, the usefulness of this method is limited. For application, it has to be extended and subjected to real-world limitations. In particular, the governing

values of the differential game system, relative distance and relative speed, have to undergo further scrutiny. These parameters have to be determined by a suitable kinetic model incorporating the forces acting on both players. This approach also includes the possibility to get a handle on each player's predicted action, as will be shown later.

There are many dynamic models for air vehicles described in literature, e.g. [112] [113] [114] [115] , which vary in their number of degrees of freedom (DOF). A model with more DOFs is able to represent real vehicle behavior more accurately, but is also more demanding on the simulation setup.

The control equations (eqns. (5.28) and (5.29)) derived in the last section provide three accelerations in an inertial reference frame for each air vehicle. These have to be incorporated in to the dynamic model, which at least has to deal with the four governing forces of flight: lift, weight, thrust and drag. These forces in turn have to be subjected to modeling as well.

A suitable model for the thrust is provided by the equation [116]

$$T = T_0 \left(\frac{v}{v_0}\right)^{n_v} \left(\frac{\rho}{\rho_0}\right)^{n_\rho} \tag{5.30}$$

where T is the achievable engine thrust, v the airspeed and ρ the air density ρ. The latter depends on the altitude of the aircraft (Fig. A.14). This equation describes the dependency of thrust on speed and altitude in the vicinity of an arbitrary reference point, denoted by the index 0.

The parameters n_v and n_ρ are constants depending on the type of engine[4]. In the following, small GA-type aeroplanes with a single piston engine are of interest. For such an engine, output power P is in good approximation independent of airspeed [116]. With $P = T \cdot v$ at constant air density (i.e. altitude), the parameter n_v has to be -1 for P to be constant. The parameter n_ρ , which describes the increase/decrease of thrust with changing altitude, is within 0.6 to 1 for air-breathing engines. For a piston engine, the influence of ρ is taken into account by $n_\rho = 0.75$ [116].

Next the magnitude of the drag, lift and weight force of the aircraft is determined by

$$D = c_D \; A \; \frac{\rho \; v^2}{2} \tag{5.31}$$

$$L = c_L \; A \; \frac{\rho \; v^2}{2} \tag{5.32}$$

$$W = m \; g \tag{5.33}$$

where c_D and c_L are the coefficients of drag and list, respectively. Both are functions of the angle of attack α [116]. A useful chart showing the relationship between c_L, c_D and α is called the *drag-polar* plot (Fig. A.10)). The area A is a characteristic measure of the aircraft (usually wing area). The quantity $(\rho \; v^2/2)$ is called the *dynamic pressure*,

---

[4]For values of n_v and n_ρ for various types of propulsion, see Fig. A.9 in Appendix.

where v is the airspeed and ρ is the air density, respectively. The mass of the aircraft is denoted by m.

The dynamic model should produce avoidance maneuvers which adhere to *coordinated flight*, in which the aircraft is flying with a zero sideslip (β=0, Fig. A.6). This condition is preferred because it induces less drag on the aircraft and is more comfortable to the occupants [113] [117].

The dynamic model for β=0 is shown in Fig. 5.2. Because of that, the axes x_A and x_B are both in the aircraft's symmetry plane. The direction of the thrust vector $\boldsymbol{T}$ is along the aircraft's longitudinal axis x_B and its magnitude is given by eqn. (5.30). The lift vector $\boldsymbol{L}$ is perpendicular and the drag vector $\boldsymbol{D}$ is antiparallel to the x_A-axis [116]. The weight vector $\boldsymbol{W}$ is parallel to the z_I-axis. In this simplified model, wind is zero.
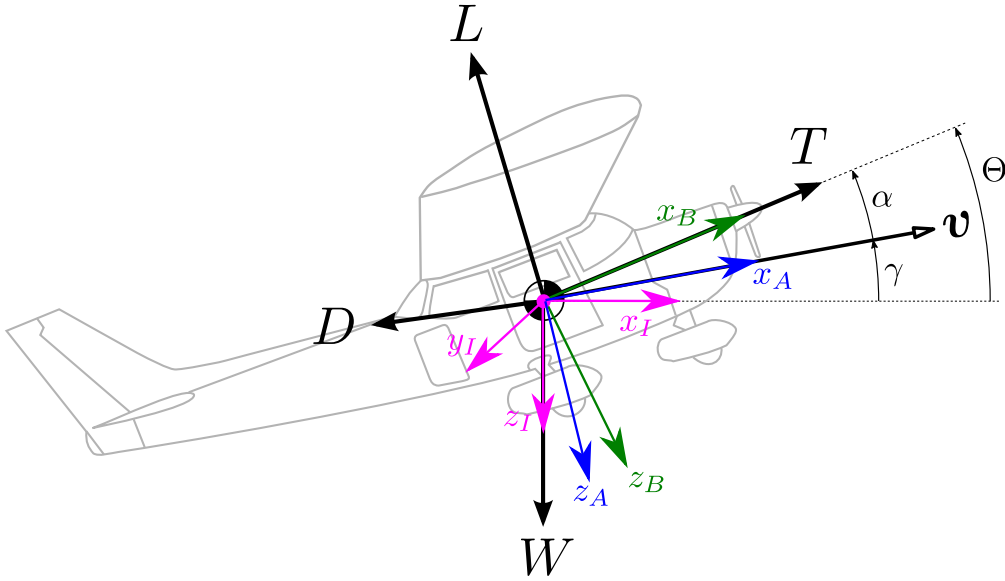
Figure 5.2: Dynamic model for aircraft motion. The four basic forces acting on an aeroplane in flight: thrust, drag, weight, lift ($\boldsymbol{T}$, $\boldsymbol{D}$, $\boldsymbol{W}$, $\boldsymbol{L}$). The inertial, body-fixed and aerodynamic reference frames are denoted with the axis-sets $\{x_I,\ y_I,\ z_I\}$, $\{x_B,\ y_B,\ z_B\}$ and $\{x_A,\ y_A,\ z_A\}$, respectively. The transformation between these frames is described in section A.3. The angles γ, α and Θ are called the flight-path angle, angle of attack and pitch angle, respectively.

The aircraft is furthermore symmetric with respect to its vertical plane and has a negligible fuel consumption during the evasion maneuver, leading to a constant mass. Gyroscopic effects from the engine are neglected. A non-rotating flat-earth model is used for gravity along with a constant gravitational acceleration of g=9.81 m/s². The equation of motion for the center of gravity of the aircraft using the geometry in

Fig. 5.2 and eqn. (5.30) for the thrust vector yield

$$
m \begin{pmatrix} \ddot{x} \\ \ddot{y} \\ \ddot{z} \end{pmatrix} = \boldsymbol{R}_A^I \begin{pmatrix} -D \\ 0 \\ -L \end{pmatrix} + \boldsymbol{R}_B^I \begin{pmatrix} T \\ 0 \\ 0 \end{pmatrix} + \begin{pmatrix} 0 \\ 0 \\ W \end{pmatrix} =
$$

$$
= \boldsymbol{R}_A^I \left[\begin{pmatrix} -D \\ 0 \\ -L \end{pmatrix} + \boldsymbol{R}_B^A \begin{pmatrix} T \\ 0 \\ 0 \end{pmatrix} \right] + \begin{pmatrix} 0 \\ 0 \\ mg \end{pmatrix} \qquad (5.34)
$$

This equation describes a model with three DOF. The expressions for $\ddot{x}$, $\ddot{y}$ and $\ddot{z}$ are the accelerations of the center of mass measured in the inertial reference frame. The transformation matrices $\boldsymbol{R}_A^I$ and $\boldsymbol{R}_B^A$ between the reference frames depicted in Fig. 5.2 are given by eqns. (A.5) and (A.9), respectively. With $\beta = 0$, these matrices simplify to

$$
\boldsymbol{R}_A^I = \begin{pmatrix} c\gamma\ c\chi & c\chi\ s\gamma\ s\mu - c\mu\ s\chi & c\mu\ c\chi\ s\gamma + s\mu\ s\chi \\ c\gamma\ s\chi & c\mu\ c\chi + s\gamma\ s\mu\ s\chi & c\mu\ s\gamma\ s\chi - c\chi\ s\mu \\ -s\gamma & c\gamma\ s\mu & c\gamma\ c\mu \end{pmatrix}, \quad \boldsymbol{R}_B^A = \begin{pmatrix} c\alpha & 0 & s\alpha \\ 0 & 1 & 0 \\ -s\alpha & 0 & c\alpha \end{pmatrix}
$$

where $\boldsymbol{c}$ and $\boldsymbol{s}$ is shorthand for the cos and sin-functions. The angles χ, γ and μ are called the flight-path azimuth, flight-path and bank angle, respectively. In typical flight conditions and for $\beta = 0$, the bank angle μ is nearly the same as the roll angle Φ [113]. A derivation of this claim is provided by section A.4. However in the following, the bank angle μ in matrix $\boldsymbol{R}_A^I$ will not be exchanged with Φ to remain consistent with the coordinate transformation shown in section A.3.1.

Eqn. (5.34) yields

$$
m\ \ddot{x} = (T\cos\alpha - D)\cos\gamma\cos\chi - (T\sin\alpha + L)(\sin\gamma\cos\mu\cos\chi + \sin\mu\sin\chi) \qquad (5.35)
$$
$$
m\ \ddot{y} = (T\cos\alpha - D)\cos\gamma\sin\chi - (T\sin\alpha + L)(\sin\gamma\cos\mu\sin\chi - \sin\mu\cos\chi) \qquad (5.36)
$$
$$
m\ \ddot{z} = -(T\cos\alpha - D)\sin\gamma - (T\sin\alpha + L)\cos\gamma\ \cos\mu + m\ g \qquad (5.37)
$$

Furthermore, the velocity vector in the inertial frame reads

$$
\begin{pmatrix} \dot{x} \\ \dot{y} \\ \dot{z} \end{pmatrix} = \boldsymbol{R}_A^I \begin{pmatrix} v \\ 0 \\ 0 \end{pmatrix} = \begin{pmatrix} v\ \cos\gamma\ \cos\chi \\ v\ \cos\gamma\ \sin\chi \\ -v\ \sin\gamma \end{pmatrix} \qquad (5.38)
$$

where v is the airspeed of the aeroplane. Time differentiation yields the acceleration

$$
\begin{pmatrix} \ddot{x} \\ \ddot{y} \\ \ddot{z} \end{pmatrix} = \begin{pmatrix} \dot{v}\ \cos\gamma\ \cos\chi - v\ \dot{\gamma}\ \sin\gamma\ \cos\chi - v\ \dot{\chi}\ \cos\gamma\ \sin\chi \\ \dot{v}\ \cos\gamma\ \sin\chi - v\ \dot{\gamma}\ \sin\gamma\ \sin\chi + v\ \dot{\chi}\ \cos\gamma\ \cos\chi \\ -\dot{v}\ \sin\gamma - v\ \dot{\gamma}\ \cos\gamma \end{pmatrix} \qquad (5.39)
$$

To later apply restrictions to the control algorithm presented in section 5.1 and for trajectory calculation, it is useful to determine the time derivatives of v, χ and γ. For

this task it is very useful to transform the components in eqn. (5.39) with the matrix

$$\boldsymbol{R}_I^M := \boldsymbol{R_2}(\gamma)\,\boldsymbol{R_1}(\chi) = \begin{pmatrix} \cos\gamma\,\cos\chi & \cos\gamma\,\sin\chi & -\sin\gamma \\ -\sin\chi & \cos\chi & 0 \\ \cos\chi\,\sin\gamma & \sin\gamma\,\sin\chi & \cos\gamma \end{pmatrix}$$

where $\boldsymbol{R_1}(\chi)$ and $\boldsymbol{R_2}(\gamma)$ are both part of the coordinate transformation from the inertial to the aerodynamic frame and are provided by eqns. (A.1) and (A.2), respectively.

The result is

$$\boldsymbol{R}_I^M \begin{pmatrix} \ddot{x} \\ \ddot{y} \\ \ddot{z} \end{pmatrix} = \begin{pmatrix} \dot{v} \\ v\,\dot{\chi}\,\cos\gamma \\ -v\,\dot{\gamma} \end{pmatrix} \tag{5.40}$$

Taking the expressions for $\ddot{x}$, $\ddot{y}$ and $\ddot{z}$ from the eqns. (5.35), (5.36) and (5.37) and also multiplying these with $\boldsymbol{R}_I^M$ yields

$$\boldsymbol{R}_I^M \begin{pmatrix} \ddot{x} \\ \ddot{y} \\ \ddot{z} \end{pmatrix} = \frac{1}{m} \begin{pmatrix} T\cos\alpha - D - mg\sin\gamma \\ (T\sin\alpha + L)\,\sin\mu \\ -(T\sin\alpha + L)\cos\mu + mg\cos\gamma \end{pmatrix}$$

The right hand sides of this equation and eqn. (5.40) have to be the same, resulting in the useful equations

$$m\,\dot{v} = T\cos\alpha - D - mg\sin\gamma \tag{5.41}$$
$$m\,v\,\cos\gamma\,\dot{\chi} = (T\sin\alpha + L)\sin\mu \tag{5.42}$$
$$m\,v\,\dot{\gamma} = (T\sin\alpha + L)\cos\mu - mg\cos\gamma \tag{5.43}$$

These differential equations provide the basis to solve eqn. (5.38) for the positions x, y and z and to plot the trajectory. In the following, the eqns. (5.35), (5.36) and (5.37) will be used to include the optimal control derived in section 5.1.

5.2.1 Control input equations

In oder to render the eqns. (5.35), (5.36) and (5.37) suitable for the optimal control algorithm (eqns. (5.28) and (5.28), respectively), they have to express the terms $(T\cos\alpha - D)$, $(T\sin\alpha + L)$ and μ in dependence of the accelerations $\ddot{x}$, $\ddot{y}$ and $\ddot{z}$. These terms are then inserted into eqns. (5.41), (5.42) and (5.43) to yield differential equations in $\dot{v}$, $\dot{\chi}$ and $\dot{\gamma}$.

To obtain the term $(T\cos\alpha - D)$, eqn. (5.35) is multiplied by $\cos\chi$ and eqn. (5.36) by $\sin\chi$:

$$m\ddot{x}\cos\chi = (T\cos\alpha - D)\cos\gamma\cos^2\chi - (T\sin\alpha + L)\left(\sin\gamma\cos\mu\,\cos^2\chi + \sin\mu\sin\chi\cos\chi\right)$$

$$m\ddot{y}\sin\chi = (T\cos\alpha - D)\cos\gamma\sin^2\chi - (T\sin\alpha + L)\left(\sin\gamma\,\cos\mu\sin^2\chi - \sin\mu\sin\chi\cos\chi\right)$$

The addition of these equations simplifies to

$$m\,(\ddot{x}\,\cos\chi + \ddot{y}\,\sin\chi) = (T\cos\alpha - D)\cos\gamma - (T\sin\alpha + L)\cos\mu\sin\gamma \qquad (5.44)$$

Next, this equation is multiplied by $\cos\gamma$ and eqn. (5.37) by $(-\sin\gamma)$:

$$m\,(\ddot{x}\,\cos\chi + \ddot{y}\,\sin\chi)\,\cos\gamma = (T\cos\alpha - D)\cos^2\gamma - (T\sin\alpha + L)\cos\mu\,\sin\gamma\,\cos\gamma$$

$$-m\,\ddot{z}\sin\gamma = (T\cos\alpha - D)\sin^2\gamma + (T\sin\alpha + L)\cos\gamma\,\cos\mu\,\sin\gamma - mg\sin\gamma$$

The addition of these equations yields

$$m\,[(\ddot{x}\,\cos\chi + \ddot{y}\,\sin\chi)\,\cos\gamma - \ddot{z}\,\sin\gamma] = (T\cos\alpha - D) - mg\,\sin\gamma$$

Reformulation leads to the first desired expression

$$T\cos\alpha - D = m\,[(\ddot{x}\,\cos\chi + \ddot{y}\,\sin\chi)\cos\gamma + (g - \ddot{z})\sin\gamma] \qquad (5.45)$$

To obtain the next expression, $(T\sin\alpha - L)$, the first three steps from the previous procedure are repeated, yielding again eqn. (5.44). However this time, eqn. (5.44) has to be multiplied by $\sin\gamma$ and eqn. (5.37) by $\cos\gamma$:

$$m(\ddot{x}\,\cos\chi + \ddot{y}\,\sin\chi)\,\sin\gamma = (T\cos\alpha - D)\sin\gamma\,\cos\gamma - (T\sin\alpha + L)\cos\mu\,\sin^2\gamma$$

$$m\ddot{z}\,\cos\gamma = -(T\cos\alpha - D)\sin\gamma\,\cos\gamma - (T\sin\alpha + L)\,\cos\mu\,\cos^2\gamma + mg\,\cos\gamma$$

The addition of these equations results in

$$m\,[(\ddot{x}\,\cos\chi + \ddot{y}\,\sin\chi)\,\sin\gamma + \ddot{z}\,\cos\gamma] = -(T\sin\alpha + L)\cos\mu + mg\,\cos\gamma$$

Reformulation leads to the second desired expression

$$T\sin\alpha + L = \frac{m}{\cos\mu}\Big[(g - \ddot{z})\cos\gamma - (\ddot{x}\,\cos\chi + \ddot{y}\,\sin\chi)\sin\gamma\Big] \qquad (5.46)$$

However, the bank angle μ has yet to be resolved for this expression to be useful. This is done by multiplying eqn. (5.35) by $\sin\chi$ and eqn. (5.36) by $\cos\chi$:

$$m\,\ddot{x}\,\sin\chi =$$
$$(T\cos\alpha - D)\cos\gamma\,\sin\chi\,\cos\chi - (T\sin\alpha + L)\big(\sin\gamma\,\cos\mu\,\sin\chi\,\cos\chi + \sin\mu\,\sin^2\chi\big)$$

$$m\,\ddot{y}\,\cos\chi =$$
$$(T\cos\alpha - D)\cos\gamma\,\sin\chi\,\cos\chi - (T\sin\alpha + L)\big(\sin\gamma\,\cos\mu\,\sin\chi\,\cos\chi - \sin\mu\,\cos^2\chi\big)$$

Subtracting the second from the first equation results in

$$m(\ddot{x}\,\sin\chi - \ddot{y}\,\cos\chi) = -(T\sin\alpha + L)\sin\mu$$

The term $(T \sin \alpha + L)$ from the right side of this equation is the same as the left side of eqn. (5.46). Equating this parts and solving for the bank angle μ leads to

$$\tan \mu = \frac{\ddot{x} \, \sin \chi - \ddot{y} \, \cos \chi}{(\ddot{x} \, \cos \chi + \ddot{y} \, \sin \chi \,) \sin \gamma + (\ddot{z} - g) \cos \gamma} \tag{5.47}$$

Inserting μ from this equation into eqn. (5.46) using $\cos(\arctan(\cdot)) = \frac{1}{\sqrt{1 + (\cdot)^2}}$ leads to an alternative expression for eqn. (5.46), which does not depend on μ:

$$T \sin \alpha + L = m \, \sqrt{\left[(\ddot{x} \, \cos \chi + \ddot{y} \, \sin \chi) \, \sin \gamma + (\ddot{z} - g) \cos \gamma \right]^2 + \left[\ddot{x} \, \sin \chi - \ddot{y} \, \cos \chi \right]^2} \tag{5.48}$$

The eqns. (5.45), (5.47) and (5.48), which are set by the optimal control (eqns. (5.28) and (5.29)), can now be inserted in eqns. (5.41), (5.42) and (5.43). The values for the thrust, bank angle and lift have to be subjected to limitations, discussed in the following.

5.3 Restrictions on the controls

So far, the control algorithm is blind to aerodynamic and structural limits of the aircraft and therefore might create commands leading to inadmissible attitudes and airspeeds. Thrust is varied and limited by multiplying T_0 in eqn. (5.30) with a throttle factor η, which is defined in the interval $[0, 1]$. A analogous limitation can be applied to the limits of the bank angle μ. For normal flight operations, μ should not exceed the interval $[-25°, 25°\,]$, which will be used in the following as a safety measure.

To calculate the limitations on the lift L, it is useful to use the ratio of lift to weight, called the *load factor* $n = L/W$. Calculation and experimental evaluation of the load factor provides the basis to determine the permissible flight regime of any aircraft. The borders of this regime, shaped by the aerodynamic and structural limits, are called the *maneuvering envelope*. Fig. 5.3 depicts the aircraft limit load factor as a function of airspeed (v-n diagram) for the *normal category* [118], which represent most of the aircraft in the small aeroplane category (section 1.1).
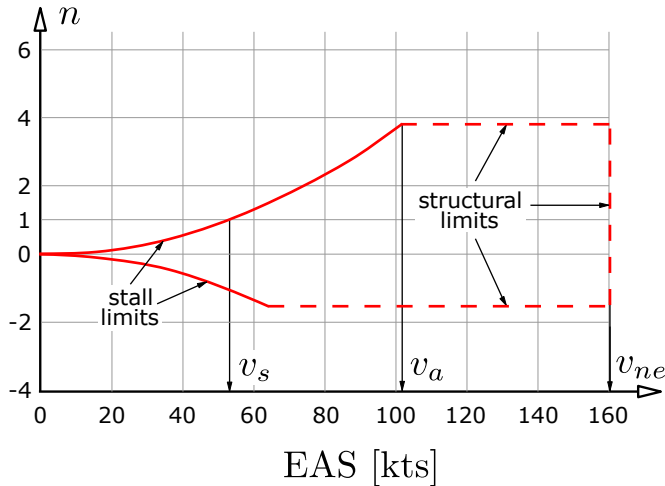
Figure 5.3: The v–n diagram for a normal category aircraft (flaps up), derived from Table A.2 and [119]. The load factor n is 1 for straight and level flight. The term EAS refers to the *equivalent airspeed*, which is the airspeed at sea level at which the dynamic pressure is the same as the dynamic pressure at the true airspeed (TAS). The speeds v_a and v_{ne} refer to the *maneuvering speed* and the *never-exceed speed*, respectively. The speed v_s is the *stall speed* for n=1.

The maximum positive load factor for speeds lower than v_a is determined by the stall limit, which depends on the maximum coefficient of lift $c_{L,\text{max}}$ (eqn. (5.32)) the aircraft's wing is capable to provide during flight.

The limits for n and v at airspeeds higher than v_a are determined by the structural integrity limits of the plane. The load factors for different categories of aircraft are regulated by the FAA, which for the *normal* category of aircraft prescribe a maximum positive load factor of at least 3.8 [119]. This load factor must not be exceeded during flight to avoid damage to the airplane. The limit for negative load factors[5] is more stringent than for positive load factors. For the normal category, the aircraft has to at least withstand a negative load factor 0.4 times of the maximum positive load factor.

The simulation results presented in the next section are based upon the assertion that both the evader and pursuer aircraft are Cessna 172S's. In its aerodynamic and structural limits, this aircraft's characteristics [120] are representative for the small aeroplane category. In section 1.1, aircraft under this category were identified to be most often involved in midair collisions.

5.3.1 Trajectory calculation

The path of both the pursuer and the evader is calculated with one numerical integration, involving 12 differential equations of first order and 12 accompanying boundary conditions.

First, the expressions given by the right sides of eqns. (5.45), (5.47) and (5.48) are evaluated for the pursuer and the evader. In these expressions, the second derivatives for the pursuer ($\ddot{x}_p$, $\ddot{y}_p$, $\ddot{z}_p$) and the evader ($\ddot{x}_e$, $\ddot{y}_e$, $\ddot{z}_e$) are the right hand sides of eqns. (5.28) and (5.29), which represent the optimal control.

Next, the values for T, μ and L are subjected to the limits discussed in the previous section. Because the value for the commanded lift L can not be calculated explicitly, it is estimated using the expression $(T \sin \alpha + L)$ (eqn. (5.48)). Because the thrust T

---

[5]for example occurring during a pull-down maneuver

is only about 20% of the lift for the simulated Cessna 172S aircraft (Table A.2) and the absolute value of the angle of attack α is lower than 15° (Fig. A.10), the value of the term $(T \sin \alpha)$ can be neglected[6] $(T \sin \alpha \ll L)$. From this estimated value of the commanded lift force, the corresponding load factor $n = L/W$ can be evaluated and limited if it exceeds the maneuvering envelope (Fig. 5.3). With the estimated value for L and the drag-polar plot (Fig. A.10), the coefficients of lift and drag (c_L and c_D) and the angle of attack α can be worked out using eqns. (5.31) and (5.32).

This provides the means to calculate the derivatives of v, χ and γ (from eqns. (5.41), (5.42) and (5.43), respectively)

for the pursuer:

$$\dot{v}_p = \frac{1}{m_p} (T_p \cos \alpha_p - D_p) - g \sin \gamma_p$$

$$\dot{\chi}_p = \frac{(T_p \sin \alpha_p + L_p) \sin \mu_p}{m \, v_p \, \cos \gamma_p}$$

$$\dot{\gamma}_p = \frac{\cos \mu_p}{m \, v_p} (T_p \sin \alpha_p + L_p) - \frac{g}{v_p} \cos \gamma_p$$

for the evader:

$$\dot{v}_e = \frac{1}{m_e} (T_e \cos \alpha_e - D_e) - g \sin \gamma_e$$

$$\dot{\chi}_e = \frac{(T_e \sin \alpha_e + L_e) \sin \mu_e}{m \, v_e \, \cos \gamma_e}$$

$$\dot{\gamma}_e = \frac{\cos \mu_e}{m \, v_e} (T_e \sin \alpha_e + L_e) - \frac{g}{v_e} \cos \gamma_e$$

The trajectories of the pursuer and the evader can be influenced by choosing one or more of the equations for $\dot{v}$, $\dot{\gamma}$ and $\dot{\chi}$ to be zero. For example, if all of these quantities are set to zero for the pursuer, its trajectory will resemble an aircraft which has not recognized the evader (i.e. ownship) and maintains speed, flight-path azimuth and flight-path angle. This represents a realistic behaviour considering the main contributing factor in midair collisions: a breakdown of see-and-avoid (Fig. 1.8). It is vice versa also possible to set some of these derivatives for the evader to zero, in order to only produce trajectories which only avoid the other aircraft in a vertical or horizontal way (setting $\dot{\chi}_e$ or $\dot{\gamma}_e$ to zero, respectively). Vertical maneuvers mimic the avoidance algorithm used by the TCAS II system (Table 2.1), whereas horizontal maneuvers are compliant to the rules of the air [1] (section 1.1).

The components of the velocity vector in the inertial frame (eqn. (5.38)) conclude the 12 first-order differential equations for the system. These are

for the pursuer:

$$\dot{x}_p = v_p \cos \gamma_p \, \cos \chi_p$$
$$\dot{y}_p = v_p \cos \gamma_p \, \sin \chi_p$$
$$\dot{z}_p = -v_p \sin \gamma_p$$

for the evader:

$$\dot{x}_e = v_e \cos \gamma_e \, \cos \chi_e$$
$$\dot{y}_e = v_e \cos \gamma_e \, \sin \chi_e$$
$$\dot{z}_e = -v_e \sin \gamma_e$$

The corresponding 12 boundary equations are defined at $t = t_0 = 0$ at the begin of an encounter

---

[6] $T \sin \alpha \approx 0.2 \, L \cdot \sin 15° \approx 0.05 \, L$

<u>for the pursuer:</u>

start speed and attitude

$$v_p(0) = v_{p,0} \quad \chi_p(0) = \chi_{p,0} \quad \gamma_p(0) = \gamma_{p,0}$$

start position (inertial frame)

$$x_p(0) = x_{p,0} \quad y_p(0) = y_{p,0} \quad z_p(0) = z_{p,0}$$

<u>for the evader:</u>

start speed and attitude

$$v_e(0) = v_{e,0} \quad \chi_e(0) = \chi_{e,0} \quad \gamma_e(0) = \gamma_{e,0}$$

start position (inertial frame)

$$x_e(0) = x_{e,0} \quad y_e(0) = y_{e,0} \quad z_e(0) = z_{e,0}$$

Finally, the resulting system of differential equations is numerically integrated with respect to time to yield $x(t)$, $y(t)$, $z(t)$, $v(t)$, $\chi(t)$ and $\gamma(t)$ for the pursuer and the evader, respectively.

5.4 Simulation Results

This section presents five example evasion trajectories from the algorithm derived in the previous sections. The origin of the earth-fixed inertial reference system used to describe the movements of the pursuer and the evader is shown in Fig. 5.4. In all
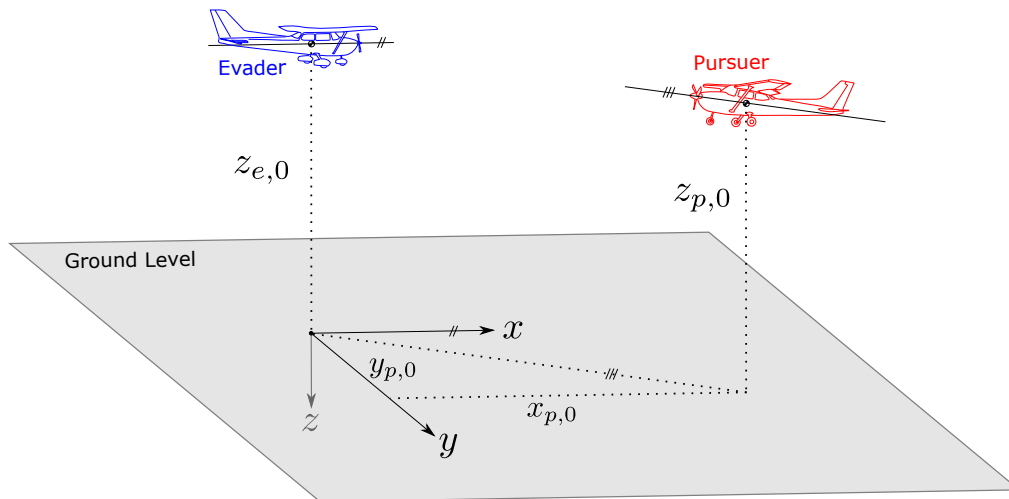
Figure 5.4: Start position of the simulation and the coordinate system used to describe the movements

collision scenarios presented in the following, the evader starts at $x_{e,0} = 0$ m, $y_{e,0} = 0$ m and $z_{e,0} = -600$ m. In this coordinate system, the latter represents the altitude above sea level. It is chosen to reflect the altitude range where most midair collision occur (Fig. 1.4).

The pursuer, in order to mimic a breakdown of the see-and-avoid principle (section 1.1), does not recognize the evader (i.e. the ownship) and maintains course, speed and altitude ($\dot{v}_p = \dot{\chi}_p = \dot{\gamma}_p = 0$). Furthermore, both the evader and the pursuer start in level flight ($\gamma_{p,0} = 0$ and $\gamma_{e,0} = 0$, respectively).

Aerodynamic and engine characteristics for both aircraft are taken from Cessna 172S data (section A.6). The near-sea level altitude of the scenarios allows the calculation of engine thrust (eqn. 5.30) to use a reference point at sea level (Table A.2). The air density ρ was determined using the ICAO standard atmosphere chart (Fig. A.14). For both the pursuer and the evader, the reference thrust T_0 (i.e. the throttle factor η) was held constant during the maneuver.

The elements of weighing matrices for the distance $\boldsymbol{S}$ (eqn. (5.5)) were set at $s_{xy} = 140$ and $s_z = 195$. The weighing matrices $\boldsymbol{W}_p$ and $\boldsymbol{W}_e$ (eqn. (5.6)) were set equal with $a_{p,xy} = a_{e,xy} = 3.8$ and $a_{p,z} = a_{e,z} = 7.6$ to imply the same maneuvering capabilities on the evader and the pursuer.

Table 5.1 lists the geometric and kinematic properties at the start of each scenario for the pursuer and the evader.

| | Scenario | | | | | | Scenario | | | | |
Evader	A	B	C	D	E	**Pursuer**	A	B	C	D	E
$x_{e,0}$ [m]	0	0	0	0	0	$x_{p,0}$ [m]	-200	2000	1770	1035	1035
$y_{e,0}$ [m]	0	0	0	0	0	$y_{p,0}$ [m]	-50	-50	680	965	-965
$z_{e,0}$ [m]	-600	-600	-600	-600	-600	$z_{p,0}$ [m]	-600	-600	-600	-600	-600
$v_{e,0}$ [m/s]	45	50	50	50	50	$v_{p,0}$ [m/s]	55	50	50	50	50
$\chi_{e,0}$ [°]	0	0	0	0	0	$\chi_{p,0}$ [°]	0	180	-135	-90	90
$\gamma_{e,0}$ [°]	0	0	0	0	0	$\gamma_{p,0}$ [°]	0	0	0	0	0

Table 5.1: Overview of the scenario conditions for the example evasion trajectories (Figs. 5.5 to 5.9). The pursuer's movement is restricted to rectilinear and level flight

Figs. 5.5 to 5.9 show the resulting trajectories based on these values. The evader was restricted to only perform a horizontal avoidance maneuver ($\dot{\gamma}_e = 0$) in the scenarios A to D. For scenario E, only vertical movement was allowed ($\dot{\chi}_e = 0$). The trajectories were acquired using a numerical integration function of Wolfram Mathematica.

In each of the figures, the pursuer's trajectory is depicted with a red line from the start position to the point of closest approach. For the evader, this point is depicted in blue on its trajectory, for the pursuer in red. Additionally, the evader's trajectory is plotted beyond that point with a dashed line. The numbers beside each trajectory refer to the time traveled in the scenario (in seconds).

Furthermore, crosses in blue and red show the points of closest approach for the evader and the pursuer, respectively, if the evader would not take evasive action. In every scenario, these points are at $t = 20$ seconds[7] and 50 meters apart. Therefore, the time horizon t_f for the optimal control (eqns. (5.28) and (5.29)) is *a priori* set to $t_f = 20$ seconds. For $t > t_f$, the signs of the terms $(t - t_f)$ in eqns. (5.28) and (5.29) reverse. As the Figs. 5.6 to 5.9 show, this produces a trajectory that curves back to the original track.

---

[7] A method to calculate the time to closest approach is presented in section A.5.1.
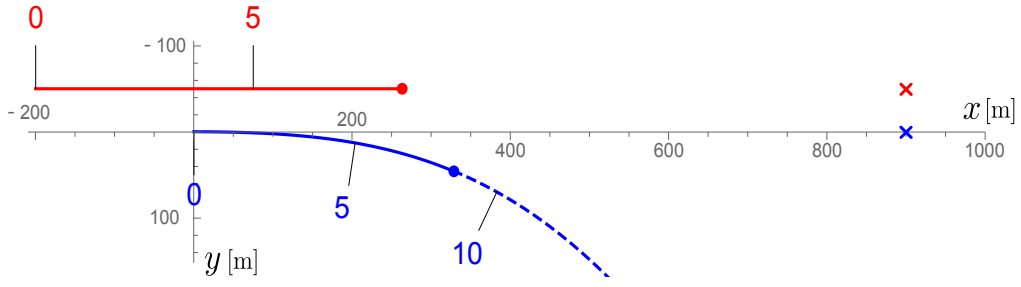
(a) Aircraft positions with time. Intruder: red line, ownship: blue line.
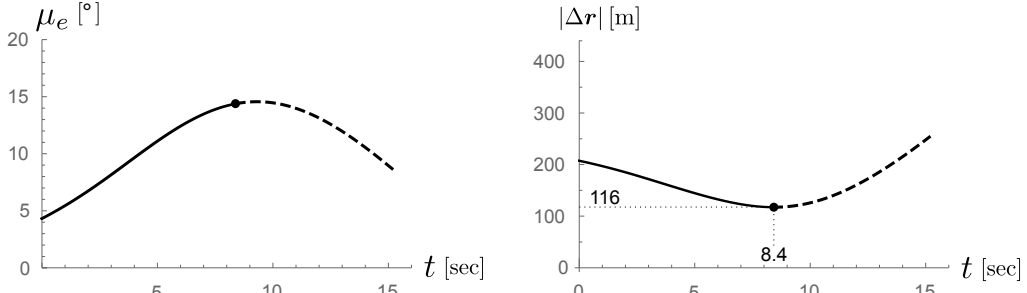
(b) Bank angle μ_e for the evader and relative distance $|\Delta r|$ in scenario A

Figure 5.5: Coplanar movement of an intruder and an evading ownship in an overtaking maneuver (Scenario A, Table 5.1). The crosses in (a) depict CPA for inaction.
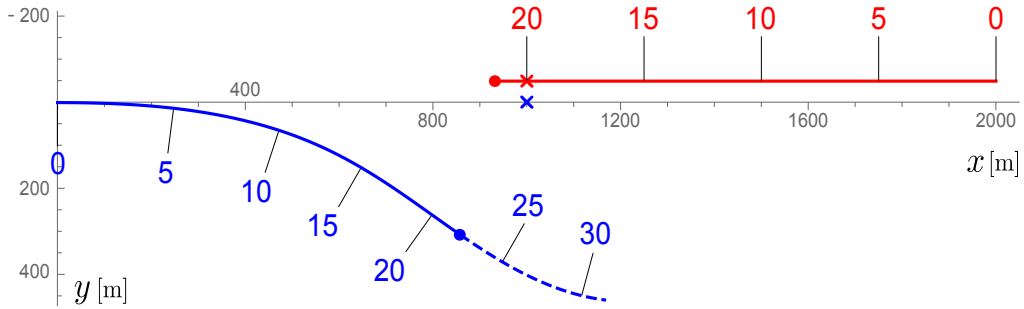
(a) Aircraft positions with time. Intruder: red line, ownship: blue line.
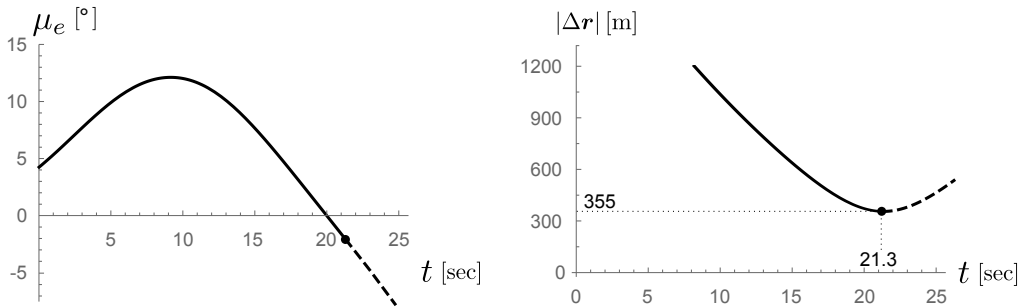
(b) Bank angle μ_e for the evader and relative distance $|\Delta r|$ in scenario B

Figure 5.6: Coplanar movement of an intruder and an evading ownship in a head-on encounter (Scenario B, Table 5.1). The crosses in (a) depict CPA for inaction.
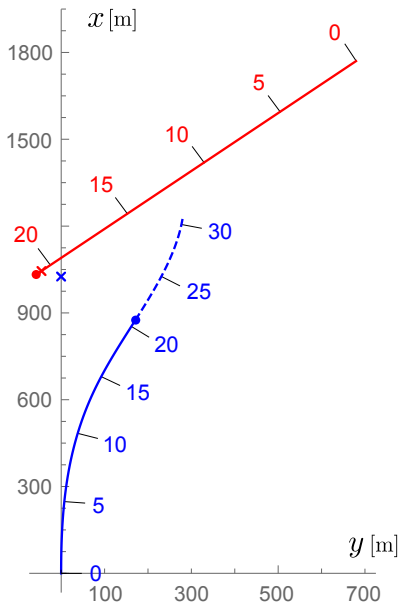
(a) Aircraft positions with time.
Intruder: red line, ownship: blue line
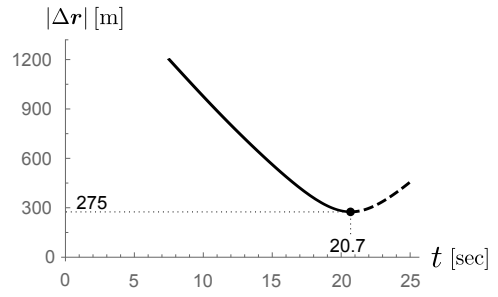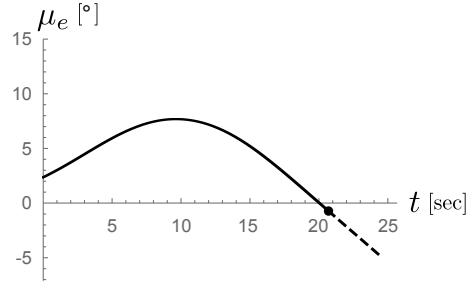
(b) Bank angle μ_e and heading angle χ_e for the evader in scenario C

Figure 5.7: Coplanar movement of an intruder and an evading ownship in a oblique-angle encounter (Scenario C, Table 5.1). The crosses in (a) depict CPA for inaction.
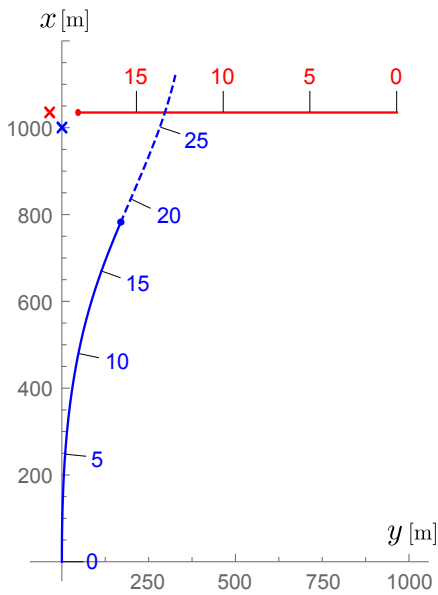
(a) Aircraft positions with time.
Intruder: red line, ownship: blue line
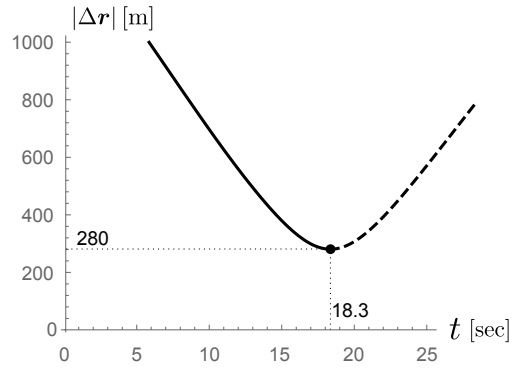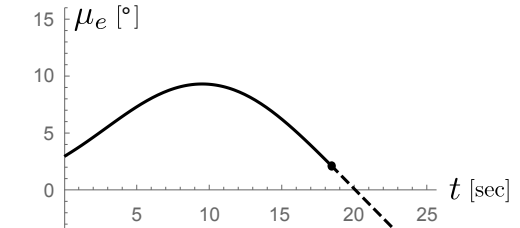
(b) Bank angle μ_e and heading angle χ_e for the evader in scenario D

Figure 5.8: Coplanar movement of an intruder and an evading ownship in a right-angle encounter (Scenario D, Table 5.1). The crosses in (a) depict CPA for inaction.
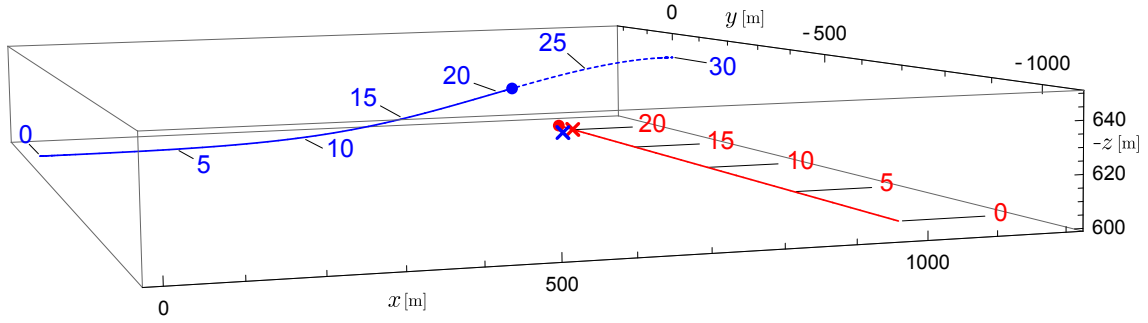
(a) Aircraft positions with time. Intruder: red line, ownship: blue line
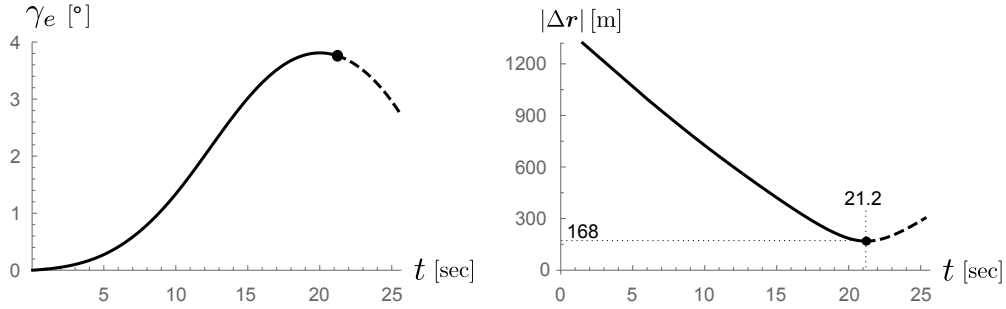
(b) Flight path angle γ_e for the evader and relative distance $|\Delta r|$ in scenario E

Figure 5.9: Movement of an intruder (in red) and a vertically evading ownship in an right-angle encounter (Scenario E, Table 5.1). The crosses in (a) depict CPA for inaction.

5.5 Display Implementation Concept

As a traffic conflict progresses and a collision becomes imminent, the problem for the pilot will shift from just traffic avoidance to last-resort traffic evasion. In such a situation, the use of predictive display methods aides the pilot in assessing appropriate action.

For the ownship, this prediction can include information about the future track of the intruder, but also a course of action to avoid the traffic. The depiction of this maneuver should only be in cases where the relative trackline (display variant D, Fig. 4.6d) is crossing close at the ownship symbol and in close proximity to the other aircraft regarding time-to-CPA.

The algorithm output leading to a vertical avoidance (scenario E, Fig. 5.9) could be adapted to a resolution advisory similar to TCAS II displays, where only vertical avoidance is intended [48]. Here, the pitch angle[8] to be flown in order to ensure separation is depicted by a pitch cue on the primary flight display. This idea is shown in the example synthetic vision display in Fig. 5.10a. In the depicted case, the aircraft should climb in order to place the tip of the airplane symbol (black triangles) in the gap indicated by the upper and lower pitch cue. The display variant D (Fig. 4.6d), which in section 4 was identified to perform best among the display variants tested, is shown in the center of the display. It provides predictive cues about the encounter, such as the direction and the aircraft category of the threat.

---

[8]determined by $\Theta = \gamma + \alpha$ (Fig. 5.2)
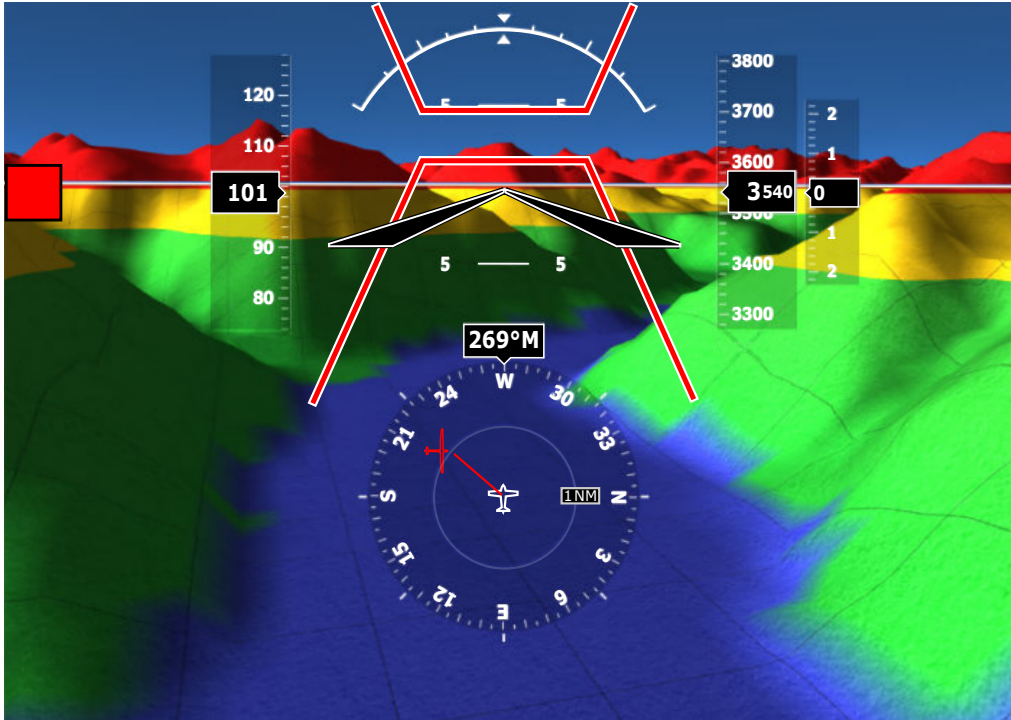
(a) Example display with a pitch cue. Vertical speed advisory is provided right of the vertical speed indicator (red-green sections).
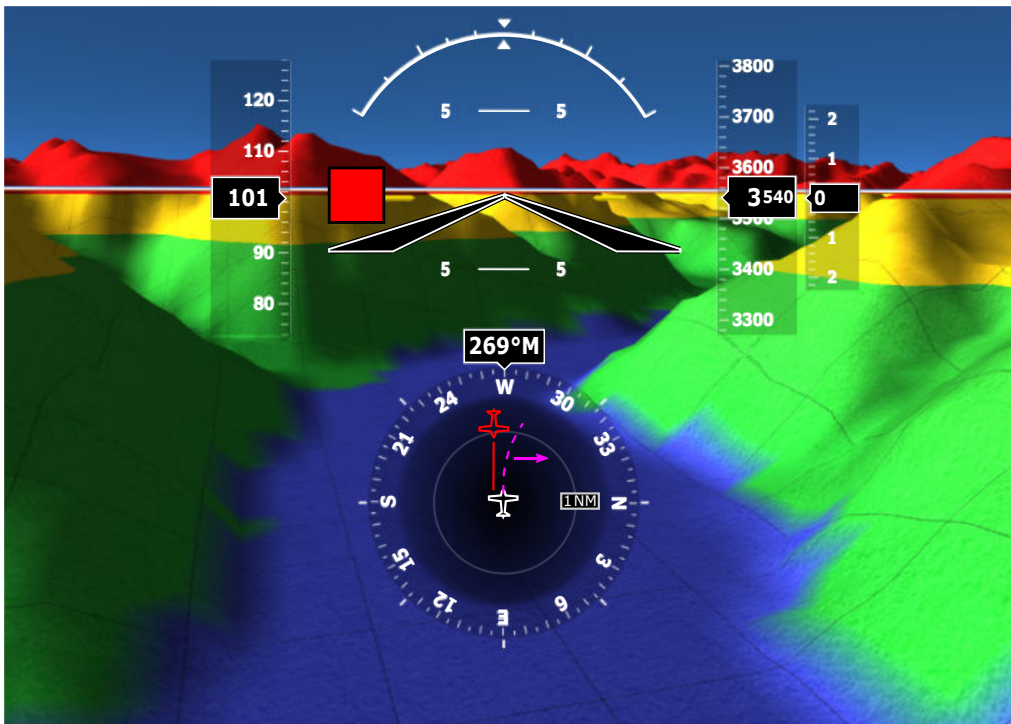
(b) Example display with a horizontal resolution advisory. Horizontal track advisory is provided by a dashed line and an arrow in magenta.

Figure 5.10: Example traffic advisory displays. The terrain display in the background is based on [121]. The intruder is both symbolized by a red square in the horizon view and the display variant D (Fig. 4.6d) in the lower center.

For the horizontal maneuvers (Fig. 5.5 to Fig. 5.8), however, a novel display solution would have to be introduced. An example of such a display is shown in Fig. 5.10b, which depicts a head-on traffic encounter.

A dashed line indicating the evasion path and an arrow for direction is used to depict how to avoid the intruder. In any case, such displays (e.g. Figs. 5.10a and 5.10b) should be considered a further area of research in the future.

5.6 Limitations

The simulation results shown in section 5.4 depict the consequences of the objectives included in the payoff function (eqn. (5.4)). As can be seen in Figs. 5.5 to 5.8, the resulting bank angle $\mu_e(t)$ commands an instantaneous value at $t = 0$. This satisfies the payoff function, but an aircraft would only be able to approximate this. It is therefore useful to implement a low-pass filter (eqn. (A.21)) to the algorithm's result.

Furthermore, the elements of the distance-weighing matrix $\boldsymbol{S}$ (eqn. (5.5)) were constant during all simulated traffic encounters in section 5.4. For further investigation, these elements could be made dependent on the relative velocity of the conflicting aircraft. The distance traveled during the reaction time (Fig. 1.18) can be accounted for in this way. Also, it may prove useful to change the weights when flying behind a larger aircraft which produces wing-tip vortices[9]. These can induce a sudden roll, leading to an uncontrollable attitude.

For the simulated scenarios, the time horizon t_f was a priori set to the predicted time of closest approach (eqn. (A.17)). An improved control on the resulting trajectory can be achieved by varying the value for t_f from its a priori value. For example, in order to achieve a defined passing distance at $|\Delta\boldsymbol{r}|(t_f)$, the required value for t_f could be determined using an iterative method[10] for finding the root of

$$f(t_f) := |\Delta\boldsymbol{r}(t_f)| - |\Delta\boldsymbol{r}|_f$$

where $|\Delta\boldsymbol{r}|_f$ is the pre-defined passing distance at $t{=}t_f$.

As of now, the payoff function (eqn. (5.4)) does not include an objective for the evader to return to the original path after the encounter, and therefore is only applicable to short term avoidance (as suggested by the example scenarios in the last section). Therefore it may prove useful to change the payoff function *after* the avoidance maneuver has been carried out to

$$J(\boldsymbol{u}_e) = \frac{1}{2}\,\boldsymbol{\zeta}^T(t_f)\,\boldsymbol{S}\,\boldsymbol{\zeta}(t_f) + \frac{1}{2}\int\limits_{t_0}^{t_f}\boldsymbol{u}_e^T\,\boldsymbol{W}_e\,\boldsymbol{u}_e\;\mathrm{d}t \qquad (5.49)$$

where $\boldsymbol{\zeta}$ represents the distance vector from the evader to a desired waypoint. The matrices $\boldsymbol{W}_e$ and $\boldsymbol{S}$ are weights regarding the control effort and the final passing distance,

---

[9]also called *wake turbulence*

[10]for example the Bisection method [122]

respectively. As before, the goal of the controls $\boldsymbol{u}_e$ is to minimize J. The resulting composite trajectory, determined firstly by traffic avoidance and secondly by original track capture, could also be useful for unmanned aerial vehicles (UAV) when negotiating traffic and waypoint objectives simultaneously.

The avoidance algorithm as presented in section 5.1 is intended as a last resort solution for collision avoidance. It therefore does not factor in the right-of-way rules, which would have to be applied beforehand. However, it is desirable to include these into an evasion maneuver before a collision becomes imminent. This is supported by the findings discussed in section 3.8, where in head-on collision scenarios only 55% of the pilots did follow the right-of-way rules.

One method for rule-based evasion, which is based on the previous algorithm, is outlined in the next section.

5.7 Incorporating the the Right-of-way rules

The original avoidance algorithm expressed by the acceleration terms for the ownship (eqn. (5.29)) is designed to achieve separation using the saddle-point condition (section 1.6) on the payoff function (eqn. (5.4)). Because the right-of-way rules are not part of this process, the resulting avoidance trajectory may not produce compliant results. Rule-based maneuvers are formulated using the approach angle, the category of the ownship and oncoming aircraft and their mode of operation [1].

Fig. 5.11 illustrates the rules if the oncoming aircraft is of the same category as the ownship and both are in cruise flight. In the following, this case is taken as an example to formulate the accelerations $\ddot{x}$ and $\ddot{y}$ for rule-based avoidance. In any case, the ownship shall avoid passing over, under or in front of the other aircraft. The former is accomplished by $\ddot{z} = 0$ during the rule-based portion of the avoidance maneuver. The latter can be done by a maneuver turning into the direction of the approaching aircraft.
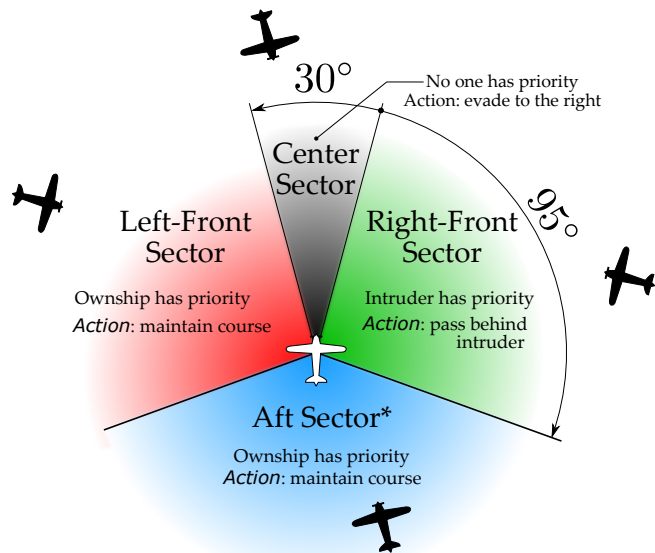
* If the ownship approaches in the Aft Sector of another aircraft, it shall keep out of the way of the other aircraft by altering its heading to the right.

Figure 5.11: Maneuver selection for the ownship during a traffic conflict according to the right-of-way rules. The intruder is of the same aircraft category as the ownship (center). The maneuvers of the ownship depend on the sector from which the intruder is approaching. The angle of the Center Sector is chosen to be 30°, because regulation only refers such encounters to be "head-on or approximately so" [1].

The avoidance algorithm produces trajectories which *increase* the angle δ between the relative distance vector $\Delta\boldsymbol{r}$ and relative velocity vector $\Delta\boldsymbol{v}$ (Fig. 5.12) during the encounter.
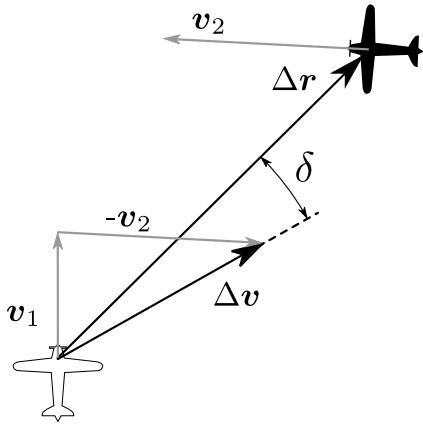
(a) Geometric defintion of the angle δ. A collision occurs if $\delta = 0$.
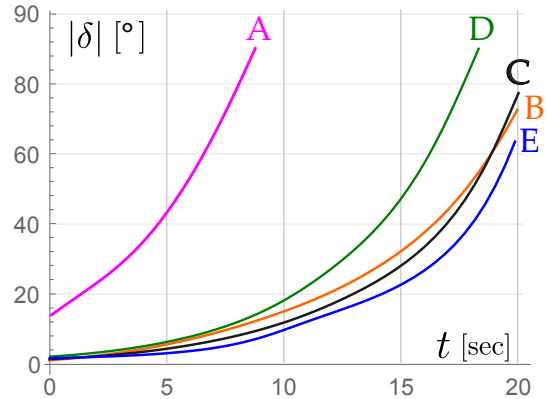
(b) Progress of the angle δ with time for the simulated traffic scenarios A to E in section 5.4.

Figure 5.12: Angle between the relative distance vector $\Delta\boldsymbol{r}$ and relative velocity vector $\Delta\boldsymbol{v}$. The value for this angle $\delta(t)$ does not cross zero.
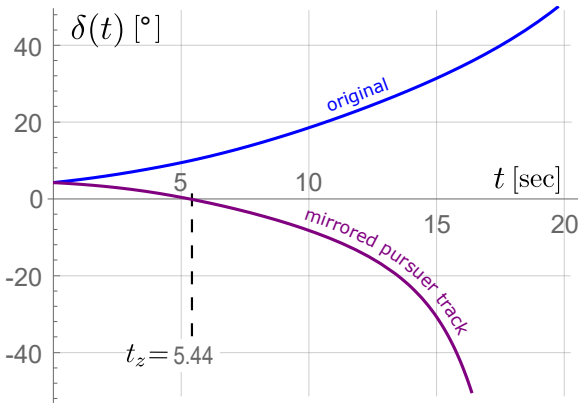
Figure 5.13: Simulation for the angle δ between the relative distance vector $\Delta\boldsymbol{r}$ and relative velocity vector $\Delta\boldsymbol{v}$ during a right-angle encounter. The pursuer is approaching from the right. The unmodified algorithm produces a maneuver to the left ($\delta(t) > 0$, blue line), which does not follow regulations. The purple line shows $\delta(t)$ for the mirrored pursuer track.

If $\Delta\boldsymbol{v}$ is to the right of $\Delta\boldsymbol{r}$, the algorithm will produce a maneuver to the right and vice versa. If the right-of-way rules are violated in the process, the direction of the avoidance maneuver has to be inverted temporarily. This can be done by mirroring the pursuer trajectory along the x-axis, which produces an avoidance maneuver by the evader in the desired (opposite) direction. The mirrored trajectory has to be at least maintained until $t = t_z$, where $\delta(t)$ crosses zero (Fig. 5.13). After that, the original geometrical configuration is restored. In the following, this procedure will be called the *modified algorithm*.

Fig. 5.13 shows a simulation result for $\delta(t)$ where the intruding aircraft is approaching from the right (Scenario G, Table 5.2). Here, the original algorithm would produce a $\delta(t)$ shown by the blue line while the purple line shows the result for the mirrored pursuer track.

Evader	Scenario F	Scenario G	Pursuer	Scenario F	Scenario G
$x_{e,0}$ [m]	0	0	$x_{p,0}$ [m]	2000	910
$y_{e,0}$ [m]	0	0	$y_{p,0}$ [m]	50	955
$z_{e,0}$ [m]	-600	-600	$z_{p,0}$ [m]	-600	-600
$v_{e,0}$ [m/s]	50	50	$v_{p,0}$ [m/s]	50	45
$\chi_{e,0}$ [°]	0	0	$\chi_{p,0}$ [°]	180	-90
$\gamma_{e,0}$ [°]	0	0	$\gamma_{p,0}$ [°]	0	0

Table 5.2: Overview of the scenario conditions for the example evasion trajectories (Figs. 5.14 and 5.15)

When re-activating the unmodified algorithm at a time between t_z and the time horizon at t_f, the position and velocity vectors at this time will result in a trajectory which continues the direction of the maneuver.

This is illustrated in the following by two example evasion scenarios[11] (initial conditions in Table 5.2). The coordinate system is the same as in the simulations in section 5.4 (Fig. 5.4). All other weights and constants from these simulations were retained. The time after which the original pursuer track was reestablished was set at t_s=8 seconds, leaving 12 seconds to the time horizon at t_f=20 seconds. Scenario F (Fig. 5.14) describes a situation in which the intruder is approach-
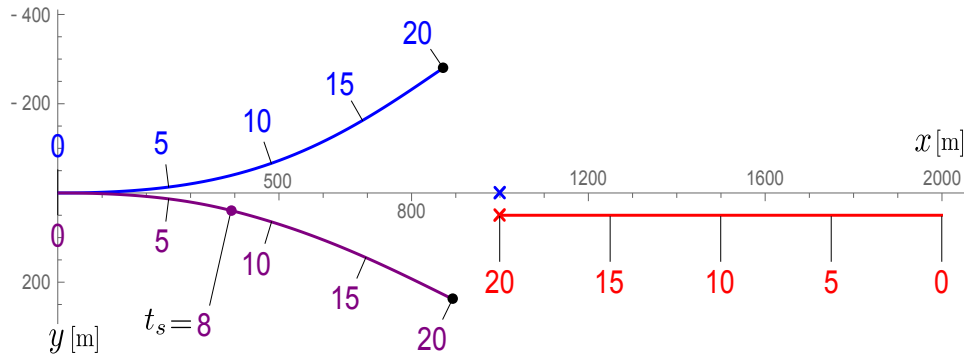
(a) Aircraft positions with time
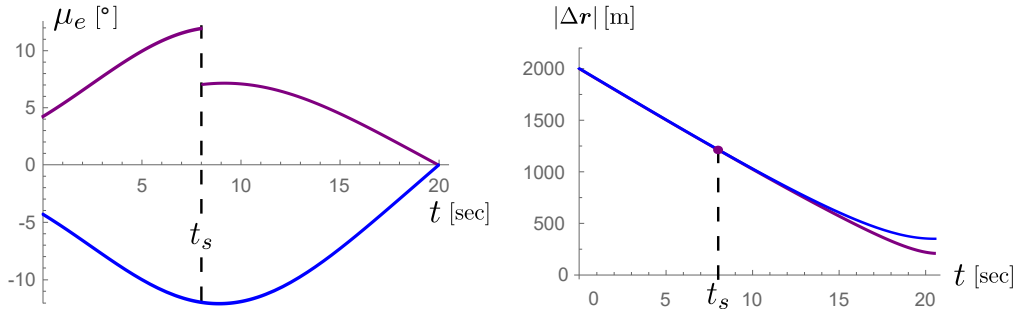
(b) Bank angle μ_e for the evader and relative distance $|\Delta \boldsymbol{r}|$ in scenario A

Figure 5.14: Coplanar movement of an intruder and an evading ownship in a head-on encounter (Scenario F, Table 5.2). Intruder: red line, ownship (original algorithm): blue line, ownship (modified algorithm): purple line. The crosses in (a) depict CPA for inaction.

---

[11]Scenario G is the same one as in Fig. 5.13

ing in the Center section (Fig. 5.11). According to the right-of-way rules, the avoidance maneuver has to be a turn to the right. The original algorithm (blue line) does not comply, however, it produces a slightly higher separation $|\Delta r|$ at $t_f = 20$ seconds (Fig. 5.14b) than the trajectory of the modified algorithm (purple line).

This can also be observed for scenario G, which resembles a right-angle traffic scenario (Fig. 5.15). Here, the intruder has the right-of-way. The ownship should avoid passing in front of the intruder, which is achieved by the modified algorithm.

(a) Aircraft positions with time

(b) Bank angle μ_e for the evader and relative distance $|\Delta r|$ in scenario A
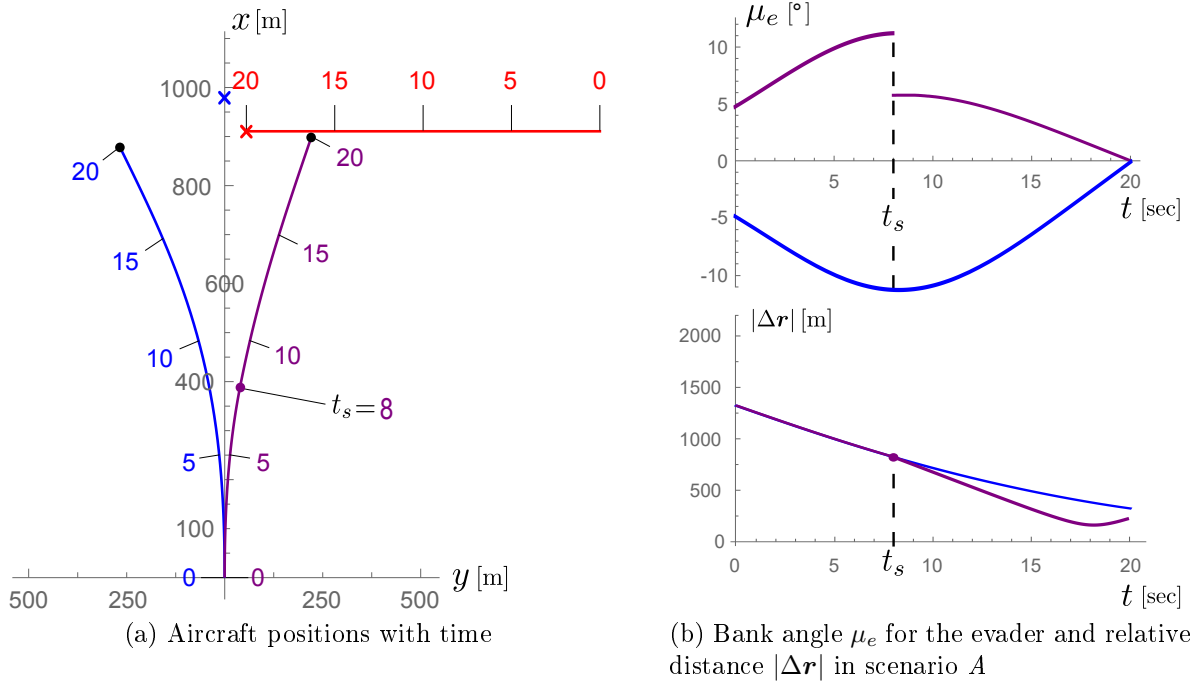
Figure 5.15: Coplanar movement of an intruder and an evading ownship in a right-angle encounter (Scenario G, Table 5.2). Intruder: red line, ownship (original algorithm): blue line, ownship (modified algorithm): purple line. The crosses in (a) depict CPA for inaction.

If the encounter takes place in the Left-Front sector (Fig. 5.11), the ownship has priority. Following the rules, the ownship should maintain course, altitude and speed ($\ddot{x} = \ddot{y} = 0$). The same is applicable for an approaching intruder in the Aft sector. If on the other hand the ownship is overtaking, it shall avoid to the right, which the modified algorithm can achieve in the same way as for an approach in the Center section.

Both the application of the original and the modified (rule-based) avoidance algorithm have to be restricted to a domain shortly before a collision. One way to formulate an activation criterion is to construct a triangular domain for values of the time to CPA and the distance between the aircraft at CPA (t^* and $|\Delta r|_{\mathrm{CPA}}$, respectively)[12]. If *both* of these are located in the activation domain (in red, Fig. 5.16), the original algorithm

---

[12]The calculation of t^* in shown in section A.5.1.
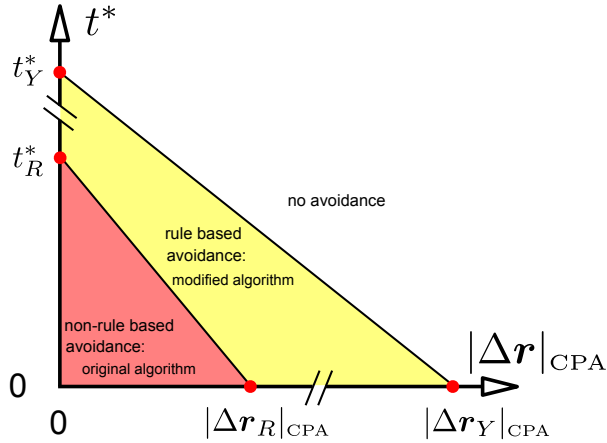
Figure 5.16: Criterion to activate the avoidance algorithm (eqn. (5.29)). From section 1.3.3, the value of t_R^* should not be lower than 12.5 seconds, which is considered the minimum time to avoid a midair collision.

(eqn. (5.29)) applies. This way, last-resort measures are separated from cases where rule-based avoidance is preferable. Subsequently, the latter has to take place in an adjacent domain (depicted in yellow), which separates it from values of t^* and $|\Delta \boldsymbol{r}|_{\mathrm{CPA}}$ where no avoidance is necessary. For future development, each one of the values defining the vertices of both domains (t_R^*, $|\Delta \boldsymbol{r}_R|_{\mathrm{CPA}}$, t_Y^*, $|\Delta \boldsymbol{r}_Y|_{\mathrm{CPA}}$) has to be evaluated using pilot and expert knowledge.

6 Conclusion

This thesis addresses technological means to reduce the number of midair collisions between General Aviation aircraft in uncontrolled airspace. These envelop the majority of flights around the world, with roughly 200,000 currently active aircraft in the United States alone.

Data from the UK Airprox Board was used to determine the conditions under which the precursors of midair collisions occur. As reported by involved air traffic controllers or pilots, 75% of such events were identified to be operated under Visual Flight Rules (VFR) and in uncontrolled airspace (61%).

The Rules of the Air, as defined by ICAO, state that pilots which are flying in VMC have the ultimate responsibility of keeping proper separation. The see-and-avoid principle was formulated as a means to regulate and standardize traffic situations. It defines traffic rules which state a coordinated way to avoid a collision by prioritizing one aircraft over the other, depending on the geometry of the encounter and aircraft category. Furthermore, methods of how to stay vigilant of the traffic outside of the cockpit are specified. The proportion of time allocated for scanning the cockpit instruments should be limited to a maximum of 4 to 5 seconds for every 16 seconds of scanning for hazards outside. However, both vigilance and avoidance are influenced by human factors such as physiological and psychological constraints. The human visual system and information processing are particularly important for the ability to react in traffic situations.

These factors are the most likely culprit of events where the separation between aircraft is lost. This is backed up by a summary of past mid-air collisions, showing the circumstances and probable causes in order to assess human limitations and ways for improvement. In that regard, this thesis focuses on on-board display systems showing the traffic situation in order to reduce pilot workload when flying small aeroplanes in congested airspace. Currently, such systems are not mandatory for this category.

A simulator study was conducted in order to show benefits and limitations of a collision warning system for VFR flight. The symbology used in the experiments resembled the TCAS system, which is the industry standard for commercial aircraft. Eighteen pilots were confronted with single and multiple traffic, visible both on a moving map display and on the visual system of a simulator. The participants were also interviewed to gather expert opinion on how to improve the TCAS display design.

The results demonstrate the benefits of the collision warning system in identifying traffic. However, the avoidance maneuvers initiated by the pilots did not always conform with the regulations. Under multiple traffic conditions the pilots exhibited slower reaction times when confronted with the traffic warning. They also reported higher levels of workload and reduced situational awareness in comparison to the conditions of single traffic. Using the pilots' feedback technical requirements for the future development of

collision avoidance systems for VFR were identified.

The study provided the necessary impetus to design a traffic warning display adapted to the obligation of VFR pilots to be vigilant of the view outside the cockpit. The resulting system has to primarily perform better on the time needed to asses whether an oncoming aircraft is a threat or not. The faster this decision can accurately be made, the more time is available to choose proper action. Therefore, a second study was carried out which proposes and investigates a novel predictive traffic visualization display concept which integrates a moving map and predictive features. The predictive features of the concept are the visualization of traffic by oriented air vehicle symbols, of the relative track, and of priority cues in case of conflict. These features were applied to four display variants resulting in different levels of automation. As a baseline, a display using TCAS-like diamond symbols was used. A purpose-built application was written to design proper test scenarios for the experiments using 3-dimensional graphics and realistic terrain data.

Using this application, simulated traffic scenarios were used in an experiment with 21 pilots. The results show that the depiction of relative track and priority cues resulted in significantly faster recognition of conflict or non-conflict situations compared to the TCAS baseline and other predictive cues. Apart from that, also pilots' reaction to imminent mid-air collisions was investigated and reviewed in context with international regulation procedures. It was found that using the predictive cues pilots were (in all but one case) able to apply the right-of-way rules correctly, a significant improvement over the results in the first study. Furthermore, relative track and priority cues were less mentally demanding and scored higher in pilots' preference.

With modifications, a version of this application is discussed which could find further use in collision avoidance. Furthermore, an algorithm for collision avoidance is presented and applied to the dynamics of a small aeroplane. These aircraft are used in the majority of flights operated under VFR. The algorithm is based on optimal control theory, which is able to provide an algebraic solution for the accelerations during an avoidance maneuver.

Simulation results of different traffic encounter geometry are presented and possibilities of how to integrate these in a traffic display are discussed. Furthermore, methods of modifying the algorithm to incorporate the right-of way-rules are proposed.

Bibliography

[1] *Annex 2 to the Convention on International Civil Aviation*, International Civil Aviation Organization (ICAO) Std., 2005.

[2] *Regulation of Air Traffic 2010 - Verordnung über die Regelung des Luftverkehrs 2010*, Bundesministerium für Verkehr, Österreich (Austria) Std.

[3] National Transportation Safety Board. (2015) NTSB Accident Query. Search terms – Date range: 1 Jan 2010 to 31 Dec 2014, Keyword: Midair collisions. [Online]. Available: http://www.ntsb.gov/_layouts/ntsb.aviation/index.aspx

[4] Skybrary. (2015, jan) Airprox Description. [Online]. Available: http://www.skybrary.aero/index.php/AIRPROX

[5] UK Airprox Board. (2015, jan) Airpox Statistics. [Online]. Available: http://www.airproxboard.org.uk/

[6] *CFR Part 91 General Operating And Flight Rules, Sec. 91.205*, Federal Aviation Administration Std., 2015.

[7] *CFR Part 91 General Operating And Flight Rules, Sec. 91.155*, Federal Aviation Administration Std., 2015.

[8] *Annex 11 to the Convention on International Civil Aviation*, International Civil Aviation Organization (ICAO) Std., 2001.

[9] International Virtual Aviation Organisation (IVAO). (2015, may) Classification of Airspace. [Online]. Available: http://ivao.co.uk/pilot/classes

[10] *Annex 6 to the Convention on International Civil Aviation*, International Civil Aviation Organization (ICAO) Std., 2010.

[11] Bureau of Transportation Statistics, "Transportation Statistics Annual Report 2013," US Department of Transportation, Washington DC, Tech. Rep., 2013.

[12] Aircraft Owners and Pilots Association. (2015, jul) Active General Aviation Aircraft in the U.S. [Online]. Available: http://www.aopa.org/About-AOPA/General-Aviation-Statistics/Active-General-Aviation-Aircraft-in-the-U-S

[13] SKYbrary. (2015, jul) Altitude, Flight Level and Height. [Online]. Available: http://www.skybrary.aero/index.php/Altitude,_Flight_Level_and_Height

[14] *Manual of the ICAO standard atmosphere Doc 7488/3*, International Civil Aviation Organization (ICAO) Std., 1993.

[15] NASA. (2014, jun) Guide to NASA'sWorld Wind. [Online]. Available: http://goworldwind.org/

[16] National Transportation Safety Board. (2015, jul) Aircraft accident summary report - Midair collision over Hudson River. [Online]. Available: http://www.ntsb.gov/investigations/AccidentReports/Reports/AAR1005.pdf

[17] ——. (2015, jul) Mid-air collision of electronic news gathering helicopters. [Online]. Available: http://www.ntsb.gov/investigations/accidentreports/reports/aar0902.pdf

[18] ——. (2015, aug) Narrative of NTSB Report NYC04FA185A. [Online]. Available: http://www.ntsb.gov/about/employment/_layouts/ntsb.aviation/brief2.aspx?ev_id=20040812X01202&ntsbno=NYC04FA185A&akey=2

[19] Bundesstelle für Flugunfalluntersuchung. (2015, jul) Untersuchungsbericht zur Kollision zwischen Tornado Kampfflugzeug und einem Gleiter. [Online]. Available: http://www.bfu-web.de/DE/Publikationen/Untersuchungsberichte/1998/Bericht_3X191-1-2.98.pdf

[20] *Pilot's Role in Collision Avoidance*, Federal Aviation Administration Std. Advisory Circular 90-48C, 1983.

[21] Australian Transport Safety Bureau. (2015, aug) Limitations of the See-and-Avoid Principle. [Online]. Available: http://www.skybrary.aero/bookshelf/books/259.pdf

[22] World Health Organization. (2015, sep) Definition of human factors. [Online]. Available: http://www.who.int/patientsafety/research/methods_measures/human_factors/en/

[23] S. S. Krause, *Avoiding Mid-Air Collisions*. Tab Books, 1995.

[24] *Spatial Disorientation*, ser. Safety Advisor: Physiology No. 1, no. 4, AOPA, 2004.

[25] G. Salvendy, *Handbook of human factors and ergonomics*. John Wiley & Sons, 2012.

[26] R. C. Atkinson and R. M. Shiffrin, "Human memory: A proposed system and its control processes," *The psychology of learning and motivation*, vol. 2, pp. 89–195, 1968.

[27] S. Lutz and W. Huitt, "Information processing and memory: Theory and applications," *Educational Psychology Interactive*, 2003.

[28] J. A. Wise, V. D. Hopkin, and D. J. Garland, *Handbook of aviation human factors*. CRC Press, 2009.

[29] C. Eliasmith. (2015, aug) Dictionary of Philosophy of Mind. [Online]. Available: https://sites.google.com/site/minddict/memory

[30] National Transportation Safety Board. (2015, aug) Accident Report of Eastern Airlines 401. [Online]. Available: http://www.ntsb.gov/investigations/ AccidentReports/Pages/AAR7314.aspx

[31] Garmin. (2015, oct) GTS: Garmin Traffic Systems. [Online]. Available: http://www8.garmin.com/aviation/brochures/03734GTSSeriesSpecSheet/ 03734GTSSeriesSpecSheet.pdf

[32] CASA, *Safety Behaviours: Human Factors for Engineers*. Civil Aviation Safety Authority Australia, 2013.

[33] R. Parasuraman, T. B. Sheridan, and C. D. Wickens, "Situation awareness, mental workload, and trust in automation: Viable, empirically supported cognitive engineering constructs," *Journal of Cognitive Engineering and Decision Making*, vol. 2, no. 2, pp. 140–160, 2008.

[34] R. M. Yerkes and J. D. Dodson, "The relation of strength of stimulus to rapidity of habit-formation," *Journal of comparative neurology and psychology*, vol. 18, no. 5, pp. 459–482, 1908.

[35] Psychology Dictionary. (2015, aug) What is Automatictiy? [Online]. Available: http://psychologydictionary.org/automaticity/

[36] R. Hemm and A. Busick, "Safety analysis of the separation assurance function in today's national airspace system," *AIAA Paper*, vol. 7123, 2009.

[37] H. J. Ebermann, P. Jordan, G. Fahnenbruck *et al.*, *Human Factors im Cockpit*, H. J. Ebermann and J. Schneiderer, Eds. Springer, 2011.

[38] Federal Aviation Administration, "Aeronautical Information Manual: Official Guide to Basic Flight Information and ATC Procedures," 2014. [Online]. Available: http://www.faa.gov/air_traffic/publications/media/AIM_Basic_4-03-14.pdf

[39] ——, *Advanced Avionics Handbook - FAA-H-8083-6*, 1st ed. Skyhorse Publishing, Inc., 2013.

[40] C. Wickens, X. Xu, J. Helleberg, R. Carbonari, and R. Marsh, "The allocation of visual attention for aircraft traffic monitoring and avoidance: Baseline measures and implications for free flight (technical report arl-00-2/faa-00-2)," *Savoy, IL: University of Illinois, Aviation Research Lab*, 2000.

[41] T. Haberkorn, I. Koglbauer, R. Braunstingl, and B. Prehofer, "Requirements for future collision avoidance systems in visual flight: A human-centered approach," *Human-Machine Systems, IEEE Transactions on*, vol. 43, no. 6, pp. 583–594, 2013.

[42] R. F. Stengel, *Optimal control and estimation*. Courier Corporation, 2012.

[43] A. E. Bryson, *Applied optimal control: optimization, estimation and control*. CRC Press, 1975.

[44] Eurocontrol. (2015, may) History of Airborne Collision Avoidance. [Online]. Available: https://www.eurocontrol.int/articles/history-future-airborne-collision-avoidance

[45] *Traffic Advisory System (TAS) Airborne Equipment (TSO-C147)*, Federal Aviation Administration Std., 1998.

[46] Bendix King. (2015, oct) Pilot's Guide CAS-66A TCAS I. [Online]. Available: http://www.bendixking.com/HWL/media/Pilot-Guides/006-08746-0000_7.pdf

[47] Garmin. (2015, oct) GTS 850 TCAS/ACAS I. [Online]. Available: https://buy.garmin.com/en-US/US/in-the-air/avionics-safety/traffic-solutions/gts-850-tcas-acas-i/prod14727.html

[48] Federal Aviation Administration. (2015, aug) Introduction to TCAS II version 7.1. [Online]. Available: http://www.faa.gov/documentLibrary/media/Advisory_Circular/TCAS%20II%20V7.1%20Intro%20booklet.pdf

[49] Honeywell. (2014, jun) Traffic System CAS-67A TCAS II. [Online]. Available: http://www.omnijet.com/mods/tcas67apilotguide.pdf

[50] ACSS. (2014, jun) Traffic Alert & Collision Avoidance System TCAS-3000SP. [Online]. Available: http://www.acss.com/products/tcas-3000sp/

[51] L-3 Avionics Systems. (2014, jun) Skywatch Collision Avoidance Systems. [Online]. Available: http://www.l-3avionics.com/products/skywatch

[52] Avidyne. (2015, oct) TAS-A Series ADS-B-capable Traffic Advisory Systems. [Online]. Available: http://www.avidyne.com/downloads/brochures/AV633-TAS600_hr.pdf

[53] Dynon. (2014, jun) Dynon Avionics SkyView Pilot's User's Guide. [Online]. Available: http://dynonavionics.com/downloads/User_Manuals/SkyView_Pilots_User_Guide-Rev_V_v13.0.pdf

[54] FLARM. (2015, mar) Operating manual FLARM collision avoidance System . [Online]. Available: http://flarm.com/wp-content/uploads/2015/03/FLARM_OperatingManual_E.pdf

[55] PowerFLARM. (2015, oct) PowerFLARM manual. [Online]. Available: http://flarm.com/wp-content/uploads/2015/03/PowerFLARM_Portable_Manual_EN.pdf

[56] Zaon Flight Systems. (2014, jun) Zaon PCAS. [Online]. Available: http://www.aircraftspruce.com/catalog/pdf/XRX_Manual_1-0.pdf

[57] *Commission Regulation (EU) No 1332/2011*, European Commission Std., 2011.

[58] E. S. Fleming, "Developing a training program for the traffic alert and collision avoidance system in context," *Georgia Tech Theses and Dissertations*, 2013.

[59] A. E. Coso, E. S. Fleming, and A. R. Pritchett, "Characterizing pilots' interactions with the aircraft collision avoidance system," in *Proceedings of the 16th International Symposium on Aviation Psychology, Dayton, Ohio*, 2011.

[60] *Automatic Dependent Surveillance-Broadcast (ADS-B) out equipment and use, 14 CFR 91.225*, Code of Federal Regulations Std., 2010.

[61] Federal Aviation Administration. (2015, oct) FAA NextGEN-Equip ADS-B. [Online]. Available: http://www.faa.gov/nextgen/equipadsb/

[62] D. H. Merwin and C. D. Wickens, "Evaluation of perspective and coplanar cockpit displays of traffic information to support hazard awareness in free flight," University of Illinois Institute of Aviation, Tech. Rep. ARL-96-5/NASA-96-1, 1996.

[63] S. B. J. Van Dam, A. L. M. Abeloos, M. Mulder, and M. M. van Paassen, "Functional presentation of travel opportunities in flexible use airspace: An EID of an airborne conflict support tool," in *Systems, Man and Cybernetics, 2004 IEEE International Conference on*, vol. 1.   IEEE, 2004, pp. 802–808.

[64] R. Parasuraman, T. B. Sheridan, and C. D. Wickens, "A model for types and levels of human interaction with automation," *IEEE Trans Syst Man Cybern A*, vol. 30, no. 3, pp. 286–297, May 2000.

[65] C. D. Wickens, K. Gempler, and M. E. Morphew, "Workload and reliability of predictor displays in aircraft traffic avoidance," *Transportation Human Factors*, vol. 2, no. 2, pp. 99–126, 2000.

[66] S. B. J. Van Dam, C. L. A. Steens, M. Mulder, and M. M. van Paassen, "Evaluation of two pilot self-separation displays using conflict situation measurements."   IEEE, Oct 2008, pp. 3558–3563.

[67] S. Casner, "General aviation pilots' attitudes toward advanced cockpit systems," *International Journal of Applied Aviation Studies*, vol. 8, no. 1, pp. 88–112, 2008.

Bibliography

[68] I. Koglbauer, R. Braunstingl, K. Frühwirth, E. Grubmueller, and S. Loesch, "Usability of cockpit automation in managing normal and abnormal aircraft operations," in *Proceedings of the International Symposium on Aviation Psychology, Dayton, Ohio*, 2011, pp. 609–614.

[69] Eurocontrol. (2014, jun) EVAIR Safety Bulletin No. 5. 2006-2009 Evolution. [Online]. Available: http://www.eurocontrol.int/sites/default/files/content/documents/nm/safety/safety-evair-safety-bulletin-n5-2006-2009.pdf

[70] B. A. Prehofer and R. Braunstingl, "A geometric algorithm for the calculus of multidimensional airborne conflict resolution trajectories," 2011, paper presented at the Deutscher Luft- und Raumfahrtkongress 2011, DGLR, Bremen.

[71] Aviation Safety Reporting System. (2013, jul) NASA. [Online]. Available: http://asrs.arc.nasa.gov/

[72] Eurocontrol. (2015, may) Changes To ICAO Rules Regarding TCAS RAs. [Online]. Available: https://www.eurocontrol.int/sites/default/files/article/content/documents/nm/safety/ACAS/safety-acas-report-changes-icao-rules-ra-200801.pdf

[73] ——. (2015, may) Principles of Mode S Operation and Interrogator Codes. [Online]. Available: http://www.eurocontrol.int/sites/default/files/publication/files/surveillance-modes-principles-of-modes-operation-and-interrogator-codes-20030318.pdf

[74] C. D. Wickens, J. Hellenberg, and X. Xu, "Pilot maneuver choice and workload in free flight," *Human Factors: The Journal of the Human Factors and Ergonomics Society*, vol. 44, no. 2, pp. 171–188, 2002.

[75] L. C. Thomas and C. D. Wickens, "Display dimensionality and conflict geometry effects on maneuver preferences for resolving in-flight conflicts," *Human Factors: The Journal of the Human Factors and Ergonomics Society*, vol. 50, no. 4, pp. 576–588, 2008.

[76] J. Helleberg, C. D. Wickens, and X. Xu, "Pilot Maneuver Choice and Safety in a Simulated Free Flight Scenario," University of Illinois Institute of Aviation, Tech. Rep. ARL-00-1/FAA-00-1, 2007.

[77] K. S. Gempler and C. D. Wickens, "Display of predictor reliability on a cockpit display of traffic information," *University of Illinois Institute of Aviation Final Technical Report (ARL-98-6/ROCKWELL-98-1). Savoy, IL: Aviation Res Lab.*, 1998.

[78] C. Wickens and E. Morphew, "Predictive features of a cockpit traffic display: A workload assessment," University of Illinois Institute of Aviation, Tech. Rep. ARL-97-6/NASA-97-3, 1997.

[79] C. Wickens and J. Helleberg, "Interactive perspective displays for airborne hazard awareness," University of Illinois Institute of Aviation, Tech. Rep. ARL-99-1/ROCKWELL-99, 1999.

[80] A. L. Alexander and C. D. Wickens, "Cockpit display of traffic information: The effects of traffic load, dimensionality, and vertical profile orientation," in *Proceedings of the Human Factors and Ergonomics Society Annual Meeting*, vol. 45, no. 2. SAGE Publications, 2001, pp. 105–109.

[81] E. M. Rantanen and C. D. Wickens, "Conflict resolution maneuvers in air traffic control: Investigation of operational data," *The International Journal of Aviation Psychology*, vol. 22, no. 3, pp. 266–281, 2012.

[82] E. M. Rantanen, J. Yang, and S. Yin, "Comparison of pilots' and controllers' conflict resolution maneuver preferences," in *Human Factors and Ergonomics Society Annual Meeting Proceedings*, vol. 50, no. 1. Human Factors and Ergonomics Society, 2006, pp. 16–19.

[83] Graz University of Technology. (oct) Research Platform Flight Simulation. [Online]. Available: http://www.flightsimulation.tugraz.at

[84] Becker Avionics. (2015, oct) AirScout 2D Multi Function Display MFD6203. [Online]. Available: http://www.becker-avionics.com/download/Brochures/Light% 20Aircrafts/Datasheets/AirScout_MFD6203_datasheet_Issue7_2015.pdf

[85] S. G. Hart and L. E. Staveland, *Development of NASA-TLX (Task Load Index): Results of Empirical and Theoretical Research*, ser. Advances in Psychology. Elsevier, 1988, pp. 139–183.

[86] E. Jeannot, C. Kelly, and D. Thompson, "The development of situation awareness measures in atm systems," *EATMP report. Eurocontrol HRS/HSP-005-REP-01.*, 2003.

[87] I. Koglbauer, R. Braunstingl, and T. Haberkorn, "Modeling human and animal collision avoidance strategies," in *Proceedings of the 17th International Symposium on Aviation Psychology, Dayton, Ohio*, 2013, pp. 554–559.

[88] C. C. Morris, "Midair collisions: Limitations of the see-and-avoid concept in civil aviation," *Aviation, Space, and Environmental Medicine*, vol. 76, no. 4, pp. 357–365, 2005.

[89] N. Leveson, *Engineering a safer world: Systems thinking applied to safety.* MIT Press, 2011.

[90] J. V. Nickerson and R. R. Reilly, "A model for investigating the effects of machine autonomy on human behavior," in *System Sciences, 2004. Proceedings of the 37th Annual Hawaii International Conference on.* IEEE, 2004.

[91] Aviation Safety Network. (2013, jul) Accident description July 1st 2002. [Online].
Available: http://aviation-safety.net/database/record.php?id=20020701-1

[92] D. E. Grilley. (2005) Resolution requirements for passive sense & avoid. Alion
Science & Technology.

[93] C. E. Lin and Y.-Y. Wu, "TCAS solution for low altitude flights," in *Integrated
Communications Navigation and Surveillance Conference (ICNS), 2010.* IEEE,
2010, pp. I4–1.

[94] J. S. McCarley and C. D. Wickens, *Human factors implications of UAVs in the
national airspace.* University of Illinois at Urbana-Champaign, Aviation Human
Factors Division, 2005.

[95] *Policy for Unmanned Aerial Vehicle (UAV) certification, A-NPA No 16-2005*, European Aviation Safety Agency Std.

[96] Atlantic Council. (2013, jul) Germany cancels EuroHawk
drone program. [Online]. Available: http://www.acus.org/natosource/
germany-cancels-euro-hawk-drone-program

[97] Eurocontrol. (2014, jun) Report detailing Light Aviation SSR transponder
(LAST) requirements - Annex B. Report No. STA/R/460/0001/1. [Online]. Available: http://www.eurocontrol.int/sites/default/files/publication/files/
surveillance-annex-b-study-to-address-the-detection-and-recognition-of-light-aircraft-in-the-cur
pdf

[98] *Collision Avoidance, Strategies and Tactics*, ser. Safety Advisor: Operations and
Proficiency, no. 4, AOPA, 2009.

[99] VERSA Verkehrssicherheitsarbeit für Österreich, "Zusammenstoß in der Luft eines
Motorflugzeuges Type DV 20 und eines Hubschraubers Type AS 332," Unfalluntersuchungsstelle des Bundes - Fachbereich Luftfahrt, Tech. Rep. GZ. BMVIT-
85.121/0002-II/BAV/UUB/LF/2008, 2008.

[100] I. Koglbauer, R. Braunstingl, T. Haberkorn, and B. Prehofer, "How do pilots
interpret and react to traffic display indications in VFR flight?" in *Proc. of The
30th EAAP Conference, 24th - 28th September, Vilassimius, Italy*, 2012, pp. 554–
559.

[101] M. R. Endsley *et al.*, "Theoretical underpinnings of situation awareness: A critical
review," *Situation awareness analysis and measurement*, pp. 3–32, 2000.

[102] C. Santel, P. Gerber, S. Mehringskoetter, S. Schocholow, J. Vogt, and U. Klingauf,
"How glider pilots misread the FLARM collision alerting display: A laboratory
study," *Aviation Psychology and Applied Human Factors*, 2014.

[103] *Appendix A: Extended Squitter and TIS-B, Formats and Coding Definitions*, Federal Aviation Administration Std., 2009.

[104] A. L. Alexander, C. D. Wickens, and D. H. Merwin, "Perspective and coplanar cockpit displays of traffic information: Implications for maneuver choice, flight safety, and mental workload," *International Journal of Aviation Psychology*, vol. 15, no. 1, pp. 1–21, 2005.

[105] *Certificates and ratings issued under this part, 14 CFR 61.5(b)*, Federal Aviation Administration Std., 1997.

[106] K. J. Vicente and J. Rasmussen, "Ecological interface design: Theoretical foundations," *Systems, Man and Cybernetics, IEEE Transactions on*, vol. 22, no. 4, pp. 589–606, 1992.

[107] D. B. Kaber, A. L. Alexander, E. M. Stelzer, S.-H. Kim, K. Kaufmann, and S. Hsiang, "Perceived clutter in advanced cockpit displays: measurement and modeling with experienced pilots," *Aviation, space, and environmental medicine*, vol. 79, no. 11, pp. 1007–1018, 2008.

[108] M. M. Spapé and D. J. Serrien, "Prediction of collision events: An EEG coherence analysis," *Clinical Neurophysiology*, vol. 122, no. 5, pp. 891–896, 2011.

[109] J. Stevens, *Intermediate Statistics: A Modern Approach.* Mahwah, New Jersey: LEA, 1999.

[110] S. Holm, "A simple sequentially rejective multiple test procedure," *Scandinavian Journal of Statistics*, pp. 65–70, 1979.

[111] A. Hofer, *Entwurf optimaler Systeme.* Institut für Regelungs- und Automatisierungstechnik, Technische Universität Graz (Austria), 2012.

[112] G. Brüning, X. Hafer, and G. Sachs, *Flugleistungen: Grundlagen, Flugzustände, Flugabschnitte. Aufgaben und Lösungen.* Springer, 2006.

[113] R. F. Stengel, "Flight dynamics," *Aircraft Engineering and Aerospace Technology*, vol. 77, no. 3, 2005.

[114] J. G. Leishman, *Principles of Helicopter Aerodynamics with CD Extra.* Cambridge university press, 2006.

[115] D. G. Hull, *Fundamentals of Airplane Flight Mechanics.* Springer, 2007.

[116] F. Heitmeir, *Flugleistungen-Flugmechanik.* Institut für Thermische Turbomaschinen und Maschinendynamik, Technische Universität Graz (Austria), 2012.

[117] Downwind Mag. (2016, jan) Flight Training – Coordinated Flight. [Online]. Available: http://www.downwindmag.com/2009/11/149/

[118] *CFR Part 14 Airplane categories, Sec. 23.3*, Federal Aviation Administration Std., 2015.

[119] *Limit maneuvering load factors, 14 CFR 23.337*, Code of Federal Regulations Std., 2011.

[120] Cessna, *172S Skyhawk Information Manual*. Cessna - A Textron Company, 1998.

[121] ForeFlight. (2015, jun) ForeFlight Products: Synthetic Vision. [Online]. Available: http://foreflight.com/

[122] R. W. Hamming, *Numerical Methods for Scientists and Engineers*, 2nd ed. Dover Publications, 3 1987.

[123] AustroControl. (2015, may) Österreichische Luftraumstruktur. [Online]. Available: https://www.austrocontrol.at/jart/prj3/austro_control/main.jart?rel=de&content-id=1360157906930

[124] M. Sami Fadali. (2015, nov) Solution of Linear StateSpace Equations. [Online]. Available: http://wolfweb.unr.edu/~fadali/ee472/SolState.pdf

[125] Temporal Images. (2014, jun) Cessna Skyhawk II / 100 Performance Assessment. [Online]. Available: http://www.temporal.com.au/c172.pdf

[126] Aerospaceweb. (2014, jun) Drag Coefficient & Lifting Line Theory. [Online]. Available: http://www.aerospaceweb.org/question/aerodynamics/q0184.shtml

[127] Airfoil tools. (2014, aug) Airfoil Plotter. AOPA. [Online]. Available: http://airfoiltools.com/

[128] RTL-SDR. (2015, jun) Cheap ADS-B Aircraft Radar. [Online]. Available: http://www.rtl-sdr.com/adsb-aircraft-radar-with-rtl-sdr/

A Appendix

A.1 Traffic Generator
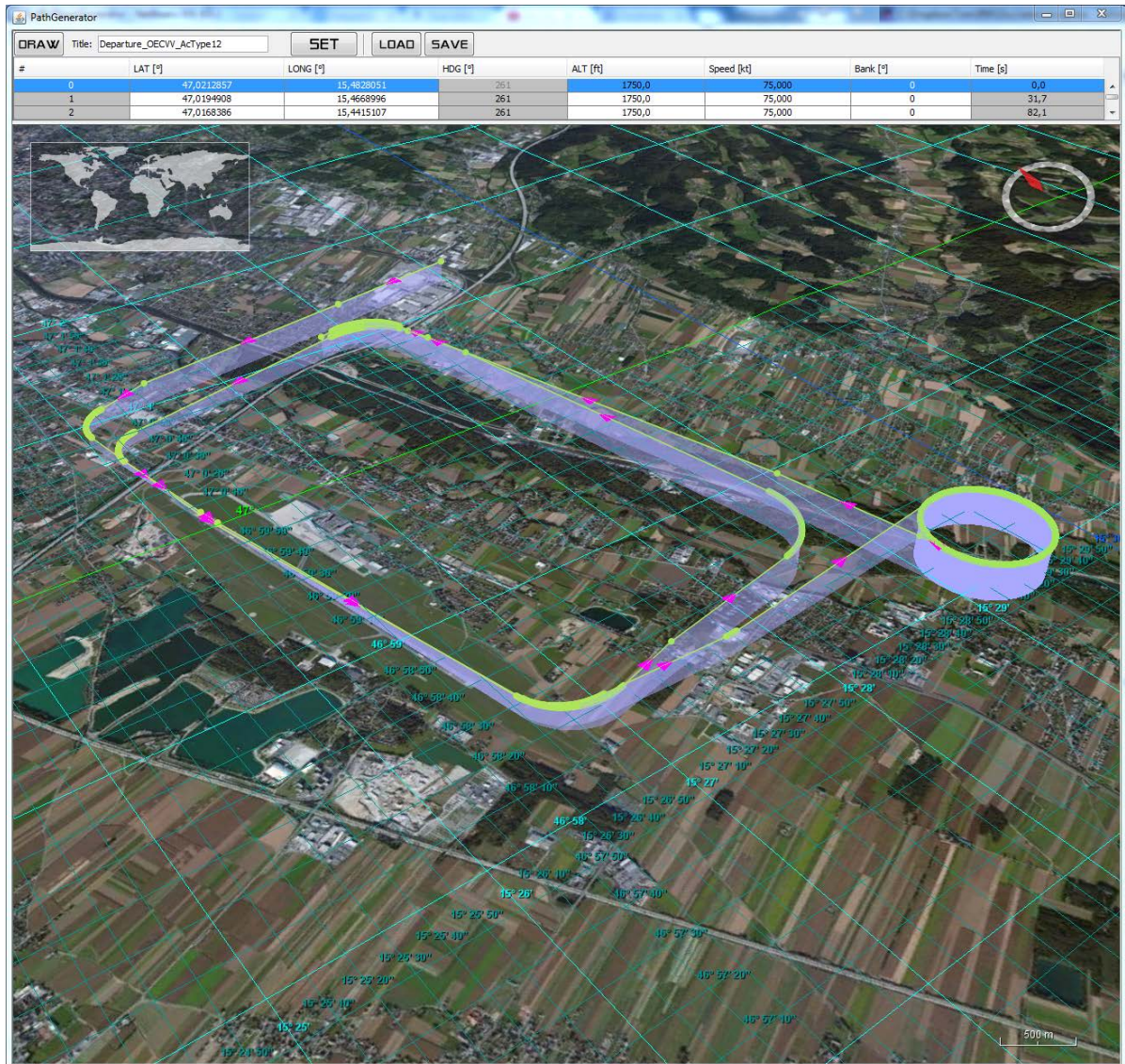
Figure A.1: Software used for trajectory generation for the experiments described in section 4. The list at the top stores all vertices of the path with the time traveled with respect to the starting point.
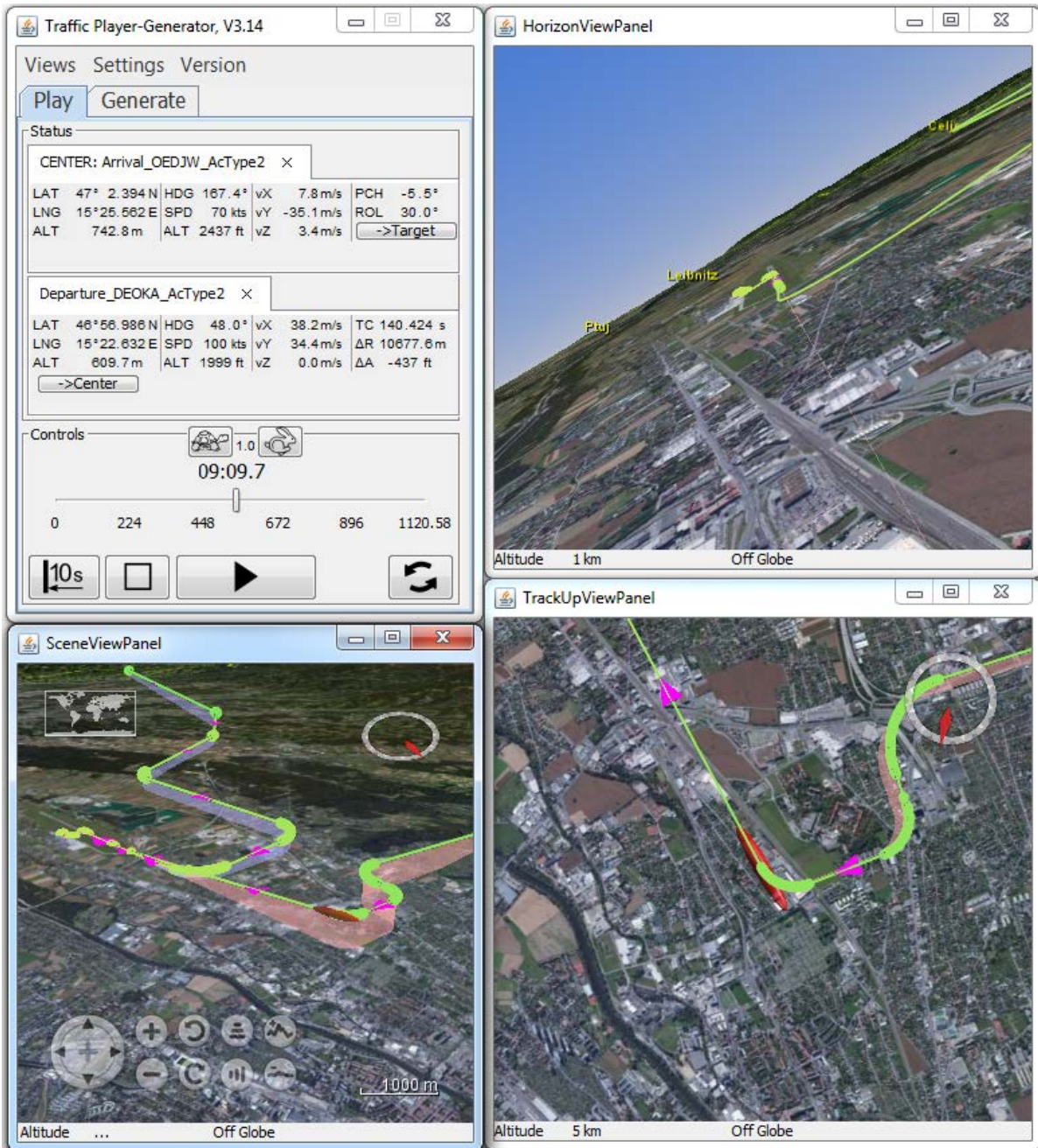
Figure A.2: Software used for trajectory visualization to enable easier editing for a collision scenario. The top left window shows the loaded aircraft paths and player-type control elements, enabling to play/pause/stop or loop.
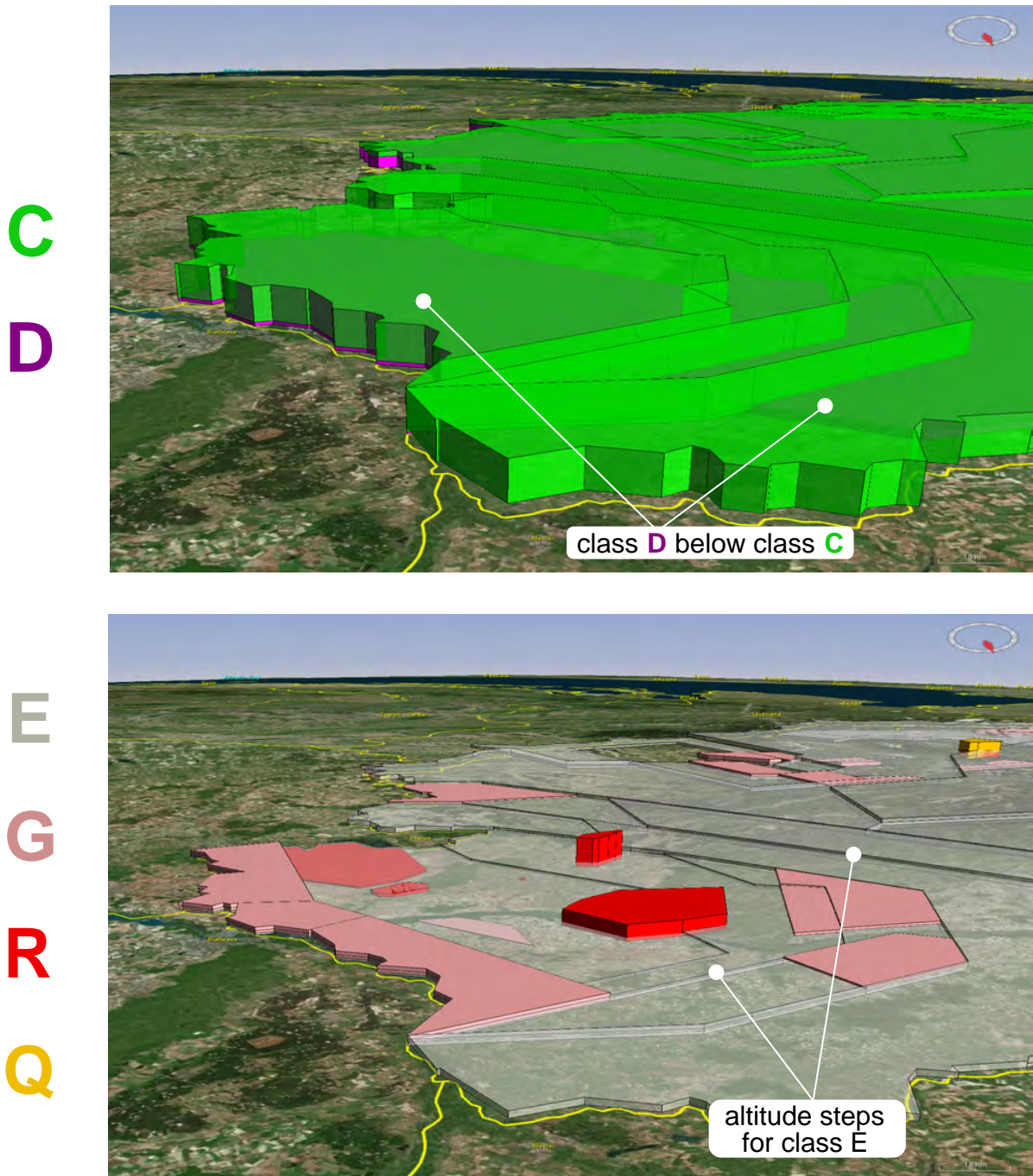
Figure A.3: Image of the Airspaces over Vienna, Austria as viewed from the North. Because of the overlapping structure and for clarity, the airspaces C and D are shown in the top image and the remaining airspaces in the bottom image. The colors of the airspace designations on the left correspond to the airspace colors on the right. Class D airspace is near the ground and covered by class C airspace. Class R is a restricted and Q is a danger area. The classes A, B and F are not used in Austria. The image was created using data from AustroControl [123] visualized in a custom JAVA program with NASA's WORLDWIND [15] library.

A.2 Experiment Environment Software
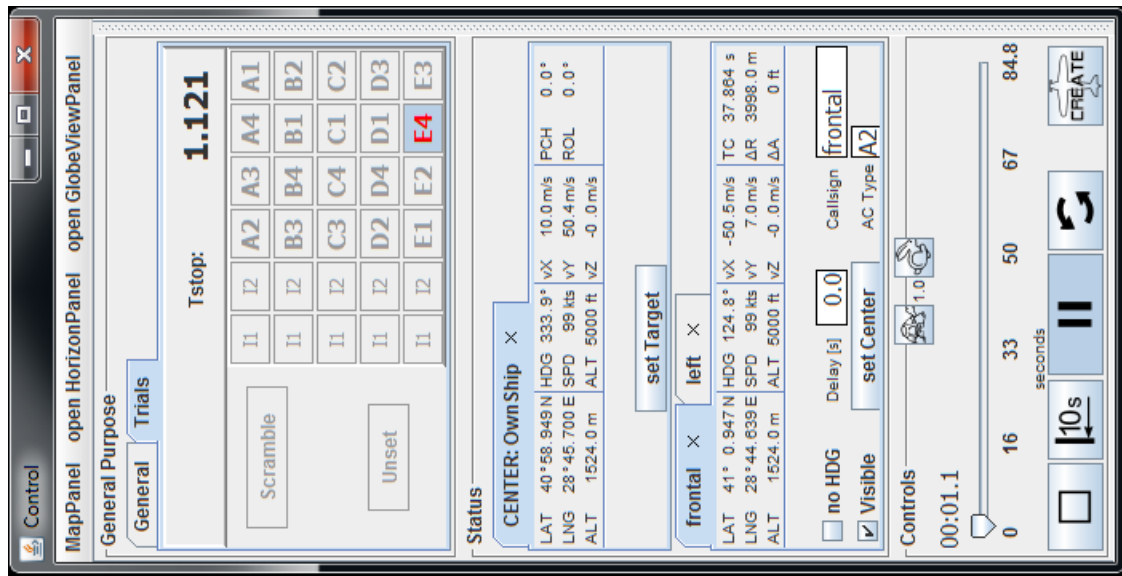
(a)

(b)

Figure A.4: Experiment Environment Software.
(a) Experiment Control Panel to register reaction time and set the trials.
(b) Sample screen for the participant showing display variant E

A.3 Coordinate Transformation

In the following, the coordinate systems in which the components of the accelerations and forces are measured are all right-handed orthogonal coordinate systems, called *frames*. In order to formulate Newton's second law with forces attached to different and rotating reference frames, it is useful to use coordinate transformations reflecting the orientation of these frames. Three of them are in particular useful in aeronautics:

- Inertial frame $\{x_I, y_I, z_I\}$
  This frame is non-rotating and non-accelerating, thereby the only one in which Newton's second law is valid. For describing aircraft motion, the flat Earth reference frame is assumed to be an inertial frame for the application of Newton's laws [113], as the earth's acceleration in space is insignificant compared to the aircraft's.

- Aerodynamic frame $\{x_A, y_A, z_A\}$
  The origin of this frame is in the center of gravity (COG) of the aircraft. The x_A-axis points in the direction of the wind-velocity vector of the COG. This vector is the sum of the wind speed vector and the aircraft's own speed relative to the moving atmosphere. The z_A-axis is in the symmetry plane on the aircraft [116]. The y_A-axis is perpendicular to a_A and z_A. Under zero wind conditions, which will be assumed in the following, the x_A-axis is tangential to the flight path.

- Body-fixed frame $\{x_B, y_B, z_B\}$
  The origin of this frame is in the center of gravity (COG). The x_B, y_B and z_B axes are aligned with the longitudinal, lateral and vertical axes of the aircraft, respectively. The y_B-axis points in the direction of the right wing.

These frames and the transformations between them are depicted in the following.

A.3.1 Transformation from the Inertial to the Aerodynamic Frame

This frame is useful when the direction of force or momentum vectors is parallel or antiparallel to the velocity vector. The transformation from the inertial frame is accomplished by three rotations (Fig. A.7). These are expressed through matrices, which are successively multiplied. This procedure is not commutative, therefore the rotations have to be made in the order specified in the following.

The first rotation with the heading or yaw angle χ is about the z_I-axis, yielding an intermediary frame. The corresponding rotation matrix is

$$\boldsymbol{R}_1(\chi) = \begin{pmatrix} \cos\chi & \sin\chi & 0 \\ -\sin\chi & \cos\chi & 0 \\ 0 & 0 & 1 \end{pmatrix} \tag{A.1}$$
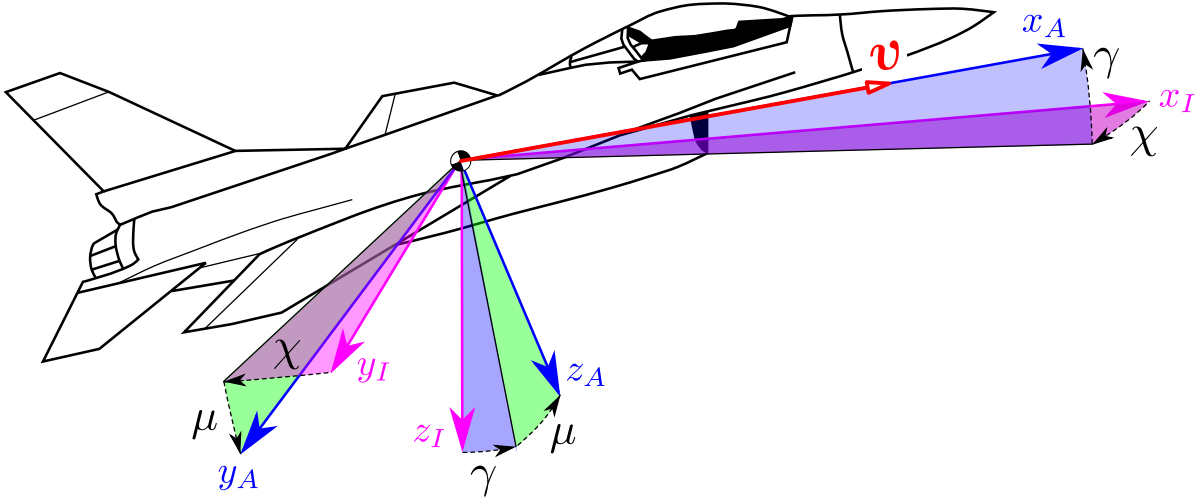
Figure A.5: Transformation from the Inertial to the Aerodynamic Coordinate System. Starting from the inertial frame $\{x_I,\ y_I,\ z_I\}$, the aerodynamic frame $\{x_B,\ y_B,\ z_B\}$ is reached by three rotations. The sequence of the angles of these rotations has to be $\chi \to \gamma \to \mu$.

where the subindex 1 refers to the first rotation from the inertial base system. The angle χ is called the *flight-path azimuth*.

Next, the second rotation is about the y-axis of the intermediary frame with the *flight-path angle* γ, aligning the new x-axis with the longitudinal axis of the aircraft. This yields another intermediary frame. The corresponding rotation matrix is

$$\boldsymbol{R}_2(\gamma) = \begin{pmatrix} \cos\gamma & 0 & -\sin\gamma \\ 0 & 1 & 0 \\ \sin\gamma & 0 & \cos\gamma \end{pmatrix} \tag{A.2}$$

Finally, the third rotation is about the new x-axis from the last step, aligning the y-axis with the lateral axis of the aircraft.

$$\boldsymbol{R}_3(\mu) = \begin{pmatrix} 1 & 0 & 0 \\ 0 & \cos\mu & \sin\mu \\ 0 & -\sin\mu & \cos\mu \end{pmatrix} \tag{A.3}$$

The final rotation angle μ is called the *bank angle*.

The entire transformation is given by

$$\boldsymbol{R}_I^A = \boldsymbol{R}_3(\mu)\,\boldsymbol{R}_2(\gamma)\,\boldsymbol{R}_1(\chi) = \begin{pmatrix} \boldsymbol{c}\gamma\,\boldsymbol{c}\chi & \boldsymbol{c}\gamma\,\boldsymbol{s}\chi & -\boldsymbol{s}\gamma \\ \boldsymbol{c}\chi\,\boldsymbol{s}\gamma\,\boldsymbol{s}\mu - \boldsymbol{c}\mu\,\boldsymbol{s}\chi & \boldsymbol{c}\mu\,\boldsymbol{c}\chi + \boldsymbol{s}\gamma\,\boldsymbol{s}\mu\,\boldsymbol{s}\chi & \boldsymbol{c}\gamma\,\boldsymbol{s}\mu \\ \boldsymbol{c}\mu\,\boldsymbol{c}\chi\,\boldsymbol{s}\gamma + \boldsymbol{s}\mu\,\boldsymbol{s}\chi & \boldsymbol{c}\mu\,\boldsymbol{s}\gamma\,\boldsymbol{s}\chi - \boldsymbol{c}\chi\,\boldsymbol{s}\mu & \boldsymbol{c}\gamma\,\boldsymbol{c}\mu \end{pmatrix} \tag{A.4}$$

where $\boldsymbol{c}$ and $\boldsymbol{s}$ is shorthand for cos and sin, respectively.

A vector $\boldsymbol{r}_A$ with components measured in the aerodynamic frame is

$$\boldsymbol{r}_A = \boldsymbol{R}_I^A \ \boldsymbol{r}_I$$

where $\boldsymbol{r}_I$ is a vector with components measured in the inertial system.

Because the transformation matrices are orthogonal, each of them has the property that the transpose of the matrix is equal to the inverse. Therefore, the inverse transformation reads

$$\boldsymbol{r}_I = \boldsymbol{R}_1^T(\chi) \ \boldsymbol{R}_2^T(\gamma) \ \boldsymbol{R}_3^T(\mu) \ \boldsymbol{r}_A$$
$$\boldsymbol{r}_I = \boldsymbol{R}_A^I \ \boldsymbol{r}_A = \left(\boldsymbol{R}_I^A\right)^{-1} \ \boldsymbol{r}_A$$
$$\Rightarrow \boldsymbol{r}_I = \left(\boldsymbol{R}_I^A\right)^T \ \boldsymbol{r}_A$$

with

$$\left(\boldsymbol{R}_I^A\right)^T = \boldsymbol{R}_A^I = \begin{pmatrix} \boldsymbol{c}\gamma \ \boldsymbol{c}\chi & \boldsymbol{c}\chi \ \boldsymbol{s}\gamma \ \boldsymbol{s}\mu - \boldsymbol{c}\mu \ \boldsymbol{s}\chi & \boldsymbol{c}\mu \ \boldsymbol{c}\chi \ \boldsymbol{s}\gamma + \boldsymbol{s}\mu \ \boldsymbol{s}\chi \\ \boldsymbol{c}\gamma \ \boldsymbol{s}\chi & \boldsymbol{c}\mu \ \boldsymbol{c}\chi + \boldsymbol{s}\gamma \ \boldsymbol{s}\mu \ \boldsymbol{s}\chi & \boldsymbol{c}\mu \ \boldsymbol{s}\gamma \ \boldsymbol{s}\chi - \boldsymbol{c}\chi \ \boldsymbol{s}\mu \\ -\boldsymbol{s}\gamma & \boldsymbol{c}\gamma \ \boldsymbol{s}\mu & \boldsymbol{c}\gamma \ \boldsymbol{c}\mu \end{pmatrix} \qquad \text{(A.5)}$$

A.3.2 Transformation from the Aerodynamic to Body Fixed Coordinate System

The body-fixed frame is useful when dealing with forces parallel or antiparallel to the aircraft frame (e.g. engine thrust, thrust reverse). From the aerodynamic frame, this frame is reached through two rotations (Fig. A.6)

The first rotation with the sideslip angle β is about the z_A-axis, yielding an intermediary frame. Because of the right-hand rule, the corresponding rotation matrix has to be calculated using a negative value for the angle ($-\beta$)

$$\boldsymbol{R}_4(-\beta) = \begin{pmatrix} \cos\beta & -\sin\beta & 0 \\ \sin\beta & \cos\beta & 0 \\ 0 & 0 & 1 \end{pmatrix} \qquad \text{(A.6)}$$

where the subindex 4 refers to the fourth rotation from the initial inertial base system (section A.3.1).

Next, the second rotation is about the y-axis of the intermediary frame with the *angle of attack* α, aligning the new x-axis with the longitudinal axis of the aircraft. This yields the body-fixed frame. The corresponding rotation matrix is

$$\boldsymbol{R}_5(\alpha) = \begin{pmatrix} \cos\alpha & 0 & -\sin\alpha \\ 0 & 1 & 0 \\ \sin\alpha & 0 & \cos\alpha \end{pmatrix} \qquad \text{(A.7)}$$

The full transformation is given by
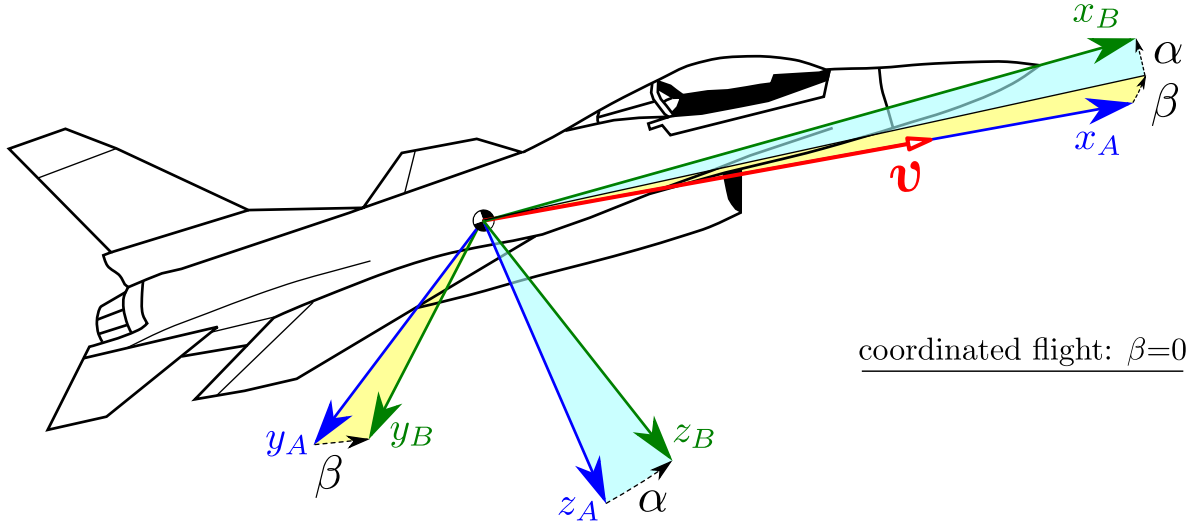
Figure A.6: Transformation from the Aerodynamic to Body Fixed Coordinate System. Starting from the aerodynamic system $\{x_A,\ y_A,\ z_A\}$, the body-fixed system $\{x_B,\ y_B,\ z_B\}$ is reached by two rotations. The sequence of the angles of these rotations has to be $-\beta \rightarrow \alpha$. The angles α and β are called the *angle of attack* and the *sideslip angle*, respectively. Flight with a sideslip angle β=0 is called *coordinated flight* [113].

$$\boldsymbol{R}_A^B = \boldsymbol{R}_5(\alpha)\ \boldsymbol{R}_4(-\beta) = \begin{pmatrix} \boldsymbol{c}\alpha\ \boldsymbol{c}\beta & -\boldsymbol{c}\alpha\ \boldsymbol{s}\beta & -\boldsymbol{s}\alpha \\ \boldsymbol{s}\beta & \boldsymbol{c}\beta & 0 \\ \boldsymbol{c}\beta\ \boldsymbol{s}\alpha & -\boldsymbol{s}\alpha\ \boldsymbol{s}\beta & \boldsymbol{c}\alpha \end{pmatrix} \tag{A.8}$$

with the inverse (i.e. transpose)

$$\boldsymbol{R}_B^A = \begin{pmatrix} \boldsymbol{c}\alpha\ \boldsymbol{c}\beta & \boldsymbol{s}\beta & \boldsymbol{c}\beta\ \boldsymbol{s}\alpha \\ -\boldsymbol{c}\alpha\ \boldsymbol{s}\beta & \boldsymbol{c}\beta & -\boldsymbol{s}\alpha\ \boldsymbol{s}\beta \\ -\boldsymbol{s}\alpha & 0 & \boldsymbol{c}\alpha \end{pmatrix} \tag{A.9}$$

A.3.3 Transformation from the Inertial to the Body Fixed Coordinate System

A coordinate transformation from the inertial to the body-fixed frame using the aerodynamic system as an intermediary frame is determined by

$$\boldsymbol{r}_B = \boldsymbol{R}_A^B\ \boldsymbol{R}_I^A\ \boldsymbol{r}_I$$

with the vectors $\boldsymbol{r}_B$ and $\boldsymbol{r}_I$ measured in the body-fixed and in the inertial frame, respectively. The matrices are taken from eqns. (A.4) and (A.8). A matrix multiplication

yields the combined transformation matrix

$$\boldsymbol{R}_I^B(\beta,\alpha,\chi,\gamma,\mu) = \boldsymbol{R}_A^B\ \boldsymbol{R}_I^A =$$

$$
\left(
\begin{array}{c|c|c}
\begin{array}{c} \boldsymbol{c\alpha\ c\beta\ c\gamma\ c\chi} - \boldsymbol{s\alpha\ c\mu\ c\chi\ s\gamma} \\ +\boldsymbol{s\mu\ s\chi} - \boldsymbol{c\alpha\ s\beta\ c\chi\ s\gamma\ s\mu} \\ -\boldsymbol{c\mu\ s\chi} \end{array} &
\begin{array}{c} \boldsymbol{c\alpha\ c\beta\ c\gamma\ s\chi} - \boldsymbol{s\alpha\ c\mu\ s\gamma\ s\chi} \\ -\boldsymbol{c\chi\ s\mu} - \boldsymbol{c\alpha\ s\beta\ c\mu\ c\chi} \\ +\boldsymbol{s\gamma\ s\mu\ s\chi} \end{array} &
\begin{array}{c} -\boldsymbol{c\gamma\ c\mu\ s\alpha} \\ -\boldsymbol{c\alpha\ c\beta\ s\gamma} \\ -\boldsymbol{c\alpha\ c\gamma\ s\beta\ s\mu} \end{array} \\
\hline
\begin{array}{c} \boldsymbol{c\gamma\ c\chi\ s\beta} + \boldsymbol{c\beta\ c\chi\ s\gamma\ s\mu} \\ -\boldsymbol{c\mu\ s\chi} \end{array} &
\begin{array}{c} \boldsymbol{c\gamma\ s\beta\ s\chi} + \boldsymbol{c\beta\ c\mu\ c\chi} \\ +\boldsymbol{s\gamma\ s\mu\ s\chi} \end{array} &
\begin{array}{c} \boldsymbol{c\beta\ c\gamma\ s\mu} \\ -\boldsymbol{s\beta\ s\gamma} \end{array} \\
\hline
\begin{array}{c} \boldsymbol{c\beta\ c\gamma\ c\chi\ s\alpha} - \boldsymbol{s\beta\ c\chi\ s\gamma\ s\mu} \\ -\boldsymbol{c\mu\ s\chi\ s\alpha} + \boldsymbol{c\alpha\ c\mu\ c\chi\ s\gamma} \\ +\boldsymbol{s\mu\ s\chi} \end{array} &
\begin{array}{c} \boldsymbol{c\beta\ c\gamma\ s\alpha\ s\chi} + \boldsymbol{c\alpha\ c\mu\ s\gamma\ s\chi} \\ -\boldsymbol{c\chi\ s\mu} - \boldsymbol{s\alpha\ s\beta\ c\mu\ c\chi} \\ +\boldsymbol{s\gamma\ s\mu\ s\chi} \end{array} &
\begin{array}{c} \boldsymbol{c\alpha\ c\gamma\ c\mu} \\ -\boldsymbol{c\beta\ s\alpha\ s\gamma} \\ -\boldsymbol{c\gamma\ s\alpha\ s\beta\ s\mu} \end{array}
\end{array}
\right)
$$

$$(\text{A.10})$$

The inverse transformation is done with the matrix

$$\boldsymbol{R}_B^I = \left(\boldsymbol{R}_I^B\right)^T =$$

$$
\left(
\begin{array}{c|c|c}
\begin{array}{c} \boldsymbol{c\alpha\ c\beta\ c\gamma\ c\chi} - \boldsymbol{s\alpha\ c\mu\ c\chi\ s\gamma} \\ +\boldsymbol{s\mu\ s\chi} - \boldsymbol{c\alpha\ s\beta\ c\chi\ s\gamma\ s\mu} \\ -\boldsymbol{c\mu\ s\chi} \end{array} &
\begin{array}{c} \boldsymbol{c\gamma\ c\chi\ s\beta} \\ +\boldsymbol{c\beta\ c\chi\ s\gamma\ s\mu} \\ -\boldsymbol{c\mu\ s\chi} \end{array} &
\begin{array}{c} \boldsymbol{c\beta\ c\gamma\ c\chi\ s\alpha} - \boldsymbol{s\beta\ c\chi\ s\gamma\ s\mu} \\ -\boldsymbol{c\mu\ s\chi\ s\alpha} + \boldsymbol{c\alpha\ c\mu\ c\chi\ s\gamma} \\ +\boldsymbol{s\mu\ s\chi} \end{array} \\
\hline
\begin{array}{c} \boldsymbol{c\alpha\ c\beta\ c\gamma\ s\chi} - \boldsymbol{s\alpha\ c\mu\ s\gamma\ s\chi} \\ -\boldsymbol{c\chi\ s\mu} - \boldsymbol{c\alpha\ s\beta\ c\mu\ c\chi} \\ +\boldsymbol{s\gamma\ s\mu\ s\chi} \end{array} &
\begin{array}{c} \boldsymbol{c\gamma\ s\beta\ s\chi} \\ +\boldsymbol{c\beta\ c\mu\ c\chi} \\ +\boldsymbol{s\gamma\ s\mu\ s\chi} \end{array} &
\begin{array}{c} \boldsymbol{c\beta\ c\gamma\ s\alpha\ s\chi} + \boldsymbol{c\alpha\ c\mu\ s\gamma\ s\chi} \\ -\boldsymbol{c\chi\ s\mu} - \boldsymbol{s\alpha\ s\beta\ c\mu\ c\chi} \\ +\boldsymbol{s\gamma\ s\mu\ s\chi} \end{array} \\
\hline
\begin{array}{c} -\boldsymbol{c\gamma\ c\mu\ s\alpha} \\ -\boldsymbol{c\alpha\ c\beta\ s\gamma} \\ -\boldsymbol{c\alpha\ c\gamma\ s\beta\ s\mu} \end{array} &
\begin{array}{c} \boldsymbol{c\beta\ c\gamma\ s\mu} \\ -\boldsymbol{s\beta\ s\gamma} \end{array} &
\begin{array}{c} \boldsymbol{c\alpha\ c\gamma\ c\mu} \\ -\boldsymbol{c\beta\ s\alpha\ s\gamma} \\ -\boldsymbol{c\gamma\ s\alpha\ s\beta\ s\mu} \end{array}
\end{array}
\right)
$$

$$(\text{A.11})$$

It is also useful to use a transformation which combines the ones shown in section A.3.1 and A.3.2. Here, three rotations are involved (Fig. A.7).

The sequence of rotation axes is the same as in section A.3.1: first with the *pitch angle* Ψ (*yaw* or *heading angle*) about the z-axis and secondly with the angle Θ about the new y-axis, aligning the resulting x-axis with the longitudinal axis of the aircraft. The last step is to rotate with the *roll angle* Φ about the longitudinal axis to align the z-axis with the aircraft's symmetry plane.

The matrices in eqns. (A.1), (A.2) and (A.3) can be reused with the angles Ψ, Θ and Φ, respectively. Therefore, the entire transformation is given by

$$
\boldsymbol{R}_I^B = \boldsymbol{R}_3(\Phi)\ \boldsymbol{R}_2(\Theta)\ \boldsymbol{R}_1(\Psi) =
\left(
\begin{array}{ccc}
\boldsymbol{c\Theta\ c\Psi} & \boldsymbol{c\Theta\ s\Psi} & -\boldsymbol{s\Theta} \\
\boldsymbol{c\Psi\ s\Theta\ s\Phi} - \boldsymbol{c\Phi\ s\Psi} & \boldsymbol{c\Phi\ c\Psi} + \boldsymbol{s\Theta\ s\Phi\ s\Psi} & \boldsymbol{c\Theta\ s\Phi} \\
\boldsymbol{c\Phi\ c\Psi\ s\Theta} + \boldsymbol{s\Phi\ s\Psi} & \boldsymbol{c\Phi\ s\Theta\ s\Psi} - \boldsymbol{c\Psi\ s\Phi} & \boldsymbol{c\Theta\ c\Phi}
\end{array}
\right)
$$

$$(\text{A.12})$$
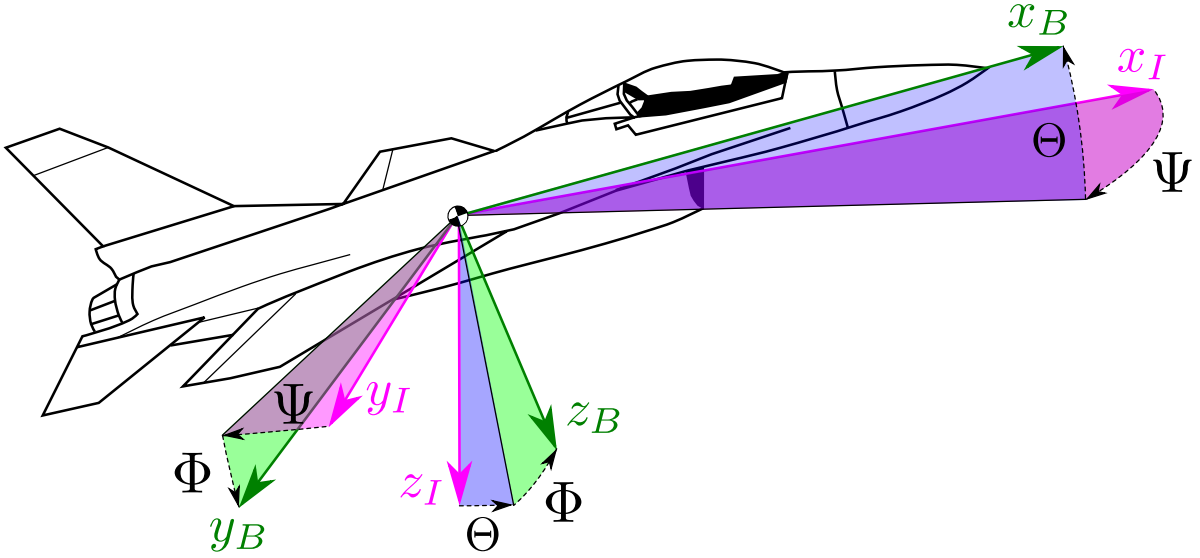
Figure A.7: Transformation from the Inertial to the Body Fixed Coordinate System. Starting from the aerodynamic system $\{x_I, y_I, z_I\}$, the body-fixed system $\{x_B, y_B, z_B\}$ is reached by two rotations. The sequence of the angles of these rotations has to be $\Psi \to \Theta \to \Phi$ (yaw-pitch-roll).

The inverse transformation reads

$$\boldsymbol{R}_B^I = \left(\boldsymbol{R}_I^B\right)^T = \begin{pmatrix} c\Theta\ c\Psi & c\Psi\ s\Theta\ s\Phi - c\Phi\ s\Psi & c\Phi\ c\Psi\ s\Theta + s\Phi\ s\Psi \\ c\Theta\ s\Psi & c\Phi\ c\Psi + s\Theta\ s\Phi\ s\Psi & c\Phi\ s\Theta\ s\Psi - c\Psi\ s\Phi \\ -s\Theta & c\Theta\ s\Phi & c\Theta\ c\Phi \end{pmatrix} \quad \text{(A.13)}$$

A.4 Comparison between bank and roll angle

A comparison between the matrices $\boldsymbol{R}_B^I(\chi, \gamma, \mu, \beta, \alpha)$ and $\boldsymbol{R}_B^I(\Psi, \Theta, \Phi)$, which both transform between the inertial and body-fixed reference frames, provides another useful simplification. This comparison for the element in row 3, column 2 of both matrices (eqns. (A.11) and (A.13)) with $\beta = 0$ (coordinated flight condition) yields

$$\cos \gamma\ \sin \mu = \cos \Theta\ \sin \Phi$$

With $\Theta = \gamma + \alpha$ (Fig. A.6) and a trigonometric addition formula, this results in

$$\frac{\sin \mu}{\sin \Phi} = \frac{\cos \gamma\ \cos \alpha - \sin \gamma\ \sin \alpha}{\cos \gamma}$$

Furthermore, it is reasonable to assume that for normal non-aerobatic flight $|\gamma|$ and $|\alpha|$ are below 15°, which renders the product of the sin-functions of γ and α comparatively

small to the product of the cos-functions. This assumption leads to

$$\frac{\sin \mu}{\sin \Phi} \approx \cos \alpha \approx 1$$
$$\rightarrow \mu \approx \Phi$$

This is supported by [113].

A.5 Supporting mathematical relations

A.5.1 Calculation of the time until the closest point of approach

Consider two aircraft, both on non-parallel tracks (Fig. A.8). The current velocities,
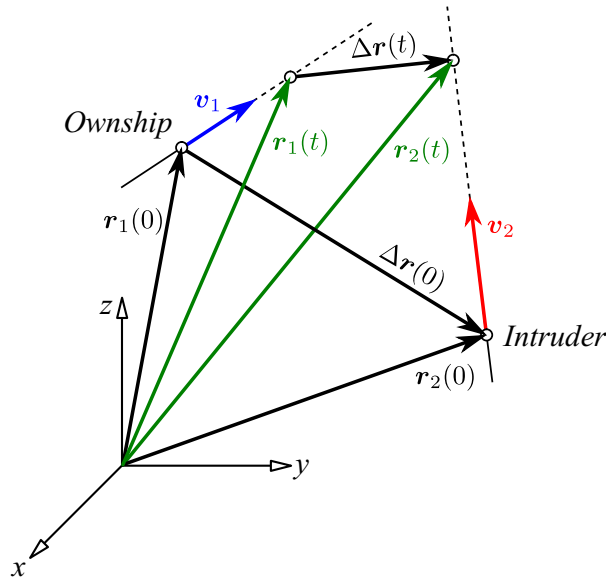
Figure A.8: Calculation of the time until the closest point of approach

measured in an earth-fixed frame, for the ownship (index 1) and the intruder (index 2) are $\boldsymbol{v_1}$ and $\boldsymbol{v_2}$, respectively. The position vectors at a given, future point in time t are

$$\boldsymbol{r}_1(t) = \boldsymbol{r}_1(0) + \boldsymbol{v}_1\ t$$
$$\boldsymbol{r}_2(t) = \boldsymbol{r}_2(0) + \boldsymbol{v}_2\ t$$

with $\boldsymbol{r}_1(0)$ and $\boldsymbol{r}_2(0)$ referring to the current positions of the ownship and the intruder.

This relation formulates a linear path for both aircraft, moving at constant speeds $\boldsymbol{v_1}$ and $\boldsymbol{v_2}$, respectively. The relative position vector from the ownship to the intruder is $\Delta \boldsymbol{r}(t) := \boldsymbol{r}_2(t) - \boldsymbol{r}_1(t)$, which yields for above defined position vectors

$$\Delta \boldsymbol{r}(t) = \boldsymbol{r}_2(0) - \boldsymbol{r}_1(0) + (\boldsymbol{v}_2 - \boldsymbol{v}_1)\ t = \Delta \boldsymbol{r}(0) + \Delta \boldsymbol{v}\ t \tag{A.14}$$

In order to find time to the closest point of approach, this length of this vector has to reach a minimum:

$$\left. \frac{\mathrm{d}|\Delta\boldsymbol{r}|}{\mathrm{d}t} \right|_{t=t^*} = 0$$

where $|\Delta\boldsymbol{r}| = \sqrt{\Delta\boldsymbol{r}^T \cdot \Delta\boldsymbol{r}}$ and t^* has to be determined. The square root has no bearing on the time t^* where the minimum of $|\Delta\boldsymbol{r}|$ is located. Thus differentiation yields

$$\Delta\dot{\boldsymbol{r}}^T \, \Delta\boldsymbol{r} + \Delta\boldsymbol{r}^T \, \Delta\dot{\boldsymbol{r}} = 0 \tag{A.15}$$

where $\Delta\dot{\boldsymbol{r}} = \boldsymbol{v}_2 - \boldsymbol{v}_1$ from eqn. (A.14). Inserting the vectors with components yields

$$\begin{pmatrix} \Delta v_x & \Delta v_y & \Delta v_z \end{pmatrix} \cdot \begin{pmatrix} \Delta r_x(t^*) \\ \Delta r_y(t^*) \\ \Delta r_z(t^*) \end{pmatrix} + \begin{pmatrix} \Delta r_x(t^*) & \Delta r_y(t^*) & \Delta r_z(t^*) \end{pmatrix} \cdot \begin{pmatrix} \Delta v_x \\ \Delta v_y \\ \Delta v_z \end{pmatrix} = 0 \tag{A.16}$$

where $\Delta r_x(t^*) = \Delta\boldsymbol{r}_x(0) + \Delta\boldsymbol{v}_x \, t^*$ (from eqn. (A.14)). Similar indices apply to $\Delta r_y(t^*)$ and $\Delta r_z(t^*)$, respectively.

Multiplication and simplification of eqn. (A.16) yields

$$\Delta\boldsymbol{v}^T \cdot \Delta\boldsymbol{v} \,\, t^* + \Delta\boldsymbol{v}^T \cdot \Delta\boldsymbol{r}(0) = 0$$

which leads to

$$t^* = -\left(\Delta\boldsymbol{v}^T \cdot \Delta\boldsymbol{v} \right)^{-1} \Delta\boldsymbol{v}^T \cdot \Delta\boldsymbol{r}(0) = -\boldsymbol{\Psi}(\Delta\boldsymbol{v}) \, \boldsymbol{r}(0) \tag{A.17}$$

The row vector $\boldsymbol{\Psi}(.)$ is called the Pseudoinverse and is also used for the error-optimal solution of an underdetermined system of linear equations.

A.5.2 Estimation of the time until the closest point of approach used by the TCAS system

TCAS collision detection logic [48] uses an estimation to determine the time to closest point of approach (CPA) between the ownship and the intruder. It is defined as

$$\tau = \frac{|\Delta\boldsymbol{r}|}{|\Delta\dot{\boldsymbol{r}}|} = \frac{|\Delta\boldsymbol{r}| \,\, |\Delta\boldsymbol{r}|}{\Delta\boldsymbol{v} \, \boldsymbol{e}_r \,\, |\Delta\boldsymbol{r}|} = \frac{\Delta\boldsymbol{r} \cdot \Delta\boldsymbol{r}}{\Delta\boldsymbol{v} \cdot \Delta\boldsymbol{r}} \tag{A.18}$$

where $|\Delta\boldsymbol{r}|$ (Fig. A.8) is the range and $|\Delta\dot{\boldsymbol{r}}|$ is the range rate between the ownship and the intruder. The vector $\Delta\boldsymbol{v}$ is the relative speed vector and $\boldsymbol{e}_r$ a unit vector in the direction of $\Delta\boldsymbol{r}$.

The time τ and the actual time to the CPA (shown in section A.5.1) coincide only when the aircraft are on a collision course and not changing speeds. τ is only an approximation

of time to CPA when the aircraft will pass near each other, because shortly before actual CPA is reached the number of τ will increase sharply, approaching infinity (division by zero at CPA, because $\Delta \dot{\boldsymbol{r}} = 0$ there).

A.5.3 Solution of a linear, time invariant system

$$\text{given} \qquad \dot{\boldsymbol{x}}(t) = \boldsymbol{A}\,\boldsymbol{x}(t) + \boldsymbol{B}\,\boldsymbol{u}(t) \qquad \text{with} \qquad \boldsymbol{x}(t_0) = \boldsymbol{x}_0$$

Laplace transformation of that is

$$s\,\bar{\boldsymbol{x}}(s) - \boldsymbol{x}_0 = \boldsymbol{A}\,\bar{\boldsymbol{x}}(s) + \boldsymbol{B}\,\bar{\boldsymbol{u}}(s)$$
$$\bar{\boldsymbol{x}}(s) = (s\,\boldsymbol{I} - \boldsymbol{A})^{-1}\,\boldsymbol{x}_0 + (s\,\boldsymbol{I} - \boldsymbol{A})^{-1}\,\boldsymbol{B}\,\bar{\boldsymbol{u}}(s) \tag{A.19}$$

The state-transition matrix [124] is defined with an inverse Laplace transformation: $\boldsymbol{\Phi}(t,t_0) := \mathscr{L}^{-1}\{(s\,\boldsymbol{I} - \boldsymbol{A})^{-1}\}$ from time t_0 to t. This determines the time-domain solution of eqn. (A.19), using the convolution theorem for the second summand:

$$\boldsymbol{x}(t) = \underbrace{\boldsymbol{\Phi}(t,t_0)\,\boldsymbol{x}_0}_{\text{Zero-input Response}} + \underbrace{\int_{t_0}^{t} \boldsymbol{\Phi}(t,\tau)\,\boldsymbol{B}\,\boldsymbol{u}(\tau)\,\mathrm{d}\tau}_{\text{Zero-state Response}} \tag{A.20}$$

A.5.4 Low-pass filter

$$p_0 = k_t\,\dot{p} + p \tag{A.21}$$

where p_0 is the commanded value (e.g. φ_e), k_t is the time constant and p is the filtered value. The solution of this equation is

$$p(t) = p_0\left(1 - e^{-\frac{t}{k_t}}\right)$$
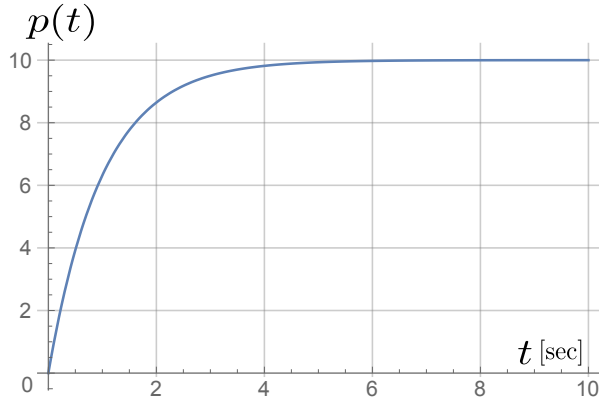
Example for $p_0 = 10$ and $k_t = 0.1$

A.5.5 Some useful matrix expressions

$$\left(\boldsymbol{x}^T\,\boldsymbol{A}\right) = \left(\boldsymbol{A}\,\boldsymbol{x}\right)^T \qquad \frac{\mathrm{d}}{\mathrm{d}\boldsymbol{x}}\left(\boldsymbol{A}\,\boldsymbol{x}\right) = \boldsymbol{A} \qquad \frac{\mathrm{d}}{\mathrm{d}\boldsymbol{x}}\left(\boldsymbol{x}^T\,\boldsymbol{A}\,\boldsymbol{x}\right) = 2\,\boldsymbol{A}\,\boldsymbol{x}$$

Table A.1: Some useful matrix expressions

A.6 Aircraft characteristics for the Cessna 172S
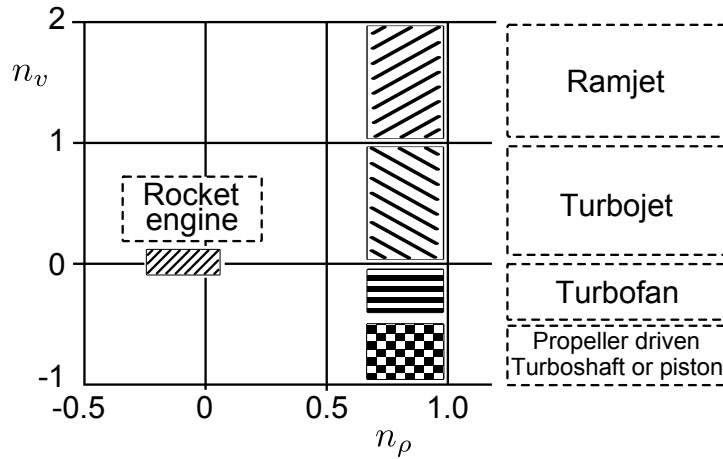
Figure A.9: Ranges for n_v and n_ρ for different propulsion systems [112]. The Cessna 172S is located within the propeller-driven region.

	Imperial		Metric	
Maximum take-off weight (MTOW)	2550	lb	1156.6	kg
Maximum speed at sea level	126	kts	64.8	m/s
Stall speed (flaps up, no bank angle)	53	kts	27.3	m/s
Maneuvering speed with MTOW	102	kts	52.5	m/s
Never exceed speed	160	kts	82.3	m/s
Usable fuel capacity	53	gal. US	200.6	l
Wing span	36.08	ft	11	m
Wing area	174	ft^2	16.2	m^2
Engine brake horsepower	180	bhp	134	kW
Max. wing loading	14.7	lb/ft^2	71.77	kg/m^2
Service ceiling	14000	ft	4267	m
Max. rate of climb at sea level	730	fpm	3.7	m/s
Max. thrust at sea level	446	lb	1983.8	N
Max. lift at sea level	2175	lb	9677	N

Table A.2: Basic characteristics of a Cessna 172S aircraft [120] [125]
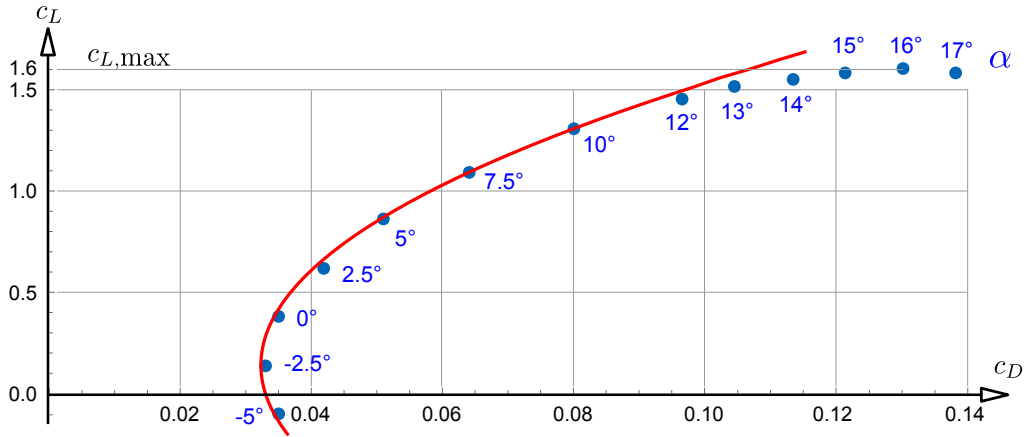
Figure A.10: Drag polar for the Cessna 172S. This plot is created for NACA 2412 airfoil profile of this aircraft (Fig. A.11) [126]. The axes c_L and c_D represent the coefficients of lift and drag, respectively, which both depend on the angle of attack α. The dots represent the data provided by the sources, the red line the widely-used parabolic approximation function $c_D = c_{D,0} + k\,(c_L - c_{L,0})^2$ [116]. The parameters used for this equation were $c_{D,0} = 0.033$, $c_{L,0} = 0.14$ and $k = 0.035$.
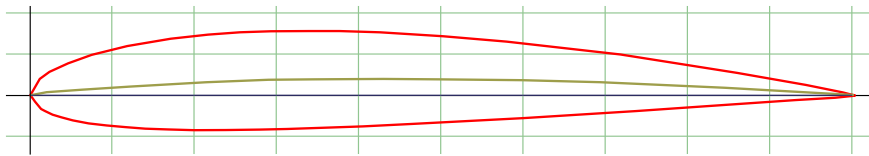
Figure A.11: Airfoil NACA 2412 used for the Cessna 172S [127]

A.7 Miscellaneous

Sleep deprivation [h]	Comparable number of glasses beer
8	10 - 11
6	7 - 8
4	5 - 6
2	2 - 3

Table A.3: Comparison between sleep deprivation and alcohol consumption [37].

Frame 1   Frame 2   Frame 3

Figure A.12: Three frames from a video showing the aircraft shortly before and after the collision over the Hudson river [16]
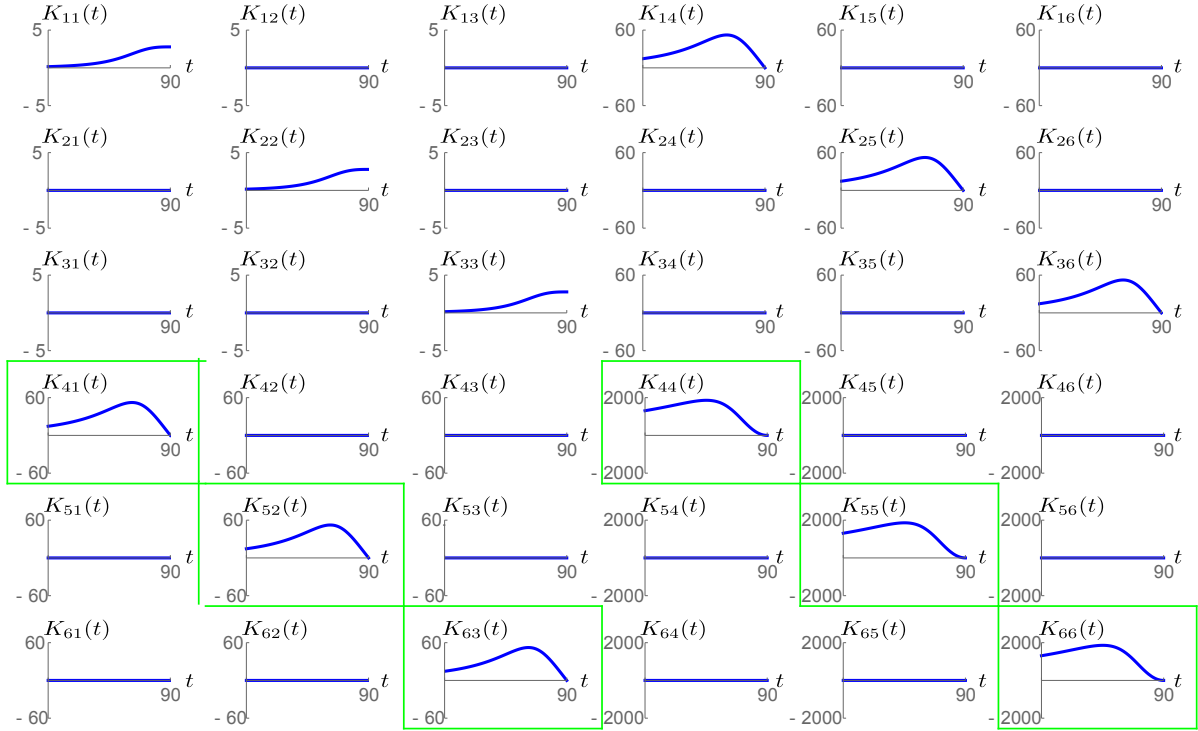
Figure A.13: Numerical evaluation of the Riccati-matrix $K(t)$. The parameters used for numerical integration of eqn. (5.16) were $t_f = 90$, $a_{p,xy} = a_{p,z} = 5 \cdot 10^{-3}$, $a_{e,xy} = a_{e,z} = 1 \cdot 10^{-3}$ and $s_{xy} = s_z = 0.6$ for the matrices $\boldsymbol{W}_p$, $\boldsymbol{W}_e$ and $\boldsymbol{S}$, respectively. When using this result with eqns. (5.13), (5.7) and (5.8) to obtain the control law, all but the elements of $\boldsymbol{K}(t)$ highlighted in green cancel out because of the zero-elements in the matrices $\boldsymbol{Q}$ and $\boldsymbol{P}$.

Rating	Description
A	**Risk of Collision**. Aircraft proximity in which serious risk of collision has existed.
B	**Safety not assured**. Aircraft proximity in which the safety of the aircraft may have been compromised
C	**No risk of collision**. Aircraft proximity in which no risk of collision has existed
D	**Risk not determined**. Aircraft proximity in which insufficient information was available to determine the risk involved, or inconclusive or conflicting evidence precluded such determination.
E	Met the criteria for reporting but, by analysis, it was determined that normal procedures, safety standards and parameters pertained.

Table A.4: Risk ratings used by the UK Airprox Board [5]
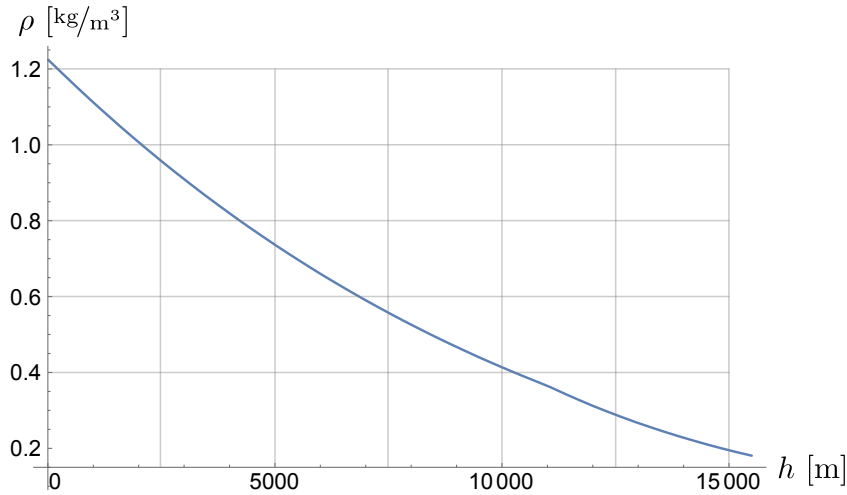
Figure A.14: Air density ρ as a function of the altitude h above mean sea level [14].

Mode S Transponder	ADS-B
The Mode S protocol is an updated version of the Mode A/C protocol used in transponders since the 1940s. Mode S datagrams include altitude (to facilitate separation control) and a unique airframe identifier (called the *ICAO number*). A Mode S-equipped aircraft replies to radar interrogation by either ground radar (secondary surveillance) or other aircraft (*Traffic Collision Avoidance System*, or TCAS).	Automatic Dependent Surveillance-Broadcast (ADS-B) is a communication protocol using the Extended Squitter (ES) capability of the Mode S Transponder transport layer. In ascending order, the protocol is: • **A**utomatic : no pilot input is necessary • **D**ependent : it is primarily dependent on GPS location and altimeter. Other aircraft characteristics my be predefined and also transmitted. • **S**urveillance : it provides current information about the transmitting aircraft • **B**roadcast : it is one-way, meaning that the information is broadcast to all receivers within range

Table A.5: Mode S Transponder [73] and ADS-B [103]